Springer Series in Chemical Physics 104

Kaoru Yamanouchi
Katsumi Midorikawa *Editors*

Progress in Ultrafast Intense Laser Science IX

Springer
PUILS
JILS

Springer Series in
CHEMICAL PHYSICS 104

Springer Series in

CHEMICAL PHYSICS

The purpose of this series is to provide comprehensive up-to-date monographs in both well established disciplines and emerging research areas within the broad fields of chemical physics and physical chemistry. The books deal with both fundamental science and applications, and may have either a theoretical or an experimental emphasis. They are aimed primarily at researchers and graduate students in chemical physics and related fields.

Kaoru Yamanouchi • Katsumi Midorikawa
Editors

Progress in Ultrafast Intense Laser Science

Volume IX

Springer

Editors
Professor Kaoru Yamanouchi
Department of Chemistry
The University of Tokyo
Tokyo, Japan

Dr. Katsumi Midorikawa
Extreme Photonics Research Group
RIKEN
Saitama, Japan

Series editors:
Professor A.W. Castleman Jr.
Department of Chemistry
The Pennsylvania State University
University Park, USA

Professor K. Yamanouchi
Department of Chemistry
University of Tokyo
Tokyo, Japan

Professor J.P. Toennies
Max-Planck-Institut für
Strömungsforschung
Göttingen, Germany

Professor W. Zinth
Institut für Medizinische Optik
Universität München
München, Germany

ISSN 0172-6218 Springer Series in Chemical Physics
ISBN 978-3-642-35051-1 ISBN 978-3-642-35052-8 (eBook)
DOI 10.1007/978-3-642-35052-8
Springer Heidelberg New York Dordrecht London

Library of Congress Control Number: 2006927806

Preface

We are pleased to present the ninth volume of Progress in Ultrafast Intense Laser Science. As the frontiers of ultrafast intense laser science rapidly expand ever outward, there continues to be a growing demand for an introduction to this interdisciplinary research field that is at once widely accessible and capable of delivering cutting-edge developments. Our series aims to respond to this call by providing a compilation of concise review-style articles written by researchers at the forefront of this research field, so that researchers with different backgrounds as well as graduate students can easily grasp the essential aspects.

As in previous volumes of PUILS, each chapter of this book begins with an introductory part, in which a clear and concise overview of the topic and its significance is given, and moves onto a description of the authors' most recent research results. All chapters are peer-reviewed. The articles of this ninth volume cover a diverse range of the interdisciplinary research field, and the topics may be grouped into four categories: ultrafast molecular responses to an intense laser field (Chaps. 1–3), advanced techniques for attosecond pulse generation (Chaps. 4–6), atomic and molecular responses to attosecond and XUV pulses (Chaps. 7–10), and attosecond pulse interaction with solid materials (Chaps. 11 and 12).

From the third volume, the PUILS series has been edited in liaison with the activities of the Center for Ultrafast Intense Laser Science at the University of Tokyo, which has also been responsible for sponsoring the series and making the regular publication of its volumes possible. From the fifth volume, the Consortium on Education and Research on Advanced Laser Science, the University of Tokyo, has joined this publication activity as one of the sponsoring programs. The series, designed to stimulate interdisciplinary discussion at the forefront of ultrafast intense laser science, has also collaborated since its inception with the annual symposium series of ISUILS (http://www.isuils.jp/), sponsored by JILS (Japan Intense Light Field Science Society). The present volume has been compiled as a special edition commemorating the discussions at the ICOMP12-ATTO3 joint conference (the 12th International Conference on Multiphoton Processes and the 3rd International Conference on Attosecond Physics) held in Sapporo, Japan, in July 2011. Presenters

from this conference have kindly contributed to this volume, introducing us to their fields and reporting on their latest research results.

We would like to take this opportunity to thank all of the authors who have kindly contributed to the PUILS series by describing their most recent work at the frontiers of ultrafast intense laser science. We also thank the reviewers who have read the submitted manuscripts carefully. One of the co-editors (KY) thanks Ms. Chie Sakuta for her help with the editing processes. Last but not least, our gratitude goes out to Dr. Claus Ascheron, Physics Editor of Springer-Verlag at Heidelberg, for his kind support.

We hope this volume will convey the excitement of ultrafast intense laser science to the readers, and stimulate interdisciplinary interactions among researchers, thus paving the way to explorations of new frontiers.

Tokyo, Japan — Kaoru Yamanouchi
Saitama, Japan — Katsumi Midorikawa

Contents

Chapter 1
Trajectory-Based Coulomb-Corrected Strong Field Approximation

T.-M. Yan, S.V. Popruzhenko, and D. Bauer

Abstract The strong field approximation (SFA) is one of the most successful theoretical approaches to tackle the problem of atomic or molecular ionization in intense laser fields. In the semi-classical limit, the SFA possesses an appealing interpretation in terms of interfering quantum trajectories, which mathematically originate from the saddle point approximation to the SFA transition matrix element. The trajectories not only allow to interpret particular features in photoelectron spectra in an intuitive way in terms of possible electron pathways typical for a quantum mechanical "multi-slit experiment" but also serve as a starting point for adopting Coulomb corrections.

1.1 Introduction

The development of ultrafast intense laser technology has offered the unprecedented opportunity to explore the dynamics of atomic and molecular systems. With the external light field strong enough to invoke nonperturbative multiphoton absorption and the temporal resolution of ultrafast lasers high enough to resolve the motion of electrons on the attosecond time scale, researchers are able to image electronic dynamics by means of diverse strong field processes. Among these strong field phenomena, atomic single-ionization is undoubtedly the fundamental key process and the prerequisite for the further understanding of strong field physics [1].

Experimentally, differential photoelectron momentum distributions are of essential interest because they provide a kinematically complete picture of the ionization process under study. Such measurements are possible since the invention of

T.-M. Yan · D. Bauer (✉)
Institut für Physik, Universität Rostock, 18051 Rostock, Germany
e-mail: dieter.bauer@uni-rostock.de

T.-M. Yan
Max-Planck-Institut für Kernphysik, Postfach 103980, 69029 Heidelberg, Germany

S.V. Popruzhenko
National Research Nuclear University "Moscow Engineering Physics Institute",
Kashirskoe Shosse 31, 115409 Moscow, Russia

K. Yamanouchi, K. Midorikawa (eds.), *Progress in Ultrafast Intense Laser Science*,
Springer Series in Chemical Physics 104, DOI 10.1007/978-3-642-35052-8_1,

the so-called "reaction microscope" (COLTRIMS, cold target recoil ion momentum spectroscopy) [2].

Theoretically, the most accurate tool to explore the non-relativistic dynamics of atomic ionization is solving the corresponding time-dependent Schrödinger equation (TDSE). However, solving the TDSE for strong laser pulses in full dimensionality is prohibitive for more than two electrons. Even in the case of only one active electron, the numerical demand is very high for long wavelengths or elliptical polarization. Moreover, the result from an *ab initio* TDSE solution often lacks physical insight because the essential physics behind the appearance of particular spectral features remains hidden.

The (almost) analytical strong field approximation (SFA) [3–5] yields maximum physical insight, provided the photoelectron transition matrix element is written in terms of (interfering) quantum trajectories [1]. However, the neglect of the long-range Coulomb interaction in the ionization of neutral atoms in the SFA leads to severe discrepancies when SFA results are compared to experiment or *ab initio* numerical solutions, particularly in the low energy regime. Such disagreements include Coulomb-induced asymmetries in both elliptically [6, 7] and few-cycle linearly polarized fields [8], cusps and horn-like structures in photoelectron momentum distributions in the tunneling regime [9, 10], experimentally observed near-threshold radial structures [9, 11], and the "low-energy structure" at long wavelengths [12, 13].

Many strategies based on the SFA have been proposed in order to include Coulomb interaction, for instance a trajectory-based perturbation theory with a matching procedure for the calculation of ionization rates [14], the Coulomb–Volkov approximation (CVA) [15, 16], the eikonal-Volkov approximation (EVA) [17], the trajectory-based Coulomb-corrected strong field approximation (TCSFA) [18, 19], or the doubly distorted-wave method (DDCV) [20].

In this work, a general overview of the TCSFA is given, intending to provide an improved theoretical tool beyond the plain SFA. The introduction of the method is accompanied by a test case in which Coulomb effects are important, namely atomic hydrogen interacting with a few-cycle long-wavelength laser pulse. Interference fringes in the photoelectron spectrum are analyzed using bivariate histograms of trajectory data.

1.2 Theoretical Description of Atomic Strong Field Ionization

1.2.1 Strong Field Approximation

The idea behind the SFA is the assumption that after the electron enters the continuum at time $t = t_r$, only the interaction between the electron and the external field needs to be considered, while the influence of the binding potential is neglected. In its simplest form, the SFA accounts only for the so-called "direct" ionization, i.e., without "rescattering". The final state of the electron characterized by the

asymptotic momentum $\mathbf{p}$ in the Keldysh–Faisal–Reiss amplitude [3–5] is a Gordon–Volkov state,

$$\left|\psi_{\mathbf{p}}^{(\mathrm{GV})}(t)\right\rangle = e^{-iS_{\mathbf{p}}(t)}\left|\mathbf{p}+\mathbf{A}(t)\right\rangle, \quad S_{\mathbf{p}}(t) = \int^{t} \frac{1}{2}\left(\mathbf{p}+\mathbf{A}\left(t'\right)\right)^2 dt',$$

leading to the transition matrix element [21, 22],

$$M_{\mathbf{p}}^{(0)} = -i\int_0^{\infty} \left\langle \mathbf{p}+\mathbf{A}\left(t'\right)\middle|\mathbf{r}\cdot\mathbf{E}(t)|\psi_0\right\rangle e^{iS_{I_p,\mathbf{p}}(t)}\, dt, \tag{1}$$

with $|\psi_0\rangle$ the initial bound state of the electron, I_p the ionization potential of the atom, $\mathbf{A}(t)$ the vector potential of the light pulse, $\mathbf{E}(t) = -\partial_t \mathbf{A}(t)$ the electric field vector under the dipole approximation, and the action

$$S_{I_p,\mathbf{p}}(t) = \int^{t}\left[\frac{1}{2}\left(\mathbf{p}+\mathbf{A}\left(t'\right)\right)^2 + I_p\right] dt'.$$

Atomic units are used unless noted otherwise.

The SFA has achieved gratifying agreement with *ab initio* results for atomic systems with a short-range potential (as is the case for electron detachment from negative ions [23]). However, the neglect of the interaction between released electrons and the long-range binding potential is shown to result in large deviations from experimental or *ab initio* results, which implies the necessity of Coulomb corrections to the SFA model.

1.2.2 Steepest Descent Method Applied to the SFA

Although the time integration in Eq. (1) can be carried out numerically with ease, the transition amplitude may be simplified using the steepest descent method [24], which is also the crucial step to implement the TCSFA. If the number of photons N of energy $\hbar\omega$ required to overcome the ionization potential I_p is large, $N = I_p/\hbar\omega \gg 1$, the time integral in the SFA matrix element is approximated by a sum over all saddle points $\{t_s^{(\alpha)}\}$,

$$M_{\mathbf{p}}^{(0)} \sim \sum_{\alpha} \frac{e^{iS_{I_p,\mathbf{p}}(t_s^{(\alpha)})}}{S''_{I_p,\mathbf{p}}(t_s^{(\alpha)})}, \tag{2}$$

where S'' denotes the second-order time derivative of S. The proportionality constant depends on I_p only [1] and is omitted here. Note that there is $S''_{I_p,\mathbf{p}}(t_s^{(\alpha)})$ in the denominator and not the square-root of it, as a modified steepest descent approach is required for the Coulomb potential [1].

The coherent summation over different trajectories which end up with the same asymptotic momentum $\mathbf{p}$ is a manifestation of the "multi-slit-in-time"-nature [27–29] of the quantum mechanical ionization process, leading to quantum interference. In addition, since $t_s^{(\alpha)}$ is complex, the calculation of trajectories has been naturally extended into the complex plane, known as the imaginary time method (ITM)

(see [30] for a review). The ITM straightforwardly includes tunneling effects. Although the SFA starts with an assumption neglecting the Coulomb interaction, the intuitive concept of quantum trajectories allows us to incorporate Coulomb effects by modifying the action integral and the trajectories accordingly.

The αth saddle point $t_s^{(\alpha)}$ satisfies the stationary phase condition or saddle-point equation (SPE)

$$\left.\frac{\partial S_{I_p,\mathbf{p}}}{\partial t}\right|_{t_s^{(\alpha)}} = 0 \quad \Rightarrow \quad \frac{1}{2}\left(\mathbf{p} + \mathbf{A}\left(t_s^{(\alpha)}\right)\right)^2 = -I_p. \tag{3}$$

It is evident that, as $I_p > 0$ and $\mathbf{p}$ is real, the solution $t_s^{(\alpha)}$ is complex. Generally, smaller $\mathrm{Im}\, t_s$ assign larger weights to the corresponding terms in Eq. (2). Usually, the terms with smallest $\mathrm{Im}\, t_s$ have t_r near the times when the absolute value of the electric field is around a local maximum.

Expression (2), besides approximating the integral (1), also offers deeper physical insight into the ionization process by virtue of "quantum orbits" [25, 26]. At $t_s^{(\alpha)}$ a trajectory is launched, with $S_{I_p,\mathbf{p}}(t_s^{(\alpha)})$ being the corresponding action integral. The complex trajectories are a natural extension of classical trajectories which are calculated from Newton's equation of motion, but the time propagation is along the vertical path of constant-t_r in the complex-time plane. Without Coulomb interaction the complex trajectories are

$$\mathbf{r}(t) = \int_{t_s}^{t} \left[\mathbf{A}\left(t'\right) + \mathbf{p}\right] dt' + \mathbf{r}(t_s).$$

In order to fulfill $\mathrm{Re}\,\mathbf{r}(t_s) = 0$ (the electron starts at the position of the nucleus in the origin) we require a purely imaginary $\mathbf{r}(t_s) = i\,\mathrm{Im}\,\mathbf{r}(t_s)$ as one initial condition. The other initial condition is determined by the chosen asymptotic momentum and the solution t_s of the SPE (3),

$$\dot{\mathbf{r}}|_{t=t_s} = \mathbf{v}(t_s) = \mathbf{A}(t_s) + \mathbf{p}.$$

At time $t_r = \mathrm{Re}\, t_s$ the electron reaches the classically allowed region at the "tunnel exit"

$$\begin{aligned}\mathbf{r}(t_r) = \mathbf{r}(\mathrm{Re}\, t_s) &= \int_{t_s}^{t_r} \left[\mathbf{A}\left(t'\right) + \mathbf{p}\right] dt' + \mathbf{r}(t_s) \\ &= -i\,\mathbf{p}\,\mathrm{Im}\, t_s + \mathbf{a}(t_r) - \mathbf{a}(t_s) + i\,\mathrm{Im}\,\mathbf{r}(t_s),\end{aligned}$$

where the excursion of a free electron in a laser field

$$\mathbf{a}(t) = \int^{t} \mathbf{A}\left(t'\right) dt'$$

has been introduced. We can always choose the initial, purely imaginary position $i\,\mathrm{Im}\,\mathbf{r}(t_s)$ such that $\mathrm{Im}\,\mathbf{r}(t_r) = 0$. Then, the tunnel exit lies in real position space,

$$\mathbf{r}(t_r) = \mathrm{Re}\,\mathbf{r}(t_r) = \mathbf{a}(t_r) - \mathrm{Re}\,\mathbf{a}(t_s),$$

and for all real times $t > t_r$ the position

$$\mathbf{r}_{t\geq t_r}(t) = \int_{t_r}^{t} \left[\mathbf{A}(t') + \mathbf{p}\right] dt' + \mathbf{r}(t_r)$$

remains real.

1.2.3 Trajectory-Based Coulomb Correction

In this section, the key idea of the TCSFA is introduced, namely including the effect of the Coulomb potential via the modification of the quantum orbits. Henceforth, the subscript "0" is used to indicate plain SFA, "Coulomb-free" variables. The action as a function of the saddle point $t_s^{(\alpha)}$ can be recast into

$$S_{I_p,\mathbf{p}}\left(t_{s0}^{(\alpha)}\right) = C(\mathbf{p}) - \int_{t_{s0}^{(\alpha)}}^{\infty} \left[\frac{1}{2}\mathbf{v}_0^2(t) + I_p\right] dt, \tag{4}$$

where $\mathbf{v}_0(t) = \mathbf{p} + \mathbf{A}(t)$ is the velocity of an electron in the field described by $\mathbf{A}(t)$. The term $C(\mathbf{p}) = \int_0^{\infty} [\frac{1}{2}\mathbf{v}_0^2(t) + I_p]\, dt$ varies with different asymptotic momenta $\mathbf{p}$, but it is independent of individual saddle points $t_{s0}^{(\alpha)}$ for the same $\mathbf{p}$. Consequently, $C(\mathbf{p})$ does not contribute to the final ionization probability, since it can be factored out of the summation and eventually cancels as a phase factor.

The integrand in the second term corresponds to the Hamiltonian $H_0(t) = \frac{1}{2}\mathbf{v}_0^2(t)$ for a free electron in the electromagnetic field so that

$$S_{I_p,\mathbf{p}}\left(t_{s0}^{(\alpha)}\right) = C(\mathbf{p}) - \int_{t_{s0}^{(\alpha)}}^{\infty} \left[H_0(t) + I_p\right] dt. \tag{5}$$

When the Coulomb field is switched on, the motion of the electron is altered, i.e., $\mathbf{r}_0 \to \mathbf{r}$ and $\mathbf{v}_0 \to \mathbf{v}$, and the Hamiltonian in the action (5) is modified to include the Coulomb potential [18],

$$H_0 \to H = H_0 + U_{\text{Coulomb}} = H_0 - \frac{Z}{|\mathbf{r}(t)|}.$$

Moreover, the saddle-point times for a given *asymptotic* momentum $\mathbf{p}$ will be changed too, $t_{s0}^{(\alpha)} \to t_s^{(\alpha)}$, as the saddle-point equation (3) becomes

$$\frac{1}{2}\mathbf{v}^2\left(t_s^{(\alpha)}\right) = \frac{1}{2}\left(\mathbf{p}_0 + \mathbf{A}\left(t_s^{(\alpha)}\right)\right)^2 = -I_p \tag{6}$$

because the initial canonical momentum $\mathbf{p}_0 = \mathbf{p}(t_s^{(\alpha)})$ is not conserved anymore. As a consequence, also the term $C(\mathbf{p})$ in (4) will be different for different $t_s^{(\alpha)}$ that lead to the same asymptotic momentum. In the current work, we neglect this change in $C(\mathbf{p})$.

With these modifications, we have the Coulomb-corrected transition amplitude

$$M_{\mathbf{p}}^{(0)} \sim e^{iC(\mathbf{p})} \sum_{\alpha} \frac{\exp[-i \int_{t_s^{(\alpha)}}^{\infty} (\frac{1}{2}\mathbf{v}^2(t) - \frac{Z}{|\mathbf{r}(t)|} + I_p)\, dt]}{S''(t_s^{(\alpha)})} \equiv e^{iC(\mathbf{p})} \sum_{\alpha} M_{\mathbf{p}}\big(t_s^{(\alpha)}\big). \tag{7}$$

In practice, the integration in (7) from $t_s^{(\alpha)}$ to infinity

$$W_{\mathbf{p}} = \int_{t_s^{(\alpha)}}^{\infty} \left(\frac{1}{2}\mathbf{v}^2(t) - \frac{Z}{|\mathbf{r}(t)|} + I_p \right) dt \tag{8}$$

is split into two parts: the sub-barrier part $W_{\mathbf{p},\mathrm{sub}} = \int_{t_s^{(\alpha)}}^{t_r^{(\alpha)}}$ and the real-time propagation part $W_{\mathbf{p},\mathrm{re}} = \int_{t_r^{(\alpha)}}^{\infty}$.

1.2.4 Applications and Numerical Implementation

Because of the azimuthal symmetry about the polarization axis of a linearly polarized laser field in dipole approximation, it is sufficient to consider a 2D momentum plane $\mathbf{p} = (p_z, p_x)$ where $p_z = p_\parallel$ is in the polarization direction and $p_x = p_\perp$ is in any perpendicular direction.

The steps to evaluate the transition matrix element of atomic ionization are:

(i) Given $\mathbf{p}_0$ and $t_{\mathrm{guess}}^{(\alpha)}$, solve the SPE (6) with a complex root-finding method to obtain the saddle point $t_s^{(\alpha)}$. For the value of $t_{\mathrm{guess}}^{(\alpha)}$, one may choose the corresponding plain-SFA value.

(ii) Calculate the sub-barrier action $W_{\mathbf{p},\mathrm{sub}}$. The current work neglects the sub-barrier Coulomb correction. Hence, $W_{\mathbf{p},\mathrm{sub}}$ can be calculated analytically, as in plain (quantum orbit) SFA.

(iii) Solve the ordinary differential equations of motion in real position space

$$\dot{\mathbf{r}}(t) = \mathbf{p}(t) + \mathbf{A}(t), \tag{9}$$

$$\dot{\mathbf{p}}(t) = -\frac{Z\mathbf{r}(t)}{|\mathbf{r}(t)|^3} \tag{10}$$

for real times $t > t_r$ until the laser is switched-off at time T_p. The initial conditions are

$$\mathbf{r}(t_r) = \mathrm{Re}\,\mathbf{r}(t_r) = \mathbf{a}(t_r) - \mathrm{Re}\,\mathbf{a}(t_s), \qquad \mathbf{p}(t_r) = \mathbf{p}_0. \tag{11}$$

(iv) Calculate $W_{\mathbf{p},\mathrm{re}}$ along the trajectory $\mathbf{r}$ for the real time propagation. Steps (iii) and (iv) can be performed simultaneously.

(v) After the laser is switched off at T_p the asymptotic momentum $\mathbf{p}$ can be found employing Kepler's formulas [11].

(vi) Calculate the individual transition amplitude $M_{\mathbf{p}}(t_s^{(\alpha)})$ in Eq. (7) for this trajectory.

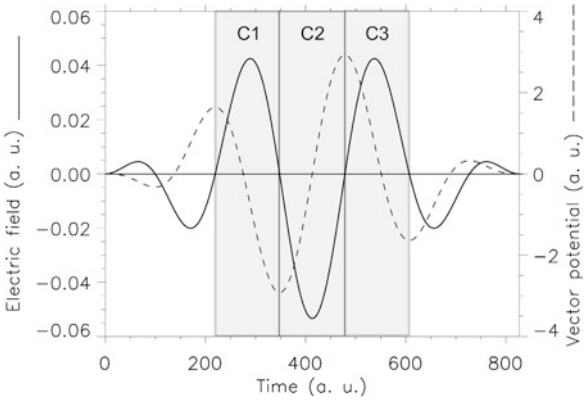

Fig. 1.1 The $\sin^2$ vector potential and the electric field, $\omega = 0.0228$ (wavelength 2 μm), $E_0 = 0.0534$ (intensity 1×10^{14} W/cm^2) and $N_c = 3$. To facilitate the analysis of the electron emission times, we indicate three time intervals C1–C3

If the laser pulse covers several cycles, each choice of $\mathbf{p}_0$ generally leads to several saddle-points and thus to several trajectories. However, since only the saddle points with the lowest imaginary parts possess the largest weights, in practical calculations only a few trajectories need to be taken into account for each $\mathbf{p}_0$.

While the trajectory-based calculation is conceptually simple, a large data set of trajectories is required to obtain smooth spectra with good statistics. Fortunately, the method is trivial to parallelize because of the independence of the trajectories. In practice, we launch trajectories with random, uniformly sampled $\mathbf{p}_0$. For each trajectory, one obtains the asymptotic momentum $\mathbf{p}$ and the individual transition matrix element $M_{\mathbf{p}}(t_s^{(\alpha)})$ using the recipe above. All information related to this trajectory can be stored for further analysis.

With all trajectories available, one can calculate the momentum distribution of the ionization probability on a grid representing the final momentum $\tilde{\mathbf{p}}$. To that end trajectories are binned according to their asymptotic momentum $\mathbf{p}$, and the total transition amplitude for momentum $M_{\tilde{\mathbf{p}}}$ is the sum over all transition amplitudes $M_{\mathbf{p}}^{(i)}$, $M_{\tilde{\mathbf{p}}} = \sum_i M_{\mathbf{p}}^{(i)}$. Here, the trajectory whose corresponding transition amplitude is $M_{\mathbf{p}}^{(i)}$ should have its asymptotic momentum $\mathbf{p}$ in the bin centered at $\tilde{\mathbf{p}}$, and i represents the index of trajectories satisfying this condition.

1.3 Results and Discussion

In order to demonstrate the usefulness of the TCSFA method as a tool for a detailed analysis of photoelectron spectra, we consider the test case of atomic hydrogen ($I_p = 0.5$) in a linearly polarized (along the z-axis in the $(p_z p_x)$-plane) light field described by the vector potential

$$A(t) = -\frac{E_0}{\omega} \sin^2\left(\frac{\omega t}{2N_c}\right) \sin \omega t, \tag{12}$$

where ω is the laser frequency, E_0 is the peak electric field strength, and N_c is the number of optical cycles. The parameters are listed in the caption of Fig. 1.1.

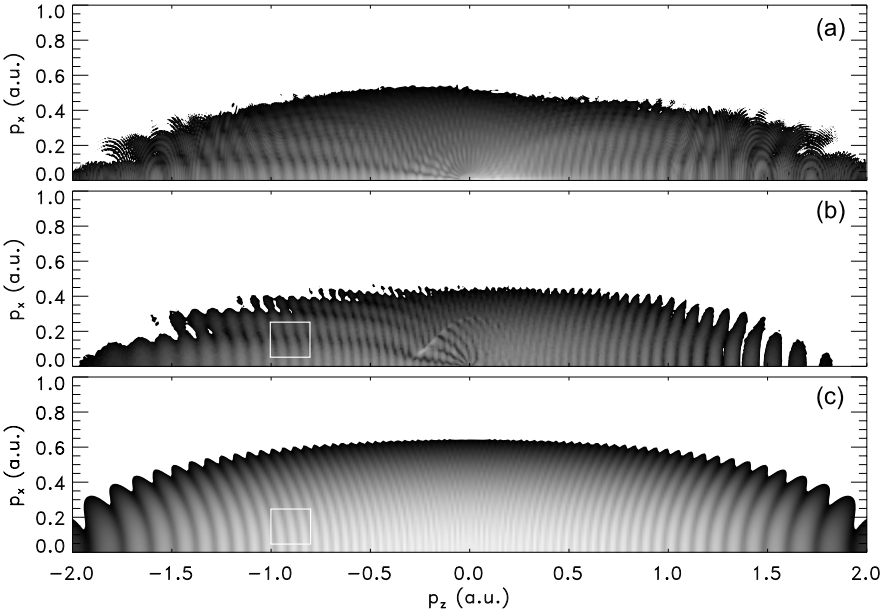

Fig. 1.2 Logarithmically scaled photoelectron momentum distributions in the $(p_z p_x)$-plane $(p_\parallel = p_z)$ calculated using (**a**) TDSE, (**b**) TCSFA, and (**c**) SFA. Each spectrum was normalized to its maximum value, with orders of magnitudes 4, 4.4 and 2, respectively, for the convenience of comparison. The white box-frames in (**b**) and (**c**) indicate the zoomed regions to be studied

Figure 1.2 shows the photo-electron momentum distributions calculated with different methods: the TDSE [31], the TCSFA and the plain SFA. The TDSE result serves as a benchmark to check the validity of other methods. Several important spectral features are observed. Firstly, the momentum spectrum exhibits a globally asymmetrical distribution along the z-direction due to the few cycles in the laser pulse [32]. In addition, the distribution reveals a near-threshold ($\mathbf{p} \simeq 0$) spoke-like pattern [11]. At higher energies side-lobes are visible for $p_z < 0$, which have been shown to originate from the intra-cycle interference of quantum trajectories [33]. All these Coulomb effects are well reproduced by the TCSFA calculation, while lacking in the plain SFA result Fig. 1.2(c). If the conversion from the momentum distribution to the energy spectra is made, the caustic with the semi-classical calculation in Fig. 1.2(b) is shown to form the reported spike-like peak in mid-infrared fields, known as the low-energy structure (LES) [12, 13, 19, 34, 35].

1.3.1 Categorization of Trajectories and Partial Reconstruction

The origin of the difference between the excellent TCSFA result in Fig. 1.2(b) and the poor plain-SFA result in Fig. 1.2(c) can now be traced back to the modification

Table 1.1 Categorization of the trajectories in the TCSFA

Types	Longitudinal condition	Transversal condition
T1	$p_z(\infty)z(t_r) > 0$	$p_x(t_r)p_x(\infty) > 0$
T2	$p_z(\infty)z(t_r) < 0$	$p_x(t_r)p_x(\infty) > 0$
T3	$p_z(\infty)z(t_r) < 0$	$p_x(t_r)p_x(\infty) < 0$
T4	$p_z(\infty)z(t_r) > 0$	$p_x(t_r)p_x(\infty) < 0$

of quantum orbits because of the Coulomb potential acting on the emitted electron. Two types of trajectories are known in plain SFA, commonly called "short" and "long" [36]. In the following we label these trajectories T1 and T2, respectively. However, two additional types of trajectories, T3 and T4, need to be introduced when long-range Coulomb interaction is included [19]. The definitions of the trajectory types 1–4 are listed in Table 1.1. The short trajectories T1 start at a tunnel exit that points already towards the detector, with the initial transversal canonical momentum and the asymptotic one having the same sign. In other words, the electron flies from the beginning on "into the right direction". The long trajectories T2 instead start in the "wrong" direction but already with the "right" sign of the transversal canonical momentum. In plain SFA, the canonical momentum is conserved so that there is no other way for the electron than having the "right" asymptotic canonical momentum from the very beginning. With Coulomb attraction at work, however, the lateral momentum may be reversed, leading to trajectories T3, not present in plain SFA. Finally, trajectories of type T4 start off in the "right" direction with respect to the laser polarization direction but with a transversal canonical momentum that changes sign during the propagation towards the detector.

With the above categorization as a natural extension of the quantum orbits in the plain SFA, "partial spectra" can be reconstructed using only partial type(s) of trajectories. It is possible to infer the role of trajectories which satisfy certain conditions by comparing their partial spectra with the full spectra. Momentum spectra constructed from individual types of trajectories are shown in Fig. 1.3. For T1, a ring-like distribution because of significant interference is visible in the negative-half momentum plane $p_z < 0$ while a structureless distribution emerges in the positive-half plane. The interference in the negative-half plane originates from the coherent superposition of trajectories whose t_r fall into the time interval C1 and C3 (as indicated in Fig. 1.1). Since $\mathbf{E}(t)$ in C1 and C3 are the same in magnitude, the weights for trajectories born in these intervals are similar, leading to significant inter-cycle interferences. Instead, in the positive-half plane, since the tunneling probability depends exponentially on the field strength, the ionization is mainly confined to trajectories born within the time interval C2 around the main peak of $\mathbf{E}(t)$. The weights of these trajectories are typically larger than those from the side-peaks. Thus, hardly can any clear interference develop. Similarly, the explanation also applies to the partial spectra of T2. However, since T2 represents the "long" trajectory with the initial "tunnel exit" $z(t_r)$ opposite to that of T1, the spectrum is reversed with respect to p_z.

For the trajectory-types T1 and T2, the transversal momentum does not change its sign, and the Coulomb-corrections are rather small, as can be seen by comparison

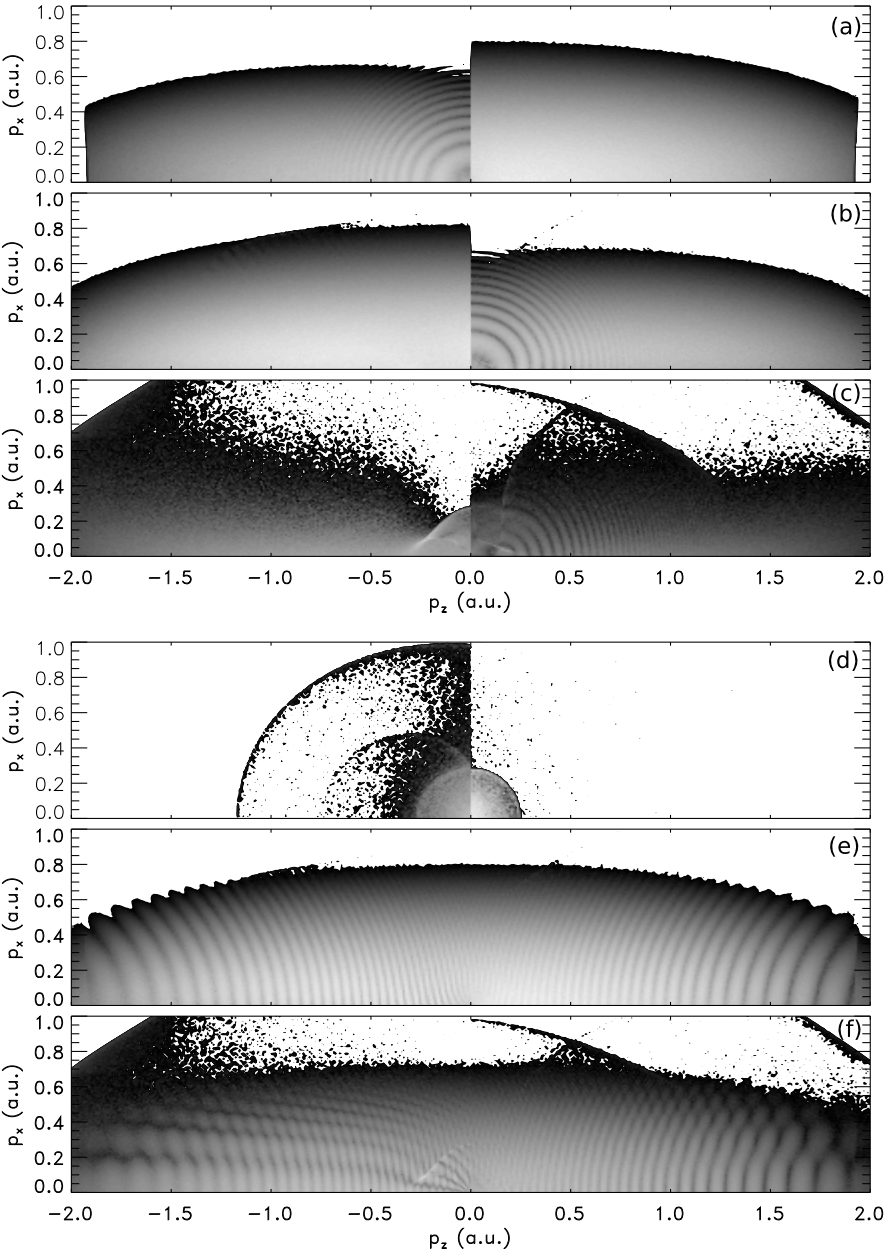

Fig. 1.3 Partial distributions constructed from different types of trajectories: (**a**) T1, (**b**) T2, (**c**) T3, (**d**) T4, (**e**) T1 + T2 and (**f**) T1 + T2 + T3

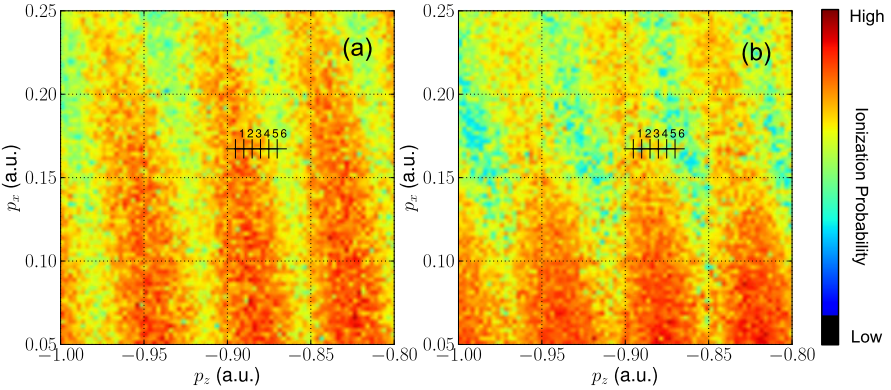

Fig. 1.4 Zoom into spectra of Fig. 1.2(c) and Fig. 1.2(b), where the *white box-frames* indicate the zoomed regions, for the SFA (**a**) and the TCSFA (**b**). At selected points, shown by *crosses* ($p_z \in [-0.9, -0.87]$, $p_x = 0.17$) and labeled 1–6, the relation between constructive or destructive interference and quantum trajectories will be illustrated below

between the SFA result in Fig. 1.2(c) and the spectra for T1 + T2 in Fig. 1.3(e). Because the Coulomb-corrected T1 and T2 alone do not yield the correct spectrum, T3 and T4—not existent in plain SFA—are obviously important. In fact, good agreement is achieved when trajectories of type T3 are included, as is shown in Fig. 1.3(f). Trajectories T3 change the sign of the transversal momentum while moving from the tunnel exit to the detector. This is only possible because of a rather strong interaction with the Coulomb field. It results in some striking features, as is shown in Fig. 1.3(c): (i) The weights of trajectories T3 are sufficiently large, comparable to those of T1 or T2, to form the side-lobes. Exaggerated local maxima, known as caustics, are also visible. In Fig. 1.3(c), a caustic is located at $\mathbf{p} = (-0.2, 0.1)$, related to the recently discovered LES [12, 13], as discussed in [19].

1.3.2 Statistical Trajectory-Based Analysis

The partial spectra can be used for a global analysis, but sometimes one is more interested in the origin of certain spectral features, for instance interference fringes.

Figure 1.4 presents a zoom into Figs. 1.2(b, c) with sampling points 1–6 indicated. The points connect an interference peak with the right-neighboring interference dip caused by intra-cycle interference. Since the TCSFA is equivalent to the SFA when $Z = 0$, the SFA has been also implemented with the trajectory-based method. The selected points reside in the valley between two side-lobes in the TCSFA result Fig. 1.2(b).

Figures 1.5(a–f) show the individual trajectories' $M_{\mathbf{p}}$ in the complex plane that contribute to the spectrum $\Delta p = 0.005$ around the sampling points 1–6 in Fig. 1.4(a). Each plot has two arcs defined as A1 and A2. The points in the origin represent $M_{\mathbf{p}}$ with negligibly small norms. As we move from sampling point

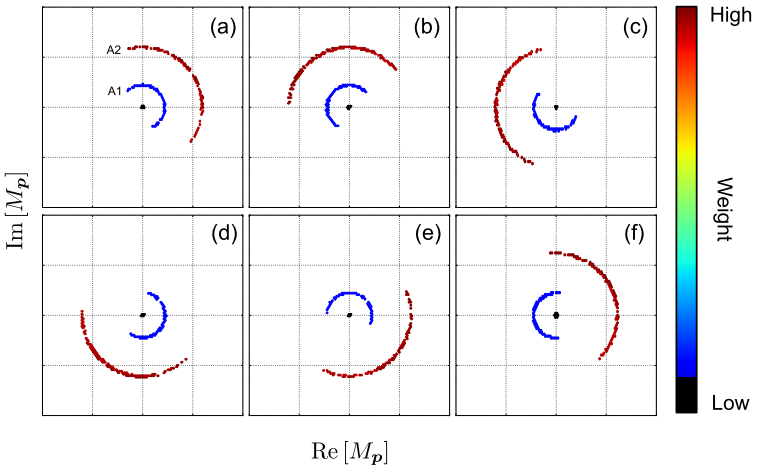

Fig. 1.5 Bivariate histograms of $M_{\mathbf{p}}$ in the complex plane for the SFA. The plots (**a**)–(**f**) may be viewed as "phase diagrams" for the points 1–6 in Fig. 1.4(a). The final-momentum bin in the (p_z, p_x)-plane for each of the points had a radius $\Delta p = 0.005$. Each of the points $M_{\mathbf{p}}$ with similar norms $|M_{\mathbf{p}}|$ construct arcs. In each panel two arcs [labeled by A1 and A2 in (**a**)] are visible. The color represents the weight of the $M_{\mathbf{p}}$-distribution in hexagonal bins (the weight is defined as $\sum_{\alpha=1}^{n_i} |M_{\mathbf{p}}^{(i,\alpha)}|$ with n_i the number of trajectories in the ith bin and $|M_{\mathbf{p}}^{(i,\alpha)}|$ the norm of the αth $M_{\mathbf{p}}$)

1 to point 6 in Fig. 1.4(a), the two arcs rotate counter-clockwise at different rates, which leads to a change in the phase difference between them. The **p**-dependent phase difference in the doubly-differential momentum spectra forms the interference pattern: when A1 and A2 align in the same direction, as shown in Fig. 1.5(a), the condition for constructive interference is satisfied to form the maximum in the spectrum. The opposite alignment of A1 and A2, as shown in Fig. 1.5(f), leads to destructive interference and a minimum.

When we apply the same analysis to the TCSFA, as shown in Fig. 1.6, one more arc than for the SFA-case is observed. Indeed, the outermost arc A3 belongs to the new trajectory-type T3 because of the Coulomb potential. The inner two arcs are the counterparts of the two arcs present in the plain-SFA result Fig. 1.5. They only differ by a phase shift due to Coulomb interaction. Similar to the phase diagram for the SFA, the arcs A1 and A2 rotate at different rates, which forms the vertically aligned interference fringes. However, because of A3, which aligns opposite to A2 while rotating at a similar rate, the net contribution of trajectories associated with A2 is reduced. This destructive interference results in a side-lobe minimum clearly visible in the center of the white box in Fig. 1.2(b).

The statistical analysis in the complex $M_{\mathbf{p}}$-plane provides direct evidence that the trajectories of A3 play the essential role in building up the side-lobes. The comparison of SFA and TCSFA results allows to quantify relative phase shifts because of Coulomb interaction.

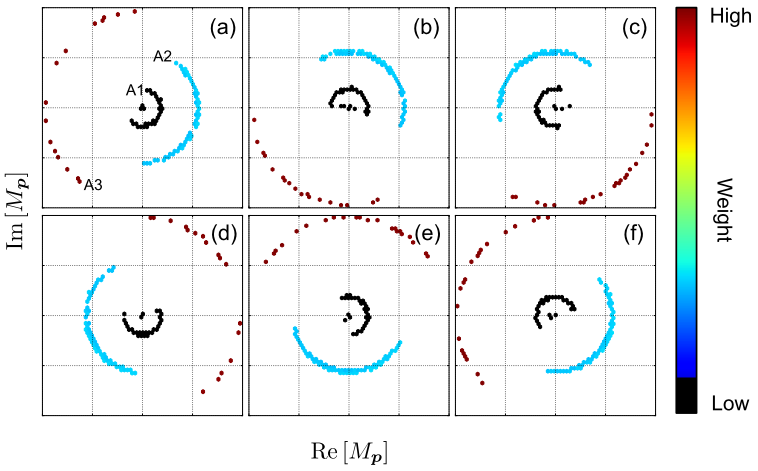

Fig. 1.6 Same as Fig. 1.5 but for the TCSFA

By mapping the individual transition amplitudes to other trajectory-related quantities a detailed insight in any spectral feature may be gained. Figure 1.7 gives an example for the first sampling point in 1.4(b). Figure 1.7(a) maps the arcs in the complex $M_{\mathbf{p}}$-plane to the trajectory-type, showing that A1 consists of T1, A2 of T2, and A3 of T3 trajectories. The trajectories T4 map into a dot at the origin in the complex $M_{\mathbf{p}}$-plane due to their negligibly small weights. Figure 1.7(b) together with the knowledge from (a) shows that the T1 trajectories originate from a tunnel exit at $z(t_r) \simeq -11$ while T2 and T3 start both from the opposite side at $z(t_r) \simeq 10$. From the remaining two panels in Fig. 1.7 we infer, e.g., that T3 trajectories are born close to the peak of the electric field [see Fig. 1.7(c)] within the time interval C1 of Fig. 1.1, with the smallest imaginary part of the saddle-point time [see Fig. 1.7(d)].

Figure 1.8 visualizes the trajectories for sampling point 1 in Fig. 1.4 for both TCSFA and SFA. Trajectories T1 are directly driven from the tunnel exit to the detector, and the Coulomb field does not influence T1 substantially. T2-trajectories are slightly influenced by the Coulomb attraction while T3-orbits owe their mere existence to the Coulomb potential. Only with the Coulomb potential present is it possible to reverse the lateral momentum.

1.4 Conclusion

The momentum distributions of photoelectrons after strong-field ionization exhibit rich structures, even for the simplest system of atomic hydrogen in a linearly polarized field. To understand the ionization dynamics that leads to particular spectral features, the quantum orbit-based TCSFA method has been introduced. Coulomb interaction between the outgoing electron and the residual ion is taken into account by

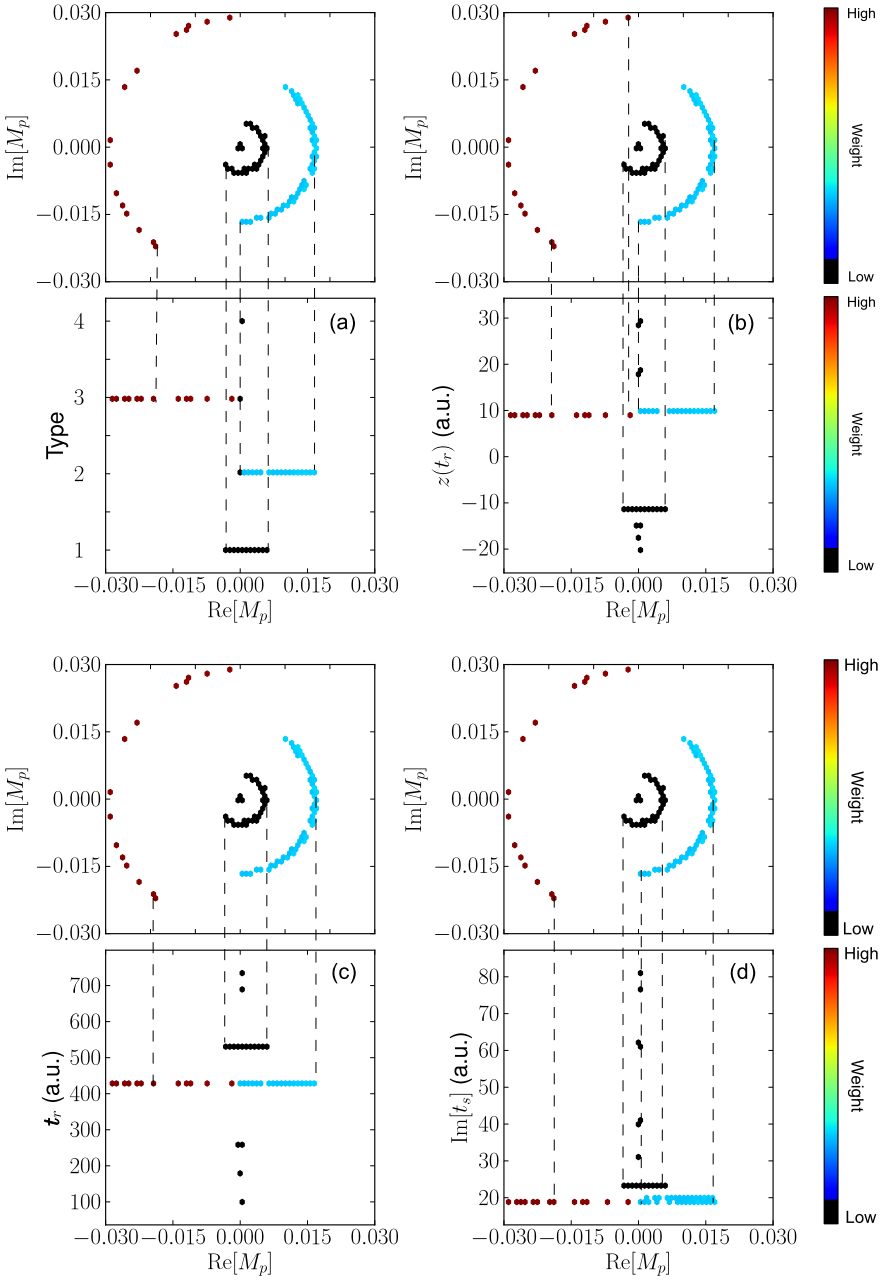

Fig. 1.7 Further analysis of Fig. 1.6(a). Mapping from the complex $M_\mathbf{p}$-plane to the trajectory type (**a**), tunnel exit (**b**), emission time t_r (**c**), and imaginary part of the saddle-point time (**d**)

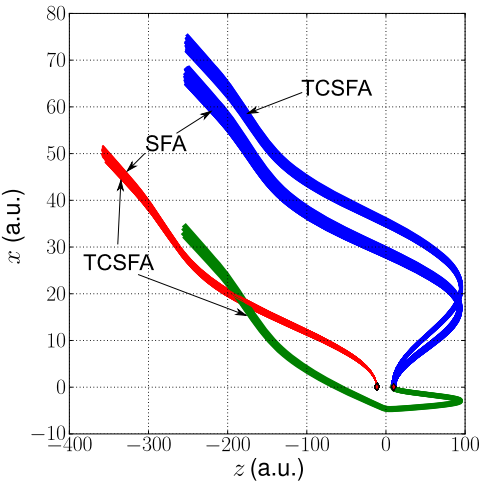

Fig. 1.8 Trajectories associated with the sampling point 1 for both the TCSFA and the plain SFA: T1 (*red*), T2 (*blue*) and T3 (*green*, exists only in TCSFA). Trajectories T2 and T3 are born within the time interval C2 at positive z, while T1 is born within C1 with the tunnel exit located at negative z

modifying the plain-SFA quantum orbits accordingly. The 2 μm case study demonstrated good agreement of TCSFA results and *ab initio* TDSE calculations. Because of the semi-classical condition $I_p/\hbar\omega \gg 1$ the TCSFA yields less satisfactory results for shorter wavelengths.

Coulomb effects influence the left-right asymmetry in photoelectron spectra, they modify the interference structure, leading, e.g., to side-lobes, and they create LESs. The analysis of trajectories in the TCSFA shows that the Coulomb interaction introduces new types of trajectories which may modify both the interference pattern (leading, e.g., to side-lobes) and the number of orbits ending up in a final momentum bin (leading, e.g., to the LES). Recent work has been devoted to the Coulomb-correction of the sub-barrier electron dynamics [37].

Acknowledgements The work was partially supported by the Deutsche Forschungsgemeinschaft (SFB 652) and the Russian Foundation for Basic Research. T.-M. Yan acknowledges support from the International Max Planck Research School for Quantum Dynamics (IMPRS-QD) in Heidelberg.

References

1. D.B. Milošević, G.G. Paulus, D. Bauer, W. Becker, J. Phys. B **39**, R203 (2006)
2. J. Ullrich, R. Moshammer, A. Dorn, R. Dörner, L.P.H. Schmidt, H. Schmidt-Böcking, Rep. Prog. Phys. **66**, 1463–1545 (2003)
3. L.V. Keldysh, Zh. Éksp. Teor. Fiz. **47**, 1945 (1964)
4. F.H.M. Faisal, J. Phys. B, At. Mol. Phys. **6**, L89 (1973)
5. H.R. Reiss, Phys. Rev. A **22**, 1786 (1980)
6. S.P. Goreslavski, G.G. Paulus, S.V. Popruzhenko, N.I. Shvetsov-Shilovski, Phys. Rev. Lett. **93**, 233002 (2004)
7. S.V. Popruzhenko, G.G. Paulus, D. Bauer, Phys. Rev. A **77**, 053409 (2008)
8. S. Chelkowski, A.D. Bandrauk, Phys. Rev. A **71**, 053815 (2005)

9. A. Rudenko, K. Zrost, C.D. Schröter, V.L.B. de Jesus, B. Feuerstein, R. Moshammer, J. Ullrich, J. Phys. B **37**, L407 (2004)
10. R. Moshammer, J. Ullrich, B. Feuerstein, D. Fischer, A. Dorn, C.D. Schröter, J.R. Crespo Lopez-Urrutia, C. Hoehr, H. Rottke, C. Trump, M. Wittmann, G. Korn, W. Sandner, Phys. Rev. Lett. **91**, 113002 (2003)
11. D.G. Arbó, S. Yoshida, E. Persson, K.I. Dimitriou, J. Burgdörfer, Phys. Rev. Lett. **96**, 143003 (2006)
12. C.I. Blaga, F. Catoire, P. Colosimo, G.G. Paulus, H.G. Muller, P. Agostini, L.F. DiMauro, Nat. Phys. **5**, 335 (2009)
13. W. Quan, Z. Lin, M. Wu, H. Kang, H. Liu, X. Liu, J. Chen, J. Liu, X.T. He, S.G. Chen, H. Xiong, L. Guo, H. Xu, Y. Fu, Y. Cheng, Z.Z. Xu, Phys. Rev. Lett. **103**, 093001 (2009)
14. A.M. Perelomov, V.S. Popov, Zh. Éksp. Teor. Fiz. **52**, 514 (1967) [Sov. Phys. JETP **25**, 336 (1967)]
15. F.H.M. Faisal, G. Schlegel, J. Phys. B **38**, L223–L231 (2005)
16. D.G. Arbó, J.E. Miraglia, M.S. Gravielle, K. Schiessl, E. Persson, J. Burgdörfer, Phys. Rev. A **77**, 013401 (2008)
17. O. Smirnova, M. Spanner, M. Ivanov, Phys. Rev. A **77**, 033407 (2008)
18. S.V. Popruzhenko, D. Bauer, J. Mod. Opt. **55**, 2573 (2008)
19. T.-M. Yan, S.V. Popruzhenko, M.J.J. Vrakking, D. Bauer, Phys. Rev. Lett. **105**, 253002 (2010)
20. M.S. Gravielle, D.G. Arbó, J.E. Miraglia, M.F. Ciappina, J. Phys. B **45**, 015601 (2012)
21. W. Gordon, Z. Phys. **40**, 117 (1926)
22. D.V. Volkov, Z. Phys. **94**, 250 (1935)
23. M.V. Frolov, N.L. Manakov, A.F. Starace, Phys. Rev. A **79**, 033406 (2009)
24. D.B. Milošević, G.G. Paulus, W. Becker, Phys. Rev. Lett. **89**, 153001 (2002)
25. W. Becker, F. Grasbon, R. Kopold, D.B. Milošević, G.G. Paulus, H. Walther, Adv. At. Mol. Opt. Phys. **48**, 35 (2002)
26. P. Salières, B. Carré, L. Le Déroff, F. Grasbon, G.G. Paulus, H. Walther, R. Kopold, W. Becker, D.B. Milošević, A. Sanpera, M. Lewenstein, Science **292**, 902 (2001)
27. F. Lindner, M.G. Schätzel, H. Walther, A. Baltuška, E. Goulielmakis, F. Krausz, D.B. Milošević, D. Bauer, W. Becker, G.G. Paulus, Phys. Rev. Lett. **95**, 040401 (2005)
28. R. Gopal, K. Simeonidis, R. Moshammer, T. Ergler, M. Dürr, M. Kurka, K.-U. Künel, S. Tschuch, C.-D. Schröter, D. Bauer, J. Ullrich, A. Rudenko, O. Herrwerth, T. Uphues, M. Schultze, E. Goulielmakis, M. Uiberacker, M. Lezius, M.F. Kling, Phys. Rev. Lett. **103**, 053001 (2009)
29. G.G. Paulus, D. Bauer, in *Time in Quantum Mechanics II*. Lecture Notes in Physics (Springer, Berlin, 2010)
30. V.S. Popov, Phys. At. Nucl. **68**, 686 (2005)
31. D. Bauer, P. Koval, Comput. Phys. Commun. **174**, 396 (2006)
32. S. Chelkowski, A.D. Bandrauk, Phys. Rev. A **71**, 053815 (2005)
33. Y. Huismans, A. Rouzée, A. Gijsbertsen, J.H. Jungmann, A.S. Smolkowska, P.S.W.M. Logman, F. Lépine, C. Cauchy, S. Zamith, T. Marchenko, J.M. Bakker, G. Berden, B. Redlich, A.F.G. van der Meer, H.G. Muller, W. Vermin, K.J. Schafer, M. Spanner, M.Y. Ivanov, O. Smirnova, D. Bauer, S.V. Popruzhenko, M.J.J. Vrakking, Science **331**, 61 (2011)
34. C. Liu, K.Z. Hatsagortsyan, Phys. Rev. Lett. **105**, 113003 (2010)
35. A. Kästner, U. Saalmann, J.M. Rost, Phys. Rev. Lett. **108**, 033201 (2012)
36. M. Lewenstein, P. Salières, A. L'Huillier, Phys. Rev. A **52**, 4747–4754 (1995)
37. T.-M. Yan, D. Bauer, Phys. Rev. A **86**, 053403 (2012)

Chapter 2
The Role of Nuclear Vibrational Motion in Molecular High Harmonic Generation in a Mid-Infrared Laser Field

Ruxin Li, Yinghui Zheng, Zhinan Zeng, Pengfei Wei, Yuxin Leng, and Zhizhan Xu

Abstract Compared to atoms, molecules inevitably introduce a further complexity in high harmonic generation (HHG) due to the additional degree of freedom for nuclear wave packet motion. Recent progress on investigating the role of nuclear vibrational motion in molecular HHG driven by a mid-infrared laser field at SIOM is reviewed, including two results: isolated attosecond pulse (IAP) generation and driving wavelength effect of molecular HHG. First, we found IAP in the water window can be generated in H_2^+ molecules driven by a multi-cycle 2400-nm mid-infrared laser field due to the charge-resonance enhanced ionization which is caused by molecular vibrational motion, as shown by the numerical solution of a Non-Born–Oppenheimer time-dependent Schrödinger equation. Second, we observed experimentally that the HHG in molecules subjected to a tunable mid-infrared laser field around the vibrational resonance is more sensitive to the driving laser wavelength than that in atoms with comparable ionization potential, as a result of the vibrational motion in molecules. These findings are interesting and invaluable for the future detection and control of the nuclear dynamics in molecules by means of HHG.

R. Li (✉) · Y. Zheng · Z. Zeng · P. Wei · Y. Leng · Z. Xu
State Key Laboratory of High Field Laser Physics, Shanghai Institute of Optics and Fine Mechanics, Chinese Academy of Sciences, Qinghe Rd 390, Jiading District, Shanghai 201800, China
e-mail: ruxinli@mail.shcnc.ac.cn

Y. Zheng
e-mail: yhzheng@siom.ac.cn

Z. Zeng
e-mail: zhinan_zeng@siom.ac.cn

Y. Leng
e-mail: lengyuxin@siom.ac.cn

Z. Xu
e-mail: zzxu@mail.shcnc.ac.cn

P. Wei
College of Physics and Electronic Information Engineering, Wenzhou University, Wenzhou 325035, China
e-mail: personinjoy@163.com

K. Yamanouchi, K. Midorikawa (eds.), *Progress in Ultrafast Intense Laser Science*, Springer Series in Chemical Physics 104, DOI 10.1007/978-3-642-35052-8_2,

2.1 Introduction

High harmonic generation (HHG) during the interaction between a high-intensity ultra-short laser pulse and atoms or molecules is proved to be an effective way to generate an extreme-ultraviolet (XUV) light source [1, 2] and an isolated attosecond pulse (IAP) [3], which have already been proven ideal for capturing the motion of electrons in atoms, molecules and solid materials [4, 5].

Compared to atoms, molecules inevitably introduce a further complexity in the high-field interaction due to the additional degree of freedom for nuclear wave packet motion, causing various unique nonlinear responses, such as the charge resonance-enhanced ionization (CREI) induced by the bond elongation at distances larger than the equilibrium bond length [6, 7], the chemical bond being softened by multiphoton couplings [8]. Lein [9] showed that HHG is sensitive to the laser-induced vibrational motion according to the numerical solution of the time-dependent Schrödinger equation for vibrating hydrogen molecules, which represents that the more intense harmonics are generated in the heavier isotopes and the difference becomes more obvious with the higher harmonic frequency.

High field molecular behavior was investigated earlier at fixed inter-nuclear distance under the Born–Oppenheimer approximation, which ignores the couplings between the electronic motion and the nuclear motion. Recently, non-Born–Oppenheimer (NBO) time-dependent Schrödinger equation (TDSE) simulations have revealed a variety of unique nonlinear responses, such as allowing the shortening of the trains of generated attosecond pulses [10] and monitoring electron-nuclear dynamics on an attosecond time scale since the harmonic signal can be modified by the nuclear motion [11, 12].

In this chapter, we address the recent progress at SIOM: a theoretical prediction of IAP generation in a multi-cycle mid-infrared laser field due to the CREI, and the driving wavelength effect on molecular HHG due to the proton vibration by tuning the wavelength of the infrared driving laser pulse.

2.2 IAP Generation in the Water Window

In the so-called water window, from 4.4 to 2.3 nm (from 280 to 550 eV), water is comparatively transparent and organic materials are absorptive for carbon-containing biological samples. Thus, high-contrast biological spectroscopy in this spectral window has long been one of the most important objectives of the development of coherent XUV sources [13]. The generation of IAP in the water window has an extremely vital significance for studying the ultrafast electronic dynamics of biological samples in water. With the rapid development in ultrafast laser technology, the intense ultrafast laser sources in the mid-infrared region have been achieved [14–18] and have been employed experimentally [2, 19], which makes it possible to realize the attosecond pulse generation in the water window. Several approaches

have so far been proposed to achieve a single attosecond pulse in this spectral region, including the detuned mid-infrared two-color scheme [20], mid-infrared polarization gating modulated by a weaker linearly polarized pulse [21, 22], and the double optical gating with very high intensity [23]. However, the above methods have high demands for the driving laser field and depend on a complex shaped laser field. Thus, we aim to find an approach to generate IAP in the water window based on the directly available driving laser pulses with moderate intensity.

We propose a scheme to produce IAP in the water window using a 2400-nm mid-infrared laser pulse with moderate intensity interacting with H_2^+ molecules. By using numerical solutions of NBO TDSE, a single attosecond pulse is achieved resulting from the CREI.

2.2.1 NBO TDSE Model

In this work, we follow the numerical treatment described in Ref. [24]. Up to now, the HHG of the aligned molecules has been a proven technique [25–27]. Therefore, the molecular axis is assumed to be parallel to the polarization direction of the linearly polarized laser field and electron moves along the molecular axis. Here the moving electron and nuclei are allowed to be calculated using complete one-dimensional (1D) TDSE. The NBO TDSE simulation is a single-molecular modeling, and the macroscopic propagation effects of the harmonic emission are not taken into account because of the heavy computational cost. Such a simplified 1D H_2^+ model has been verified by many previous studies [10, 25, 28, 29]. The 1D TDSE is written as ($e = \hbar = m_e = 1$ in atomic units (a.u.), which are used throughout unless otherwise indicated):

$$i\frac{\partial\psi(z,R,t)}{\partial t} = \left[T_R + T_e + V(z,R) + V_I(z,t)\right]\psi(z,R,t), \tag{1}$$

where R is the internuclear distance, and z is the electronic coordinate with respect to the center of mass of the two nuclei. $T_R = -\frac{1}{m_p}\frac{\partial^2}{\partial R^2} + \frac{1}{R}$, where $-\frac{1}{m_p}\frac{\partial^2}{\partial R^2}$ denotes the nuclear kinetic-energy operator, and $T_e = -\frac{1}{2\gamma}\frac{\partial^2}{\partial z^2}$ denotes electronic kinetic-energy operator. $m_p = 1836$ is the proton mass, and $\gamma = \frac{2m_p}{1+2m_p}$ is the nuclei-electron reduced mass. The soft-Coulomb potential $V(z,R)$ reads

$$V(z,R) = -\frac{1}{\sqrt{(z+R/2)^2+1}} - \frac{1}{\sqrt{(z-R/2)^2+1}}. \tag{2}$$

The external interaction $V_I(z,t)$ between the laser field and molecule reads

$$V_I(z,t) = \frac{2m_p+2}{2m_p+1} zE(t), \tag{3}$$

where $E(t) = E_0 f(t)\sin(\omega t)$ denotes the linearly polarized driving field with peak amplitude E_0, envelope function $f(t)$, and frequency ω. In the TDSE calculations, the Schrödinger equation (1) is numerically solved by the second-order split-operator technique [30]. The high harmonic intensity spectrum is proportional to

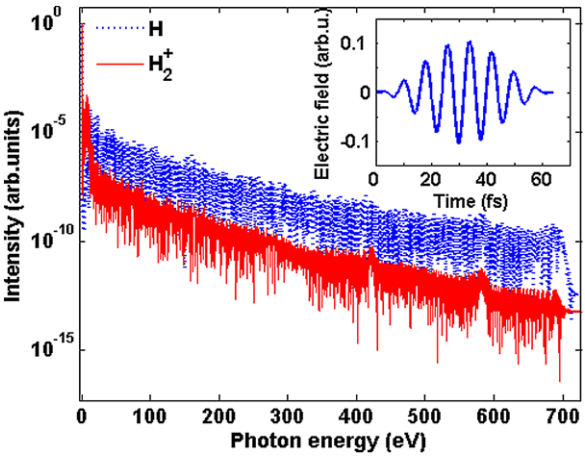

Fig. 2.1 High-order harmonic spectra for the H_2^+ molecule (*red solid curve*) and the H atom (*blue dotted curve*), respectively. The *inset* shows the sketch of the driving laser pulse with a peak intensity of 4×10^{14} W/cm^2 and a wavelength of 2400 nm

the squared modulus of the Fourier transform of the dipole acceleration expectation value.

In the simulation, we employ an envelope function $f(t) = \sin(\pi t/T)^2$, where T is the total pulse duration. The ground state of the field-free H_2^+ molecular system with Hamilton operator $H_0 = T_R + T_e + V(z, R)$, obtained by propagating the field-free Schrödinger equation in imaginary time [31], is chosen to be the initial wave function. The H_2^+ molecular ground-state energy is set to be -21.1 eV. The wave function $\psi(z, R, t)$ is discrete on a two-dimensional grid containing 16384 grid points on the z axis with the step of 0.2 a.u. and 1024 grid points in R axis with the step of 0.05 a.u. The time step of wave function propagation is $dt = 0.08$ a.u. In order to avoid spurious reflections of the wave packet from the boundary, the wave function is multiplied by a $\cos^{1/8}$ mask function [32].

2.2.2 Results and Discussion

The high-order harmonic spectra are shown in Fig. 2.1 for the H_2^+ molecule (red solid curve) and the H atom (blue dotted curve) respectively, driven by the laser pulse with a peak intensity of 4×10^{14} W/cm^2, a wavelength of 2400 nm, and a duration (the full width at half maximum) of about four optical cycles shown in the inset of Fig. 2.1. In the simulation, the softening parameter is properly set for the H atom so that its ground-state energy is equal to that of the H_2^+ molecule $E_0 = -21.1$ eV. As can be seen, the harmonic intensity of the H_2^+ molecule is more than one order of magnitude lower than that of the H atom. The calculation performed by Bandrauk *et al*. [10] also showed that the harmonic yield from the fixed nuclear model is more intense than that from the moving nuclear model in H_2 and D_2 molecules.

Figure 2.2 shows the temporal profiles of the harmonic emission by performing an inverse Fourier transform of the spectra using a square-wave filter function,

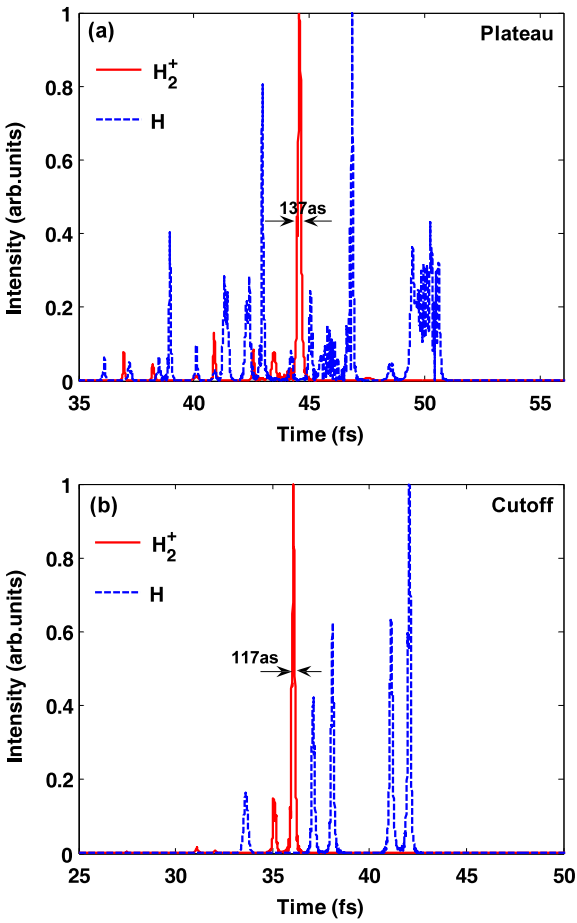

Fig. 2.2 Temporal profiles of the harmonic emission by performing an inverse Fourier transform of the spectra from 258 to 323 eV in the plateau region (**a**), and from 626 to 691 eV in the cutoff (**b**)

selecting from 258 to 323 eV in the plateau region [Fig. 2.2(a)], and from 626 to 691 eV in the cutoff [Fig. 2.2(b)], respectively. One can see that an IAP is generated not only in the cutoff but also in the region of plateau for the H_2^+ molecule (red solid curve) taking the vibrational motion into account, while attosecond pulse trains are obtained for the H atom (blue dotted curve). The durations of the single attosecond pulse generated in the plateau region and in the cutoff are 137 as and 117 as, respectively. Due to the nonlinear chirped phase and some high-order dispersion, it is difficult to generate a single attosecond pulse if the continuum is too broad, attosecond pulse train instead. In the calculations, we scan the position and bandwidth of the spectrum, and the spectrum from 258 to 323 eV in the plateau region and that from 626 to 691 eV in the cutoff are found to support the IAP generation.

The IAP generation is attributed to the CREI just as shown in the following text. As we known, the harmonic emission process can be well explained by a three-step model: Active electrons first tunnel through the potential barrier, are accelerated by laser fields, and then recombine with parent ions to emit high-energy photons [33].

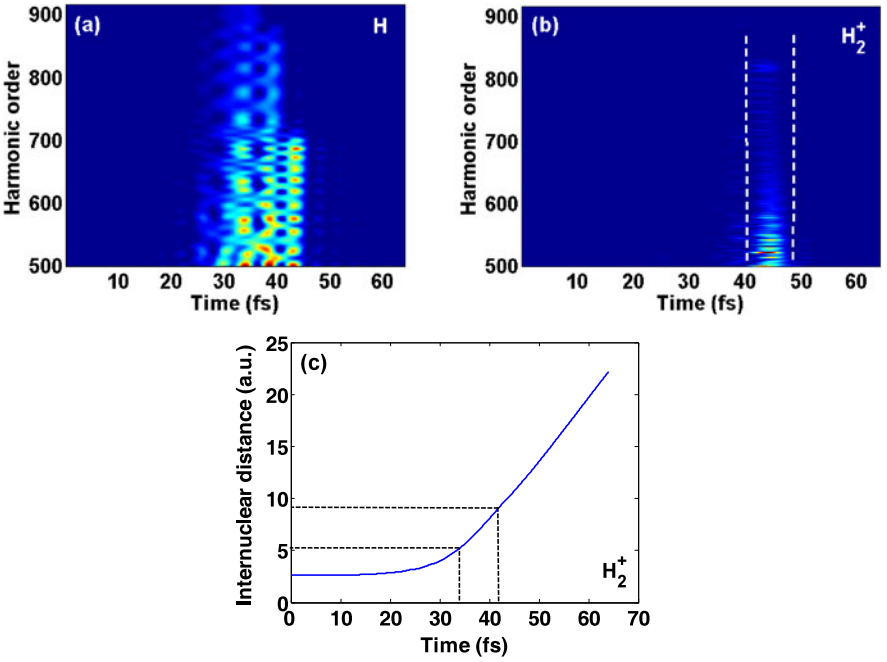

Fig. 2.3 Time profiles of the each harmonics from 499th (258 eV) to 915th (473 eV) for the H atom (**a**) and for the H_2^+ molecule (**b**). (**c**) Time-dependent internuclear distance for the H_2^+ molecule

The electrons are ionized at about half of an optical cycle earlier than the crest of the electric oscillation adjacent to the moment when the electrons recombine with parent ions. Figures 2.3(a) and 2.3(b) present the time profiles of the each harmonics from 499th (258 eV) to 915th (473 eV). For example, for the 499th harmonic, we use a square-wave filter function to select the spectral region of 499th harmonic, and then performed an inverse Fourier transform. The rest can be done in the same manner. It is interesting to note that for the H atom, the attosecond pulses are generated every half-cycle, whereas, for the H_2^+ molecule the harmonic generation is restricted in the region of 40.3–48.9 fs marked by the dashed line. The moment of harmonic emission is considered as the time of electronic recombination. This means that the electrons are ionized in the time range from 34.0 to 41.9 fs by backward reasoning. In this time region, the internuclear distance ranges from 5.2 to 9.1 a.u., as shown in Fig. 2.3(c). As is well known, when R increases to intermediate-to-large internuclear separations ($5 < R < 12$ a.u.), CREI in the H_2^+ molecule is remarkable [6, 10]. For the H_2^+ molecule the vibrational motion is taken into account, which is the main difference between the H_2^+ molecule and the H atom in our model. Thus, by comparing the results in the two cases, we think that the CREI caused by the molecular vibrational motion results in the selective generation of attosecond pulse appearing in the region of 40.3–48.9 fs with all the other pulses suppressed. When selecting the range of harmonic spectra properly, an IAP can be produced for the

H_2^+ molecule, while for the H atom, attosecond pulse trains created, as shown in Fig. 2.2. Our scheme suggests that IAPs in two spectral regions, i.e. 258–323 eV which is well within the water window and 626–691 eV which is beyond the water window, can be produced and is attributed to the enhanced ionization and concomitant vibrational motion of H_2^+ molecule driven by a 2400-nm, 4×10^{14} W/cm^2 laser field with a duration longer than the vibrational period.

In order that the role of the molecular vibrational motion played in the process of IAP generation is presented more significantly, we employ an envelope function $f(t)$ that rises during the first half of an optical cycle, decreases during the last half of an optical cycle, and holds constant for the middle fifteen optical cycles. The intensity of the laser pulses is 2×10^{14} W/cm^2. Figures 2.4(a), 2.4(b) and 2.4(c) show the temporal profiles of the harmonic emission at the cutoff with a bandwidth of ∼30 eV for the H_2^+ molecule (red solid curve) and for the H atom (blue dotted curve), respectively. Figures 2.4(d), 2.4(e), and 2.4(f) present the time profiles of harmonics for the H_2^+ molecule by performing an inverse Fourier transform of each harmonic from 13th (20 eV) to 55th (85 eV) [Fig. 2.4(d)], from 43th (33 eV) to 237th (184 eV) [Fig. 2.4(e)], and from 351st (181 eV) to 725th (375 eV) [Fig. 2.4(f)]. Figures 2.4(g), 2.4(h), and 2.4(i) illustrate the time-dependent internuclear distance for the H_2^+ molecule. The central wavelengths of the driving laser pulses are 800 nm [Fig. 2.4(a), 2.4(d), 2.4(g)], 1600 nm [Fig. 2.4(b), 2.4(e), 2.4(h)] and 2400 nm [Fig. 2.4(c), 2.4(f), 2.4(i)], respectively. One can see from these figures that the driving wavelength effect in the generation of a bunch of attosecond pulse trains is obvious. The duration of the generated attosecond pulse train becomes shorter for the longer wavelength. The relevant internuclear distances when the attosecond pulses are generated are from 3.5 to 7.7 a.u. in Fig. 2.4(g), from 3.4 to 7.5 a.u. in Fig. 2.4(h), and from 3.4 to 7.4 a.u. in Fig. 2.4(i). The regions of the internuclear distance in which the attosecond pulses are selected to generate are the same for the different wavelengths. All these prove that the CREI give rise to the generation of IAP.

2.3 Driving Wavelength Effect on Molecular HHG in a Tunable MIR Laser Field

Recently, with the development of high-energy and broadband-tunable infrared parametric source for HHG [14–18], the driving laser wavelength can be tuned to the infrared absorption of molecule. It is possible to investigate and even to control the proton dynamics in molecular HHG by tuning the infrared wavelength of the driving laser.

We experimentally investigate the driving wavelength effects on the molecular HHG (CH_4) and on the atomic HHG (Xe) by using a tunable infrared laser. We tune the wavelength of the driving laser to approach the vibrational absorption of CH_4 molecules (1670 nm), and unambiguously observe that the yield of molecular HHG is much sensitive to the infrared wavelength while the yield of atomic HHG

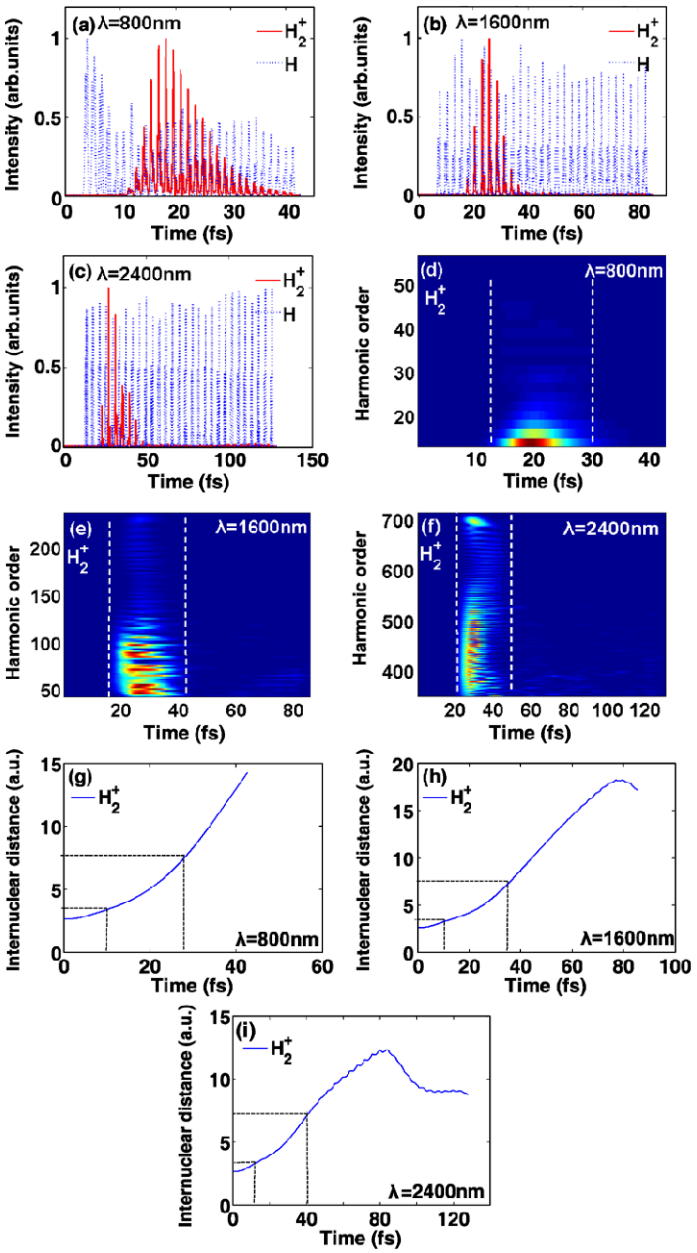

Fig. 2.4 Temporal profiles of the harmonic emission at the cutoff for the H_2^+ molecule (*red solid curve*) and for the H atom (*blue dotted curve*), respectively, driven by laser pulse with (**a**) $\lambda = 800$ nm, (**b**) $\lambda = 1600$ nm, and (**c**) $\lambda = 2400$ nm. Time profiles of each harmonics at the cutoff for the H_2^+ molecule driven by the laser pulse with (**d**) $\lambda = 800$ nm, (**e**) $\lambda = 1600$ nm, and (**f**) $\lambda = 2400$ nm. Time-dependent internuclear distance for the H_2^+ molecule driven by laser pulse with (**g**) $\lambda = 800$ nm, (**h**) $\lambda = 1600$ nm, and (**i**) $\lambda = 2400$ nm

is not. The results can be attributed to the resonance between the driving infrared laser and the vibrational transition energy, which allows us to create highly excited vibrational states. The results indicate that the infrared wavelength can be used to control the proton vibration in molecular HHG.

2.3.1 Experimental Setup

A home-build infrared optical parametric amplifier (OPA) is used in this work, which is pumped by a commercial Ti:sapphire based chirped pulse amplification laser (Coherent Inc.). The details of the OPA are described in [17]. The OPA system can produce ∼45 fs/1 kHz output pulses. The output pulses are tunable from 1.5 μm to 1.9 μm, and the maximum output pulse energy is 1.7 mJ at 1.6 μm. The infrared output pulses are focused in a gas cell (the focal length 150 mm, and the length of gas cell ∼2.5 mm) located in a high-vacuum interaction chamber. The output pulse energy from the OPA is kept ∼1.2 mJ, which can be controlled by the pump energy of the 800 nm pump laser. The size of the focal spot is ∼150 μm which can be controlled by the size of the iris which lies in the output beam from the OPA. The Raleigh length is ∼5 mm, and the average intensity is estimated to be $\sim 1.5 \times 10^{14}$ W/cm^2 in the interaction region within the gas. The stagnation pressure of the gas is around 100 torr. The generated high-order harmonics are detected by a home-made flat-field grating spectrometer equipped with a soft-X-ray charge-coupled device camera (CCD, Princeton Instruments, SX 400), and Al foil with 500 nm thickness is used in the spectrometer to stop the driving laser.

2.3.2 Difference of Driving Wavelength Effect Between CH_4 Molecules and Xe Atoms

We choose CH_4 molecules and Xe atoms as the investigative objects due to three reasons. First, 1670 nm is one of the infrared absorption peaks due to the first overtone of A_1 mode of C–H. Second, the proton motion can be easily induced by the driving laser, and the carbon motion can be considered to be frozen during the HHG process. Third, their ionization potentials are similar (12.7 eV for CH_4, 12.1 eV for Xe), and it is reasonable to neglect the differences in phase-matching conditions for harmonic generation in the two cases [11]. Additionally, the molecular HHG has been proved to be sensitive to the laser-induced nuclear vibration [9–11] (the less intense harmonics are generated with the faster moving nuclei), and the atoms without nuclear vibration are adopted contrastively as the reference of harmonic intensity from fixed nuclear modeling.

First, we measure the harmonic spectra driven by the 800 nm laser being far off-resonant with the vibrational absorption. The harmonic spectra from CH_4 molecules and Xe atoms are measured at the equal gas density and at the same laser condition

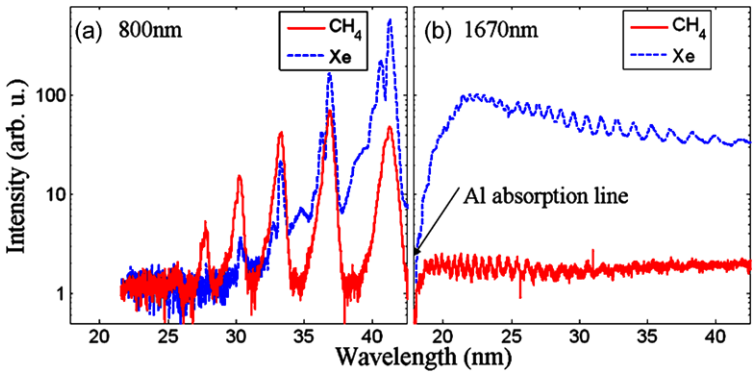

Fig. 2.5 Measured angle-integrated spectra from CH_4 molecules and Xe atoms at equal gas density, driven by the laser pulses at (**a**) 800 nm and (**b**) 1670 nm, respectively

shown in Fig. 2.5(a). Contrastively, we also measure the harmonic spectra driven by the infrared parametric source at the 1670 nm working wavelength within the vibrational absorption shown in Fig. 2.5(b). We unambiguously observe that the integrated yield of molecular HHG is much lower by 20 times than the yield of atomic HHG at the 1670 nm working wavelength in Fig. 2.5(b), while their harmonic yields are similar at the 800 nm driving wavelength in Fig. 2.5(a).

In order to ensure that the harmonic yields from both gases are measured at the optimal condition, we also measure the harmonic yields at different focus location, and find that the optimal harmonic yields from both gases are at the same focus location due to their similar ionization potentials. The differences between the molecular HHG and the atomic HHG, beyond or within the wavelength of the vibrational absorption, can be attributed to the resonance between the driving infrared laser and the vibrational transition energy.

Using the driving wavelength effect on the molecular vibrational dynamics, which can be identified by the yield of harmonic generation, we think that the proton motion can be controlled by tuning the infrared wavelength where the atomic HHG can be used as the reference of yield of harmonic generation. In Fig. 2.6(a), the harmonic yields from CH_4 molecules are weak and different (the spectral peaks are: 7.0 for 1550 nm, 1.9 for 1670 nm, 2.1 for 1800 nm, and 1.0 for the background). In Fig. 2.6(b), the harmonic yields from Xe atoms are strong and similar (the spectral peaks are: 104 for 1550 nm, 100 for 1670 nm, 101 for 1800 nm, and 1.0 for the background) in our observing window 18–42 nm. Therefore, the harmonic yields from CH_4 molecules are weaker and much more sensitive to the infrared wavelength than that from Xe atoms. They are shown that the yield of the molecular HHG is sensitive to the infrared wavelength, while the yield of the atomic HHG is not sensitive to the wavelength at the same laser condition. The molecular HHG is sensitive to the nuclear vibration and the resonance between the driving infrared laser and the vibrational transition energy is sensitive to the infrared wavelength. Thus, the phenomena that molecular HHG is much more sensitive to the infrared wavelength than

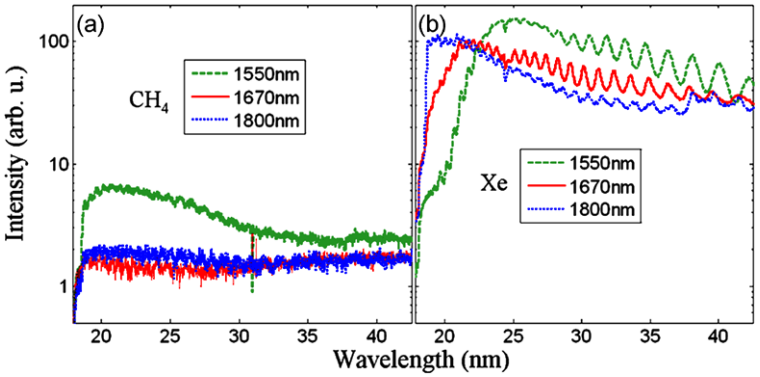

Fig. 2.6 Measured angle-integrated spectra at different wavelengths of the driving laser pulse from (**a**) CH_4 molecules and (**b**) Xe atoms, respectively

atomic HHG can be attributed to the resonance between the driving infrared laser and the vibrational transition energy.

2.3.3 Discussion

In Fig. 2.5, for the 800 nm driving laser field, the harmonic yield of CH_4 molecules is similar to that of Xe atoms, while for the 1670 nm driving laser field, the harmonic yields from CH_4 molecules are much weaker than that from Xe atoms. This is because the photon energy of 800 nm is very far away from the molecular vibrational energy, the vibrational amplitude of CH_4 molecules when the driving laser wavelength is 800 nm is much smaller than that with the driving wavelength of 1670 nm which is one of the infrared absorption peaks as mentioned above. In Fig. 2.6, for CH_4 molecules, there are both quantum yield effect and resonant effect which are both dependent on the driving laser wavelength. For the resonant effect, the harmonic yield is lower, when the driving laser wavelength is closer to 1670 nm. For the quantum yield effect, the harmonic yield is lower when the driving laser wavelength is longer. Therefore, the harmonic yield decreases rapidly when the driving laser wavelength changes from 800 nm to 1670 nm, due to that the two effects are consistent. When the laser wavelength is longer than 1670 nm, the two effects are opposite and the harmonic yield is too weak to observe in our experimental condition. Therefore, the harmonic yield weakly depends on the driving laser wavelength when the driving wavelength is longer than 1670 nm. For Xe atoms, the driving wavelength effect on harmonic yield is inconspicuous, while the driving wavelength effect on HHG of CH_4 is much more remarkable than that of Xe. The obvious difference between CH_4 molecule and Xe atom, which is concerned in our work, is induced by the molecular vibrational motion. The small change in the case of Xe can be explained by the theoretical results [34–36], which are mainly about the theoretical calculation of atomic HHG with the wavelength effect. Because our analysis

is just a qualitative explanation of these phenomena, a more comprehensive theory of HHG in molecules that takes into account the nuclear motion is necessary for a better account for the underlying physics.

2.4 Summary

We have shown two recent results on understanding the role of nuclear vibrational motion in molecular HHG in the mid-infrared laser field: First, IAP in the water window is predicted to be generated by using a part of the spectrum of the high-harmonics generated from H_2^+ molecules interacting with a multicycle 2400-nm mid-infrared laser field with moderate intensity. Second, we have observed experimentally that the molecular HHG in a tunable mid-infrared laser field around the vibrational resonance is more sensitive to the driving laser wavelength than the atomic HHG with comparable ionization potential, as a result of the nuclear (proton) vibrational motion. These findings are interesting and invaluable for the future detection and control of the nuclear dynamics in molecules.

Acknowledgements We acknowledge the financial support from the National Natural Science Foundation (Grants No. 10734080, No. 60921004, No. 11134010, No. 10904157, and No. 61078022), 973 Project (Grant No. 2011CB808103), Chinese Academy of Sciences and Shanghai Commission of Science and Technology (Grant No. 10QA1407600). Related correspondence should be addressed to ruxinli@mail.shcnc.ac.cn and zzxu@mail.shcnc.ac.cn.

References

1. Z. Chang et al., Phys. Rev. Lett. **79**, 2967 (1997)
2. E.J. Takahashi et al., Phys. Rev. Lett. **101**, 253901 (2008)
3. G. Sansone et al., Science **314**, 443 (2006)
4. M. Drescher et al., Nature **419**, 803 (2002)
5. E. Goulielmakis et al., Science **320**, 1614 (2008)
6. T. Zuo, A.D. Bandrauk, Phys. Rev. A **52**, R2511 (1995)
7. T. Seideman et al., Phys. Rev. Lett. **75**, 2819 (1995)
8. P.H. Bucksbaum et al., Phys. Rev. Lett. **64**, 1883 (1990)
9. M. Lein, Phys. Rev. Lett. **94**, 053004 (2005)
10. A.D. Bandrauk et al., Phys. Rev. Lett. **101**, 153901 (2008)
11. S. Baker et al., Science **312**, 424 (2006)
12. T. Bredtmann et al., Phys. Rev. A **84**, 021401 (2011)
13. Ch. Spielmann et al., Science **278**, 661 (1997)
14. X. Gu et al., Opt. Express **17**, 62 (2009)
15. G. Andriukaitis et al., Opt. Lett. **36**, 2755 (2011)
16. C.P. Hauri et al., Opt. Lett. **32**, 868 (2007)
17. C. Zhang et al., Opt. Lett. **34**, 2730 (2009)
18. C. Li et al., Opt. Express **19**, 6783 (2011)
19. M.-C. Chen et al., Phys. Rev. Lett. **105**, 173901 (2010)
20. P. Zou et al., Chin. Phys. B **19**, 019501 (2010)
21. W. Hong et al., Opt. Express **18**, 11308 (2010)

22. H. Du, B. Hu, Opt. Express **18**, 25958 (2010)
23. H. Mashiko et al., Opt. Lett. **34**, 3337 (2009)
24. A.D. Bandrauk et al., Phys. Rev. A **67**, 013407 (2003)
25. D.G. Lappas, J.P. Marangos, J. Phys. B **33**, 4679 (2000)
26. R. Velotta et al., Phys. Rev. Lett. **87**, 183901 (2001)
27. J. Itatani et al., Phys. Rev. Lett. **94**, 123902 (2005)
28. T. Kreibich et al., Phys. Rev. Lett. **87**, 103901 (2001)
29. M. Lein et al., Phys. Rev. A **65**, 033403 (2002)
30. M.R. Hermann, J.A. Fleck Jr., Phys. Rev. A **38**, 6000 (1988)
31. D. Bauer, P. Koval, Comput. Phys. Commun. **174**, 396 (2006)
32. H. Yu, A.D. Bandrauk, Phys. Rev. A **56**, 685 (1997)
33. P.B. Corkum, Phys. Rev. Lett. **71**, 1994 (1993)
34. J. Tate et al., Phys. Rev. Lett. **98**, 013901 (2007)
35. P. Colosimo et al., Nat. Phys. **4**, 386 (2008)
36. M. Frolov et al., Phys. Rev. Lett. **102**, 243901 (2009)

Chapter 3
Attosecond Dynamics of Coherent Electron–Nuclear Wave Packets in Molecules

André D. Bandrauk, Timm Bredtmann, and Szczepan Chelkowski

Abstract The natural time scale of electron motion in atoms is the attosecond (10^{-18} s). In molecules, this time scale becomes strongly dependent on nuclear motion which occurs on femtosecond (10^{-15} s) time scales. Numerical solutions of the time-dependent Schrödinger equation, TDSE, for the one electron H_2^+ molecule as compared to the H atom, provide schemes for studying attosecond electron motion in a coherent electron wave packet (CEWP). Ionization of CEWP's by attosecond laser pulses result in large asymmetries in the ionization yields which follow electron motion and transfer inside CEWP's. High-order harmonic generation (HHG) is shown to be an even more sensitive tool for monitoring attosecond electron motion using few femtosecond, intense, mid-infrared probe laser pulses. The strong variation of harmonic intensities as function of time delay between the pump pulse (i.e., the pulse which prepared a CEWP) and the probe pulse is interpreted with the help of the Strong Field Approximation (SFA) and the three step recollision model.

3.1 Introduction

Investigations of light-matter interactions and motion in the microcosm have entered a new temporal regime, the regime of attosecond physics. It is a main 'spin-off' of strong field (i.e., intense laser) physics, in which nonperturbative effects are fundamental. Attosecond pulses open up new avenues for time-domain studies of multi-electron dynamics in atoms, molecules, plasmas, and solids on their natural, quantum mechanical time scale and at dimensions shorter than molecular

A.D. Bandrauk (✉) · T. Bredtmann · S. Chelkowski
Laboratoire de Chimie Théorique, Faculté des Sciences, Université de Sherbrooke, Sherbrooke, Québec, Canada J1K 2R1
e-mail: Andre.Dieter.Bandrauk@USherbrooke.ca

S. Chelkowski
e-mail: s.chelkowski@usherbrooke.ca

T. Bredtmann
Institut für Chemie und Biochemie, Freie Universität Berlin, Takustr. 3, 14195 Berlin, Germany
e-mail: bredt@chemie.fu-berlin.de

K. Yamanouchi, K. Midorikawa (eds.), *Progress in Ultrafast Intense Laser Science*, Springer Series in Chemical Physics 104, DOI 10.1007/978-3-642-35052-8_3,

Table 3.1 Atomic units expressed in Gaussian-cgs electromagnetic units ($e = \hbar = m_e = 1$; $c = 137.036 =$ inverse of the fine structure constant)

Distance (Bohr radius):	$a_0 = \hbar^2/m_e e^2 = 0.05292$ nm
Potential energy:	$V_0 = e^2/a_0 = \hbar^2/m_e a_0^2 = 1$ Hartree $= 27.211$ eV
Electric field:	$E_0 = V_0/ea_0 = e/a_0^2 = 5.14 \times 10^9$ V cm^{-1}
Intensity:	$I_0 = cE_0^2/8\pi = 3.54 \times 10^{16}$ W cm^{-2}
Time:	$t_0 = \hbar/V_0 = 24.2 \times 10^{-18}$ s $= 24.2$ asec,
	$2\pi t_0 = 152$ asec
	$t_c = \hbar/m_e c^2 = 1.29 \times 10^{-21}$ s
Momentum:	$p_0 = \hbar/a_0$
Velocity:	$v_0 = p_0/m_e = a_0/t_0 = 2.19 \times 10^8$ cm s^{-1}

and even atomic scales. These capabilities promise a revolution in our microscopic knowledge and understanding of matter. The recent development of intense, phase-stabilized femtosecond (10^{-15} s) lasers [1–3] is allowing for the first time the generation and measurement of isolated light pulses as well as trains of pulses on the attosecond (1 asec $= 10^{-18}$ s) time scale, the natural time scale of the electron itself (e.g., the orbital period of an electron in the ground state of the H atom) is 152 asec (Table 3.1). This development is facilitating (and even catalysing) a new class of ultrashort time domain studies in photobiology, photochemistry [4, 5] and photophysics [6, 7]. These new coherent, sub-fs pulses generated at frequencies in the extreme ultraviolet and soft-X-ray spectral regions, along with their intense, synchronized near-infrared driver waveforms and novel metrology based on sub-fs control of electron-light interactions, are spawning the new science of attosecond physics, whose aims are to monitor, to visualize, and, ultimately, to control electrons on their own time and spatial scales, i.e., the attosecond time scale and the sub-nanometer (Ångstrom) spatial scale typical of atoms and molecules [8]. Additional goals for experiment are to advance the enabling technologies for producing attosecond pulses at higher intensities and shorter durations. According to theoretical predictions, novel methods for intense attosecond pulse generation may in future involve using overdense plasmas and/or relativistic electrons [9].

Electronic processes on sub-atomic spatio-temporal scales are the basis of chemical physics, atomic, molecular, and optical physics, materials science, and even some life science processes [4, 10]. Research in these areas using the new attosecond tools will advance together with the ability to control electrons themselves. Indeed, we expect that developments will advance in a way that is similar to advances that have occurred on the femtosecond time scale, in which much previous experimental and theoretical work on the interaction of coherent light sources has led to the development of means for ‘coherent control’ of nuclear motion in molecules [11, 12].

An important nonlinear process, High-Order Harmonic Generation (HHG) is the current most convenient source of attosecond pulses [1, 2, 13, 14]. This rapid development of ultrashort intense laser pulses allows nowadays for shaping and focusing

such pulses to higher intensities creating electric fields E greater than the atomic unit, a.u., $E_0 = 5 \times 10^9$ V cm^{-1} at the 1s orbit radius $a_0 = 0.0529$ nm of the H atom. This corresponds to an a.u. of intensity $I_0 = cE_0^2/8\pi = 3.54 \times 10^{16}$ W/cm^2. Such pulses can be compressed to times of several femtoseconds (1 fs $= 10^{-15}$ s), and thus are capable of creating radiative coherences that are shorter than molecular nonradiative (radiationless) relaxation times [15, 16]. In Table 3.1 we summarize the atomic units, a.u., for various physical quantities and/or parameters used to describe the physical processes occurring under the "extreme" conditions of these new pulses. The ultimate time scale is the zeptosecond (10^{-21} s) corresponding to excitations and creations of electron–positron ($e^+ + e^-$) pairs [17]. Whereas at the end of the 20th century the focus was on femtosecond (fs) photochemistry and photophysics culminating with a Nobel prize to A.H. Zewail (Caltech) for "Femto Chemistry" [18, 19], a major effort is now underway to develop single attosecond (as) optical pulses based on the nonperturbative physics of HHG in atoms and MHOHG, Molecular High-Order Harmonic Generation. These attosecond pulses presage the control of electron motion in molecules, the "Holy Grail" of many atomic and molecular sciences [4, 10].

The motion of electrons is the fundamental basis of chemistry. Watching such motion will help chemists understand why some atoms bind while others do not, why reactions take the time they do, why certain molecular geometries exist and change. Therefore the ability to manipulate electrons in molecules is important because electron sharing and transfer are essential to chemical bonding and chemical reactions. Other possible applications are envisaged in magnetic information storage devices, X-ray lasers for medical imaging, chemical catalysis and more sophisticated and efficient light capturing devices for future energy technologies [20].

A major role for theory in attosecond science is to elucidate novel ways to investigate and to control electronic processes in matter on attosecond time scales. The ingredients of appropriate theoretical formulations should be the fundamental concept of laser driven, electron-ion rescattering [21, 22], the unique aspects of few cycle laser pulse-matter interactions and a nonperturbative theoretical framework which is necessary to describe highly nonlinear multiphoton processes. Much theoretical progress has been achieved in the field of non-perturbative laser–atom interactions [23]. Molecules introduce a new complexity due to the nuclear degrees of freedom with their own natural time scale, the femtosecond [8]. The first simulations of the nonlinear nonperturbative response of the simplest one-electron molecule, H_2^+, were performed beyond the Born–Oppenheimer approximation, i.e., by including the complete nonseparable 3-body, electron–protons dynamics [24]. It has been shown previously that MHOHG can be used to generate and amplify efficiently attosecond pulses [14] as a result of the nonlinear nonperturbative response of the induced dipole moment to short ($t_p < 10$ fs) intense ($I \geq 10^{14}$ W/cm^2), 800 nm laser pulses both linearly and circularly polarized. In order to find possible applications, we have been exploring and proposing recently methods of observing electron motion in molecules [25–32], a necessary first step in the goal to control electronic processes at the molecular level.

3.2 Attosecond Photoionization of Coherent Electron Wave Packets (CEWP's)

We study analytically and numerically the possibility for monitoring electron motion in a molecules, by photoionization spectroscopy, using two ultrashort laser pulses. The first prepares a coherent superposition of two or more electronic states whereas the second (attosecond) pulse photoionizes the molecule. As shown previously, the electron motion in such coherent states evolves on an attosecond time scale and therefore requires attosecond pulses to follow the ensuing electron motion [25–28]. Such a pump-probe scheme illustrates the conclusion that interesting and useful information about the ensuing electron dynamics can be obtained simply from the measurement of the photoionization spectra as a function of the time delay between the two pulses: the pump which creates the coherent (quantum mechanical) superposition of electronic states (or wave packet, CEWP), and the attosecond probe pulse, which allows for measurement of the attosecond evolution. Ultrashort pulses automatically lead to coherent wave packets in the electron continua, from superposition of nuclear, electronic, or combined electron–nuclear states [33]. A characteristic of ultrashort pulses is that they induce the asymmetry in the photoelectron angular distributions even from single ground states. Such asymmetry results in a universal law allowing for measurement of the absolute or Carrier Envelope Phase, CEP, of ultrashort mid-infrared intense pulses [34, 35]. Thus using attosecond pulses, the resulting asymmetries in photoelectron angular distributions provide a simple signature of the electron motion within the time-dependent coherently coupled molecular states. Both asymmetries and kinetic energy spectra of electrons show very strong two-center interference patterns, typical for diatomic molecular systems [36]. We illustrate these effects using as an example a dissociating hydrogen molecular ion, H_2^+, probed by attosecond pulses. Such a molecule is a one-electron system for which the electron spectrum is exactly analytically solvable and has been used to illustrate imaging of molecular orbitals with intense attosecond electron pulses [37].

The central idea of a scheme for monitoring electron motion is the preparation by an ultrashort (femtosecond) pump pulse of a coherent superposition of two electronic states or (bound electron) wave functions $\Psi_1(\mathbf{r})$ and $\Psi_2(\mathbf{r})$:

$$\Psi(\mathbf{r},t) = \alpha_1 \Psi_1(\mathbf{r}) \exp\left(i I_p^{(1)} t\right) + \alpha_2 \exp(-i\beta) \Psi_2(\mathbf{r}) \exp\left(i I_p^{(2)} t\right), \tag{1}$$

where $I_p^{(1)}$ and $I_p^{(2)}$ are the ionization potentials of states $\Psi_1(\mathbf{r})$ and $\Psi_2(\mathbf{r})$, α_1^2 and α_2^2 are the corresponding populations and β is an initial phase which depends on the excitation scheme. This initial phase will in fact become a measurable parameter via attosecond photoionization. As in previous work [24], we assume the molecule is aligned along the z-Cartesian axis and both nuclei are fixed in space (Born–Oppenheimer approximation). Aligning molecules in space is a technique developed by the Corkum group at NRC and is currently used for tomographic imaging of molecular orbitals [38]. Such alignment allows for having the laser polarization vector $\mathbf{e}$ parallel to the molecular z-axis. The second ionizing attosecond pulse is assumed to be a linearly chirped X-ray pulse. Such a pulse is described by a vector

potential $A(t)$ or equivalently by an electric field $E(t) = -\frac{\partial}{\partial t}A(t)$ with total area zero [23, 34], i.e.,

$$\int_{-\infty}^{\infty} E(t)\,dt = A(-\infty) - A(\infty) = 0, \tag{2}$$

$$\mathbf{A} = A(t)\mathbf{e} = (A_0/2)\exp\left[-i\Omega t - (t-t_0)^2/2(1-i\xi)\tau^2\right]\mathbf{e}. \tag{3}$$

The zero area condition (2) is equivalent to the requirement that the Fourier transform of the electric field $E(t)$ is zero at frequency $\omega = 0$. In other words, this condition means that the electromagnetic wave $E(t)$ has no DC-field component—an obvious requirement for the fields far from charges. The Gaussian envelope of this pulse has a maximum at the time $t = t_0$ and the pulse is linearly polarized along the vector (direction) $\mathbf{e}$. The central frequency Ω is larger than both ionization potentials $I_p^{(j)}$ in order to induce an ionization by a one-photon absorption. The parameter τ is related to the physical pulse duration:

$$\tau_{\mathrm{FWHM}} = 2\tau\sqrt{\ln 2}\sqrt{1+\xi^2}. \tag{4}$$

ξ is the dimensionless chirp parameter [39]: a positive (negative) value of ξ corresponds to an up-chirped (down-chirped) pulse, i.e. the instantaneous frequency $\Omega_{\mathrm{inst}}(t)$ is an increasing (decreasing) function of time t. Such chirp is generated in the synthesis of "isolated" single cycle attosecond pulses [40]. The coherent superposition of electron wave functions $\Psi_1(\mathbf{r})$ and $\Psi_2(\mathbf{r})$, described by Eq. (1), is characterized by three important parameters: α_1, α_2 and β, which are controlled by the pump pulse. For a pump pulse: $E_p(t) = \varepsilon_p(t)\cos[\omega_p(t-t_p) + \Phi_p]$, where ω_p, t_p and Φ_p are the pump pulse frequency, time of the envelope peak and phase, one can deduce from the two-level system that in case of exact resonance, $\omega_p = \Delta I_p = I_p^{(1)} - I_p^{(2)}$, the level populations α_1^2, α_2^2 are simple trigonometric functions of the area under the pump pulse envelope $\int_{-\infty}^{\infty}\varepsilon_p(t)\,dt$ [26] and that the initial phase is

$$\beta = \Phi_p + \pi/2 - \Delta I_p t_p, \tag{5}$$

see [26], where $\Delta I_p = I_p^{(1)} - I_p^{(2)}$ is the separation between two electronic levels at a fixed internuclear distance R. The duration of the pump pulse and the time delay $t_{\mathrm{del}} = t_0 - t_p$ between the pump and the probe attosecond pulse must be shorter than the relaxation times of the medium. In the case of a dissociating molecule, such as H_2^+, the relaxation times are of the order of few femtoseconds, since the natural frequency for proton motion in H_2^+ is ~5 fs [15]. Thus, attosecond experiments allow for measuring electron motion with frozen nuclei, corresponding to the standard Born–Oppenheimer approximation in photochemistry.

The photon energy $\hbar\Omega$ corresponding to the central frequency Ω of the attosecond pulse is assumed to be much larger than the molecular ionization potential (X-ray frequency region). As a result, photoionization transition amplitudes are mainly associated with single photon transitions. Multiphoton absorptions in the ionized continuum, called ATI, Above Threshold Ionization, require (in this high frequency regime) very high intensities, $I \gg 10^{15}$ W/cm^2 [41, 42], for which no attosecond

pulses have yet been made. One can therefore use the first order time-dependent perturbation theory to calculate the coherent transition probability amplitude $M_{\rm coh}$ for finding the electron in the final continuum state $\psi_{\mathbf{p}}$, where $\mathbf{p}$ is the asymptotic electron momentum and $\psi_{\mathbf{p}}$ is a corresponding two-center continuum wave function. The transition amplitude from the initial bound coherent state (1) is given in [39]:

$$M_{\rm coh} = M_0 \varepsilon \big[\gamma_1 M_1 + \gamma_2 e^{-i\Phi(\xi,p,t_0)} M_2\big], \tag{6}$$

where $M_0 = A_0 \tau [\pi(1-i\xi)/2]^{1/2}$. M_1 and M_2 are the photoionization amplitudes for the two bound states $\Psi_1(\mathbf{r})$ and $\Psi_2(\mathbf{r})$ in the coherent superposition (1). Equation (6) shows that attosecond photoelectron spectra generated by this superposition depend on the pulse duration τ through the factors

$$\gamma_j = \alpha_j \exp\big(-\omega_j^2 \tau^2/2\big), \quad \text{where } \omega_j = p^2/2 + I_p^{(j)} - \Omega,\ j = 1, 2$$

and $\varepsilon = \exp(i\omega_1 t_0 + i\xi\omega_1^2\tau^2/2)$ is a common phase factor.

The relative phase $\Phi(\xi, p, t_0)$ between the two amplitudes emanating from each separate state Ψ_1 or Ψ_2 depends on the initial relative phase β (present in (1)), the time t_0, the photoelectron momentum $\mathbf{p}$, and on the chirp rate ξ [39],

$$\Phi(\xi, p, t_0) = \delta(t_0) + \phi(\xi, p), \quad \delta(t_0) = \beta + \Delta I_p t_0 = \Phi_p + \pi/2 + \Delta I_p t_{\rm del}. \tag{7}$$

The chirp dependent part of the phase Φ is given by

$$\phi(\xi, p) = \xi \tau^2 \Delta I_p \big[p^2/2 + I_p^{(\rm av)} - \Omega\big], \tag{8}$$

where $I_p^{(\rm av)} = (I_p^{(1)} + I_p^{(2)})/2$ is the average ionization potential of the coherently excited electronic states $\Psi_1(\mathbf{r})$ and $\Psi_2(\mathbf{r})$. The phase $\Phi(\xi, p, t_0)$ defined in (7) is a universal quantity as it introduces interferences between single state photoionization amplitudes M_1 and M_2. It depends linearly on the chirp ξ through the relation (8). It also depends linearly on the time delay $t_{\rm del} = t_0 - t_p$ between the pump and the attosecond (probe) pulse. This time delay defines the phase $\delta(t_0) = \Delta I_p t_{\rm del} + \Phi_p + \pi/2$ in (6) from which by varying $t_{\rm del}$ one should be able to measure ΔI_p, and the relative phase β between the states Ψ_1 and Ψ_2. Varying the chirp ξ should give the chirp free pulse duration τ which defines the physical pulse duration $\tau_{\rm FWHM}$ via relation (4). Note that the pulse defined by (3) has the same bandwidth as a non-chirped pulse with much shorter duration τ. One can envisage therefore chirping attosecond pulses to give the same optical properties (measured via photoelectron spectra) as transform-limited, i.e., no-chirped zeptosecond (10^{-21} s) pulses which may be used for laser control of nuclear reactions.

To illustrate the monitoring and even characterizing of electron wave functions through attosecond pulse photoionization, we focus on two cases of superpositions of states Ψ_1 and Ψ_2 of the H_2^+ molecular ion: first, a case when both states have the opposite parity (*gerade* + *ungerade*) and the second case when both states have the same parity (*gerade* + *gerade*). More specifically, the appropriate electronic wave functions are represented for sufficiently large internuclear distance R by the following linear combinations of atomic orbitals, LCAO, as in [43]

$$\psi_{\sigma_g 1s}(\mathbf{r}) = N_{\sigma_g 1s}\big[\phi_{1s}(\mathbf{r}_1) + \phi_{1s}(\mathbf{r}_2)\big], \tag{9}$$

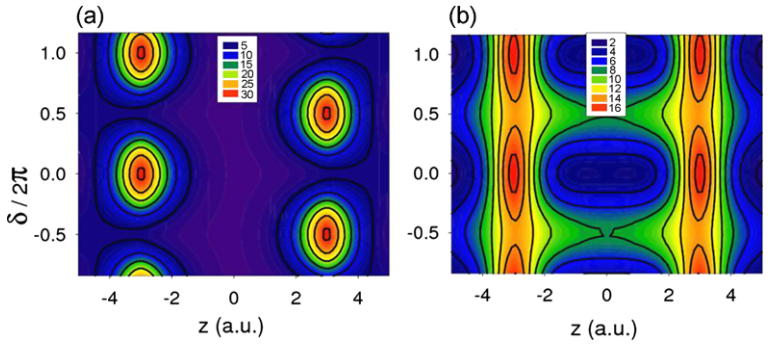

Fig. 3.1 Electron probability density in H_2^+ at the internuclear separation $R = 6$ a.u. as a function of phase shift δ and coordinate z along the molecular axis for a coherent superposition of (**a**) the $\sigma_g 1s + \sigma_u 2s$ states and of (**b**) the $\sigma_g 1s + \sigma_g 2s$ states

for the ground state, and

$$\psi_{\sigma_u 2s}(\mathbf{r}) = N_{\sigma_u 2s}\big[\phi_{2s}(\mathbf{r}_1) - \phi_{2s}(\mathbf{r}_2)\big],$$

or (in the second case) the excited state is

$$\psi_{\sigma_g 2s}(\mathbf{r}) = N_{\sigma_g 2s}\big[\phi_{2s}(\mathbf{r}_1) + \phi_{2s}(\mathbf{r}_2)\big] \tag{10}$$

for the excited state, where N's are the normalization factors and 1s, 2s are atomic orbitals of the H-atom. Figure 3.1a and 3.1b show the electron probability density $|\psi(\mathbf{r}, t)|^2$ (integrated over coordinates perpendicular to the molecular axis) from Eq. (1) for the $1\sigma_g + 2\sigma_u$ and $1\sigma_g + 2\sigma_g$ coherent state superposition, respectively. Calculations (for Fig. 3.1) have been performed for the internuclear distance $R = 6$ a.u. (1 a.u. $= 0.0529$ nm and is equal to the radius of the electron lowest orbit in the Bohr's atom model) as a function of phase shift δ, defined in Eq. (7), and the electron coordinate z along the internuclear axis R. We have chosen equal amplitudes, i.e. $\alpha_1 = \alpha_2 = 1/\sqrt{2}$. We note that in Fig. 3.1a the electron "hops" from one nucleus to another with a period $T_0 = 2\pi/\Delta I_p$ as this corresponds to the coherent superposition of states each having opposite inversion symmetry (with respect to the center-of-mass of the two nuclei) yielding asymmetric total probability density. The time scale for such electron transfer can be estimated from $\Delta I_p \simeq \varepsilon_{2s} - \varepsilon_{1s} = 3/8$ a.u. (atomic energy units, 1 a.u. 27.2 eV), giving $T_0 = 340$ attoseconds. By contrast, Fig. 3.1b shows a symmetric probability distribution (with respect to the inversion in z-variable) since we consider here a superposition of wave functions having same inversion symmetry whereas in Fig. 3.1a we observe a clear electron transfer between nuclei, now in Fig. 3.1b the probability densities oscillates symmetrically at each nucleus with the same period T_0. There is no electron transfer but the temporal evolution is that of a pulsating binodal ("breather") mode. One of the characteristics of intense mid-infrared ultrashort pulses is that they can produce CEP dependent asymmetric photoelectron angular distributions along the laser polarization. We have shown that one can use such asymmetry to measure the CEP and the duration of intense ultrashort pulses [31, 32]. Asymmetric ionization yields also occur in the

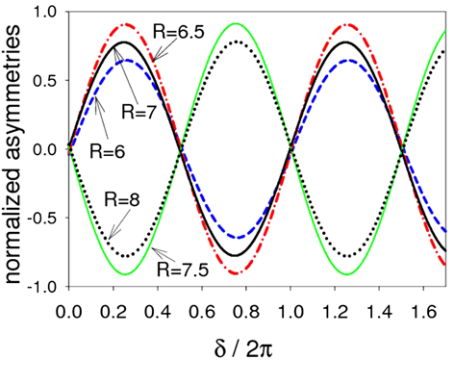

Fig. 3.2 Normalized asymmetries at the electron momentum $p = 2.5$ a.u. as function of δ at $R = 6$, 6.5, 7.0, 7.5 and 8.0 a.u. for the attosecond pulse probing the same coherent superposition for a coherent superposition $\sigma_g 1s + \sigma_u 2s$ displayed in Fig. 3.1a

framework of the pump-probe schemes considered in this section and can be controlled via the time delay t_0 and the chirp parameter ξ for pulses defined by Eq. (3). As an example we study the attosecond photoionization from the nonsymmetric coherent state $1\sigma_g + 2\sigma_u$ for which the electron density evolution is illustrated in Fig. 3.1a. We use a central attosecond photon energy = 100 eV, attosecond pulse duration $\tau_{\text{FWHM}} = 150$ asec (the time for a 1s classical orbit) and equal populations $\alpha_1 = \alpha_2 = 1/\sqrt{2}$. The angle between measured electron momentum **p** and laser polarization **e** is set at $\theta = 60°$. From the coherent photoionization amplitude (6), we can derive the angle and momentum resolved photoelectron spectra [26, 39],

$$\frac{d^3 P_{\text{coh}}(p,\theta,\varphi)}{dp\, d\Omega_e} \equiv S(p,\theta,\varphi) = p^2 |M_{\text{coh}}|^2 \tag{11}$$

where P_{coh} is the momentum resolved ionization probability, $d\Omega_e = \sin\theta\, d\theta\, d\varphi$ is the solid angle and φ is an azimuthal angle in spherical coordinates with z-axis parallel to the laser polarization. We define the asymmetry as

$$\Delta(p,\theta,\varphi) = \frac{S(p,\theta,\varphi) - S(p,\pi-\theta,\varphi)}{S(p,\theta,\varphi) + S(p,\pi-\theta,\varphi)}. \tag{12}$$

This quantity represents the ratio between the difference in forward and backward directions to total ionization yield for a fixed momentum $p = |\mathbf{p}|$ and angular orientation $\theta, \varphi = 0$. Figure 3.2 summarizes the calculated asymmetry Δ at momentum $p = 2.5$ a.u. ($E = 85$ eV) as a function of the phase $\delta(t_0)$ and for different internuclear distances $R = 6$–8 a.u. From Fig. 3.2, we observe zero asymmetry ($\Delta = 0$) at phases $\delta/2\pi = 0$, 1/2, 1, etc. This corresponds precisely to "turning points" of the coherent electron wave packet formed from the $1\sigma_g + 2\sigma_u$ states. At $R = 6$ in Fig. 3.2, maximum asymmetry occurs at $\delta/2\pi = 1/4$ which corresponds to the electron motion from left proton ($z = -3$) to the right proton ($z = +3$). This also correlates with the positive momentum in the electron coherent state after a suitable Fourier transform of $\psi(\mathbf{r}, t)$ to $\psi_F(\mathbf{p}, t)$ [28]. We also note that there exist a specific "magic" bond length (between $R = 7$ and $R = 7.5$ a.u.) at which no asymmetry exists for all delay δ. Such effect is indeed expected from Eq. (15a) in [26] which predicts that the asymmetry is approximately (using the plane wave approximation in the continuum) proportional to the function $\sin(\mathbf{p} \cdot \mathbf{R})$ which has zero at

$R = 7.5$ a.u. for the electron momentum chosen in Fig. 3.2. Attosecond photoelectron spectroscopy allows therefore for measuring turning points and directions of electron wave packets in a coherent superposition of the two bound electron states, see [26] for a more complete discussion of Fig. 3.2. Including nuclear motion, i.e., a complete non-Born Oppenheimer simulation, highlights "decoherence" effects [44] due to decoupling of electronic states at large internuclear distances [45]. The signature of such nuclear induced decoherence is the vanishing of asymmetry in the photoionization resulting from reduction of the coherent state to a single electronic state. This vanishing of asymmetry is a consequence of the loss of the overlap between the two corresponding nuclear wave packets.

3.3 Molecular High-Order Harmonic Generation (MHOHG) from Coherent Electron Wave Packets (CEWP)

As shown in the previous section, the simplest experimental and theoretical (numerical) scheme making it possible to visualize electron motion inside an atom [46, 47] and inside a molecule [25] relies on the preparation of the coherent superposition of two bound electronic states followed by an attosecond pulse leading to ultrafast photoionization. Measuring the photoelectron signal or momentum distributions as a function of time delay between the two pulses allows us to monitor the oscillatory motion of the electron on its natural attosecond time scale. Molecules add a further complexity due to nuclear motion on the femtosecond (fs) time scale. We have investigated earlier such schemes for monitoring electron motion in H_2^+ on attosecond time scales, first at fixed internuclear distance [25–28] and more recently with nuclear motion included [45]. In the present section, we examine the use of MHOHG for monitoring attosecond electron motion in CEWP's. HHG from CEWP's has been investigated earlier in atoms [48–50] and MHOHG in molecules at fixed internuclear distance [25, 31, 32, 51]. In this approach, much longer (few femtosecond) intense probe pulses are used and HHG spectra are measured [29–32, 51], instead of asymmetries in the photoionization signal as discussed in detail in the previous section. Nevertheless, this scheme (based on HHG) allows to monitor attosecond motion of an electron in CEWP due the fact that high-order harmonic emission time is 2–3 hundred attoseconds, as expected for a three-step recollision model of harmonic generation [21, 22].

To investigate the effect of nuclear motion, one has to solve a full molecular non-Born Oppenheimer time dependent Schrödinger equation, TDSE, for each fixed time delay t_{del} between the pump and probe. We present this method for the 1-D H_2^+ molecular ion [29, 30] for which Fig. 3.3a illustrates a three-state excitation by a pump-probe pulse sequence, Fig. 3.3b. The non-Born Oppenheimer TDSE for the 1-D system is written as in atomic units (a.u., $e = \hbar = m_e = 1$, see Table 3.1):

$$i\frac{\partial \psi(z, R, t)}{\partial t} = H(z, R, t)\psi(z, R, t), \tag{13}$$

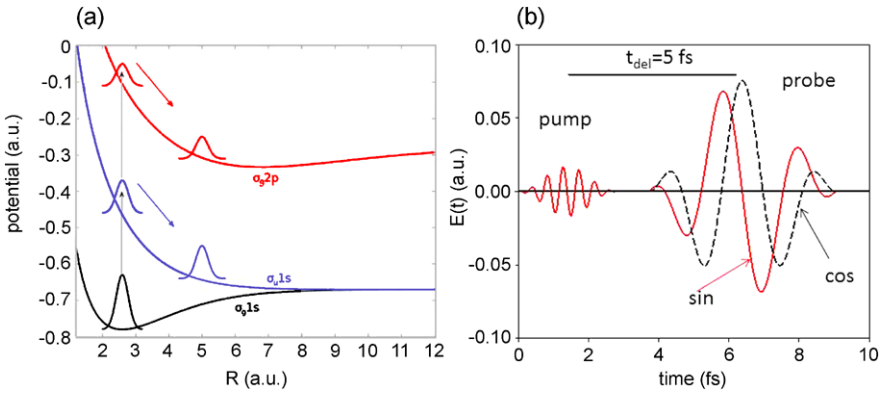

Fig. 3.3 (**a**) Illustration of the nuclear wave packet dynamics in the T_2^+ molecular ion following excitation by the pump pulse shown in Fig. 3.3(b). (**b**) Electric fields of the pump and probe pulse used in scheme (I) for a delay time $t_{\text{del}} = 5$ fs. *Solid line* in (**b**) shows the sine-like pulse ($\varphi_{\text{CEP}} = \pi/2$) used in Figs. 3.4 and 3.5, whereas dashed line shows the cos-like pulse ($\varphi_{\text{CEP}} = 0$) used in H-atom calculations presented in [30]

where z is the electron coordinate (with respect to the nuclear center of mass), R is again the internuclear distance. In (13) $H(z, R, t)$ is the *exact*, 1-D, three body Hamiltonian, obtained after separation of the center-of-mass motion, for H_2^+ and also T_2^+, the latter used for slow nuclear motion [24, 45]. The electric field used in the Hamiltonian $H(z, R, t)$ is the sum of two pulses (Fig. 3.3b), $E(t) = E_{\text{pump}}(t) + E_{\text{probe}}(t)$. The time dependent electron–nuclear wave function $\psi(z, R, t)$ for the pump-probe scheme illustrated in Fig. 3.3 is obtained numerically with the help of the second order accurate split-operator method for solving TDSE (13) [52]. It is assumed that at $t = 0$ the molecule is in its ground vibrational state ($v = 0$) on the $\sigma_g 1s$ bound potential and the frequency of the pump-pulse is chosen to be resonant with the $\sigma_g 1s \rightarrow \sigma_u 1s$ transition at the molecular equilibrium internuclear distance. Because the spacing between the two upper states ($\sigma_g 2p$ and $\sigma_u 1s$) and that of the two lower states ($\sigma_u 1s$ and $\sigma_g 1s$) are almost the same for the equilibrium internuclear distance, the second-lowest excited state can also be excited via two-photon resonance, as can the lowest excited state by a single-photon resonance (Fig. 3.3a). As a result, using a 1 fs duration UV pump laser, we are able to prepare a CEWP which is a coherent superposition of the three electronic states: the ground bound ($\sigma_g 1s$) and two excited dissociative ($\sigma_u 1s$ and $\sigma_g 2p$) electronic–nuclear states. A 800 nm few-cycle intense probe pulse induces a MHOHG spectrum from the 3-state CEWP. Each pulse shown in Fig. 3.3b is defined via its vector potential $A(t)$ and corresponding electric field $E(t) = -\frac{\partial A(t)}{\partial t}$. Sine-squared envelopes are used for the potential $A(t)$ so that the electric fields (illustrated in Fig. 3.3b) satisfy automatically the zero-area condition [23, 34], as explained in the previous section.

To obtain MHOHG spectrum, the electron acceleration $a(t)$ is calculated using the time dependent electron–nuclear wave function $\psi(z, R, t)$ obtained numerically

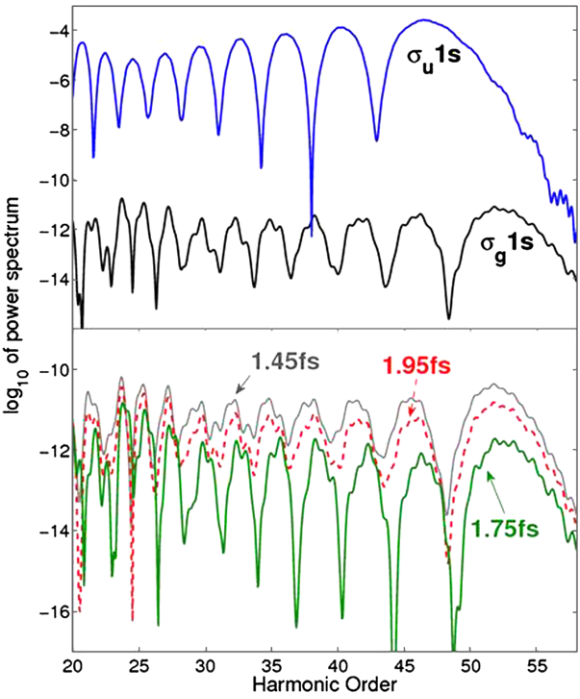

Fig. 3.4 MHOHG spectra for $I_{\text{probe}} = 4 \times 10^{14}$ W/cm^2 generated in two different ways: (**a**) Here $I_{\text{pump}} = 0$. *Lower* (*black-line*) shows the harmonic spectra for the initialization from the (pure) $\sigma_g 1s$ state and *upper*, *blue-line*, shows spectra for the initialization from the (pure) $\sigma_u 1s$. (**b**) Spectra from the coherent superposition, same spectra as in Fig. 2c in [30] (scheme III, see [30] for details) but plotted for three selected time-delays $t_{\text{del}} = 1.35$, 1.75 and 1.95 fs

from TDSE, Eq. (13): $a(t) = -E(t) - \langle\psi|\frac{\partial V_C}{\partial z}|\psi\rangle$, where $V_C(z, R)$ is the potential describing the Coulomb attraction from the two nuclei [45]. Its Fourier transform $a_F(\omega, t_{\text{del}})$ is calculated for a series of time delays t_{del}. The power spectrum of the generated harmonics equal to $|a_F(\omega, t_{\text{del}})|^2$ is illustrated in Fig. 3.4 for (a): pure initial $\sigma_g 1s$ (ground) state, and (b): for the 2-state CEWP (see details in [30]) at probe intensity $I = 4 \times 10^{14}$ W/cm^{2}and $\lambda = 800$ nm at three selected time delays $t_{\text{del}} = 1.35$, 1.75, 1.95 fs. Sharp suppressions of harmonic intensities occur at certain time delays. Interestingly, so strong suppressions are possible for very small populations (3×10^{-3}) in the excited state $\sigma_u 1s$, see Table 3.2 which gives details relative to the laser parameters and corresponding populations. Note that the signature of nuclear motion shows up very clearly in the case of scheme III displayed in Fig. 3.5c. In this scheme, the populations in the third state $\sigma_g 2p$ are very small, see Table 3.2 thus eliminating the contribution of the third state seen in Fig. 3.2a.

Table 3.2 Laser parameters and populations for schemes (I)–(III). Frequencies are in a.u. and laser intensities in W/cm^2

Scheme	ω_{pump} (a.u.)	I_{pump} (W/cm^2)	I_{probe} (W/cm^2)	$\sigma_u 1s$	$\sigma_g 2p$
(I)	0.33	10^{13}	2×10^{14}	0.16	0.03
(II)	0.33	10^{12}	4×10^{14}	0.02	4×10^{-4}
(III)	0.28	10^{11}	4×10^{14}	3×10^{-3}	3×10^{-6}

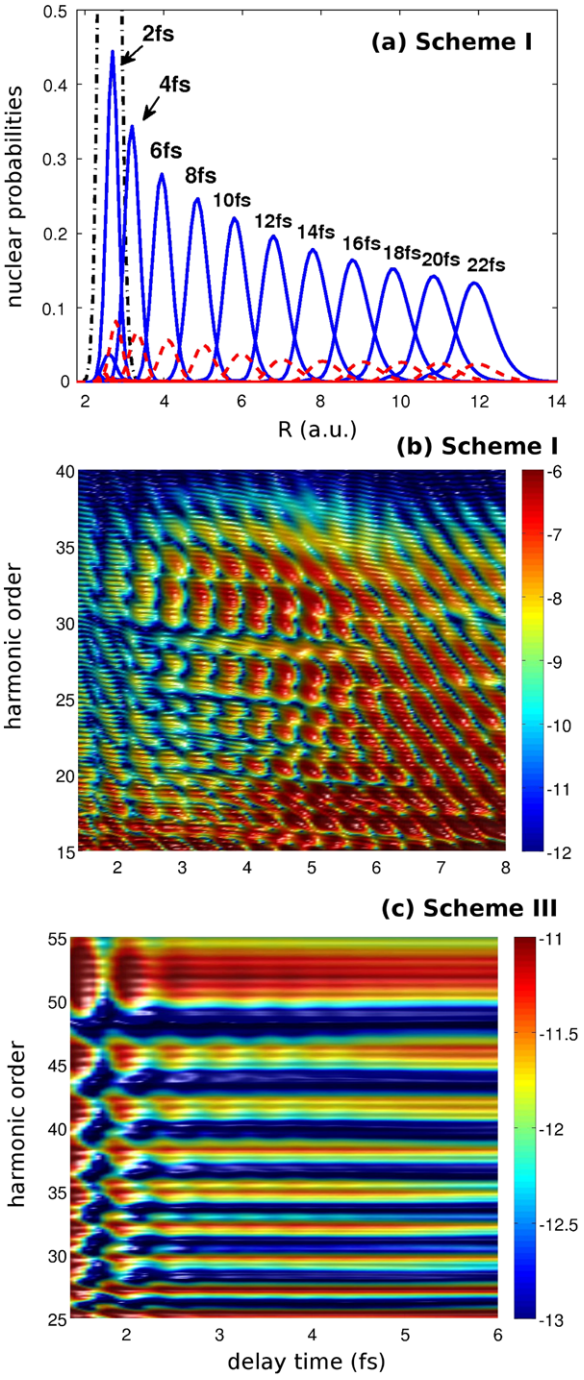

Fig. 3.5 (**a**) Populations describing nuclear wave packets at times: 2, 4–24 fs, on surfaces $\sigma_g 1s$, $\sigma_u 1s$ and on $\sigma_g 2p$ are shown in *black*, *blue* and *red*, respectively. (**b**) (**c**): Dependence of harmonic spectra on pump-probe delay time for schemes (I) and (III) (see text and Table 3.2)

Clearly, the interference in MHOHG in Fig. 3.5c disappears at time delays larger than 3 fs. This coincides with times at which the overlap between the corresponding nuclear wave packets vanishes, as seen in Fig. 3.5a. In contrast, we observe in Fig. 3.5b (scheme I) two distinct regimes: for time delays smaller than 3 fs the contribution from two lower states is seen whereas for longer time delay we observe the oscillations in MHOHG spectra originating from the superposition of the two upper states which is possible due to synchronous nuclear motion on these surfaces seen in Fig. 3.5a. In order to interpret these strong suppressions (that depend strongly on the time delay t_{del}) in the MHOHG spectrum in Fig. 3.4b and in Fig. 3.5, we develop in the next section a theory for MHOHG from CEWP based on SFA.

3.4 Quantum Theory of HHG and MHOHG from a Coherent Superposition of Two Electronic States

A quantum theory of the HHG process has been formulated in [53, 54] in the framework of the strong field approximation, SFA, permitting to derive a simple semiclassical three-step model proposed in [21] and generalized to include nonzero velocity in [55]. In a similar way as in [50], we adapt here this approach to the case when at the initial time $t = 0$ the system (atom or a molecule) is in a coherent superposition of two bound states $|\varphi_1\rangle$ and $|\varphi_2\rangle$. In this section, the molecular effects are included in the framework of the Born–Oppenheimer approximation applied to the movement on two molecular surfaces whereas in the previous section the nuclear effects were include via TDSE (beyond Born–Oppenheimer approximation). Thus, as in Eq. (3) of [53], we seek the solution of the TDSE in the $\vec{E}\cdot\vec{r}$ (length) gauge

$$i\frac{\partial|\psi(t)\rangle}{\partial t} = \left[\frac{1}{2}\hat{\vec{v}}^2 + V_C + E(t)\hat{x}\right]\big|\psi(t)\big\rangle \tag{14}$$

in the form

$$\big|\psi(t)\big\rangle = a_1 e^{-iE_1 t}|\varphi_1\rangle + a_2 e^{-iE_2 t}|\varphi_2\rangle + \int d^3v\, a^C(\vec{v},t)|\vec{v}\rangle \tag{15}$$

where $\hat{\vec{v}}$ is the momentum operator and $a^C(\vec{v},t)$ the transition amplitude from the initial bound state to the continuum state having the momentum $\vec{v}$. In other words, $a^C(\vec{v},t)$ is the continuum component of the electron wave function in the momentum representation. Inserting (15) into (14) yields, within SFA which consists in neglecting intermediate bound states and of the Coulomb potential for the electron in the continuum the following TDSE for the amplitude a^C in the momentum representation:

$$i\frac{\partial a^C(\vec{v},t)}{\partial t} = \frac{\vec{v}^2}{2}a^C + E(t)i\frac{\partial a^C}{\partial v_x} + E(t)\sum_{k=1}^{2}\langle\vec{v}|x|\varphi_k\rangle e^{-iE_k t}. \tag{16}$$

Here $i\frac{\partial}{\partial v_x}$ is the position operator $\hat{x}$ in the momentum representation. The exact solution of the above equation has the following form:

$$a^C(\vec{v},t) = -i\int_0^t dt'\, E(t')\exp\left[-i\int_{t'}^t dt''\left[\vec{p}(t)+\vec{A}(t'')\right]^2/2\right] \times\left[\sum_{k=1}^{2} a_k\langle\vec{p}(t)+\vec{A}(t')|x|\varphi_k\rangle e^{-iE_kt'}\right] \tag{17}$$

where $\vec{p}(t) = \vec{v} - \vec{A}(t)$. We rewrite (17) in the general form:

$$a^C(\vec{v},t) = \sum_{k=1}^{2} a_k e^{-iE_kt} b_k(\vec{v},t),$$

$$b_k(\vec{v},t) = -i\int_0^t dt'\, E(t')\langle\vec{p}+\vec{A}(t')|x|\varphi_k\rangle e^{-iS_k(\vec{p},t,t')}, \tag{18}$$

where

$$S_k = \int_{t'}^t dt''\left(\left[\vec{p}(t)+\vec{A}(t'')\right]^2/2 - E_k\right). \tag{19}$$

In the case of a single level k, b_k and S_k become the continuum wave function $b(\vec{v},t)$ and the quasi-classical action $S(\vec{p},t',t)$ used in [53, 54]. We rewrite now Eq. (15) in the following form:

$$|\psi(t)\rangle = a_1e^{-iE_1t}|\varphi_1\rangle + a_2e^{-iE_2t}|\varphi_2\rangle + |\psi_1^C(t)\rangle + |\psi_2^C(t)\rangle, \tag{20}$$

where

$$|\psi_k^C(t)\rangle = a_ke^{-iE_kt}\int d^3v\, b_k(\vec{v},t)|\vec{v}\rangle, \quad k=1,2. \tag{21}$$

Equation (20 shows that due to the presence of the two-state coherent superposition in the initial (prepared) state the probe laser prepares a superposition of two continuum wave packets $|\psi_1^C(t)\rangle$ and $|\psi_2^C(t)\rangle$. We farther note that this superposition at a given time is strongly dependent on the relative bound state phase $(E_2 - E_1)t$ which is directly controlled by the pump-probe delay time.

The induced dipole $d(t)$ along the x-coordinate becomes:

$$d(t) = q_e\langle\psi(t)|\hat{x}|\psi(t)\rangle = -\langle\psi_1^C + \psi_2^C|x\left|\sum_{j=1}^{2} a_je^{-iE_jt}\varphi_j\right\rangle + c.c. + d_{\text{bound}}(t), \tag{22}$$

where q_e is the electron charge which in atomic unit is equal to -1, and

$$d_{\text{bound}}(t) = \sum_{j=1}^{2}\sum_{k=1}^{2} a_k^* a_j\langle\varphi_k|x|\varphi_j\rangle e^{i(E_k-E_jt)}. \tag{23}$$

Thus, after using Eqs. (18)–(21), we obtain the total induced dipole moment

$$d(t) = -\sum_{k=1}^{2}\sum_{j=1}^{2} a_je^{-iE_jt}\langle\psi_k^C|x|\varphi_j\rangle + c.c. + d_{\text{bound}}(t)$$

$$= -\sum_{k=1}^{2}\sum_{j=1}^{2} a_k^* a_j e^{i(E_k - E_j)t} \int d^3p\, b_k^*(\vec{p}, t)\langle \vec{p} + \vec{A}(t)|x|\varphi_j\rangle + c.c. + d_{\text{bound}}(t). \tag{24}$$

Next, we calculate the Fourier transform $D(\omega)$ of the dipole $d(t)$ in which we discard the term d_{bound} since it leads to a sharp single peak in the spectrum at the relatively low resonance frequency which in the case investigated in the previous section is $\omega_{\text{pump}} = \omega_{1,2} \simeq 5.8\omega_{\text{laser}}$, where $\omega_{1,2} = E_2 - E_1$ is the energy separation between the two electronic state i.e., well below the plateau of HHG we are interested in. Note that $d_{\text{bound}} = 0$ in the case of superposition of the states having the same parity like, e.g., hydrogenic superposition 1s + 2s. The Fourier transform of (24) gives finally

$$\begin{aligned} D(\omega) &= \int dt\, e^{-i\omega t} d(t) \\ &= -\sum_{k=1}^{2}\sum_{j=1}^{2} a_k^* a_j \int dt\, e^{i(E_k - E_j - \omega)t} \int d^3p\, b_k^*(\vec{p}, t)\langle \vec{p} + \vec{A}(t)|x|\varphi_j\rangle. \end{aligned} \tag{25}$$

Note that the "cc" term is discarded in the above equation since it does not contribute in the Fourier transform as it contains the terms b_k which oscillate like factors e^{iEt} where $E > 0$ (electron continua). We investigate now how the harmonic spectra change when we change the time delay t_{del} between the two pulses. In this section, we have chosen the time variable $t = 0$ as the time when the pump pulse is turned off (after preparation of a coherent superposition of the two states) and the system evolves freely until the probe pulse is turned on. We assume that the probe envelope maximum is at $t = t_{\text{del}}$ and that for each delay the probe carrier envelope phase is zero. Thus, the probe electric field $E(t)$ and its vector potential $A(t)$ are functions of $t - t_{\text{del}}$, i.e., $A = a(t - t_{\text{del}}) \sin[\omega_{\text{laser}}(t - t_{\text{del}})]$ where $a(t - t_{\text{del}})$ is the probe envelope. First, we make a change of the integration variable t' in Eq. (18) into $\tau' = t' - t_{\text{del}}$, as well as: $\tau'' = t'' - t_{\text{del}}$ in Eq. (19), to obtain the continuum amplitude:

$$b_k = -i \int_{-t_{\text{del}}}^{t - t_{\text{del}}} d\tau'\, E(\tau')\langle \vec{p} + \vec{A}(\tau')|x|\varphi_k\rangle \exp\left[-i S_k(\vec{p}, t - t_{\text{del}}, \tau')\right], \tag{26}$$

where

$$S_k(\vec{p}, t - t_{\text{del}}, \tau') = \int_{\tau'}^{t - t_{\text{del}}} dt''\left(\left[\vec{p} + \vec{A}(t'')\right]^2/2 - E_k\right). \tag{27}$$

Thus the continuum amplitudes b_k and the actions S_k are now functions of $t - t_{\text{del}}$ only, i.e., they do not depend explicitly on the time t. We note however, that the total continuum amplitude $a^C(\vec{v}, t)$, see Eq. (18), and the resulting harmonic amplitude given in (25) depend explicitly on the time t via $\exp(-iE_k t)$ factors. Thus, after the change of integration variable t in (25) into $\tau = t - t_{\text{del}}$ we obtain for the HHG amplitude

$$\begin{aligned} D(\omega) = e^{-i\omega t_{\text{del}}}\big(&D_{1,1}(\omega) + D_{2,2}(\omega) + D_{1,2}(\omega)\exp[-i\omega_{1,2}t_{\text{del}}] \\ &+ D_{2,1}(\omega)\exp[i\omega_{1,2}t_{\text{del}}]\big), \end{aligned} \tag{28}$$

where

$$D_{k,j}(\omega) = -a_j a_k^* \int_{-\infty}^{\infty} d\tau \, \exp\left[i(E_k - E_j - \omega)\tau\right] \times \int d^3p \, b_k^*(\vec{p}, \tau)\langle \vec{p} + \vec{A}(\tau)|x|\varphi_j\rangle. \tag{29}$$

The coefficients $D_{k,j}$ depend only on the shape of the probe electric field $E(t - t_{\text{del}})$ and are identical for any value of pump-probe delay time t_{del} in the atomic case. The HHG spectrum takes on the following form for a two-state coherent superposition:

$$\left|D(\omega)\right|^2 = R(\omega) + 2\left|a(\omega)\right| \cos\left[\omega_{1,2} t_{\text{del}} + \varphi_a(\omega)\right] + 2\left|b(\omega)\right| \cos\left[2\omega_{1,2} t_{\text{del}} + \varphi_b(\omega)\right], \tag{30}$$

where

$$\begin{aligned} R &= |D_{1,1} + D_{2,2}|^2 + |D_{1,2}|^2 + |D_{2,1}|^2, \\ a &= (D_{1,1} + D_{2,2}) D_{1,2}^* + (D_{1,1}^* + D_{2,2}^*) D_{2,1}, \\ b &= D_{2,1} D_{1,2}^*, \qquad \varphi_a = \text{Arg}(a), \qquad \varphi_b = \text{Arg}(b). \end{aligned} \tag{31}$$

We conclude from (30) that the HHG spectra are periodic functions of the time-delay t_{del} [50]. The period of oscillations is $\tau_{1,2} = 2\pi/\omega_{1,2}$. $D_{1,1}(\omega)$ and $D_{2,2}(\omega)$ describe direct HHG processes from the states $|\varphi_1\rangle$ and $|\varphi_2\rangle$, respectively. Both do not depend on the delay time t_{del} in the atomic case. In the molecular case, they do depend on time via movement of the nuclear wave packet and via R-dependent ionization potentials $I_p^{(1)}$ and $I_p^{(2)}$ on each electronic surface. We note that the spectra will also contain a higher frequency component, $2\omega_{1,2}$, oscillating with the period $\tau_{1,2}/2$. However, this component has in general a much weaker amplitude due to the small value of $b(\omega)$, Eq. (31).

In the molecular case, we replace the electronic wave function φ_j by $\varphi_j^{\text{el}} \chi_j(R,t)$, where $\chi_j(R,t)$ are nuclear wave functions. Thus, the non-diagonal terms $D_{j,k}$ where $j \neq k$, will be proportional to the overlap factors $\langle \chi_j(R,t)|\chi_k(R,t)\rangle$. Thus, when the nuclear wave packets loose their overlap, as first shown in [45], i.e., when $\langle \chi_1(R,t)|\chi_2(R,t)\rangle$ vanishes, only diagonal terms $D_{j,j}$ will remain in Eq. (28) and the direct $\tau_{1,2}$ periodicity in HHG seen in (30) vanishes as reported in [56, 57]. However, since in the molecular case the ionization potentials I_P on each molecular potential are different and they depend on the internuclear distance R the diagonal terms $D_{1,1}$ and $D_{2,2}$ will depend on the time-delay t_{del} (via $I_p^{(1)}(R)$, $I_p^{(1)}(R)$) due to the displacement of nuclear wave packets as reported in [56, 57]. Thus, the harmonic intensity will show the time delay dependent interference originating from superposition of these diagonal terms, i.e., this interference will occur via the term $|D_{1,1}(\omega) + D_{2,2}(\omega)|^2$. Similar coherent effects have shown up earlier in mixed atomic gases [58, 59]. In our work, we focus on interference resulting from the $D_{1,2}$ and $D_{2,1}$ which varies at shorter time scales than the interference occurring between the diagonal terms [56, 57].

Summarizing, the laser pulse interacting with a coherent superposition of two electronic states creates two electronic wave packets in the continuum $|\psi_1^C(t)\rangle +$

$|\psi_2^C(t)\rangle$. The relative time-dependent phase between these packets is modulated via the factor $e^{i\omega_{1,2}t_{\rm del}}$. We show next how the three-step model [21, 55] elucidates this interference. Within this model the emission of a specific harmonic occurs at well defined return (recollision) time t_c which can be controlled by the pump-probe delay time.

The three-step (quasiclassical) model was formulated in [21, 55] on an intuitive basis of a continuum (classical, in its second step) electron controlled by laser fields. It was next derived in [53, 54] using SFA methods (adapted here, in the previous paragraphs to the case of coherent superposition of states) and the saddle point method. This method is based on the Taylor expansion of the semi-classical action $S(\vec{p}, t', t)$ at the extrema of the function S. These extrema conditions lead to conditions on the classical trajectories initialized at $t = t_0$ near the core with zero initial velocity and returning to the core at the recollision time t_c determined from classical equations of motion. For a fixed harmonic ω (i.e., for fixed return energy), there are two sets of solutions usually called the short an long trajectories. Before applying the saddle point conditions to the Fourier transform $D(\omega)$ given in (28) we rewrite it in the following form:

$$D(\omega) = -i \sum_{k=1}^{2} \sum_{j=1}^{2} a_k^* a_j \int dt\, e^{i(E_k - E_j - \omega)t} \int d^3p \langle \vec{p} + \vec{A}(t)|x|\varphi_j\rangle \times \int_0^t dt'\, E(t') \langle \varphi_k|x|\vec{p} + \vec{A}(t')\rangle e^{iS_k(\vec{p},t,t')}. \tag{32}$$

We rewrite Eqs. (28) and (32) in the following form:

$$D(\omega) = A_{1\to1}(\omega) + A_{2\to1}(\omega, t_{\rm del}) + A_{2\to2}(\omega) + A_{1\to2}(\omega, t_{\rm del}), \tag{33}$$

where

$$A_{j\to k} = \exp[-i\omega t_{\rm del}] D_{j,k} \exp\left[-i(E_j - E_k)t_{\rm del}\right], \quad j,k = 1,2.$$

For each of these amplitudes, after applying the saddle-point method [53, 54] we end up with the contributions from two (long an short) classical trajectories. Thus, Eq. (33) will contain the sum of eight amplitudes. Here $A_{1\to1}$, $A_{2\to2}$ are the amplitudes for direct HHG from each state, i.e. they describe the process of electron tunneling from the state $|\varphi_1\rangle$ (or $|\varphi_2\rangle$) at time t_0 (or t_0') and recombination at the same state at time t_c (or t_c'). For a fixed harmonic frequency ω, these two amplitudes do not depend explicitly on the tunneling times t_0, t_0' but only on the electron sojourn times $\tau = t_c - t_0$, $\tau' = t_c' - t_0'$. The times with prime correspond to the tunneling and recombination times for the paths in which the recombination occurs into the state E_2. This path occurs via a higher energy state in the continuum $|\varphi_2\rangle$. By contrast, two other amplitudes, $A_{2\to1}$ and $A_{1\to2}$, depend explicitly on the delay time $t_{\rm del}$ via tunneling times t_0 and t_0' because they describe the path in which the electron tunnels from the state $|\varphi_2\rangle$ and recombines into the state $|\varphi_1\rangle$, or vice versa.

For simplicity, we focus next on the interference originating from the terms corresponding to the short trajectories related to the direct process $A_{1\to1}(\omega)$ interfering with the amplitude $A_{2\to1}(\omega)$, as illustrated in Fig. 3.6. For very small populations,

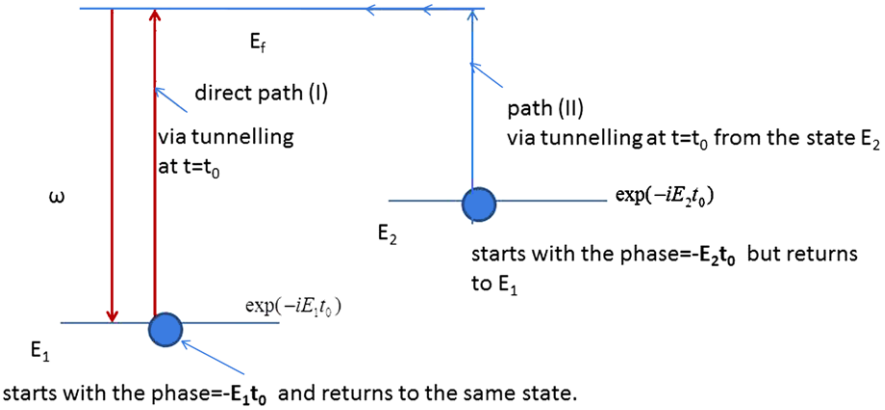

Fig. 3.6 Illustration of a possible interference between two paths (in the framework of the three-step model), related to the two specific classical trajectories: one initialized from the lower electronic state (1) and another initialized from the upper state (2). Both lead to the emission of a fixed, same order harmonic by recombination at the lower state. Same tunneling time t_0 leads for both paths to the same energy E_f in the continuum. We expect that these two paths are dominant when populations in the upper state are very small ($|a_2|^2 < 10^{-3}$)

$|a_2|^2$ in the upper state these two amplitudes will dominate. Following the saddle point method [53, 54], one thus gets from Eq. (32) the following expression:

$$A_{1\to 1}(t_0, t_{\rm del}) = |a_1|^2 A_1^{\rm tunn}(t_0 - t_{\rm del}) \exp[i S_1] A_1^{\rm rec}(\omega), \tag{34}$$

$$A_{2\to 1}(t_0, t_{\rm del}) = a_1 a_2^* A_2^{\rm tunn}(t_0 - t_{\rm del}) \exp[i S_1] \exp[i\omega_{1,2} t_0] A_1^{\rm rec}(\omega), \tag{35}$$

where $A_1^{\rm tunn}$, $A_2^{\rm tunn}$ are the amplitudes related to the tunneling occurring from the states $|\varphi_1\rangle$ and $|\varphi_2\rangle$, respectively, and $A_1^{\rm rec}$ is the amplitude for recombination into the state $|\varphi_1\rangle$ [23, 60]. Note that the tunneling amplitude is directly determined via imaginary part of the complex tunneling time resulting directly from the saddle point conditions which have only imaginary solutions. The corresponding t_0, t_c and S_1 are the real part of complex numbers found in [60]. Note that the tunneling and recombination amplitudes, as well as the semiclassical action S_1 (for a fixed harmonic frequency) do not depend on the delay time $t_{\rm del}$. They depend only on t_0 and recombination time t_c, each relative to the electric field extremum. Hence, both will share the same factor $\exp[i S_1]$ and the same recombination amplitude $A_1^{\rm rec}(\omega)$ since the electron of the same continuum energy recombines to the same state. Thus, the resulting amplitudes as function of the delay time will interfere strongly via the factor $\exp[i\omega_{1,2} t_0]$ present only in the amplitude $A_{2\to 1}$. Consequently the resulting harmonic spectra as function of $t_{\rm del}$ will oscillate with the angular frequency $\omega_{1,2} = E_2 - E_1$ (in a.u.) since the maximum of the field is shifted through the variable t_0 which is shifted when the delay time $t_{\rm del}$ is changed. Since both amplitudes described by Eqs. (34) and (35) share the same factor $\exp[i S_1] A_1^{\rm rec}(\omega)$ one expects that harmonic suppression and enhancement will occur for a wide range of harmonics order, as seen in Figs. 3.4b, 3.5 and also in [30] where we presented

HHG in the H atom. The same oscillations can be deduced from Eq. (B6) in [50] where the harmonic amplitude (derived using the SFA model) is modulated via variable $\varphi = -\omega_{1,2} t_{\mathrm{del}}$. As seen in [50], these amplitudes are given by rather complex expressions, however, our Eqs. (34), (35) clearly isolate the terms which control directly the interference, i.e., we isolate the terms which depend explicitly on the time-delay t_{del} (via tunneling time t_0).

Note that usually the tunneling rate from the lower level is several orders (depending on $I_p^{(1)}$ and $I_p^{(2)}$ and on the laser field amplitude) smaller than from the rate from upper state. This allows us to distinguish two distinct regimes of the interference effect in each regime only two terms from Eq. (33) would contribute predominantly. The theory so far [50, 51] focused on the regime of harmonic suppression in which initial populations in both states are equal. Consequently, the amplitudes $A_{1\to 1}$ and $A_{1\to 2}$, in which tunneling occurs from the lower state are smaller than two other amplitudes in which tunneling occurs from the upper state and thus in this regime the interference is controlled by the $A_{2\to 1}(\omega, t_{\mathrm{del}}) + A_{2\to 2}(\omega)$ term whereas we choose in our investigation very small populations $|a_2|^2$. As a result in the present case only two terms $A_{1\to 1}$ and $A_{2\to 1}$, Eqs. (34), (35), contribute and exact cancellations occur when their absolute values are equal.

We will discuss now two distinct cases related to the interference illustrated in Fig. 3.5: the case of long pulses and ultrashort, few cycle pulse, investigated in the previous section. We will show that for long, monochromatic laser pulses the interference illustrated in Fig. 3.5 may occur only when the energy spacing between the two states $|\varphi_1\rangle$ and $|\varphi_2\rangle$ equal to $\omega_{1,2}$ is an odd or even multiple of the laser photon energy ω_L, depending on the parity of states $|\varphi_1\rangle$ and $|\varphi_2\rangle$. In our numerical calculations, the lower state $|\varphi_1\rangle$ had even (gerade) parity whereas the upper state $|\varphi_2\rangle$ had odd (ungerade) parity. We expect similar interferences to occur if both states have same parity, as demonstrated below. In the case of long, many cycles pulses we use a quantum electrodynamic picture of HHG process as the process of absorption of n-photons and emission of a high energy photon using the dipole selection rules. Thus, we conclude that the absorption or emission processes populates the states of the opposite parity. The same conclusions can be reached in the framework of SFA, see Eqs. (14)–(17) in [53]. Thus both, perturbative argument and SFA lead to the same conclusions. First, the direct, diagonal terms $D_{1,1}$, $D_{2,2}$, defined in (29) describing the absorption of photons from the state 1 (or 2) and the recombination of the electron to the same state 1 (or 2), describe the generation of odd harmonic since after absorption of $(2n + 1)$ photons an opposite parity electron continuum state is created allowing the emission of a high energy photon whose frequency is $\omega_H = (2n + 1)\omega_L$. Second, in the case of the superposition of gerade and ungerade states, in general, the following non-harmonic peaks $\omega_H = 2m\omega_L + \omega_{1,2}$ in the non-diagonal term $D_{2,1}$ will appear, where m is an integer number, since one needs to prepare an odd parity (i.e., the same parity state as the upper sate (2)) continuum state in order to re-emit a photon via transition to the ground state (1) which has the even parity, and $D_{2,1}$ is defined in (29). Consequently, if these peaks do not overlap the interference (shown in Fig. 3.5) cannot occur. In other words, in the case of long probe pulses and in the case of the coherent superposition "$g + u$" (e.g., 1s + 2p in

a H-atom [30]) states, interference may only occur when the following condition is satisfied:

$$\omega_H = (2n+1)\omega_L = 2m\omega_L + \omega_{1,2}, \tag{36}$$

where the first equation holds for the diagonal terms and the second equation holds for non-diagonal terms. Similarly, if both states have the same parity, i.e., in the "$g+g$" (e.g., 1s + 2s in an H atom [50]) one obtains the condition:

$$\omega_H = (2n+1)\omega_L = (2m+1)\omega_L + \omega_{1,2}. \tag{37}$$

Thus, we conclude from Eq. (36) that for long probe pulses the interference illustrated in Fig. 3.5 may only occur in the "$g+u$" case when $\omega_{1,2} = E_2 - E_1$ is an odd multiple of the photon energy ω_L. Similarly, we conclude from Eq. (37) that for long probe pulses the interference illustrated in Fig. 3.5 may only occur in the "$g+g$" case when $\omega_{1,2} = E_2 - E_1$ is an even multiple of the photon energy ω_L. We will report our investigations of the "$g+g$" case in next publication.

Obviously, the case of very short probe pulses is very different since the high-order harmonic spectrum is nearly continuous. For few cycle probe pulses used in our numerical simulation (see Fig. 3.3b) the spectral width of the pulse is so large that the condition (36) is easily satisfied for high-order harmonics, i.e., by replacing in (36) $(2n+1)\omega_L$ by $(2n+1)\omega'_L$ and $2m\omega_L$ by $2m\omega''_L$ the condition (36) can be satisfied for any value of $\omega_{1,2}$, where ω'_L, ω''_L are photon energies within the spectral width of the pulse.

3.5 Conclusion

The main goal of the new attosecond science is the direct visualization, control and manipulation of ultrafast electron dynamics in atoms, molecules and solids [61]. High-order harmonic generation (HHG) in atoms and in molecules (MHOHG) driven by intense low frequency laser pulses provide practical methods for producing attosecond pulses. Electron wave packets can be created readily with ultrashort laser pulses as recently studied in laser-induced electron diffraction [62], attosecond quantum stroboscopes [63], creation of hole states in atoms [64, 65], diatomics [66] and large molecules [67], charge transfer processes in atomic collisions [68]. In this review, we have reported two distinct pump-probe methods allowing to monitor the electron–nuclear motion in coherent superposition of atomic or molecular states prepared by an ultrashort femtosecond UV pulse. The pump pulse prepares an oscillating CEWP. Its oscillation period, $\tau_{1,2} = 2\pi/\omega_{1,2}$ can be 100–400 asec (depending on the level separation of the two states inside CEWP). The first method uses an attosecond UV (or XUV) probe pulse whereas the second uses an intense few femtosecond mid-infrared probe pulse which generates high-order harmonics. The first method relies on photoionization asymmetries occurring on the attosecond time scale of the pump-probe delay time whereas in the second we measure changes in harmonic intensities also occurring on the attosecond time scale of the

pump-probe delay time. Surprisingly, using a few femtosecond probe pulse it is still possible to monitor the electron motion on the attosecond scale since the high-order harmonic emission (near cutoff) occurs on the sub-femtosecond time-scale: it takes 0.1 of optical cycle (260 asec) to emit a high energy photon when the recolliding electron achieves maximum kinetic energy near the core as confirmed by the three-step model [1] and the time-profile analysis, see Fig. 3 in [30]. The latter shows that the strong oscillations of HHG as functions of the pump-probe delay time are related to the correlation between the velocity of the recolliding electron wave packet and the electron velocity in the coherent superposition of the electron bound states [30]. This correlation was earlier discussed in [51]. In both methods the signature of nuclear motion appears via vanishing overlap between nuclear wave packets.

An important characteristic of attosecond pulses which is attracting increasing attention is the polarization state. So far only linearly polarized isolated attosecond pulses have been generated. Recent proposals for generating circularly and elliptically polarized harmonics are emerging and have been summarized in [14]. Non vanishing initial angular momentum in atoms [69, 70] and molecules [41, 42] appears to be an essential role in the generation of future circularly polarized attosecond pulses. Such new pulses will open new avenues for probing ultrafast electron dynamics whose natural time scale is the attosecond.

Acknowledgement We thank many colleagues for "illuminating" discussions on the new science of attosecond pulses: W. Becker, P.B. Corkum, F. Krausz, J. Manz, K. Midorikawa and P. Salières on MHOHG.

References

1. P.B. Corkum, F. Krausz, Nat. Phys. **3**, 381 (2007)
2. F. Krausz, M. Ivanov, Rev. Mod. Phys. **81**, 163 (2009)
3. E. Goulielmakis et al., Science **320**, 1614 (2008)
4. M. Abel et al., Laser Photonics Rev. **5**, 352 (2011)
5. H.I. Sekiguchi, T. Sekiguchi, Phys. Rev. Lett. **99**, 228102 (2007)
6. M. Kruger, M. Schenk, P. Hommelhoff, Nature **475**, 78 (2011)
7. A. Fohlisch et al., Nature **436**, 373 (2005)
8. A.D. Bandrauk, M.Y. Ivanov (eds.), *Quantum Dynamic Imaging* (Springer, New York, 2012)
9. A.A. Zholents, W.M. Fawley, Phys. Rev. Lett. **92**, 224801 (2004)
10. A.D. Bandrauk, J. Manz, M. Vrakking, Chem. Phys. **366**, 1 (2009)
11. M. Shapiro, P. Brumer, *Principles of Quantum Control of Molecular Processes* (Wiley-Interscience, New York, 2003)
12. A.D. Bandrauk, M. Delfour. C. LeBris (eds.), *Quantum Control-Mathematical and Numerical Challenges*. CRM Proceedings, vol. 33 (Oxford Univ. Press, Oxford, 2004)
13. Z. Chang, *Fundamentals of Attosecond Optics* (CRS Press, Taylor-Francis, Boca Raton, 2011)
14. K.J. Yuan, A.D. Bandrauk, J. Phys. B **44**, 000 (2012)
15. J.I. Steinfield, *Molecules and Radiation* (MIT Press, Cambridge, 1985)
16. H. Lefebvre-Brion, R.W. Field, *Spectra and Dynamics of Molecules* (Elsevier, Amsterdam, 2004)
17. J. Mourou, T. Tajima, S. Bulanov, Rev. Mod. Phys. **78**, 309 (2006)
18. A.H. Zewail, J. Phys. Chem. A **104**, 5660 (2000)
19. A.H. Zewail, Science **328**, 187 (2012)

20. The Economist, Dec. 2010, p. 56
21. P.B. Corkum, Phys. Rev. Lett. **71**, 1994 (1993)
22. A.D. Bandrauk, S. Chelkowski, K.J. Yuan, Int. Rev. At. Mol. Phys. **2**, 1 (2011)
23. T. Brabec, F. Krausz, Rev. Mod. Phys. **72**, 545 (2000)
24. S. Chelkowski, C. Foisy, A.D. Bandrauk, Phys. Rev. A **57**, 1176 (1998)
25. A.D. Bandrauk, S. Chelkowski, H.S. Nguyen, Int. J. Quant. Chem. **100**, 834 (2004)
26. S. Chelkowski, G.L. Yudin, A.D. Bandrauk, J. Phys. B **39**, S409 (2006)
27. G.L. Yudin, S. Chelkowski, A.D. Bandrauk, J. Phys. B **39**, L17 (2006)
28. G.L. Yudin, S. Chelkowski, J. Itatani, A.D. Bandrauk, P.B. Corkum, Phys. Rev. A **72**, 051401 (2005)
29. T. Bredtmann, S. Chelkowski, A.D. Bandrauk, Phys. Rev. A **84**, 021401(R) (2011)
30. S. Chelkowski, T. Bredtmann, A.D. Bandrauk, Phys. Rev. A **85**, 033404 (2012)
31. A.D. Bandrauk, S. Barmaki, Chem. Phys. **350**, 175 (2008)
32. A.D. Bandrauk, S. Barmaki, Chem. Phys. **338**, 312 (2007)
33. J.A. Yeazell, T. Uzer (eds.), *The Physics and Chemistry of Wave Packets* (Wiley Interscience, New York, 2000)
34. S. Chelkowski, A.D. Bandrauk, Phys. Rev. A **65**, 061802(R) (2002)
35. S. Chelkowski, A.D. Bandrauk, Phys. Rev. A **71**, 053815 (2005)
36. T. Zuo, A.D. Bandrauk, P.B. Corkum, Chem. Phys. Lett. **259**, 313 (1996)
37. H.-C. Shao, A.F. Starace, Phys. Rev. Lett. **105**, 263201 (2010)
38. J. Itatani et al., Nature **432**, 867 (2004)
39. G.L. Yudin, A.D. Bandrauk, P.B. Corkum, Phys. Rev. Lett. **96**, 063002 (2006)
40. G. Sansone et al., Science **314**, 443 (2006)
41. K.J. Yuan, A.D. Bandrauk, Phys. Rev. A **84**, 023410 (2011)
42. K.J. Yuan, A.D. Bandrauk, Phys. Rev. A **83**, 063422 (2011)
43. D.R. Bates, K. Ledsham, A.L. Stewart, Philos. Trans. R. Soc. A **246**, 215 (1953)
44. J. Paz, S. Habib, W.H. Zurek, Phys. Rev. D **47**, 488 (1993)
45. A.D. Bandrauk, S. Chelkowski, P.B. Corkum, J. Manz, G.L. Yudin, J. Phys. B, At. Mol. Opt. Phys. **42**, 134001 (2009)
46. F. Krausz, Physics World, September, p. 41 (2001)
47. A. Scrinzi, M. Geissler, T. Brabec, Laser Phys. **11**, 169 (2001)
48. J.B. Watson, A. Sanpera, X. Chen, K. Burnett, Phys. Rev. A **53**, R1962 (1996)
49. P.M. Paul, T.O. Clatterbuck, C. Lynga, P. Colosimo, L.F. DiMauro, P. Agostini, K.C. Kulander, Phys. Rev. Lett. **94**, 113906 (2005)
50. D.B. Milosevic, J. Opt. Soc. Am. B **23**, 308 (2006)
51. H. Niikura, D.M. Villeneuve, P.B. Corkum, Phys. Rev. Lett. **94**, 083003 (2005)
52. A.D. Bandrauk, H. Shen, J. Chem. Phys. **99**, 1185 (1993)
53. M. Lewenstein, Ph. Balcou, M.Yu. Ivanov, A. L'Huillier, P.B. Corkum, Phys. Rev. A **49**, 2117 (1994)
54. M. Lewenstein, P. Salieres, A. L'Huillier, Phys. Rev. A **52**, 4747 (1995)
55. A.D. Bandrauk, S. Chelkowski, S. Goudreau, J. Mod. Opt. **52**, 411 (2005)
56. H.J. Wörner, J.B. Bertrand, D.V. Kartashov, P.B. Corkum, D.M. Villeneuve, Nature **466**, 604 (2010)
57. H.J. Wörner, J.B. Bertrand, P.B. Corkum, D.M. Villeneuve, Phys. Rev. Lett. **105**, 103002 (2010)
58. E.J. Takahashi, T. Kanai, K.L. Ishikawa, Y. Nabekawa, K. Midorikawa, Phys. Rev. Lett. **99**, 053904 (2007)
59. T. Kanai, E.J. Takahashi, Y. Nabekawa, K. Midorikawa, Phys. Rev. Lett. **98**, 153904 (2007)
60. D.B. Milosevic, W. Becker, Phys. Rev. A **66**, 063417 (2002)
61. D.B. Milosevic, Phys. Rev. A **81**, 023802 (2010)
62. M. Peters et al., Phys. Rev. A **83**, 051403 (2011)
63. J. Mauritsson et al., Phys. Rev. Lett. **100**, 073003 (2008)
64. L. Argenti, E. Lindroth, Phys. Rev. Lett. **105**, 053002 (2010)
65. S. Pabst, L. Greenman, P.J. Ho, D.A. Mazziotti, R. Santra, Phys. Rev. Lett. **106**, 053003 (2011)

66. Y. Mairesse et al., Phys. Rev. Lett. **104**, 213601 (2010)
67. A.I. Kuleff, L.S. Cederbaum, Phys. Rev. Lett. **106**, 053011 (2011)
68. S.X. Hu, Phys. Rev. A **83**, 041401 (2011)
69. X. Xie et al., Phys. Rev. Lett. **101**, 033901 (2008)
70. C. Liu, M. Nisoli, Phys. Rev. A **85**, 013418 (2012)

Chapter 4
Gating Techniques for Shaping of Attosecond Pulses

Francesca Calegari, Candong Liu, Matteo Lucchini, Giuseppe Sansone, and Mauro Nisoli

Abstract The generation of attosecond pulses and their application to the investigation of ultrafast electron processes in atoms, molecules, nanostructures and solids, is now a mature research field. In analogy to what already achieved in the femtosecond regime, for a number of applications it is important to shape the spectral and temporal characteristics of the attosecond pulses. In this chapter we will review several shaping techniques, based on the use of gating schemes. Isolated pulses or pairs of attosecond pulses can be easily produced by using the polarization gating and the ionization gating methods, which can be also implemented for the generation of spectrally tunable pulses. A method to generate isolated attosecond pulses with elliptical polarization is also discussed, based on high-order harmonic generation in atoms with non-vanishing angular quantum number.

4.1 Introduction

After the first experimental demonstration of the generation of attosecond pulses [1, 2], in the last few years various techniques have been introduced for the generation, complete temporal characterization and application of attosecond pulses [3, 4]. So far, sub-femtosecond pulses have been mainly produced by using the process of high-order harmonic generation (HHG) in gas. As a result of the physical processes giving rise to harmonic generation, extreme-ultraviolet (XUV) pulses are emitted with duration down to the attosecond regime every half optical cycle of the fundamental radiation, as first theoretically proposed by Farkas and Toth [5]. Various schemes have been proposed and partly implemented to confine the harmonic generation process to a single event, leading to the production of isolated attosecond pulses. These schemes can be grouped into two broad classes, according to the mechanism used to select a single pulse: (i) *amplitude* gating schemes and (ii) *temporal* gating schemes. The generation of isolated pulses by spectral selection of the cutoff portion of the harmonic spectrum belongs to the first class [2, 6]. This

F. Calegari · C. Liu · M. Lucchini · G. Sansone · M. Nisoli (✉)
Department of Physics, Politecnico di Milano, Institute of Photonics and Nanotechnologies, IFN–CNR, Piazza L. da Vinci 32, 20133 Milano, Italy
e-mail: mauro.nisoli@fisi.polimi.it

K. Yamanouchi, K. Midorikawa (eds.), *Progress in Ultrafast Intense Laser Science*, Springer Series in Chemical Physics 104, DOI 10.1007/978-3-642-35052-8_4,

generation scheme requires the use of intense sub-5-fs driving pulses, with stabilized carrier-envelope phase (CEP). The high-energy portion of the XUV spectrum (cutoff region) is generated only around the peak of the driving infrared (IR) pulse, thus corresponding to light emitted only within one-half of the laser oscillation period. Isolated attosecond pulses with a temporal duration down to 80 as have been generated using this method [7].

The *temporal* gating approach is based on the dependence of the harmonic generation process on the temporal characteristics of the driving pulse in order to prevent the generation of XUV radiation out of a sub-cycle-duration temporal window. One possible way is to take advantage of the strong sensitivity of the HHG process on the degree of ellipticity of the fundamental field. If the polarization of the driving field is temporally modulated from circular to linear and back to circular, the XUV emission is limited to the temporal window in which the driving pulse is linearly polarized, as first proposed in 1994 [8]. With this method, called polarization gating (PG), isolated attosecond pulses with time duration of 130 as have been generated and characterized [9, 10]. The PG technique requires the use of few-cycle driving pulses with stable CEP. A second approach is based on the exploitation of the laser-induced ionization of the generating medium for the production of a short temporal window for XUV generation (ionization gating) [11–13]. Isolated attosecond pulses with time duration down to 155 as and an energy on target of 2.1 nJ have been generated using this method [13].

A different approach for the generation of isolated attosecond pulses is based on the use of two, or more, intense pulses with the same or different carrier wavelengths, in order to obtain a temporal gating in the harmonic generation process. In particular, the mixing of two or more laser pulses with different wavelengths but the same polarization direction is known as color gating technique [14, 15]; this scheme has been investigated in several configurations and has been experimentally demonstrated by generating continuous XUV spectra [16–19]. A different approach, named double optical gating and based on the combination between a polarization and a color gating technique, has been investigated [20, 21] and generalized to long driving pulses [22].

The control of the temporal characteristics of the isolated attosecond pulses, in terms of pulse duration, central photon energy and spectral chirp, is an important requirement for the applications of these pulses. Isolated attosecond pulses have been generated in various spectral regions upon using different gases for HHG and suitable spectral filtering elements. Ultrabroadband dispersion compensation have been demonstrated by using metallic filters [10, 23] and propagation in plasma [24]. Another important characteristics is the polarization state. In this work, we will review various techniques we have proposed and partly implemented to achieve a spectral and temporal shaping of attosecond pulses. In particular, in Sect. 4.2 the use of the polarization gating scheme is discussed: isolated pulses or pairs of attosecond pulses can be generated by simply changing the CEP of the driving field. Moreover, the simple scheme used to achieve the temporal gating, based on the use of two birefringent plates, can be employed to generate tunable isolated attosecond pulses or to spectrally and temporally modulate a pair of attosecond pulses. The use of the

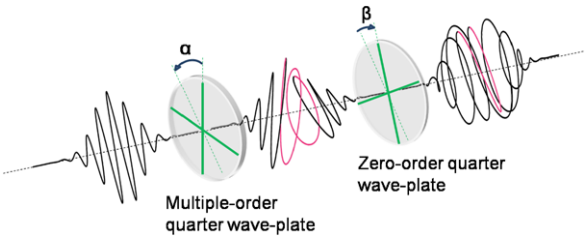

Fig. 4.1 Experimental setup used to obtain a driving field with linear polarization in a short temporal window around the pulse peak. The figure shows the angles α and β mentioned in the text

ionization gating technique for attosecond shaping is discussed in Sect. 4.3. Also in this case tunable harmonic radiation can be produced. Finally, Sect. 4.4 is devoted to the presentation of a method which can be employed for the generation of elliptically polarized isolated attosecond pulses.

4.2 Shaping of Attosecond Pulses by Polarization Gating

The modulation of the polarization state of the driving pulses is an effective technique for the generation of isolated attosecond pulses [8–10]. Moreover, the simple experimental setup used to achieve the required polarization control can be used to shape the spectral and temporal characteristics of the generated attosecond pulses. We will review various applications of the PG method for the generation of spectrally tunable isolated attosecond pulses and shaped pairs of attosecond pulses.

In order to produce a driving field characterized by almost linear polarization in a short temporal window (shorter than the separation between two consecutive attosecond pulses) it is possible to use two birefringent elements, as first proposed by Tcherbakoff *et al.* [25]. A schematic experimental setup is shown in Fig. 4.1. A first multiple-order quarter wave-plate introduces a temporal delay, τ, between the ordinary and extraordinary field components. The angle α between the axes of the plate and the incident polarization direction is usually set to $\alpha = 45°$. The second plate is a zero-order quarter wave-plate, with axis forming an angle β with respect to the polarization direction of the incident beam. When $\beta = 0°$ the second plate transforms the linear polarization into circular and vice-versa and a short temporal gate of linear polarization can be obtained (narrow gate configuration). The temporal gate of almost linear polarization, defined as the temporal interval during which the ellipticity modulus is smaller than the threshold value ϵ_{th} (corresponding to the ellipticity value for which harmonic conversion efficiency is decreased by half), can be written as:

$$\tau_g = \frac{\epsilon_{\text{th}} \tau_p^2}{\tau |\cos(2\beta)| \ln 2}, \tag{1}$$

where τ_p is the pulse duration.

In our experimental condition, the first plate was a 181-μm-thick multiple-order plate, the second one was a zero-order quarter wave-plate. After the two plates the pulse is linearly polarized around the center and circularly or elliptically polarized

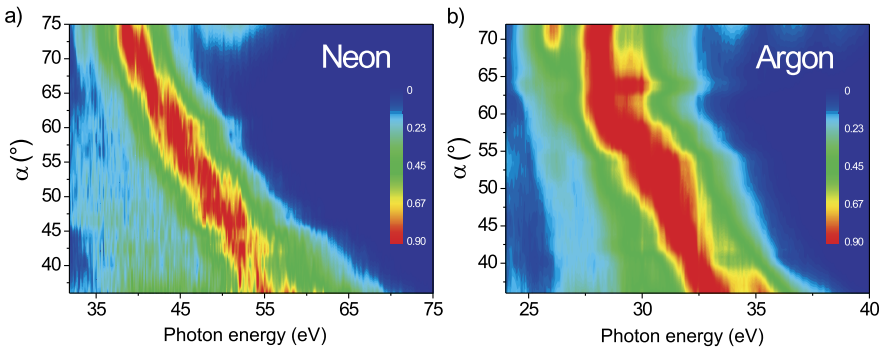

Fig. 4.2 XUV spectra measured in Neon (**a**) and Argon (**b**) for different values of the angle α between the electric field of the linearly polarized input pulse and the neutral axis of the first multiple-order waveplate

on the leading and trailing edges. Using this gating scheme, the gate position is imposed by the intensity profile of the pulse, the emission time is linked to the CEP of the electric field. It has been demonstrated that upon changing the CEP of the driving pulses it is possible to generate either one or two XUV pulses [9], as evidenced by the evolution of the spectral characteristics of the XUV radiation upon changing the CEP of the excitation pulse. A clear π periodicity of the emitted spectra was observed: the spectra generated in argon were composed by well resolved harmonics of the fundamental radiation for particular CEP values, and by a broadband continuum for other CEP values. In the case of continuum generation, pulses as short as 130 as were measured [10]. We have demonstrated that the temporal and spectral characteristics of the XUV radiation generated by using the polarization gating scheme can be easily shaped by rotating the birefringent plates used to achieve the temporal gate. In particular, in the case of isolated attosecond pulses (narrow gate configuration) it is possible to tune the XUV radiation in a relatively broad spectral range by rotating the first plate. When a pair of attosecond pulses is generated (intermediate or large gate configuration, obtained by increasing β), it is possible to obtain a complete tunability of the harmonic peak position by changing the CEP of the driving pulse.

4.2.1 Tunable Isolated Attosecond Pulses

In a first experiment, we generated broadband and continuous XUV radiation by focusing sub-6-fs pulses, with central wavelength of 750 nm, stabilized CEP and modulated polarization state, into a 3.5-mm-thick cell filled with Argon and Neon with static pressure [26]. The residual CEP fluctuations were $<$110 mrad (rms). The initial value of α was 45°, and β was fixed at $\beta = 0°$. Figure 4.2a shows the evolution of the XUV spectra measured in Neon upon changing α in the range

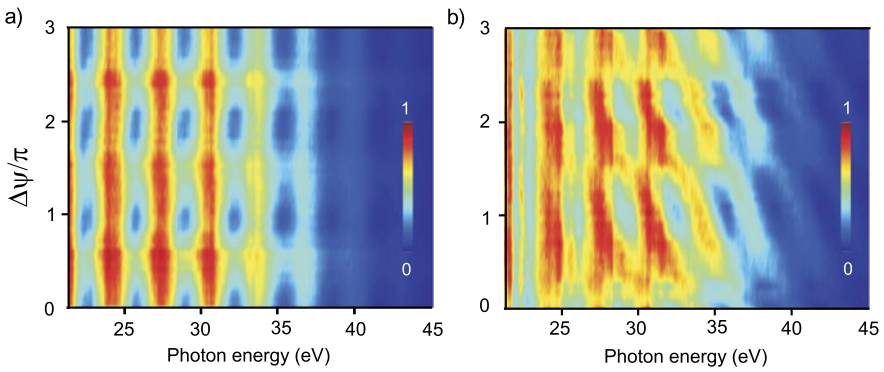

Fig. 4.3 XUV spectra generated in Argon using a polarization-modulated pulse (5-fs pulse duration) as a function of the CEP shift of the IR pulse for (**a**) $\beta = -15°$ and (**b**) $\beta = 15°$

$\sim 35° < \alpha < \sim 75°$. The XUV radiation can be continuously tuned in a broad spectral region, with a maximum spectral shift of $\sim$20 eV. Noteworthy, the spectra are continuous over the whole bandwidth for all values of α. A further increase of α determines an increase of the width of the polarization gate, which gives rise to the generation of modulated spectra. By varying the value of α, it is possible to finely change the time dependence of the polarization of the IR field and therefore the electron trajectories. In this way, the energy of the electron wave packet recolliding with the parent ion can be tuned determining the emission of tunable XUV pulses. Figure 4.2b shows the evolution of the XUV spectra measured in Argon upon changing the angle α. Also in this case the XUV radiation is continuous over all the recorded bandwidth and can be continuously tuned in a more restricted spectral region, with respect to the case of Neon, with a maximum spectral shift is $\sim$6.5 eV.

4.2.2 Temporal Shaping of Pairs of Attosecond Pulses

A direct consequence of Eq. (1) is that it is possible to increase the width of the temporal gate by increasing $|\beta|$ (with $|\beta| \leq 45°$), without affecting the intensity profile of the excitation pulse, starting from the value $\beta = 0°$, which corresponds to the situation of maximum confinement. Upon increasing β a short train of attosecond pulses can be generated. Noteworthy, the spectral characteristics of the XUV radiation are not symmetric with respect to the sign of β [27]. This is shown in Fig. 4.3, where the evolution of the spectral characteristics of the harmonic radiation as a function of the CEP of the driving pulse is reported for $\beta = \pm 15°$. In this case, the XUV spectra are always modulated, indicating the emission of at least two attosecond pulses. In the case $\beta = -15°$ (Fig. 4.3a), the position of the spectral peaks is only slightly affected by the CEP. On the contrary, for $\beta = 15°$ (Fig. 4.3b) the position of the spectral peaks is strongly affected by the CEP. We have investigated the CEP-dependence of the spectral and temporal characteristics of the XUV

radiation by using a nonadiabatic stationary phase model [28–30]. It is possible to demonstrate that the generation of harmonic radiation depends critically on particular characteristics of the IR electric field, which allows one to steer the electron trajectories on the time scale of tens of attoseconds [27]. The measured asymmetry with respect to the sign of β can be understood in the framework of the saddle-point method .

The Fourier transform of the single-atom dipole moment, $\mathbf{r}(\omega)$, can be written as a coherent superposition of various complex quantum paths, corresponding to the complex saddle-point solutions $(\mathbf{p}_s, t_s, t_s')$, where: $\mathbf{p}_s$ is the stationary value of the electron momentum, t_s' and t_s are the ionization and recombination instants, respectively. $\mathbf{r}(\omega)$ can be written as [30]:

$$\begin{aligned}\mathbf{r}(\omega) &\simeq \sum_s \left|x_s(\omega)\right| \exp\left[i\Phi_{x,s}(\omega)\right]\mathbf{u}_x + \left|y_s(\omega)\right| \exp\left[i\Phi_{y,s}(\omega)\right]\mathbf{u}_y \\ &\simeq \sum_s \frac{i2\pi}{\sqrt{\det(S'')}}\left[\frac{\pi}{\epsilon + (t_s - t_s')/2}\right]^{3/2} \mathbf{d}^*\left[\mathbf{p}_s - \mathbf{A}(t_s)\right] \\ &\times \mathbf{E}\left(t_s'\right)\cdot \mathbf{d}\left[\mathbf{p}_s - \mathbf{A}\left(t_s'\right)\right] \exp\left[-iS\left(\mathbf{p}_s, t_s, t_s'\right)\right] \end{aligned} \tag{2}$$

where ϵ is a regularization constant; $\mathbf{A}(t)$ is the vector potential associated to $\mathbf{E}(t)$; $\mathbf{d}$ is the dipole matrix element; and S is the dipole phase. The term $\det(S'')$ is the determinant of the matrix of the second time derivative of the phase $\Theta(\mathbf{p}_s, t, t') = \omega t - S(\mathbf{p}_s, t, t')$ with respect to t and t' evaluated in correspondence of the saddle-point solutions $(\mathbf{p}_s, t_s, t_s')$. The x and y components of the emission rate, $W_{x,y}(\omega)$, and the total emission rate, $W(\omega)$ can be written as follows:

$$\begin{aligned} W_{x,y}(\omega) &\propto \omega^3 \left|\mathbf{r}(\omega)\cdot \mathbf{u}_{x,y}\right|^2, \\ W(\omega) &\propto \omega^3 \left|\mathbf{r}(\omega)\right|^2. \end{aligned} \tag{3}$$

The phase term differences associated to the pair of short quantum paths contributing to the XUV generation process can be written as:

$$\Delta\Phi_i(\omega) = \omega\Delta t_i - \Delta S_i(\omega) + \Delta\chi_i(\omega), \tag{4}$$

where $\chi_i(\omega)$ is a residual phase term associated to the i-th quantum path. The phase-difference terms ΔS_i and $\Delta\chi_i$ evolve as a function of ω in a similar way for $|\beta|$ and $-|\beta|$, so that they cannot explain the different behaviors. The asymmetry is related to the phase term $\omega\Delta t_i$: indeed this term strongly depends on the CEP for $\beta = 15°$, whereas for $\beta = -15°$ only small variations as a function of the CEP can be observed. $\omega\Delta t_i$ can be decomposed into two contributions, which depend on the ionization time $t_i'(\omega)$ and the time spent by the freed electron in the continuum $\tau_i(\omega)$:

$$\omega\Delta t_i = \omega\left(\Delta t_i' + \Delta\tau_i\right). \tag{5}$$

Only the phase term related to the electron ionization times, t', turns out to induce relevant effects on the observed CEP dependence of the XUV radiation [27]. This is related to the precise electric field form and in particular to the opposite effective

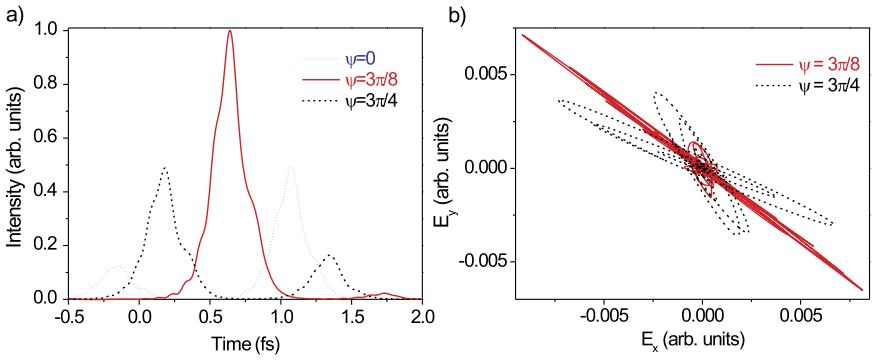

Fig. 4.4 (**a**) Temporal intensity profile of double attosecond pulses calculated using the nonadiabatic saddle-point model for three CEP values of the IR pulse. Same parameters of Fig. 4.3b. (**b**) Electric field evolution of the attosecond pulses for $\psi = 3\pi/8$ (*red solid curve*) and $\psi = 3\pi/4$ (*black dashed curve*)

chirp of the driving field [31], which is positive (negative) in the case of $\beta = 15°$, $\beta = -15°$.

We have finally investigated the temporal characteristics of the generated attosecond pulses. Figure 4.4a shows the intensity profile $I_t = |E_x(t)|^2 + |E_y(t)|^2$ of the attosecond pulses calculated using the parameters of Fig. 4.3b for three CEP values. In the case $\psi = 3\pi/8$, the XUV emission is almost entirely confined to an isolated attosecond pulse, with very small contributions from two additional adjacent pulses. For other CEP values two attosecond pulses are generated, whose relative amplitude changes with CEP. Also the polarization properties of the attosecond pulses strongly depend on the CEP, as shown in Fig. 4.4b, which displays the XUV electric field evolution for two different CEP values. The almost isolated attosecond pulse generated for $\psi = 3\pi/8$ presents a polarization very close to linear; in the other two cases $\psi = 0$ (not shown in the figure) and $\psi = 3\pi/4$ the two attosecond pulses are elliptically polarized and the orientation of the major axis of the polarization ellipse for the two pulses is, in general, different.

Upon increasing β, the number of generated attosecond pulses increases and complex structures, characterized by peaks that do not correspond to the harmonic energies, show up in the harmonic spectra [30]. In this case, the spectral characteristics depend on the energy region: for high harmonic orders, the spectra are characterized by a clear modulation, which in the temporal domain corresponds to the generation of two or three attosecond pulses. For low-order harmonics, the spectra present a complex pattern characterized by double peaks: the temporal structure of the generated XUV radiation is composed of several pulses. The physical origin of the complex interference pattern is due to the non-adiabaticity of the process and is related to the phase difference between consecutive quantum paths [30].

We can conclude that, by changing the angle β of the second birefringent plate and the CEP of the driving pulses it is possible to achieve a fine tuning of the temporal confinement of the harmonic emission, which allows one not only to select the

number of attosecond pulses produced during the harmonic generation process but also to shape the spectral and polarization properties of the XUV pulses.

4.3 Shaping of Attosecond Pulses by Ionization Gating

In the case of high-intensity driving fields, the plasma density rapidly increases on the leading edge of the pulse, thus creating a phase mismatch responsible for the suppression of HHG for all later half-cycles. Even if the excitation intensity is not high enough to create a temporal gate as narrow as required to select a single attosecond pulse, the ionization gating can be used in combination with bandpass filtering to overcome this problem [11, 12]. Recently a different approach based on the combined action of complete population depletion and spatial filtering of the XUV beam has been implemented for the generation of isolated attosecond pulses with duration down to 155 as and energy in the nanojoule range [13]. Also the ionization gating technique allows one to shape the spectral and temporal characteristics of attosecond pulses. In particular, as in the case of polarization gating, upon adjusting the peak intensity and the CEP of the driving pulses it is possible to confine the XUV generation process either to one or two attosecond pulses. The key elements of the technique are the use of linearly-polarized few-optical-cycle driving pulses with stable CEP and peak intensity above the saturation intensity and a careful optimization of the interaction geometry in terms of gas pressure, position and thickness of the gas cell and efficient spatial filtering of the XUV radiation. By using this method in the case of 5-fs excitation pulses with peak intensity ranging between 2.3 and 4.5×10^{15} W/cm^2, XUV radiation characterized by a continuous spectrum were generated in Neon, Argon, Krypton and Xenon [13]. The physical mechanisms at the basis of the experimental results have been investigated by using a three-dimensional (3D) propagation model, which takes into account both temporal plasma-induced phase modulation and spatial plasma-lensing effects on the fundamental beam [32], and nonadiabatic saddle-point simulations [28, 29]. The ionization rates have been calculated by using the Ammosov, Delone, and Krainov (ADK) theory [33], which clearly indicates a strong dependence on the value of the CEP of the driving field. This dependence strongly affects the shape of the temporal gate, thus leading to the production of one or two attosecond pulses.

4.3.1 Tunable XUV Radiation by Ionization Gating

We have recently experimentally demonstrated that by using high-intensity driving pulses with few-optical-cycle duration and stable CEP it is possible to obtain a complete spectral tunability of the harmonic peak position inside the whole XUV spectrum, by simply varying the CEP of the excitation pulse [34]. The XUV radiation was generated by focusing 5-fs infrared pulses, with stabilized CEP, into a 2.5-mm-long cell filled with Argon at low pressure (a few torr). The peak intensity was set

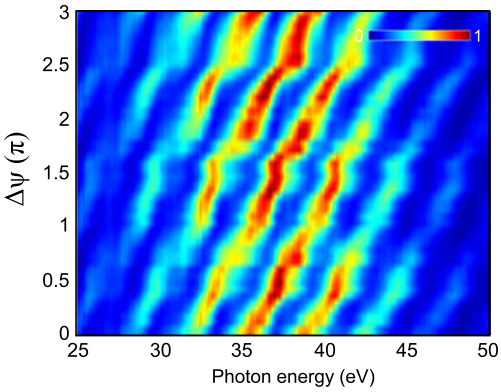

Fig. 4.5 XUV spectra generated in Argon for different CEP values of the excitation pulse. Pulse parameters: pulse duration 5 fs; peak intensity 3.5×10^{15} W/cm^2

at $\sim 3.5 \times 10^{15}$ W/cm^2 in order to generate a discrete spectrum for all the CEP values. The cell was placed after the laser focal position to select the short quantum trajectories [35]. Figure 4.5 shows the evolution of the XUV spectra as a function of the CEP of the driving field: a complete tunability of the XUV emission can be obtained upon changing the CEP. Noteworthy, the tunability of the harmonic peaks is not limited to the cutoff region, as already reported in previous works [36, 37].

This behavior has been interpreted in terms of temporal reshaping of the electric field of the driving pulses in an ionizing gas, which offers the possibility to control the electron quantum paths contributing to HHG. Indeed, while the spatial reshaping of the few-optical-cycle excitation pulse is weak, as a consequence of the very low pressure used in the experiment, the plasma-induced phase modulation strongly affects the temporal shape of the electric field of the driving pulse: this temporal distortion is responsible for the reshaping of the quantum trajectories which contribute to the HHG process. The physical processes at the basis of the XUV tunability can also be understood in the framework of a single atom approach, based on the use of the nonadiabatic saddle-point (NASP) approximation [28, 29]. Since in the case of high-intensity excitation ground-state depletion cannot be neglected, the Fourier transform of the single-atom dipole moment, $\mathbf{r}(\omega)$, can be written as [38]:

$$\mathbf{r}(\omega) = \sum_s \left|\mathbf{r}_s(\omega)\right| e^{i\Theta_s(\omega)} \exp\left[-\int_{-\infty}^{\mathrm{Re}(t_s')} w\left(t''\right) dt''\right], \tag{6}$$

where $w(t)$ is the tunnel ionization rate. Moreover, the saddle-point equations have to be solved by considering the actual electric field temporal evolution of the driving pulse, which is modified by the propagation in the ionized medium. The electric field of the IR pulse was calculated by using a three-dimensional model, in the framework of the slowly evolving wave approximation (SEWA) [39]. By using a coordinate frame that is moving at the group velocity v_g of the pulse and assuming radial symmetry, the driving electric field amplitude, $E(\mathbf{r}, t)$ ($\mathbf{r} = \mathbf{r}_\perp + z\mathbf{u}_z$, z and

$r_\perp$ are the propagation and transverse coordinates, respectively), can be obtained by numerical solution of the following equation [40]:

$$\nabla^2 E(\mathbf{r},t) - \frac{1}{c^2}\frac{\partial^2 E(\mathbf{r},t)}{\partial t^2} = \frac{1}{\epsilon_0 c^2}\frac{\partial^2 P(\mathbf{r},t)}{\partial t^2}, \tag{7}$$

where $P(\mathbf{r},t)$ is the polarization response of the medium and c is the vacuum velocity of light. We assumed that $P(\mathbf{r},t)$ in the coordinates ($r_\perp = x, y$) transversal to the propagation direction (z) is characterized by negligible variation over a distance comparable to the center wavelength. The first time derivative of the polarization $P(\mathbf{r},t)$ is dominated by the current density of the freed electrons. The second time derivative of the polarization can be written as [41]:

$$\frac{\partial^2 P(\mathbf{r},t)}{\partial t^2} = I_p \frac{\partial}{\partial t}\left(\frac{1}{E(\mathbf{r},t)}\frac{\partial n_e(\mathbf{r},t)}{\partial t}\right) + \frac{e^2}{m_e} n_e(\mathbf{r},t) E(\mathbf{r},t) \tag{8}$$

where I_p is the ionization potential of the atom, n_e is the electron density, e and m_e are the electron charge and mass, respectively. The first term in Eq. (8) is a pure loss term, which can be neglected in our experimental conditions, due to the very low pressure used in the generating cell (a few torr). In this case, Eq. (7) can be written as follows [32]:

$$\nabla^2 E(\mathbf{r},t) - \frac{1}{c^2}\frac{\partial^2 E(\mathbf{r},t)}{\partial t^2} = \frac{\omega_p^2(\mathbf{r},t)}{c^2} E(\mathbf{r},t), \tag{9}$$

where

$$\omega_p(\mathbf{r},t) = \left[\frac{e^2 n_e(\mathbf{r},t)}{\varepsilon_0 m_e}\right]^{1/2}, \tag{10}$$

is the plasma frequency of the ionized propagation medium. Equation (9) takes into account both temporal plasma-induced phase modulation and spatial plasma lensing effects, while it does not consider the linear gas dispersion and absorption of the driving beam, which are negligible under our conditions.

In order to solve the saddle-point equations for electric fields with arbitrary temporal evolution, we have employed a modified version of the method reported by Kovács and Toşa [42]. In particular, we have approximated the vector potential, $A(t)$, and its integral, $\mathcal{A}(t) = \int_{-\infty}^{t} A(t')\,dt'$ by making a polynomial fit on the real time axis and then using the analytical extension of the polynomials [43]:

$$\begin{aligned} A(t+i\zeta) &\simeq \sum_n a_n (t+i\zeta)^n, \\ \mathcal{A}(t+i\zeta) &\simeq \sum_n b_n (t+i\zeta)^n. \end{aligned} \tag{11}$$

Figure 4.6 shows the evolution of the XUV spectra as a function of the CEP calculated assuming the experimental conditions. In excellent agreement with the experimental results, the harmonic peak position shows a complete tunability over the whole spectral range (the non-perfectly continuous shift of the measured harmonic peaks is probably related to the residual fluctuation of the CEP of the driving field).

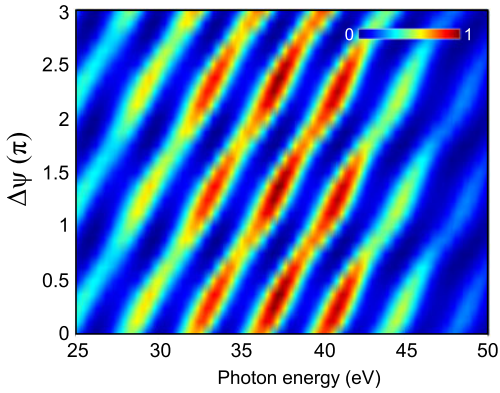

Fig. 4.6 Evolution of the XUV spectra calculated in Argon using the NASP method as a function of the CEP of the excitation pulse. Parameters used in the calculation: pulse duration 5 fs; center wavelength 750 nm; pulse peak intensity 3.5×10^{15} W/cm^2

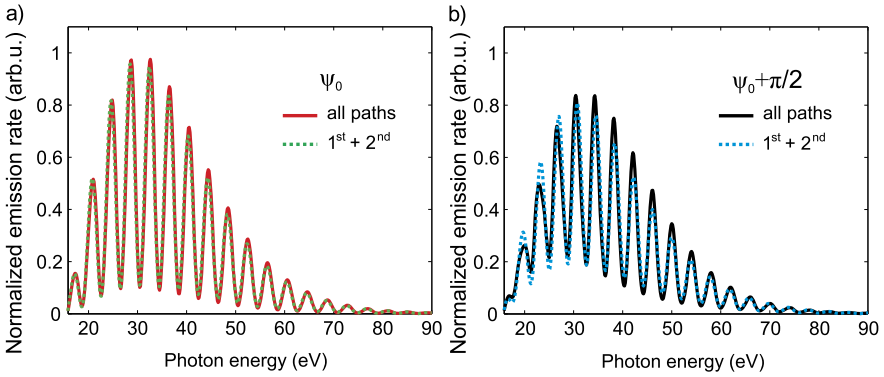

Fig. 4.7 (**a**)–(**b**) XUV emission rate for two different CEP values (ψ_0 and $\psi_0 + \pi/2$), calculated at the output of the gas cell considering all the short trajectories (*continuous curves*) and the two relevant short quantum paths (1 and 2) (*dashed curves*). Same parameters as in Fig. 4.6

Figure 4.7 shows the spectra for two different CEP values calculated at the output of the gas cell considering all the short trajectories (continuous curves) and the two relevant short quantum paths (hereafter designed as path 1 and path 2) (dashed curves). Such figure clearly demonstrate that the total emission rate can be associated to only two recollision events, so that only a pair of attosecond pulses is predominantly generated. The spectral position of the harmonic peaks is determined by the phase difference, $\Delta\Theta(\omega)$, between the two relevant electron trajectories, which can be written as in Eq. (4) and (5):

$$\Delta\Theta_{12}(\omega) = \omega\left(\Delta t'_{12} + \Delta\tau_{12}\right) - \Delta S_{12}(\omega) + \Delta\chi_{12}(\omega), \tag{12}$$

where $\Delta\Theta_{12}(\omega) = \Theta_2(\omega) - \Theta_1(\omega)$, $\Delta t'_{12} = t'_2 - t'_1$, $\Delta\tau_{12} = \tau_2 - \tau_1$, $\Delta S_{12} = S_2 - S_1$ and $\Delta\chi_{12} = \chi_2 - \chi_1$. Also in this case it is possible to demonstrate that the observed harmonic tunability is mainly related to the dependence on CEP of the phase term $\Delta t'_{12}$ related to the electron ionization times, produced by the temporal distortion of the electric field induced by the propagation inside the gas cell [34, 43].

4.4 Shaping of the Polarization of Isolated Attosecond Pulses by Amplitude Gating

In this last section, we will analyze a method, which allows one to control the polarization state of isolated attosecond pulses produced by selecting the cutoff region of the XUV radiation (amplitude gating) [44]. Several methods have been proposed and partly implemented for the generation of XUV pulses with elliptical polarization, based on the idea that elliptically-polarized harmonics can be produced by breaking the axial symmetry of the system. Control of the harmonic polarization can be obtained by combining a static electric field and a linearly polarized driving pulse [45]; elliptically polarized harmonics have been generated in aligned N_2 molecules, excited by linearly polarized laser fields [46]; circularly polarized harmonics can be produced by implementing two-color field schemes [47]; Ruiz *et al.* suggested the use of a two color (ω, 1.5ω) technique, where the two field components are linearly polarized and orthogonal to each other [48].

We have recently reported on a different technique, which allows one to control the polarization of isolated attosecond pulses, based on high-order harmonic generation in hydrogen-like systems characterized by atomic orbitals $\psi_{n\ell m}$ with $\ell \neq 0$. We have first calculated the harmonic spectrum generated in the atomic ion He^+ prepared in the $2p_0$ state, and excited by a linearly polarized driving pulse with Gaussian intensity envelope, duration 10 fs and central wavelength 1.6 μm. The electron probability density of the $2p_0$ state of He^+ is rotationally symmetric with respect to an axis, hereafter designed as z'-axis. He^+ in the $2p_0$ state can be prepared by exciting helium with linearly polarized π pulses, which can be designed to obtain a complete population transfer from the $1s$ to the $2p$ atomic orbital. The three-dimension time-dependent Schrödinger equation (3D-TDSE) has been solved by using the discrete variable representation (DVR) method [49, 50]. The initial wavefunction can be written as:

$$\psi_{n_0,\ell_0,m_0}(r,\theta,\varphi) = R_{n_0,\ell_0}(r) \sum_{m'} d^{(\ell_0)}_{m',m_0}(\beta) Y^{m'}_{\ell_0}(\theta,\varphi), \tag{13}$$

where $R_{n_0,\ell_0}(r)$, $d^{(\ell_0)}_{m',m_0}(\beta)$ and $Y^{m'}_{\ell_0}(\theta,\varphi)$ are the normalized hydrogenic bound state radial wavefunction, the rotation matrix element and the Spherical Harmonics, respectively. Here (r,θ,φ) are the spherical coordinates in xyz space, with the z-axis pointing to the polarization direction of the driving electric field. The temporal evolution of the wavefunction is obtained by Arnoldi scheme [51].

Isolated attosecond pulses, with duration of ~360 as, can be produced by selecting the cut-off portion of the calculated XUV spectra, with photon energies >165 eV. The important result of the calculations is that the calculated attosecond pulses are elliptically polarized. The calculated ellipticity, e, defined as the ratio between the minor and major polarization ellipse axis, turns out to be function of the angle, β, between the polarization direction of the driving field and the z'-axis. Figure 4.8a shows the ellipticity of the isolated attosecond pulses as a function of β. Upon changing β it is also possible to vary the direction of the major axis of the polarization ellipse, as shown in Fig. 4.8b. This direction is almost insensitive

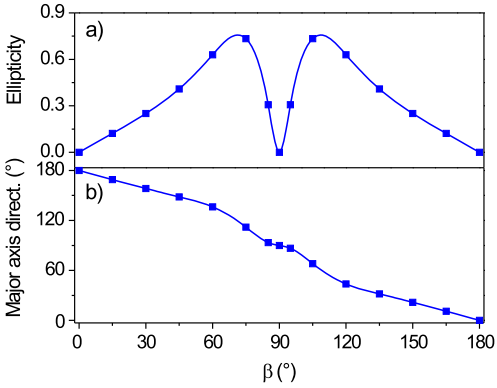

Fig. 4.8 Ellipticity (**a**) and major axis direction (**b**) of the isolated attosecond pulses as a function of the polarization direction, β, of the driving field with peak intensity $I = 1.5 \times 10^{14}$ W/cm^2

to the laser intensity variation for $\beta < 60°$ (and $\beta > 120°$). The helicity of the electric field of the attosecond pulse is positive (clock-wise rotation) for $\beta < 90°$ and negative (counter-clock-wise rotation) for $\beta > 90°$.

We demonstrated [44] that the characteristics of the polarization state of the attosecond pulses are strictly related to the tunnel ionization step in the harmonic generation process from atomic orbitals with non-vanishing angular quantum momentum. We point out that the control of the polarization characteristics of isolated attosecond pulses (i.e., ellipticity, major axis direction and helicity) might open new avenues for novel applications in probing ultrafast electron dynamics.

4.5 Conclusions

Attosecond pulses are unique tools for the investigation of important physical processes in atoms, molecules, mesoscopic systems and solids, where the dynamics of the electron play a crucial role. In this chapter, various gating schemes have been discussed, which allow one to achieve a high degree of control on the spectral and temporal characteristics of the attosecond pulses. In particular, the polarization and ionization gating techniques can be effectively used to shape XUV pulses produced by high-order harmonic generation in noble gases. Isolated or pairs of attosecond pulses can be obtained, depending on the gating characteristics, which can be spectrally tuned, with potential important implications for the applications.

Acknowledgements The research leading to the results presented in this paper has received funding from the European Research Council under the European Community's Seventh Framework Programme (FP7/2007-2013)/ERC grant agreement n. 227355—ELYCHE. We acknowledge financial support from the Italian Ministry of Research (FIRB-IDEAS RBID08CRXK), support from European Union within contract n. 228334 JRA-ALADIN (Laserlab Europe II) and from MC-RTN ATTOFEL (FP7-238362). We thank I.J. Sola, V. Strelkov, E. Mével and E. Constant for the implementation of the polarization gating technique and for the measurements shown in Fig. 4.3.

References

1. P.M. Paul, E.S. Toma, P. Breger, G. Mullot, F. Augeé, Ph. Balcou, H.G. Muller, P. Agostini, Science **292**, 1689 (2001)
2. M. Hentschel, R. Kienberger, Ch. Spielmann, G.A. Reider, N. Milosevic, T. Brabec, P.B. Corkum, U. Heinzmann, M. Drescher, F. Krausz, Nature **414**, 509 (2001)
3. F. Krausz, M. Ivanov, Rev. Mod. Phys. **81**, 163 (2009)
4. M. Nisoli, G. Sansone, Prog. Quantum Electron. **33**, 17 (2009)
5. G. Farkas, C. Toth, Phys. Lett. A **168**, 447 (1992)
6. I.P. Christov, M.M. Murnane, H. Kapteyn, Phys. Rev. Lett. **78**, 1251 (1997)
7. E. Goulielmakis, M. Schultze, M. Hofstetter, V.S. Yakovlev, J. Gagnon, M. Uiberacker, A.L. Aquila, E.M. Gullikson, D.T. Attwood, R. Kienberger, F. Krausz, U. Kleineberg, Science **320**, 1614 (2008)
8. P.B. Corkum, N.H. Burnett, M.Y. Ivanov, Opt. Lett. **19**, 1870 (1994)
9. I.J. Sola, E. Mével, L. Elouga, E. Constant, V. Strelkov, L. Poletto, P. Villoresi, E. Benedetti, J.-P. Caumes, S. Stagira, C. Vozzi, G. Sansone, M. Nisoli, Nat. Phys. **2**, 319 (2006)
10. G. Sansone, E. Benedetti, F. Calegari, C. Vozzi, L. Avaldi, R. Flammini, L. Poletto, P. Villoresi, C. Altucci, R. Velotta, S. Stagira, S. De Silvestri, M. Nisoli, Science **314**, 443 (2006)
11. M.J. Abel, T. Pfeifer, P.M. Nagel, W. Boutu, M.J. Bell, C.P. Steiner, D.M. Neumark, S.R. Leone, Chem. Phys. **366**, 9 (2009)
12. I. Thomann, A. Bahabad, X. Liu, R. Trebino, M.M. Murnane, H.C. Kapteyn, Opt. Express **17**, 4611 (2009)
13. F. Ferrari, F. Calegari, M. Lucchini, C. Vozzi, S. Stagira, G. Sansone, M. Nisoli, Nat. Photonics **4**, 875 (2010)
14. T. Pfeifer, L. Gallmann, M.J. Abel, D.M. Neumark, S.R. Leone, Opt. Lett. **31**, 975 (2006)
15. H. Merdji, T. Auguste, W. Boutu, J.P. Caumes, B. Carré, T. Pfeifer, A. Jullien, D.M. Neumark, S. Leone, Opt. Lett. **32**, 3134 (2007)
16. C. Vozzi, F. Calegari, F. Frassetto, L. Poletto, G. Sansone, P. Villoresi, M. Nisoli, S. De Silvestri, S. Stagira, Phys. Rev. A **79**, 033842 (2009)
17. F. Calegari, C. Vozzi, M. Negro, G. Sansone, F. Frassetto, L. Poletto, P. Villoresi, M. Nisoli, S. De Silvestri, S. Stagira, Opt. Lett. **34**, 3125 (2009)
18. E.J. Takahashi, P. Lan, O.D. Mücke, Y. Nabekawa, K. Midorikawa, Phys. Rev. Lett. **104**, 233901 (2010)
19. T. Siegel, R. Torres, D.J. Hoffmann, L. Brugnera, I. Procino, A. Zaïr, J.G. Underwood, E. Springate, I.C.E. Turcu, L.E. Chipperfield, J.P. Marangos, Opt. Express **18**, 6853 (2010)
20. H. Mashiko, S. Gilbertson, C. Li, S.D. Khan, M.M. Shakya, E. Moon, Z. Chang, Phys. Rev. Lett. **100**, 103906 (2008)
21. H. Mashiko, S. Gilbertson, M. Chini, X. Feng, C. Yun, H. Wang, S.D. Khan, S. Chen, Z. Chang, Opt. Lett. **34**, 3337 (2009)
22. X. Feng, S. Gilbertson, H. Mashiko, H. Wang, S.D. Khan, M. Chini, Y. Wu, K. Zhao, Z. Chang, Phys. Rev. Lett. **103**, 183901 (2009)
23. R. López-Martens, K. Varjú, P. Johnsson, J. Mauritsson, Y. Mairesse, P. Salières, M.B. Gaarde, K.J. Schafer, A. Persson, S. Svanberg, C.-G. Wahlström, A. L'Huillier, Phys. Rev. Lett. **94**, 033001 (2005)
24. K.T. Kim, K.S. Kang, M.N. Park, T. Imran, G. Umesh, C.H. Nam, Phys. Rev. Lett. **99**, 223904 (2007)
25. O. Tcherbakoff, E. Mével, D. Descamps, J. Plumridge, E. Constant, Phys. Rev. A **68**, 043804 (2003)
26. G. Sansone, E. Benedetti, C. Vozzi, S. Stagira, M. Nisoli, New J. Phys. **10**, 025006 (2008)
27. G. Sansone, E. Benedetti, J.P. Caumes, S. Stagira, C. Vozzi, M. Nisoli, L. Poletto, P. Villoresi, V. Strelkov, I. Sola, L.B. Elouga, A. Zaïr, E. Mével, E. Constant, Phys. Rev. A **80**, 063837 (2009)
28. M. Lewenstein, Ph. Balcou, M.Yu. Ivanov, A. L'Huillier, P.B. Corkum, Phys. Rev. A **49**, 2117 (1994)

29. G. Sansone, C. Vozzi, S. Stagira, M. Nisoli, Phys. Rev. A **70**, 013411 (2004)
30. G. Sansone, Phys. Rev. A **79**, 053410 (2009)
31. V. Strelkov, A. Zaïr, O. Tcherbakoff, R. López-Martens, E. Cormier, E. Mével, E. Constant, Appl. Phys. B, Lasers Opt. **78**, 879 (2004)
32. E. Priori, G. Cerullo, M. Nisoli, S. Stagira, S. De Silvestri, P. Villoresi, L. Poletto, P. Ceccherini, C. Altucci, R. Bruzzese, C. de Lisio, Phys. Rev. A **61**, 063801 (2000)
33. M.V. Ammosov, N.B. Delone, V.P. Krainov, Zh. Eksp. Teor. Fiz. **91**, 2008 (1986) [Sov. Phys. JETP **64**, 1191 (1986)]
34. F. Calegari, M. Lucchini, K.S. Kim, F. Ferrari, C. Vozzi, S. Stagira, G. Sansone, M. Nisoli, Phys. Rev. A **84**, 041802 (2011)
35. Y. Mairesse, A. de Bohan, L.J. Frasinski, H. Merdji, L.C. Dinu, P. Monchicourt, P. Breger, M. Kovačev, R. Taïeb, B. Carré, H.G. Muller, P. Agostini, P. Salières, Science **302**, 1540 (2003)
36. A. Baltuška, Th. Udem, M. Uiberacker, M. Hentschel, E. Goulielmakis, Ch. Gohle, R. Holzwarth, V.S. Yakovlev, A. Scrinzi, T.W. Hänsch, F. Krausz, Nature **421**, 611 (2003)
37. M. Nisoli, G. Sansone, S. Stagira, S. De Silvestri, C. Vozzi, M. Pascolini, L. Poletto, P. Villoresi, G. Tondello, Phys. Rev. Lett. **91**, 213905 (2003)
38. G. Sansone, E. Benedetti, J.P. Caumes, S. Stagira, C. Vozzi, S. De Silvestri, M. Nisoli, Phys. Rev. A **73**, 053408 (2006)
39. T. Brabec, F. Krausz, Phys. Rev. Lett. **78**, 3282 (1997)
40. M. Geissler, G. Tempea, A. Scrinzi, M. Schnürer, F. Krausz, T. Brabec, Phys. Rev. Lett. **83**, 2930 (1999)
41. T. Brabec, F. Krausz, Rev. Mod. Phys. **72**, 545 (2000)
42. K. Kovács, V. Toşa, J. Mod. Opt. **57**, 977 (2010)
43. M. Lucchini, K.S. Kim, F. Calegari, G. Sansone, M. Nisoli, New J. Phys. **14**, 033009 (2012)
44. C. Liu, M. Nisoli, Phys. Rev. A **85**, 013418 (2012)
45. B. Borca, A.V. Flegel, M.V. Frolov, N.L. Manakov, D.B. Milošević, A.F. Starace, Phys. Rev. Lett. **85**, 732 (2000)
46. X. Zhou, R. Lock, N. Wagner, W. Li, H.C. Kapteyn, M.M. Murnane, Phys. Rev. Lett. **102**, 073902 (2009)
47. D.B. Milošević, W. Becker, R. Kopold, Phys. Rev. A **61**, 063403 (2000)
48. C. Ruiz, D.J. Hoffmann, R. Torres, L.E. Chipperfield, J.P. Marangos, New J. Phys. **11**, 113045 (2009)
49. L. Peng, A.F. Starace, J. Chem. Phys. **125**, 154311 (2006)
50. K. Dunseath, J. Launay, M. Dunseath, L. Mouret, J. Phys. B, At. Mol. Opt. Phys. **35**, 3539 (2002)
51. T.J. Park, J.C. Light, J. Chem. Phys. **85**, 5870 (1986)

Chapter 5
Transform-Limited Attosecond Pulse Generation Through Atto-Chirp Compensation by Material Dispersion

Chang Hee Nam, Kyung Taec Kim, and Dong Hyuk Ko

Abstract High harmonics are a unique light source with ultrashort duration and superb spatial coherence in the extreme ultraviolet and X-ray region. Though regularly spaced broad harmonic spectra are suitable for generating very short pulses, they suffer from the inherent chirp due to the harmonic generation process. Here we proposed and demonstrated the method to compensate for the attosecond chirp by propagating the harmonic pulses through a medium with negative group delay dispersion. In a single Ar gas cell, we showed that the chirp compensation could be achieved in the same harmonic generation cell, obtaining near transform-limited 206-as pulses. We could demonstrate also the generation of much shorter 63-as pulses by obtaining the harmonics from Ne and by compensating for the attosecond chirp in the second gas cell of Ar. The chirp compensation in gaseous media is, thus, very effective and powerful in obtaining near transform-limited attosecond pulses—very valuable for attosecond science.

5.1 Introduction

Ultrafast phenomena in atoms and molecules can be explored by applying ultrashort light pulses. Attosecond light sources are essential for investigating ultrafast atomic and molecular dynamics occurring in the attosecond time scale. In 2001, two

C.H. Nam (✉) · K.T. Kim · D.H. Ko
Department of Physics and Coherent X-ray Research Center, KAIST, Daejeon 305-701, Korea
e-mail: chnam@kaist.ac.kr

C.H. Nam
Center for Relativistic Laser Science, Institute for Basic Science, Gwangju 500-712, Korea

C.H. Nam
Department of Physics and Photon Science, Gwangju Institute of Science and Technology (GIST), Gwangju 500-712, Korea

Present address:
K.T. Kim
Joint Attosecond Science Laboratory, Univ. of Ottawa and National Research Council, Ottawa, Canada

K. Yamanouchi, K. Midorikawa (eds.), *Progress in Ultrafast Intense Laser Science*, Springer Series in Chemical Physics 104, DOI 10.1007/978-3-642-35052-8_5,

groups at CEA Saclay and at TU Wien succeeded in measuring the production of attosecond pulse trains and isolated attosecond pulses using high harmonic generation processes, respectively [1, 2]. High harmonics emitted from atoms driven by intense femtosecond laser pulses have been intensively investigated for the generation of attosecond pulses because of their broad spectral bandwidth in the extreme ultraviolet and soft X-ray spectral region. The wide range of plateau harmonics with regular spacing resembles the spectrum of a mode-locked laser and can be an ideal condition to form attosecond pulses if a linear phase relation exists among different harmonics [3]. The phase of harmonics, however, is inherently chirped in the harmonic generation process, which broadens the harmonic pulse duration as compared to the transform-limited case—the shortest pulse duration achievable for a given harmonic spectrum [4–6]. Consequently, a suitable method, to compensate for the attosecond chirp (or "atto-chirp") of harmonic pulses, needs to be employed to achieve transform-limited attosecond harmonic pulses.

Here we have proposed the method to compensate for atto-chirp by material dispersion and demonstrated the generation of near transform-limited attosecond pulses with duration as short as 63 as [7]. The harmonics contributed from short trajectory components are positively chirped. The positive atto-chirp can be compensated by propagating through a medium with negative group delay dispersion (GDD) [5, 8]. For the atto-chirp compensation metallic filter materials, installed to block co-propagating laser pulses, can be used. In addition, gaseous materials are also found to be useful because the chirp can be controlled continuously without oxidation problem [9]. In Sect. 5.2, the basic principle of atto-chirp compensation by material dispersion is presented, along with a theoretical analysis. Candidate materials for the atto-chirp compensation in the soft X-ray region are examined according to the spectral range of interests. In addition, broadband chirp compensation, up to the energy of 300 eV, is analyzed to achieve sub-50-as pulse generation by applying intense mid-infrared femtosecond laser pulses. In Sect. 5.3, the experimental demonstration of the atto-chirp compensation in a gaseous medium is described, showing the result of self-compression. The generation of sub-100-as pulses using a separate compensation medium is presented in Sect. 5.4. Conclusion is given in Sect. 5.5.

5.2 Basic Principle of Atto-Chirp Compensation by Material Dispersion

The spectral structure of high-harmonic pulses, or the chirped structure, can be seen from a time-frequency analysis showing the change of spectral composition in time [5, 8]. The formation of the chirped structure is well explained by the semi-classical three-step model of high-harmonic generation (HHG) [10, 11]. An electron is first ionized through a tunneling process when the atomic potential is deformed by an intense laser field. The liberated electron is then accelerated by the laser field, and driven back to the parent ion due to the oscillating laser field. The semi-classical

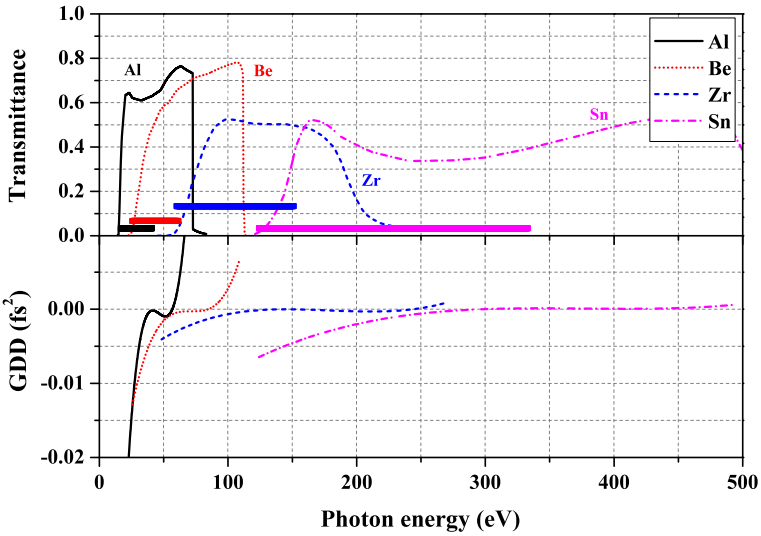

Fig. 5.1 Transmittance and GDD of metallic filters commonly used for the spectral selection of X-ray sources and for blocking co-propagating laser pulses after harmonic generation. The *bars in the transmittance curve* indicate the spectral range of negative GDD for the material of choice

model shows that the harmonic photon energy increases with time in the case of short trajectory harmonics, while the energy of long trajectory harmonics decreases. As a consequence, harmonics are positively chirped for short trajectory components and negatively chirped for long trajectory components. In most cases, the short-trajectory harmonics are responsible for the formation of attosecond pulses at the far field [12, 13]. Since the attosecond chirp of harmonic pulses originates from a sinusoidal electric field, it is intrinsic and unavoidable in the generation of attosecond harmonic pulses. In order to produce transform-limited attosecond harmonic pulses, the dispersion control of the attosecond pulse is essential.

We have proposed to make use of material dispersion for the compensation of atto-chirp [5, 8]. The dispersion of the attosecond pulse can be changed after the propagation of the medium. The chirp structure of the attosecond pulse is closely related to the dispersion characteristics of the medium. The positive chirp of harmonic pulses can be compensated in a medium with negative GDD. The refractive index information of a material can be found from the Kramers–Kronig relations that link the imaginary part of the refractive index of a medium, obtained from X-ray absorption data, with the real part [14]. The dispersion characteristics of a medium exhibits negative GDD in the frequency range of increasing transmission after a strong absorption [8]. We examined the dispersion characteristics of several metallic materials as presented in Fig. 5.1. The thickness of all filters was set to 200 nm for the comparison of transmittance and GDD. From this information, a suitable material can be chosen depending on the spectral region of interest for the compensation of atto-chirp.

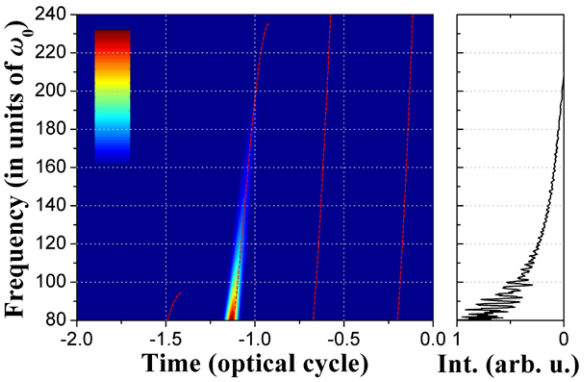

Fig. 5.2 Time-frequency analysis of the high-harmonic pulse, obtained by applying a 5-fs laser pulse above the saturation intensity, clearly shows the chirp structure of the broad harmonic pulse [5]

We examined the atto-chirp compensation by applying our idea to the case of isolated single attosecond pulses. The isolated attosecond pulse generation was realized using the ionization gating method in which few-cycle laser pulses above the saturation intensity were applied. Harmonic radiation from neon atoms exposed to a 5-fs, 800-nm laser pulse with peak intensity of 4.7×10^{15} W cm^{-2} was obtained by solving a time-dependent Schrödinger equation (TDSE) coupled with Maxwell equations. A one-dimensional propagation calculation, considering the focusing geometry and the self-phase modulation of the propagating laser pulse in an ionizing medium, was carried out [15]. The neon target of 0.5-mm length and 5-Torr pressure, placed 10 mm behind the laser focus, was used in order to select only harmonics from short trajectories after propagation [12, 13]. The time-frequency structure of the harmonic radiation in Fig. 5.2 shows the result calculated using a spectrogram method. At this laser intensity, neutral neon atoms were mostly ionized before reaching the pulse peak ($t = 0$) and the dominant harmonic radiation was generated near $t = -1.0$ (cycle). The selection of the harmonic radiation for the frequency range larger than $100\omega_0$ ($\omega_0 =$ laser frequency) allowed the generation of a single attosecond pulse since it appeared only within the half cycle at $t = -1.0$ (cycle), shown as the continuum radiation in the harmonic spectrum at the right side of Fig. 5.2. When the laser intensity, lower than the saturation intensity, was applied, the selectable continuum radiation for a single attosecond pulse generation was found to be much narrower and the generated pulses had much longer duration. Therefore, the application of laser intensity higher than the saturation intensity was clearly advantageous in attaining broad continuum spectrum.

For the case of Fig. 5.2, a metallic medium is considered for the spectral selection and chirp compensation. After the selection of an X-ray filter material with suitable transmission window and dispersion property, the thickness can be decided so as to achieve the optimum chirp compensation. In fact the filter thickness can be easily adjusted as far as the filter transmission is not too poor. The spectral phase shift induced by the X-ray filter with thickness z is then given by $\Delta\tilde{\phi}_{\text{filter}}(\omega) = -\omega\delta(\omega)z/c$, where $\delta(\omega)$ is real part of the refractive index of that filter material. The quadratic spectral phase of the linearly chirped harmonic pulse can be reasonably compensated using a 700-nm-thick Sn filter. The spectral phase of the attosecond pulse

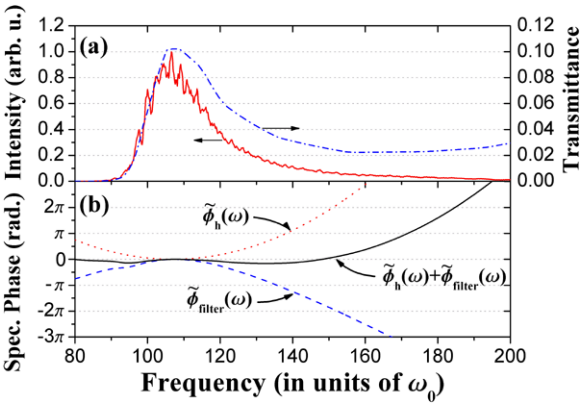

Fig. 5.3 (**a**) Broadband continuum spectrum corresponding to Fig. 5.2, transmitted through the 700-nm-thick Sn filter (*solid line*), given with the filter transmittance (*dash-dotted line*). (**b**) Chirp compensation of positively chirped harmonic radiation by the Sn filter. The spectral phase of the harmonic radiation as a positive quadratic curve centered at $107\omega_0$, $\tilde{\phi}_h(\omega)$, and the spectral phase shift induced by the Sn filter, $\Delta\tilde{\phi}_{\text{filter}}(\omega)$, are shown, respectively, by *dotted* and *dashed lines*. The spectral phase of the harmonic radiation after passing through the Sn filter is also drawn as a *solid line* [5]

obtained by TDSE calculation and the spectral phase shift $\Delta\tilde{\phi}_{\text{filter}}(\omega)$ induced by the 700-nm-thick Sn filter are shown in Fig. 5.3(b). The total spectral phase variation with the Sn filter is much less than π over the full width at half maximum (FWHM) of the transmission window of the Sn filter. The transmittance of the 700-nm-thick Sn filter, shown in Fig. 5.3(a), has transmittance over 5 % throughout its transmission window from $100\omega_0$ to $126\omega_0$ in FWHM. The spectral intensity of harmonics passing through the Sn filter is also shown in Fig. 5.3(a). As a result, the chirp-compensated harmonic radiation can be constructively added to generate a short single pulse.

Figure 5.4 shows the final pulse shape of the chirp-compensated harmonic pulse by the Sn filter. The pulse duration of the single harmonic pulse is 48 as, significantly shorter than the case of the 89-as pulse obtained without the atto-chirp compensation. The transmitted harmonic spectrum shows a long high-frequency tail with poor chirp compensation. This causes the ripple in the tail part of the single attosecond pulse, which may be removed by adding additional X-ray filter. The contrast ratio of the 48-as pulse to the one generated during the previous half-optical cycle is better than 1000, mainly due to the application of strong nonadiabatically increasing laser electric field to atoms before reaching the peak of the laser pulse for broad continuum generation.

The isolated attosecond pulse can be obtained by applying a temporal gating technique. Since the harmonic generation process repeats every half optical cycle, attosecond pulses generated from high harmonics usually consists of a pulse train separated by a half optical cycle. A simple method to generate an isolated attosecond pulse is to decrease the temporal duration of the driving laser pulse. It should be

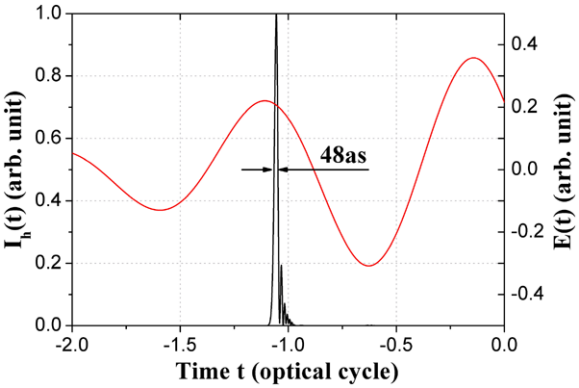

Fig. 5.4 Temporal profile of the chirp-compensated attosecond pulse by the 700-nm-thick Sn filter is plotted along with the electric field of the driving laser pulse [5]

noted that we introduced the ionization gating method for the generation of isolated attosecond pulses [5]. With laser intensity over the saturation level for optical field ionization, the harmonic generation time can be shifted to the leading edge of the laser pulse while the harmonic generation at the pulse peak is strongly suppressed due to the depletion of neutral atoms by optical field ionization. This can increase significantly the bandwidth of the continuum spectrum due to the enhanced nonadiabaticity of the harmonic generation process [16].

For achieving much shorter pulses than the case in Fig. 5.4 high harmonics with broader spectrum are required. The spectral range of plateau harmonics can be extended by adopting a long-wavelength laser, available by employing an optical parametric amplification system [17, 18]. This is not, however, a sufficient condition to produce a short pulse due to the atto-chirp existing in the temporal structure. The harmonics contributed from short-trajectory components are mostly considered for applications due to their nature of low beam divergence [19, 20]. As described above, attosecond pulses constructed with short-trajectory harmonics are positively chirped, and their atto-chirp can be determined by the scaling law as a function of intensity and wavelength of driving laser pulses. For the case of linearly chirped Gaussian pulses, the temporal duration can be written as

$$\Delta t = \sqrt{\frac{(4\ln 2)^2}{\Delta\omega^2} + \beta^2 \Delta\omega^2}, \tag{1}$$

where $\Delta\omega$ is the spectral bandwidth and β is GDD. This equation is physically reasonable since the duration is approaching the transform-limited value when GDD reduces to zero. The minimum pulse duration calculated from the Schwarz's inequality is given as

$$\Delta t_{\min} = 2\sqrt{(2\ln 2)\beta}. \tag{2}$$

The corresponding optimum bandwidth is set as $\Delta\omega_{\text{opt}} = \sqrt{\frac{4\ln 2}{\beta}}$. In the case of smaller bandwidth harmonic pulses, i.e. $\Delta\omega \ll \Delta\omega_{\text{opt}}$, the temporal duration of attosecond pulses is proportional to the inverse of harmonic bandwidth. On the other

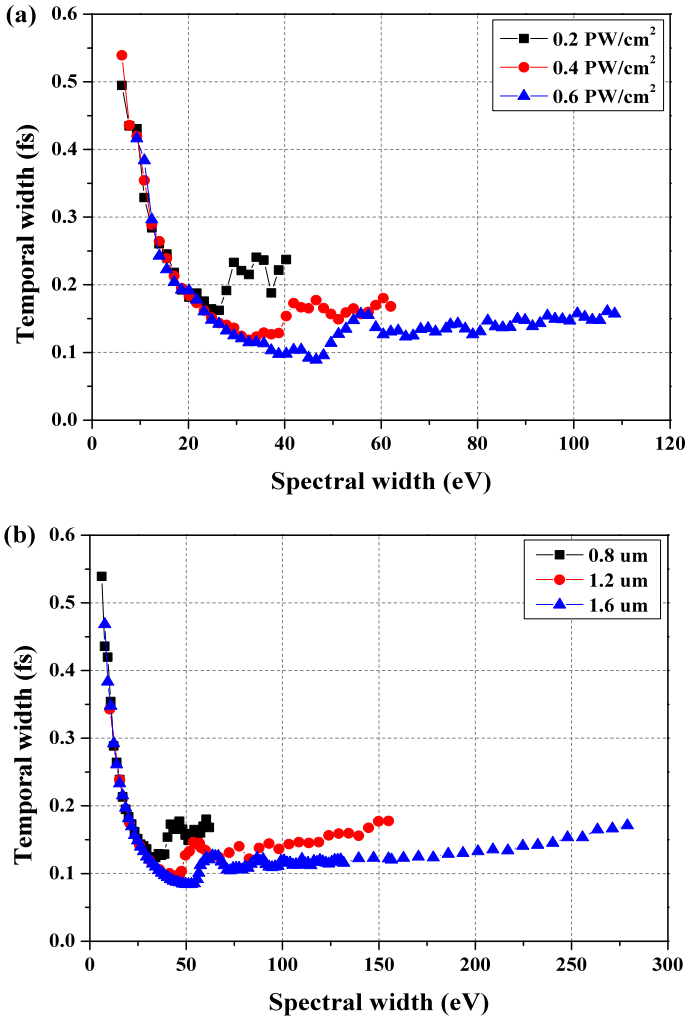

Fig. 5.5 Variation of high-harmonic pulse duration calculated with (**a**) fixed laser wavelength of 800 nm and (**b**) fixed laser intensity of 4×10^{14} W cm^{-2} [36]

limit, the temporal duration of attosecond pulses increases with harmonic bandwidth. The optimum bandwidth is, thus, set by GDD because harmonic pulses have non-zero dispersion in nature.

The temporal profile of the attosecond pulses are numerically calculated by solving a TDSE with various driving laser intensity and wavelength to verify the scaling law for the duration of the attosecond pulses and the optimum bandwidth. Figure 5.5 shows the duration of the attosecond pulses obtained in the middle of the harmonic spectrum with (a) fixed wavelength or (b) fixed intensity of the laser pulse. For the laser intensities of 2, 4, and 6×10^{14} W cm^{-2} at the wavelength of 800 nm, the

minimum duration of the attosecond pulse obtained is 160, 120, and 89 as, respectively. For the laser wavelength of 0.8, 1.2, and 1.6 μm, the minimum duration of the attosecond pulse is found to be 120, 94, and 84 as, respectively. The result verifies the scaling law for the duration of attosecond pulses,

$$\Delta t_{\min}[\text{as}] = \frac{200}{\sqrt{I_0[10^{14}\ \text{W cm}^{-2}]\lambda[\mu\text{m}]}}. \tag{3}$$

The advent of optical parametric amplifier technology enables the use of intense laser pulses at mid-infrared wavelength. Due to the cutoff law (proportional to $I_0\lambda^2$), the maximum harmonic energy may reach ~keV with a long wavelength laser driver. For example, the bandwidth of harmonic emission obtained with an intensity of 8×10^{14} W cm^{-2} at the wavelength of 3.2 μm is about 2.4 keV, whose transform-limited duration is 1.5 as. However, the minimum duration achievable is only 40 as, even if the optimized bandwidth is selected, because of atto-chirp. Consequently, the chirp compensation of attosecond harmonic pulses is essential to achieve the transform-limited pulse duration.

In order to reduce further the duration of attosecond harmonic pulses we investigated the characteristics of generated harmonics by solving the TDSE. High harmonics from Ne were examined by applying intense few-cycle mid-infrared laser pulses to obtain a broad spectrum with very small GDD. In this calculation, a broadband harmonic spectrum, up to 300 eV with GDD of 1.1×10^{-3} fs^2, could be obtained by applying a driving laser at 1600 nm with the peak intensity of 3.5×10^{15} W cm^{-2}. The duration of the laser pulse was chosen to be 7.4 fs (1.4 optical cycles) to apply the intense laser pulse. The strong depletion of the ground state of the harmonic generation medium was reached at the pulse peak [5, 8]. The calculated harmonic spectrum with the cutoff energy of about 300 eV is shown in Fig. 5.6(a). The harmonic pulse can support a transform-limited duration of 20 as, but the duration of attosecond pulses was 83 as without chirp compensation, as given in Fig. 5.6(b). For the compensation of atto-chirp, Xe was chosen to cover the spectral range from 150 eV to 300 eV, as presented in Fig. 5.7. After adjusting the pressure of a 10-mm Xe gas cell to 120 Torr, the chirp-compensated attosecond pulse with duration of 38 as could be produced, which is quite close to the transform-limited value of 34 as. The calculation result showed that a near transform-limited isolated sub-50-as pulse could be produced from Ne driven by an intense laser pulse at 1600 nm after the atto-chirp compensation in Xe.

5.3 Atto-Chirp Compensation in a Gaseous Medium: Experiment

A series of experiments have been performed to confirm the atto-chirp compensation by material dispersion. Instead of using a metallic medium for atto-chirp compensation, a gaseous material is considered for the compensation of positive atto-chirp [9]. The use of a metallic medium for chirp compensation is unfavorable because

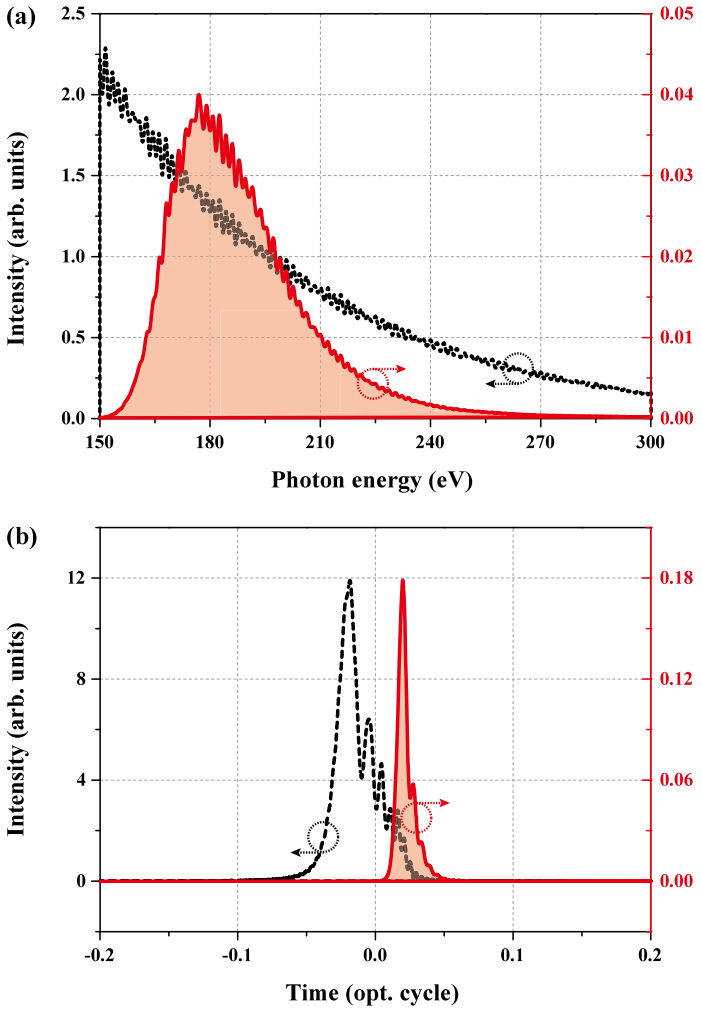

Fig. 5.6 Harmonic continuum spectra and temporal profiles of isolated attosecond pulses obtained without (*dotted without shading*) and with (*solid with shading*) atto-chirp compensation [36]

of strong absorption by the oxide layer formed on the surface of a metallic sheet [21, 22]. On the other hand, the use of a gaseous medium is much advantageous due to easy pressure control and the resilience of the gas medium to permanent damage, in addition to the elimination of the pinhole problem frequently existing in the use of thin metallic filters. The latter property is a strong favor in the choice of medium since thin metallic filters are fragile to laser pulses or mechanical stresses. Some rare gases, such as Ar, Kr, and Xe commonly used for HHG, are prospective media with suitable transmission and dispersion characteristics. These gaseous media can be used for chirp compensation as well as strong harmonic generation. The spectral

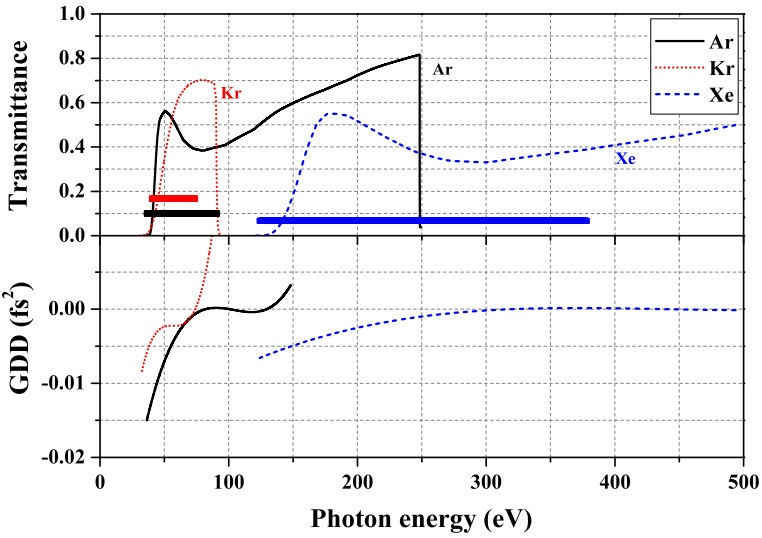

Fig. 5.7 Transmittance and GDD of candidate gaseous materials for the compensation of positive atto-chirp contained in high-harmonic pulses. The pressure and length of each medium were set to 20 Torr and 10 mm, respectively, so as to make meaningful comparison of chirp compensation characteristics. The *bar drawn under the transmittance curve* represents an available spectral region of negative GDD of each gas material

transmittance and GDD of 10-mm-long Ar gas column at a pressure of 20 Torr is shown in Fig. 5.7. The harmonics below the 26th order are strongly suppressed due to large absorption in Ar [14]. GDD is negative in the region above the 26th order in which strong harmonics are generated [23]; the compensation of the positive chirp of the harmonic pulses is obtained. It is noted that this dispersion property may adversely enhance the positive chirp for the lower order harmonics; however, it is not a serious restriction since the harmonics in this range are strongly suppressed by absorption. Other gases, such as Xe or Kr, also have negative GDD at different wavelength regions. Xe possesses negative GDD from the 90th to the 200th order. Similarly, Kr has a negative GDD region from the 25th to 50th orders. Therefore, when the dispersion characteristics of a medium are properly taken into accounts, the self-compression of attosecond harmonic pulses can occur in the harmonic generation medium itself.

A long gas cell was specially prepared for simultaneous achievement of strong harmonic generation and chirp compensation. The gas cell had a structure for differential pumping. The first and third cells were subjected to differential pumping to maintain a low gas pressure in the experimental chamber [9]. In this way the gas pressure of harmonic generation could be raised without overloading the vacuum pump. The middle gas cell was 12–mm long to achieve the compensation of the atto-chirp for the harmonics higher than the 26th order. The schematic of the experimental setup is shown in Fig. 5.8. A 30-fs kHz Ti:sapphire laser was used to generate high harmonics [24]. The laser beam was split into two parts by a beam

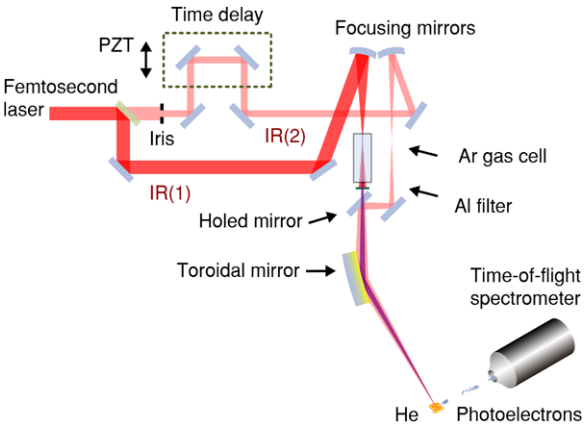

Fig. 5.8 Experimental schematics for self-compression of attosecond harmonic pulses. A 12-mm-long gas cell filled with Ar was installed for the generation and compression of harmonic pulses

splitter; the first beam was focused into the middle gas cell to obtain a sufficient intensity for HHG. The time-delayed second beam was combined with harmonics for the temporal characterization of harmonics. The laser intensity used for the harmonic generation was about 2.5×10^{14} W cm^{-2}. After harmonic generation, the transmitted laser beam was blocked by a 200-nm Al filter to completely eliminate the laser light. The harmonic and the probe beam were combined using a holed mirror and both beams were then focused together using a gold-coated toroidal mirror into a photoionization gas chamber. The generated photoelectrons were analyzed with a magnetic-bottle time-of-flight (TOF) electron spectrometer shown in Fig. 5.9 [25, 26].

We examined the atto-chirp compensation of harmonic pulses by measuring the duration of harmonic pulses. The amount of GDD in the medium depends on medium length and pressure. In our experiments, the medium length was set to 12 mm, and gas pressure was adjusted to compensate for the chirp of harmonic pulses. The temporal structure of harmonic pulses was measured using the method of reconstruction of attosecond beating by interference of two photon transitions (RABITT) [1, 4, 27]. In this method, the photoionization of He by the harmonic and time-delayed probe pulses was used to obtain the cross-correlation information between harmonic and femtosecond laser pulses. The photoelectron spectra in Fig. 5.10 clearly show the sideband signals, formed between the photoionization signals directly generated by the harmonics, when the harmonic and probe pulses were overlapped. The amplitude modulation with the time delay between the probe beam and harmonic pulses is a clear feature of the sideband signal. The spectral phase difference $\Delta\varphi_q$ between adjacent harmonics could be found by fitting the sideband amplitude modulation to the formula, $\cos(2\omega_0\tau + \varphi_{q-1} - \varphi_{q+1})$ with ω_0 being the laser frequency. In addition, the amplitude information of the harmonics was obtained from the photoelectron spectrum generated without the probe beam with the consideration of the known photoionization cross section for different harmonics [28, 29]. The photoelectron signal from He ionized by the high harmonics from Ar, while changing the gas pressure, is shown in Fig. 5.10. The waveform of

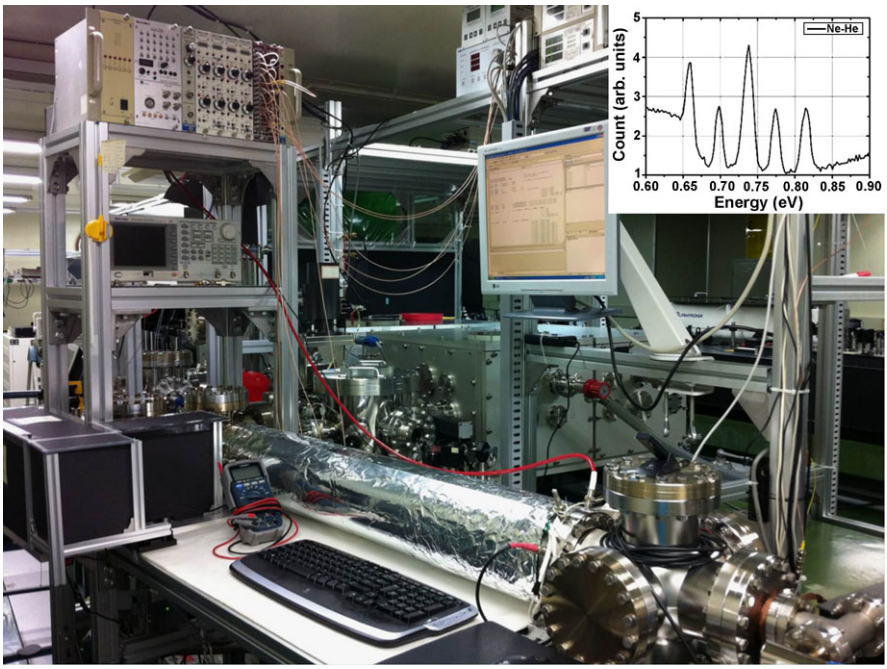

Fig. 5.9 Experimental setup with a magnetic-bottle TOF spectrometer connected to vacuum chambers for HHG. In the *inset* shows the Ne atomic emission lines, measured with the TOF spectrometer, show the energy resolution of 11 meV at the electron energy of 0.7 eV

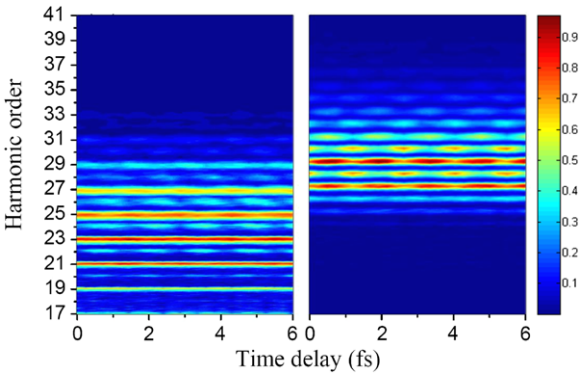

Fig. 5.10 Photoelectron spectra of He ionized by high harmonics and time-delayed infrared (IR) laser pulses. The Ar pressure in the harmonic generation cell was 15 Torr (*left*) and 40 Torr (*right*) [9]

attosecond pulse train could be reconstructed from the phase and amplitude information. It is noted that the obtained temporal structure represents that of an infinite attosecond pulse train as a natural consequence of the RABITT method that assumes a harmonic pulse with constant amplitude and phase for a given harmonic order. The spectral phase obtained still provided the necessary information on the chirp variation of harmonic pulse trains.

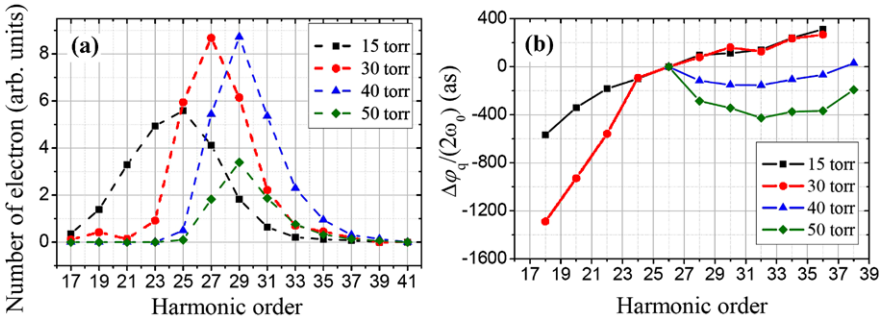

Fig. 5.11 (**a**) Measured photoelectron counts generated from He by high harmonics generated at Ar pressure of 15 Torr (*rectangles*), 30 Torr (*circles*), 40 Torr (*triangles*), and 50 Torr (*diamonds*). (**b**) Group delay $\Delta\varphi_q/2\omega_0$ measured with the RABITT method [9]

In order to extract the spectral phase information, photoelectron spectra were measured while changing the time delay between harmonic and probe laser pulses. The measurements performed with Ar pressures of 15-Torr and 40-Torr are shown in Fig. 5.11(a). The time-delay step between data points was about 200 as. The clear sideband modulation, fitted to a cosine function, was used to find the spectral phase. The measured spectral phase difference $\Delta\varphi_q$, corresponding to the group delay of the medium, between neighboring harmonics divided by $2\omega_0$ is shown in Fig. 5.11(b). Since the phase offset, or the linear spectral phase, does not affect pulse shape, it was adjusted to zero at the 26th sideband for better visualization. The positive slope of the group delay means that harmonic pulses possess positive chirp. In the 15-Torr case, the second-order spectral phase, measured by the slope of the linear fit from the 26th to the 36th, is about 0.013 fs^2. With gas density increasing up to 30 Torr, the positive chirp increases for harmonic orders below the 26th due to the positive GDD of Ar. The behavior of harmonics higher than the 26th order is still similar to that for the 15-Torr case, indicating that the single atom feature is still dominant. At the gas pressure above 40 Torr, the spectral transmittance and dispersion characteristics affected even the higher order harmonics. As seen in Fig. 5.11(b), the slope of the delay changes from negative to positive value around the 31st order, mainly due to the third-order spectral phase induced by the third-order dispersion of Ar. The second-order spectral phase, obtained by averaging the slope of the delay, is only 0.0017 fs^2 for the 40-Torr case. This shows that the intrinsic chirp of the attosecond pulses was well compensated. When the gas pressure was increased further to 50 Torr, the intrinsic chirp became over-compensated. The second-order spectral phase, estimated from Fig. 5.11(b), is -0.0057 fs^2. The intrinsic chirp was compensated too much and the attosecond pulse train became negatively chirped. In addition, the weakened photoelectron spectrum indicates that the harmonics were strongly absorbed during propagation.

From the RABITT measurements, temporal profiles of attosecond harmonic pulses were reconstructed, as shown in Fig. 5.12. The estimated pulse durations in the FWHM are 348, 295, 206, and 213 as for the 15, 30, 40, and 50-Torr cases, respectively. We obtained the shortest harmonic pulse of 206 as in the 40-Torr case.

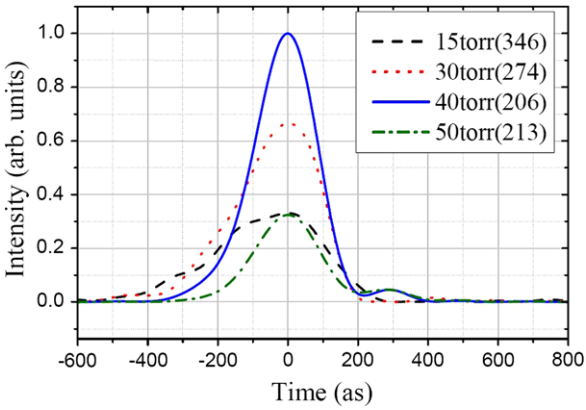

Fig. 5.12 Reconstructed attosecond pulses with respect to the pressure of Ar. The Ar pressures and the pulse durations in parentheses are given in the legend [9]

As its transform-limited duration, estimated from the harmonic signal, was 200 as, the measured pulse duration was very close to the transform limited duration, indicating a good phase locking among the harmonics. The strong advantage of chirp compensation in a gas medium can be seen from the fact that the strongest and also the shortest attosecond pulse was obtained in Ar pressure of 40 Torr. Consequently, our experimental results showed the self-compression of the harmonic pulse to the near transform-limited duration without losing its strength. Since the self-compression technique can be applied to the case of absorption-limited harmonic generation [30, 31], it allows the generation of strong, transform-limited attosecond pulses without sacrificing harmonic strength.

5.4 Generation of Sub-100-as Pulses: Experiment

In order to obtain much shorter harmonic pulses than the previous result, broadband harmonics should be produced with proper atto-chirp compensation. High harmonics with much broader bandwidth can be obtained from Ne by applying stronger laser intensity than the case of Ar harmonics. At the laser intensity of 1.5×10^{15} W cm^{-2}, the harmonic cutoff could be extended up to the 75th order. In order to deliver the broad harmonics to the interaction region, an X-ray filter, installed to block IR laser pulses, should have sufficient transmission bandwidth, for which Be, instead of Al, was chosen [14]. The transmission of Be is reasonably good from 40 to 112 eV, which is more than twice the bandwidth of Al. The broad harmonics, generated from Ne and filtered with Be, could cover more than 48 harmonic orders and, consequently, have a potential to generate attosecond pulses shorter than 50 as. The broad harmonics, however, experience the reduction of attosecond pulse duration if proper atto-chirp compensation were not implemented. Since it is not simple to find a material with negative GDD over the broad range, Ar having a large negative GDD from 38 to 60 eV was used for atto-chirp compensation, even if it cannot provide a full coverage over the Ne harmonics. The efficient chirp compensation in the low energy part of the harmonics may still contribute to short pulse formation by flattening the variation of spectral phase over a broad spectral range.

For the broad harmonic generation from Ne and the atto-chirp compensation in Ar, a two-gas-cell system was employed to separate the chirp compensation from the harmonic generation [7]. The schematics of the experimental setup are similar to the ones shown in Fig. 5.8, except the chirp compensation cell was installed after the harmonic generation cell. Strong high harmonics, from Ne driven by 30-fs pulses at 820 nm, were obtained by placing the Ne gas cell before the laser focus [19, 20], and atto-chirp compensation was achieved in the Ar gas cell. The Ar gas cell was placed after the laser focus such that no additional harmonics could be generated. The strong harmonics contributed from long trajectory components, existing in the outer part of harmonic beam, were filtered out using an aperture placed behind the Ar gas cell [32]. Harmonic spectra were measured using the magnetic-bottle TOF electron spectrometer.

Firstly, high-harmonics from Ne without chirp compensation were characterized. The measured harmonic spectrum is presented in Fig. 5.13(a), showing the harmonics from 17th to 73rd orders. These harmonics were broad enough to support a transform-limited duration of 45 as. The temporal reconstruction of harmonic pulses was carried out using the RABITT method. In this measurement the high harmonic pulse and time-delayed probe laser pulse were focused together to an effusive Ne beam, generating photoelectron spectra that consisted of harmonic and sideband signals modulated twice per optical cycle. The sideband modulation, containing the harmonic phase information, was formed due to the interference of electrons ionized through different paths. From the RABITT measurement the spectral phase of harmonic pulses was retrieved and, hence, the temporal reconstruction of attosecond harmonic pulses was made. As shown in Fig. 5.13(b), the spectral phase of Ne harmonics, presented in red squares, exhibits mainly a quadratic structure due to the inherent positive chirp of harmonic pulses. This quadratic phase structure broadened the temporal profile of harmonic pulses. The temporal profile of the uncompensated harmonic pulses in Fig. 5.14 clearly reveals these features, even showing a multi-peaked profile. The duration of the central pulse is about 160 as, which is much longer than the transform-limited value of 45 as. Consequently, the broad harmonic generation did not significantly reduce the harmonic pulse duration; it rather produced multi-peaked attosecond pulses with a broadened duration.

In order to optimize the harmonic pulse duration, atto-chirp compensation was performed in Ar. The temporal characterization of harmonic pulses was performed while changing the Ar pressure so as to find out the conditions for optimum chirp compensation. The retrieved spectral phase of the compressed harmonic pulse in Fig. 5.13(b) shows that the spectral phase variation below the 41st order was dramatically reduced because of the negative GDD of Ar in the region, as shown in Fig. 5.14. This indicates that the chirp compensation of harmonic pulses was quite effective in the low-frequency region. As a consequence, the peak intensity of the compensated case became 2.5 times stronger, even though the transmittance was reduced to half of the uncompensated case as a result of better synchronization of harmonics. The RABITT analysis showed that the formation of 63-as pulses, close to the transform-limited duration of 47 as, came from the coherent addition of the harmonics up to the 65th order. The small satellite peaks appeared mainly from the harmonics of higher orders, because they were strongly affected by the high-

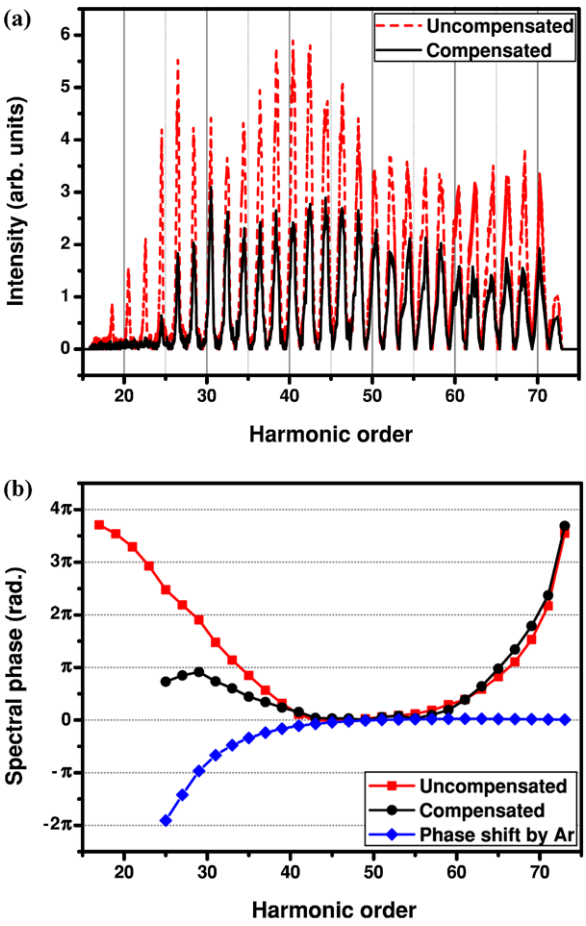

Fig. 5.13 Measured harmonic spectra and spectral phases with and without chirp compensation of harmonic pulses. (**a**) Photoelectron spectra obtained with and without atto-chirp compensation are shown as *black solid* and *red dotted lines*, respectively. The gas pressure in the Ar cell was 25 Torr for achieving transform-limited 63-as harmonic pulses. (**b**) Spectral phases measured by the RABITT method for the uncompensated (*red square*) and compensated (*black circle*) cases are presented. The spectral phase shift gained while propagating through the 9-mm cell filled with 25 Torr of Ar is also drawn for the comparison (*blue diamond*) [7]

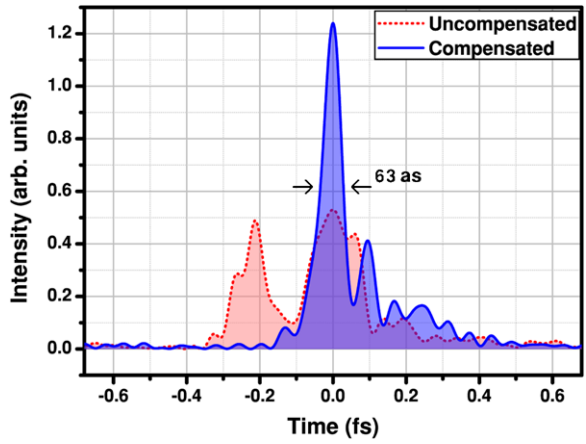

Fig. 5.14 Temporal profiles of attosecond harmonic pulses obtained with and without chirp compensation. The uncompensated harmonic pulse, represented in a *red dotted line*, has a multi-peaked profile with broadened duration. The compensated harmonic pulse, plotted as a *blue solid line*, shows a 63-as pulse, whereas the transform-limited value is 47 as [7]

frequency edge of the Be transmission window with large positive GDD. Consequently, near transform-limited 63-as harmonic pulses, corresponding to 1.2 cycles, were generated thanks to the effective atto-chirp compensation in Ar.

The generation of near transform-limited sub-100-as pulses proved well the effectiveness of atto-chirp compensation by material dispersion, especially in a gas medium. As other gases, such as Kr or Xe having negative GDD in different wavelength regions, are available, the atto-chirp compensation can be realized in a variety of wavelength regions. As it can be equally applied to the case of isolated single attosecond pulses, the atto-chirp compensation by material dispersion is a powerful and practical tool for both attosecond pulse trains and isolated attosecond pulses [33–35].

5.5 Conclusion

Comprehensive description on the chirp compensation of attosecond pulses generated from high harmonics was presented. The positive atto-chirp of harmonic pulses could be compensated in a medium with negative GDD. Though a thin metallic material can be used for the chirp compensation, we found that a gaseous medium was much better due to easy handling and control of pressure in addition to high transmission. The first demonstration of the atto-chirp in a gaseous medium was performed using the harmonic generation medium itself; the harmonic pulses produced in an Ar gas cell was self-compressed while propagating through the same medium because of the effective atto-chirp compensation in Ar, obtaining near transform-limited 206-as pulses. The self-compression of attosecond harmonic pulses showed the effectiveness of our method because the harmonic emission and the chirp compensation were accomplished in a single gas cell. Much shorter harmonic pulses could be generated by making use of the harmonics from Ne. Without atto-chirp compensation the duration of the harmonic pulses was much longer than the transform-limited value. After propagating through the second cell of Ar, we could achieve the harmonic pulses with duration of 63 as—close to the transform-limited duration of 47 as, realizing very good harmonic synchronization over the broad spectral region. For further shortening of attosecond pulse duration we proposed to apply intense laser pulses at 1600 nm. Employing the ionization gating method, we showed in our calculation that 38-as harmonic pulses could be obtained after the atto-chirp compensation in Xe. The chirp-compensated attosecond harmonic pulses will be valuable for attosecond science investigations to explore ultrafast electron dynamics, such as autoionization and Auger processes, in atoms and molecules, supporting better time-resolution than ever before.

Acknowledgements This research was supported by the Ministry of Education, Science and Technology of Korea through the National Research Foundation.

References

1. P.M. Paul, E.S. Toma, P. Breger, G. Mullot, F. Auge, Ph. Balcou, H.G. Muller, P. Agostini, Science **292**, 1689 (2001)

2. M. Hentschel, R. Kienberger, Ch. Spielmann, G.A. Reider, N. Milosevic, T. Brabec, P. Corkum, U. Heinzmann, M. Drescher, F. Krausz, Nature **414**, 509 (2001)
3. P. Antoine, A. L'Huillier, M. Lewenstein, Phys. Rev. Lett. **77**, 1234 (1996)
4. Y. Mairesse, A. de Bohan, L.J. Frasinski, H. Merdji, L.C. Dinu, P. Monchicourt, P. Breger, M. Kovacev, R. Taieb, B. Carre, H.G. Muller, P. Agostini, P. Salieres, Science **302**, 1540 (2003)
5. K.T. Kim, C.M. Kim, M.-G. Baik, G. Umesh, C.H. Nam, Phys. Rev. A **69**, 051805(R) (2004)
6. K. Varju, Y. Mairesse, P. Agostini, P. Breger, B. Carre, L.J. Frasinski, E. Gustafsson, P. Johnsson, J. Mauritsson, H. Merdji, P. Monchicourt, A. L'Huillier, P. Salieres, Phys. Rev. Lett. **95**, 243901 (2005)
7. D.H. Ko, K.T. Kim, J. Park, J. Lee, C.H. Nam, New J. Phys. **12**, 063008 (2010)
8. K.T. Kim, C.M. Kim, M.G. Baik, G. Umesh, C.H. Nam, Appl. Phys. B **79**, 563–567 (2004)
9. K.T. Kim, K.S. Kang, M.N. Park, T. Imran, G. Umesh, C.H. Nam, Phys. Rev. Lett. **99**, 223904 (2007)
10. P.B. Corkum, Phys. Rev. Lett. **71**, 1994 (1993)
11. M. Lewenstein, P. Salieres, A. L'Huillier, Phys. Rev. A **52**, 4747 (1995)
12. D.G. Lee, H.J. Shin, Y.H. Cha, K.-H. Hong, J.-H. Kim, C.H. Nam, Phys. Rev. A **63**, 021801(R) (2001)
13. P. Salieres, B. Carre, L. Le Deroff, F. Grasbon, G.G. Paulus, H. Walther, R. Kopold, W. Becker, D.B. Milosevic, A. Sanpera, M. Lewenstein, Science **292**, 902 (2001)
14. B.L. Henke, E.M. Gullikson, J.C. Davis, At. Data Nucl. Data Tables **54**, 181 (1993)
15. J.-H. Kim, C.H. Nam, Phys. Rev. A **65**, 033801 (2002)
16. H.J. Shin, D.G. Lee, Y.H. Cha, K.-H. Hong, C.H. Nam, Phys. Rev. Lett. **83**, 2544 (1999)
17. A.D. Shiner, B.E. Schmidt, C. Trallero-Herrero, H.J. Wörner, S. Patchkovskii, P.B. Corkum, J.-C. Kieffer, F. Légaré, D.M. Villeneuve, Nat. Phys. **7**, 464 (2011)
18. B.E. Schmidt, P. Bejot, M. Giguere, A.D. Shiner, C. Trallero-Herrero, E. Bission, J. Kasparian, J.-P. Wolf, D.M. Villeneuve, J.-C. Kieffer, P.B. Corkum, F. Legare, Appl. Phys. Lett. **96**, 121109 (2010)
19. H.T. Kim, I.J. Kim, D.G. Lee, K.-H. Hong, Y.S. Lee, V. Tosa, C.H. Nam, Phys. Rev. A **69**, 031805(R) (2004)
20. V. Tosa, H.T. Kim, I.J. Kim, C.H. Nam, Phys. Rev. A **71**, 063807 (2005)
21. R. Lopez-Martens et al., Phys. Rev. Lett. **94**, 033001 (2005)
22. E. Gustafsson, T. Ruchon, M. Swoboda, T. Remetter, E. Pourtal, R. Lopez-Martens, Ph. Balcou, A. L'Huiller, Opt. Lett. **32**, 1353 (2007)
23. D.G. Lee, H.T. Kim, K.H. Hong, C.H. Nam, I.W. Choi, A. Bartnik, H. Fiedorowicz, Appl. Phys. Lett. **81**, 3726 (2002)
24. J.H. Sung, J.Y. Park, T. Imran, Y.S. Lee, C.H. Nam, Appl. Phys. B **82**, 5–8 (2006)
25. P. Kruit, F.H. Read, J. Phys. E, Sci. Instrum. **16**, 313 (1983)
26. T. Tsuboi, E.Y. Xu, Y.K. Bae, K.T. Gillen, Rev. Sci. Instrum. **59**, 1357 (1988)
27. L.C. Dinu, H.G. Muller, S. Kazamias, G. Mullot, F. Auge, Ph. Balcou, P.M. Paul, M. Kovacev, P. Breger, P. Agostini, Phys. Rev. Lett. **91**, 063901 (2003)
28. J.A.R. Samson, W.C. Stolte, J. Electron Spectrosc. Relat. Phenom. **123**, 265 (2002)
29. M. Gisselbrecht, D. Descamps, C. Lynga, A. L'Huillier, C.-G. Wahlstrom, M. Meyer, Phys. Rev. Lett. **82**, 4607 (1999)
30. E. Constant, D. Garzella, P. Breger, E. Mevel, Ch. Dorrer, C. Le Blanc, F. Salin, P. Agostini, Phys. Rev. Lett. **82**, 1668 (1999)
31. M. Schnurer, Z. Cheng, M. Hentschel, G. Tempea, P. Kalman, T. Brabec, F. Krausz, Phys. Rev. Lett. **83**, 722 (1999)
32. M. Bellini, C. Lynga, A. Tozzi, M.B. Gaarde, T.W. Hansch, A. L'Huillier, C.-G. Wahlstrom, Phys. Rev. Lett. **81**, 297 (1998)
33. G. Sansone et al., Science **314**, 443 (2006)
34. E. Goulielmakis et al., Science **320**, 1614 (2008)
35. X. Feng et al., Phys. Rev. Lett. **103**, 183901 (2009)
36. D.H. Ko, K.T. Kim, C.H. Nam, J. Phys. B, At. Mol. Opt. Phys. **45**, 074015 (2012)

Chapter 6
Carrier-Envelope Phase Stabilization

Günter Steinmeyer, Bastian Borchers, and Fabian Lücking

Abstract After introducing some fundamental concepts and definitions for carrier-envelope stabilization schemes and frequency combs, measurement schemes for the carrier-envelope phase of oscillators and amplified systems are discussed. In particular, care is taken to point out typical problems in the experimental implementation of such schemes and to indicate ways to eliminate or reduce these issues. One of these potential problems is interferometer drift, another limiting factor may be shot noise in the photo detection. After this overview on detection of the carrier-envelope phase, techniques for its active stabilization are discussed. Two major approaches are addressed: the traditional feedback technique and the recently introduced feed-forward technique. Shortcomings and advantages of either technique are carefully compared and discussed. Finally, characterization methods are discussed, including example measurements that were recently obtained with the feed-forward method. These measurements indicate the smallest residual carrier-envelope phase jitter that was ever reported.

6.1 Introduction

At the end of the last millennium, ultrashort pulse generation had reached a stage where the generation of sub-10 fs pulses [1–4] started to become a routine technol-

G. Steinmeyer (✉) · B. Borchers
Max Born Institute for Nonlinear Optics and Short Pulse Spectroscopy, Max-Born-Straße 2a, 12489 Berlin, Germany
e-mail: steinmey@mbi-berlin.de

B. Borchers
e-mail: borchers@mbi-berlin.de

G. Steinmeyer
Optoelectronics Research Centre, Tampere University of Technology, Korkeakoulunkatu 3, 33720 Tampere, Finland

F. Lücking
Femtolasers Produktions GmbH, Fernkorngasse 10, 1100 Vienna, Austria
e-mail: fabian.luecking@femtolasers.com

K. Yamanouchi, K. Midorikawa (eds.), *Progress in Ultrafast Intense Laser Science*, Springer Series in Chemical Physics 104, DOI 10.1007/978-3-642-35052-8_6,

ogy, with commercial products becoming available. Comparing pulse widths of 6 fs and below [5–7] with the duration of the optical cycle, it is striking that these pulses encompass less than two oscillations of the electric field in between the full width at half maximum of their intensity envelope. However, this remarkable feat comes with a problem—in the late 90s, there was no way to measure or even control the position of the field nodes within the intensity envelope. As early measurements indicated [8], the relative phase between the electric field carrier and the intensity envelope strongly fluctuates from laser shot to laser shot. Here, we discuss methods for measuring the carrier-envelope phase (CEP) and means for its stabilization. Nowadays this long inaccessible parameter can be controlled with remarkable precision. The most recent measurements [9] indicate a residual timing jitter between carrier and envelope of less than 10 attoseconds (rms), i.e., about 0.3 % of a full optical cycle. To the best of our knowledge, this constitutes the best active synchronization ever reported. In the following, we start with giving some basic definitions and equations. We then describe various schemes for measuring the CEP. Subsequently, we discuss ways to stabilize the CEP, i.e., generate pulse trains with constant CEP.

6.2 Basic Definitions: The CEP and the Absolute Phase

Figure 6.1 depicts the field structure $E(t)$ of an ultrashort laser pulse decomposed into a field envelope $A(t)$ and a carrier oscillation of angular frequency ω_0

$$E(t) = A(t)\cos(\omega_0 t + \varphi_{\mathrm{CE}}). \tag{1}$$

Typically, $A(t)$ is chosen such that its maximum value appears at zero delay, i.e., $t = 0$. For a sufficiently long pulse duration $\tau \gg 2\pi/\omega_0$, linear propagation and nonlinear optical interaction of such pulses can be conveniently reduced to a description of the slowly-varying envelope $A(t)$. For durations below about 3 cycles, however, the slowly-varying envelope approximation breaks down, and the phase φ_{CE} between carrier and envelope starts to influence the pulse propagation and its interaction. This phase is sometimes also referred to as the "absolute phase", and it is typically defined via the temporal delay Δt between the intensity envelope maximum and the position of the closest positive field antinode, see Fig. 6.1,

$$\varphi_{\mathrm{CE}} = \Delta t\,\omega_0. \tag{2}$$

When such an optical pulse propagates through a medium with refractive index n and length L, its Fourier components experience a phase shift

$$\varphi(\omega) = -k(\omega)L = -\frac{n(\omega)\omega L}{c}, \tag{3}$$

where k is the wave number and c the speed of light. From the fundamental definitions of phase velocity $v_\varphi = \omega/k$ and group velocity $v_\mathrm{g} = \mathrm{d}\omega/\mathrm{d}k$ one finds that

$$\frac{1}{v_\mathrm{g}} = -\frac{\frac{\mathrm{d}n(\omega)}{\mathrm{d}\omega}\omega + n(\omega)}{c} = \frac{1}{v_\varphi} + \frac{\mathrm{d}n(\omega)}{\mathrm{d}\omega}\frac{\omega}{c}. \tag{4}$$

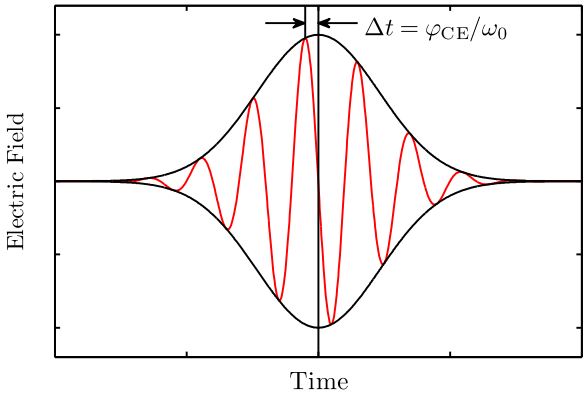

Fig. 6.1 A few-cycle laser pulse as a product of the carrier wave oscillating with the angular frequency ω_0 and the envelope $A(t)$. The time delay Δt between the envelope maximum and the closest positive field peak defines the carrier-envelope phase φ_{CE}

Typically, the difference between group and phase velocity is rather small, however, it is the offset term in Eq. (4) that affects the carrier-envelope phase φ_{CE} in a dispersive medium. As the envelope travels with the velocity v_g while the carrier propagates at v_φ, the CEP experiences a shift

$$\Delta\varphi = -\omega L\left(\frac{1}{v_g} - \frac{1}{v_\varphi}\right) = L\frac{\omega^2}{c}\frac{\mathrm{d}n(\omega)}{\mathrm{d}\omega} \tag{5}$$

upon propagation through a linear optical medium with length L and refractive index $n(\omega)$. If we consider the optical components inside a typical Ti:sapphire laser cavity [5], the crystal alone contributes a phase shift of several hundred cycles with additional contributions from mirror dispersion and the intracavity air. Moreover, geometrical dispersion, i.e., a spectrally dependent path length, may add to the total $\Delta\varphi$ if elements such as prism compressors are used. These contributions may be treated analogously by introducing a spectrally dependent $L(\omega)$ in Eq. (3). As a phase shift of 2π and integer multiples thereof do not change the actual field structure of the pulse, it is useful to eliminate full optical cycles from $\Delta\varphi$ and define the relative carrier-envelope phase as [10]

$$\Delta\varphi_{CE} = \Delta\varphi \bmod 2\pi. \tag{6}$$

It is important to understand the difference between the absolute carrier-envelope phase φ_{CE} and the phase change $\Delta\varphi_{CE}$ upon propagation through a medium with length L. If a laser pulse propagates through a cavity, it will experience a phase shift $\Delta\varphi_{CE}$ for each cavity roundtrip, giving rise to a phase slippage rate

$$f_{CE} = \frac{\Delta\varphi_{CE}}{2\pi T_R} = \frac{\Delta\varphi_{CE}}{2\pi} f_{rep}, \tag{7}$$

where T_R is the round trip time, $f_{rep} = c/2L_{cav}$ the laser repetition rate and L_{cav} the cavity length of the resonator. The frequency f_{CE} is also called the carrier-envelope offset frequency or comb offset, and it is most suitably discussed in the spectral domain. Fourier transforming an equidistant pulse train with group delay $1/f_{rep}$ and a pulse-to-pulse CE phase change $\Delta\varphi_{CE}$ gives rise to an equidistant frequency comb

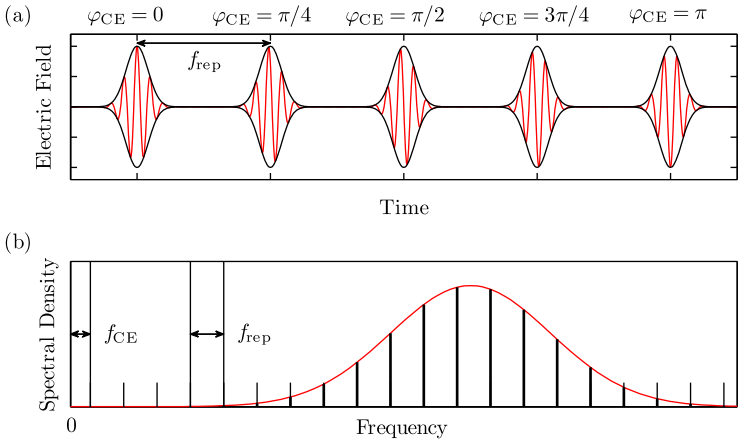

Fig. 6.2 Train of few-cycle pulses in the (**a**) time domain and (**b**) spectral domain. The slippage rate of the CE phase corresponds to a common offset of the frequency comb modes

with comb lines spaced by f_{rep} and a common offset of f_{CE}, see Fig. 6.2. Spectral content may therefore only appear at discrete positions in the spectrum given by

$$f_i = f_{CE} + i f_{rep}. \tag{8}$$

A frequency comb can therefore act like a ruler for frequencies [11, 12]. From knowledge of f_{rep} and f_{CE}, an unknown frequency f_x can be determined by its beat frequency with the comb Δf according to

$$f_x = f_{CE} + i f_{rep} \pm \Delta f. \tag{9}$$

This way, a frequency of many hundred THz can be made countable, as it is referred back to the frequency counting of three radio frequency signals. Within the last decade, frequency combs have therefore become a standard tool in frequency metrology obviating the need for the costly and very complex frequency chains [13] that were formerly used.

6.3 Concepts for CEP Measurement

6.3.1 CEP Measurement of an Oscillator

Many different methods have been proposed for measuring the pulse-to-pulse CE phase slip $\Delta\varphi_{CE}$ in an oscillator. The earliest approach relied on an interferometric cross-correlation between two subsequent pulses in the pulse train [8]. While this method requires long interferometer arms and a nonlinear optical effect for generating the correlation signal, it can be shown that linear interferometry is completely sufficient for such a phase comparison [14, 15]. All these methods inherently rely on

the stability of a delay line with length $2L$ or integer multiples thereof. Using active interferometric stabilization of the delay, such direct methods are able to determine $\Delta\varphi_{\mathrm{CE}}$ with a precision of a few ten milliradians [15]. It is straightforward to see from Eq. (7) that methods based on interferometric correlation can reach only about single MHz precision of the CE frequency.

The generation of pulse trains with stabilized CE phase has therefore relied nearly exclusively on radio frequency heterodyne detection schemes that have first been discussed by Telle *et al.* [10]. The basic idea behind these schemes is heterodyning two different harmonics of the laser pulses to directly access the carrier-envelope offset frequency. For example, it is readily seen from squaring the rhs of Eq. (1) that the second harmonic $E_{\mathrm{SH}} = \chi^{(2)} E^2$ contains oscillatory components at double the input frequency and phase [16], i.e., a $\cos(2\omega_0 t + 2\varphi_{\mathrm{CE}})$ term. As a second harmonic pulse displays double the absolute phase of the fundamental, the carrier-envelope phase drift in the pulse train is doubled, too. For the general case of the Nth harmonic comb, this gives rise to the following representation

$$f_i^{(N)} = N f_{\mathrm{CE}} + i f_{\mathrm{rep}}. \tag{10}$$

Note that the mode spacing is not affected by the nonlinear process, as it is just defined by the repetition rate of the laser. If this harmonic comb contains spectral content that overlaps with the fundamental or another harmonic frequency comb of order M, heterodyning these two combs yields the beat signal

$$f_i^{(N)} - f_j^{(M)} = N f_{\mathrm{CE}} - M f_{\mathrm{CE}} + (i - j) f_{\mathrm{rep}}. \tag{11}$$

The spectral overlap ensures that one can find several mode pairs with $i = j$, and the rf heterodyne signal generated by a simple photo diode contains a frequency component directly at the CE frequency for $N = 2$ and $M = 1$. Additionally, however, the beat signal will also contain a signal at the mirror frequencies, e.g., $f_{\mathrm{rep}} - f_{\mathrm{CE}}$ for $M = 2$ and $N = 1$. Typically, one can only distinguish the two beat signals by the introduction of material dispersion into the cavity: while observing the beat note the real CE frequency increases with additional material, whereas the mirror frequency is decreasing. Note that in contrast to the correlation-based interferometric schemes described above, the phase of the beat signal generated by rf heterodyning is directly linked to the carrier-envelope phase φ_{CE}, whereas the former schemes are only capable of detecting the pulse-to-pulse CE phase $\Delta\varphi_{\mathrm{CE}}$. However, the true value of the CEP is not retrievable from the phase of the rf beat as the interferometer introduces an unknown contribution to the phase of the beat signal.

The scheme of heterodyning even and odd harmonics as described above is frequently used in two different variants. The most straightforward case is certainly heterodyning of the fundamental and the second harmonic, see Fig. 6.3. This case is typically referred to as f-to-$2f$ interferometry, or shorter f-$2f$ interferometry. A second and probably less obvious method is difference-frequency generation between different parts of one and the same frequency comb, which formally corresponds to setting $N = 1$ and $M = 0$ in Eq. (11). Difference-frequency generation gives rise to a frequency comb with vanishing offset, see Fig. 6.4. If the generated difference frequencies overlap with the infrared tail of the fundamental spectrum,

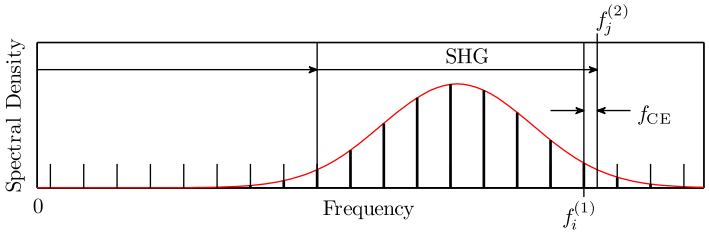

Fig. 6.3 Measurement of the CE frequency by f-$2f$ interferometry. The second harmonic of a mode from the infrared tail of the frequency comb $f_j^{(2)}$ is compared to a fundamental mode $f_i^{(1)}$. For adjacent modes ($i = j$) the beating frequency equals the offset of the fundamental comb f_{CE}

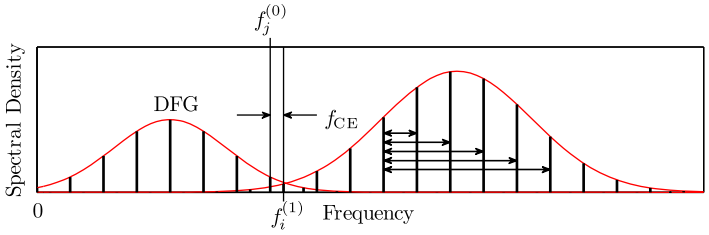

Fig. 6.4 Measurement of the CE frequency by 0-f interferometry. Difference frequency generation (DFG) between different parts of the fundamental comb creates a comb with vanishing offset. The spectral interference in the overlap of these two combs gives rise to a beat signal at f_{CE}

this method can also be used to generate a beat signal at the carrier-envelope offset frequency f_{CE}. The difference-frequency-based method is called 0-f interferometry. Compared to f-$2f$ interferometry, it is usually implemented in a monolithic device, where spectral broadening and difference frequency generation takes place in one and the same crystal [17]. While f-$2f$ interferometry measures the beat note at the short wavelength edge of the spectrum, 0-f interferometry uses a detector at the infrared edge. Nevertheless, both commonly used methods underlie the same constraint: they both require at least one octave of spectral coverage of the frequency comb. This clearly sets them apart from the initially mentioned correlation based interferometric methods, which basically work at arbitrary bandwidths [15].

Before further discussing interferometer topologies and their features, let us briefly consider the situation of measuring the CEP of amplified pulses.

6.3.2 CEP Measurement of Amplified Pulses

In the case of amplified pulses, the heterodyne method can often not be used as the repetition rates of amplified lasers are usually on the order of 1 kHz or even below, which excludes all rf methods. Therefore, these measurements are typically done by spectral interferometry [18–20]. For this method, two pulses of different harmonics

with non-vanishing delay are analyzed in a spectrometer. Let us now consider a delayed superposition of the second harmonic field $\tilde{E}^{(\mathrm{SH})}$ and the fundamental field $\tilde{E}$ in the spectral domain, i.e., we restrict ourselves to the case of f-$2f$ interferometry. At a given frequency ω in the area of spectral overlap of the two different harmonics we yield

$$\begin{aligned}\tilde{I}(\omega) &\propto \left|\tilde{E}(\omega)+\tilde{E}^{(\mathrm{SH})}(\omega)\right|^2 \\ &= \left|\exp(i\varphi_{\mathrm{CE}})\tilde{A}(\omega)+\gamma\exp(i\omega\tau_{\mathrm{D}}+2i\varphi_{\mathrm{CE}})\tilde{A}^{(\mathrm{SH})}(\omega)\right|^2 \\ &= \left|\tilde{A}(\omega)\right|^2+\gamma^2\left|\tilde{A}^{(\mathrm{SH})}(\omega)\right|^2+2\gamma\left|\tilde{A}(\omega)\tilde{A}^{(\mathrm{SH})}(\omega)\right| \\ &\quad\times\cos(\omega\tau_{\mathrm{D}}+\varphi_{\mathrm{CE}}+\pi/2),\end{aligned} \tag{12}$$

where τ_{D} is the delay between the two pulses and γ contains the susceptibility and a phase factor. In the following, we will focus our interpretation on the cosine term in Eq. (12). This term gives rise to a spectral interference pattern if τ_{D} is chosen a nonzero value. In principle, detection of the position of the spectral fringes should allow for the determination of the absolute phase φ_{CE}. Dispersive effects, however, will typically prevent a direct determination of the absolute phase using spectral interferometry. Still this method allows monitoring shot-to-shot changes of φ_{CE}, as has been described in [19, 20]. Equation (12) therefore holds the key for single-shot measurement of $\Delta\varphi_{\mathrm{CE}}$ in amplified laser systems.

We note that there is a variety of alternative methods for measurement of the CEP of amplified systems [21–23], which are somewhat out of the scope of this chapter. In particular, the method developed by G. Paulus appears promising as it enables phase detection at comparable sensitivity as f-$2f$ interferometry [22]. Paulus' method is based on an absolute phase dependence of the ionization probability in above-threshold ionization (ATI). Comparing the ion yield along the two possible orientations of the oscillating electric field of a linearly polarized laser pulse then provides information on the CEP. As this method employs two detectors for the ion yield, it is called "stereo ATI". Moreover, other nonlinear optical effects that showed a characteristic absolute phase dependence [24, 25] also appear interesting for building detectors for the absolute phase.

6.4 Practical CEP Detection Set-ups

6.4.1 CEP Detection of Oscillator Pulse Trains

Let us now shift the focus on practical issues that may arise when generating the beat signal. Ideally, if the laser possesses an octave-spanning spectrum, it is only required to focus the beam onto a sufficiently thin nonlinear optical crystal, isolate the spectral components that correspond to the different harmonics, and detect them with a photo diode. Now there are two frequent problems. First, the spectral bandwidth may be insufficient, and spectral broadening may be required prior to the

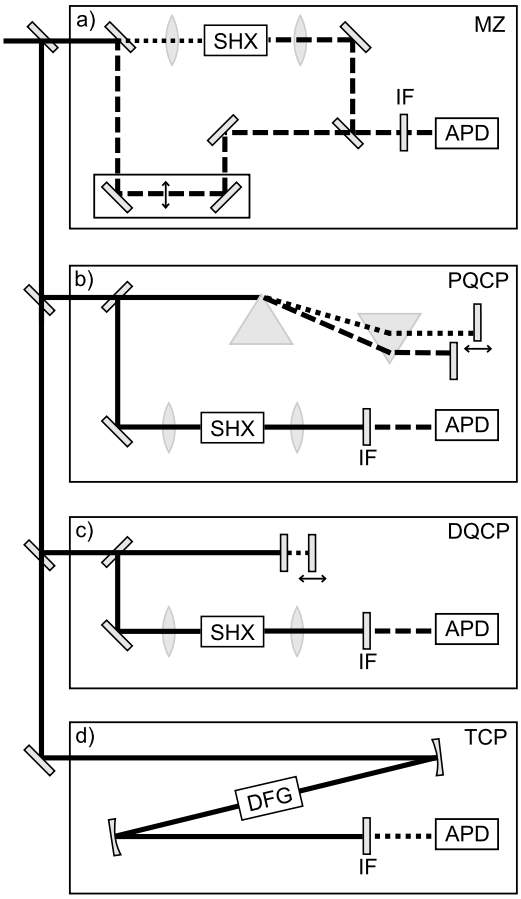

Fig. 6.5 Four different interferometer designs. (**a**) Mach-Zehnder (MZ) interferometer with long unshared beam path between fundamental and frequency-doubled components. The *dashed* and *dotted lines* correspond to the visible and the infrared components, respectively. (**b**) Prism-based quasi-common-path (PQCP) interferometer with a shorter unshared beam path and angular dispersion. (**c**) Dichroic quasi-common-path (DQCP) interferometer with even shorter unshared beam path and no angular dispersion. (**d**) Monolithic true-common-path (TCP) interferometer based on difference frequency generation (DFG) with detection in the infrared. No group delay compensation is necessary. *APD*, avalanche photo diode; *SHX*, second harmonic generation crystal; *IF*, interference filter

beat signal generation. Second, due to group delay dispersion either in the spectral broadening or in the nonlinear process used for beat signal generation, a significant delay between the two harmonics appears. In mild cases, this causes a reduction of the f_{CE} beat signal; in more severe cases, e.g., when a long piece of photonic crystal fiber [26] is used for spectral broadening, no beat signal can be observed at all without compensation of the temporal delay. To this end, an interferometer-like setup with unbalanced arm length is used. In literature, many different set-ups have been described. Most frequently the authors used either a Mach-Zehnder like set-up [27] or a Michelson interferometer [28], see Fig. 6.5(a). A possible problem with either of these interferometers is their large uncommon path length, which renders them very susceptible to noise sources such as acoustic noise, air streaks, and thermal noise. These interferometers may therefore exhibit a significant phase drift over time [29]. Generally, the design of such interferometers should take this into account by minimizing the unshared path of the different harmonics to the extent possible. One commonly used set-up [30] has been inspired by the prism compres-

sor [31] for dispersion compensation. It uses a split end mirror for compensating the delay between the fundamental and the second harmonic that have been spatially separated in a prism sequence, see Fig. 6.5(b). With this design, the unshared path can be limited to a few centimeters, which certainly results in lower interferometer noise. However, some additional noise can be expected from angular dispersion in the prism sequence which translates beam-pointing instabilities into phase noise [32]. One can estimate from the coupling strength determined for prism-based oscillators that even tiny angular deviations on the order of 1 μrad can induce phase errors of ≈10 mrad. Apart from this prism-based quasi-common-path interferometer (PQCP) the delay tuning can be realized with a combination of a dichroic and a highly reflecting mirror [Fig. 6.5(c)], somewhat similar to a Gires-Tournois interferometer [33]. This dichroic quasi-common-path interferometer (DQCP) limits the unshared path to ≈1 mm and is furthermore immune against beam-pointing instabilities as no angular dispersion is introduced. The latter two set-ups typically reduce the problem of interferometer drift to a negligible level. In a strict sense of speaking, however, they are not true common-path interferometers as they are commonly used in spectral interferometry set-ups [20]. The only true common-path interferometers are therefore the monolithic 0-f interferometer [17], see Fig. 6.5(d), or direct frequency doubling in a suitable nonlinear optical crystal [34], which requires no group delay compensation. The superior long term performance of true common-path interferometers with respect to drifts and noise has recently been demonstrated [35].

6.4.2 *Shot-to-Shot Detection of the CEP of Amplified Pulses Using Analog Processing*

We now discuss an interferometric set-up that is capable of CEP measurements at laser systems having low repetition rates. This scheme relies on spectral interferometry, as previously discussed in Sect. 6.3.2. Let us repeat the conclusion from Eq. (12), i.e., that the spectrum of a delayed superposition of a pulse and its second harmonic in the spectrally overlapping region gives rise to a modulation at a period given by the very time delay between those pulses. In particular, the position of the resulting spectral fringes is defined by the CEP. In contrast to f-$2f$ interferometers as used for oscillators, the interferometer described here can be readily implemented in a collinear fashion as the delay between the fundamental and frequency doubled components does not have to be compensated. In fact, some additional dispersive elements may actually serve to tune the spectral fringe density to a value beneficial for subsequent analysis. Other than with oscillators, the supercontinuum is usually generated by self-phase modulation in a sapphire plate [36]. The critical part of this set-up is certainly the detection of the fringe position giving access to the CEP. Most frequently, this is accomplished by digitally acquiring the spectral power density in the output plane of a spectrometer, e.g., using a CCD line-scan camera. Based on this data, it is quite straightforward to extract the CEP by Fourier filtering techniques [37]. Essentially, these computations can be reduced to two scalar

multiplications with pre-computed sinusoids, provided that the fringe frequency is nearly constant. Such numerical implementations even outperform fastest Fourier transforms [38], requiring below millisecond actual computation time on modern processor platforms. Nevertheless, latencies in the >10 ms range [39] render such optimizations futile, limiting computer-controlled servo loops to 10 Hertz reaction bandwidths at best.

Nevertheless, the ability to perform real-time shot-to-shot measurements is a very demanding task that goes beyond computational problems. Quite generally, constraints are imposed by detection shot noise rather than by the capabilities to process data [40, 41]. As the total number of photons generated in the region of spectral overlap in the sapphire plate is limited, the shot noise at the individual pixels of the CCD typically dominates the measured signal, thwarting an accurate detection of the fringe position. To compensate this effect, measurements at kHz systems are often averaged over ten or more laser shots. This raises an important question. If the residual CEP noise in an amplified system is actually white, i.e., of stochastic shot-to-shot nature, ten-shot averaging would underestimate the real shot-to-shot jitter by a factor of $\sqrt{10}$. For example, a frequently reported ≈200 mrad jitter would actually translate into 600 mrad of real shot-to-shot jitter, i.e., a value that challenges the very sensibility of the stabilization. However, if the underlying noise is not white but dominated by $1/f$ noise, ten-shot averaging may not corrupt the total phase noise balance by much. Ultimately, the question is whether white-noise contributions from the kHz pump laser dominate or whether residual phase noise from the seed laser prevails.

The only way to increase the detectivity is an optimization of the processes involved, e.g., the yield of the supercontinuum generation or the signal-to-noise ratio of the photodetection process. To this end, we employed a completely different analog detection scheme, which avoids any kind of latency, see Fig. 6.6. Moreover, as our detection front end is based on two highly efficient photomultipliers rather than CCD cameras performing poorly in the visible spectral region, we also decrease shot noise limitations. In this scheme, the temporal delay is tuned in a way to exactly map one spectral fringe onto the exit slit of a spectrometer. A metal wedge placed at the center of the slit separates the beam into a left and a right part and deflects each part onto an individual photomultiplier. The resulting two detection channels are further processed with boxcar integrators and subtracted from each other. The difference signal is a direct measure for the position of the fringe and can further be used for feedback stabilization. Given its improved detectivity, this all-analog scheme is much better suited for shot-to-shot measurements and is less corrupted by shot noise. Based on this scheme, superior stabilization performance of 210 mrad residual phase noise was demonstrated [40]. At first sight, this may not appear superior to many other numbers published (see, e.g., [42, 43]), but considering that the latter numbers were acquired through ten-shot averaging, the residual shot-to-shot jitter in [40] cannot directly be compared. Assuming a Gaussian phase noise distribution, ten-shot averaging reduces the measured noise by a factor $\sqrt{10}$. In fact, many previous reports on residual phase noise of about 200 mrad may therefore translate into shot-to-shot jitters of some 600 mrad.

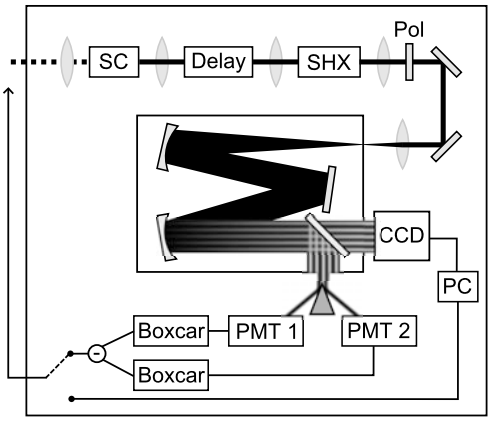

Fig. 6.6 Collinear spectral f-$2f$ interferometer including two different types of CEP detection. The supercontinuum (SC) generated in a sapphire plate passes a dispersive delay element and is focused into the second harmonic generation crystal (SHX). The analysis of the spectral fringes is done at the output of a spectrometer. The position of the fringes can be determined either digitally with a CCD linescan camera or using analog detection with a reflecting metal wedge and two photomultipliers (PMT) and two boxcar integrators

6.5 Stabilization

The generation of pulse trains with constant CEP either requires active stabilization or passive schemes [16] that generate such trains according to Eq. (10) in optical parametric amplifiers. At first sight, it appears appealing to generate zero-offset combs with the passive scheme, as this method should intrinsically ensure pulse trains with constant CEP. However, many experimental evaluations found non-ideal residual CEP noise jitters >200 mrad [44, 45] of this approach, which is most likely explained by amplitude-to-phase coupling [32] in the nonlinear optical crystals used. In particular, these crystals also exhibit self-phase modulation, and similar to the situation in Ti:sapphire lasers, amplitude fluctuations couple into CEP fluctuations. Therefore passive stabilization schemes have often been found to exhibit several hundred milliradians of residual phase jitter, when carefully analyzed in out-of-loop characterization schemes.

In the following, we therefore focus on active stabilization schemes and point out their limitations, which are actually less restrictive than in the passive schemes. Essentially, two active methods have emerged, one of which actively adjusts a laser parameter in order to control the phase and group delay inside the oscillator cavity in a feedback approach [37]. The alternative approach of feed-forward stabilization [46] places a correction device after the oscillator, but leaves the oscillator completely untouched.

6.5.1 Feedback Stabilization

The standard way of stabilizing the CEP of a pulse train requires feedback to the laser oscillator, adjusting the timing difference between the group delay and the phase delay inside the cavity. Several ways have been discussed to exert this feedback upon the laser. The most straightforward method is certainly the introduction of material dispersion into the cavity, e.g., by adjustable wedge prisms [47]. Another method is tilting of the end mirrors in a prism compressor section of the oscillator cavity [48]. Both of these approaches are fairly unpractical, as they require mechanical acceleration of optical components, limiting the feedback to a few kHz bandwidth. Even though such schemes have been demonstrated to work, they obviously require extremely low-noise pump lasers for reliable operation [49]. It has proven more practical to exploit the nonlinear phase shift present in the cavity due to the $\chi^{(3)}$-nonlinearity of the laser crystal [50], which renders the pulse-to-pulse CE phase $\Delta\varphi_{\mathrm{CE}}$ power-dependent. By electro-optic or acousto-optic modulation of the pump laser power, $\Delta\varphi_{\mathrm{CE}}$ can be controlled with higher modulation bandwidth, increasing the reliability of this stabilization scheme. Modulation bandwidths of several 10 kHz have been demonstrated [51]. Such advanced implementations reduce the requirements on the pump laser noise, albeit a laser operating on a single longitudinal mode is typically still needed.

The general scheme for feedback stabilization is depicted in Fig. 6.7. Essentially, this scheme is a phase-locked loop, deriving an error signal from a phase comparison between the CE frequency and a reference signal. Technically, the phase comparison is either performed in a simple analog double-balanced mixer or in a digital scheme [52]. The latter has the advantage of a much higher capture range, which may amount to 128π in commercial products. Nevertheless, the large capture range comes at the price of a reduced sensitivity. In the simple analog scheme, e.g., a π phase capture range is ideally mapped onto a ± 5 V voltage range, which is then further processed in subsequent electronics. For the digital scheme, however, a 128 times larger range is mapped onto the same voltage range. In the latter case, a 1 mV noise corresponds to 80 mrad, whereas direct analog processing enables much tighter servo loops, with 1 mV residual electronic noise corresponding to sub-mrad phase noise levels. These numbers have to be compared with shot-noise equivalents of several ten mrad, which are typically obtained in oscillator stabilization schemes.

In a second step, the generated error voltage is processed by the servo loop electronics, which is essentially a proportional-integral-derivative (PID) controller. Any deviation of the measured CEP from the reference signal is then fed back onto the laser by one of the previously mentioned mechanisms to eliminate the measured deviations. Regardless of what method is used for feedback, the servo loop performance is always limited by the loop bandwidth. Limitations may arise both from the PID controller itself and from the actuator. For CEP stabilization, the actuator has proven to be the more problematic component, limiting the servo loop action to a few 10 kHz at best. In the ideal case, the servo loop gain has to be adjusted such that less than unity gain is obtained for a loop phase shift of π, i.e., a situation where negative feedback as required for maintaining the servo loop is converted into

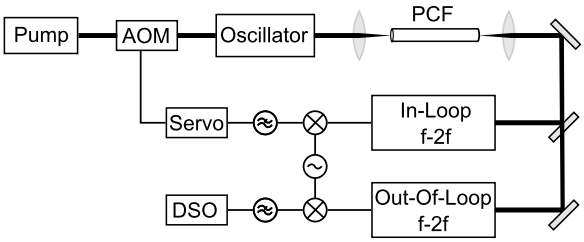

Fig. 6.7 Scheme of a feedback stabilization setup including residual noise characterization. After spectral broadening in a photonic crystal fiber (PCF), the CEP is measured in an in-loop interferometer and compared to a reference oscillator (Ref) using a double-balanced mixer. In order to close the feedback loop, the signal is first filtered and further processed in a servo, the output of which is then fed back to the laser. Adjustment of the pump power with an acousto-optical modulator (AOM) serves as the actuating mechanism. Noise characterization is achieved with an out-of-loop interferometer, mixing the stabilized beat signal and the same reference signal. The error signal is measured with a digital sampling oscilloscope (DSO)

positive feedback, causing self-oscillation and instability of the stabilization scheme [53]. While careful optimization may bring the performance close to the theoretical limit [51], practically most schemes only reach servo bandwidths that are an order of magnitude below the theoretical capabilities of the actuating element. Moreover, once locking is lost, feedback schemes will not easily reinitiate locking themselves. Even with a mechanism that automatically adjusts the system to re-lock, the pulse trains before and after the unlocked period will have no determined CEP relation. Especially in experiments demanding a long integration time, such a locking failure my thwart an entire measurement.

Many efforts went into optimization of feedback schemes. Critical evaluation of such a scheme necessarily requires independent characterization of the obtained performance in a second out-of-loop interferometer, see Sect. 6.6. The best reported performance of feedback schemes amounts to 77 mrad (rms, 2.5 mHz–10 MHz), which translates into a residual timing jitter of 33 attoseconds between carrier and envelope of the pulses [54]. This is on the order of the shortest duration of attosecond pulses generated to date [55].

6.5.2 Feed-Forward Stabilization

While the feedback approach found widespread application, in particular in the attosecond physics community, the method has some drawbacks which sometimes make its application very challenging. One disadvantage is the fact that the feedback method cannot easily be used to generate a pulse train with exactly identical electric field structure $E(t)$ in every pulse. While introduction of an acousto-optic frequency shifter into one of the interferometer arms has been demonstrated to remove this constraint [27, 56], such measures reduce the sensitivity of the set-up and

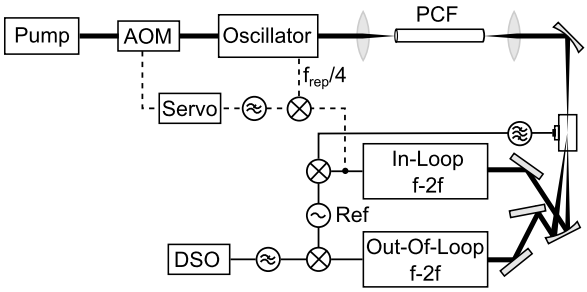

Fig. 6.8 Feed-forward stabilization setup, including residual noise characterization. The supercontinuum generated in the photonic crystal fiber (PCF) is focused into an acousto-optical frequency shifter (AOFS). The diffraction efficiency is optimized for the first order. The unaffected zeroth diffraction order can be used for the in-loop measurement. After filtering, the rf beat signal can be directly fed into the AOFS to generate a frequency comb in the first diffraction order. This comb is downshifted to zero offset. For the purpose of a sensitive out-of-loop characterization, however, the comb is shifted out of the baseband with a reference oscillator (Ref). Phase comparison of the out-of-loop measurement to this reference reveals the residual phase noise. Optionally, an additional feedback loop (*dashed lines*) can be applied to remove residual drift of the oscillator f_{CE} if the passive stability is insufficient

additionally increase its complexity. A second problematic issue is the feedback into the oscillator. As there exists no fast and simultaneously side-effect free feedback mechanism, it is particularly difficult to maintain the CEP lock for periods of hours or days. Moreover, once the CEP lock is lost, it usually requires manual interaction to re-establish the lock. Therefore, servo electronics are often designed with a large phase capture range, such that even major disturbances must not cause a drop-out of the servo. This, however, comes at a price of a relatively low sensitivity. Practical implementations of the feedback approach thus certainly deliver less-than-ideal short-term noise performance.

To overcome this limiting trade-off between reliable long-term performance and favorable phase noise performance of the feedback approach, an alternative method was recently demonstrated [57]. It relies on a feed-forward concept, using an extracavity acousto-optic frequency shifter (AOFS) to correct the CEP of the laser output. No intrusion into the laser oscillator is required, and the acousto-optic element ensures a large bandwidth of at least several 100 kHz. The working principle of this method is depicted in Fig. 6.8. The CE frequency is measured by standard means, either in an f-$2f$ interferometer or in the 0-f variant. The rf beat signal is then filtered, amplified, and directly fed forward to the acousto-optic frequency shifter that is placed directly in the output of the laser oscillator. Provided that the correct mirror frequency is utilized, the comb from Eq. (8) is then shifted exactly by f_{CE}, causing a comb with vanishing offset in the first diffraction order out of the AOFS.

The bandwidth of the feed-forward method is essentially only limited by the travel time of the acoustic wave from the actuator to the interaction zone with the optical beam. Minimizing the distance between optical beam and actuator, travel times on the order of 1 μs can be achieved, which translates into a bandwidth of the

method of 0.5 MHz. Such values exceed the best reported bandwidths [58] of feedback systems and are clearly sufficient to eliminate all conceivable laser dynamics up to the typical Q-switching frequencies of solid-state lasers. The effectiveness of the feed-forward method is also proven by the remarkably low residual phase jitters that have been reported in [9, 35, 57]. These jitters correspond to timing differences between carrier and envelope of less than 10 attoseconds. Again, this is about a factor four better than residual timing jitters that were reported for feedback systems.

Keeping in mind the current trend of up-scaling the repetition rate of few-cycle pulse sources, feed-forward stabilization provides another important advantage because it does not require the source to be a soliton mode-locked oscillator, as opposed to the feed-back approach which relies on controlling the phase slip per roundtrip. In fact, the source does not even have to be an oscillator. As long as its carrier-envelope frequency is measurable, any source can be CEP-stabilized using the feed-forward method. For example, the source could be an externally compressed thin-disk laser [59] or an OPCPA chain seeded by supercontinuum generation [60]. As either of these approaches relies entirely on diode-pumped lasers such as Yb:YAG, it is easily scalable in output energy or repetition rate. However, CEP stabilization of such systems was out of reach prior to the invention of feed-forward stabilization.

It has to be mentioned that the feed-forward approach removes some of the major caveats of the feedback approach, but also introduces some problems of its own. One of the potential issues is the angular dispersion of the beam in the first diffraction order of the AOFS. As the acoustic wave creates an index grating, the Bragg angle depends on the optical wavelength. To first order, this unwanted dependence can be compensated by a prism in the deflected beam. Using a fused silica AOFS at 85 MHz center frequency, e.g., a BK7 prism with 18° apex angle was found to provide suitable compensation of angular dispersion for a near-octave spanning spectrum centered at 800 nm [35]. Moreover, the Bragg angle of the AOFS does not only depend on the optical wavelength but also on the driver frequency, an effect that is used for beam steering in acousto-optic deflectors. Therefore, care has to be taken that f_{CE} stays in the vicinity of the center frequency of the AOFS. On short time scales up to a few minutes, this is easy to fulfill and can be accomplished by acoustic and environmental isolation of the laser oscillator itself. Typically such passive measures suffice to keep the CE frequency within a 100 kHz range around the center frequency. As the phase of the acoustical wave at the center of the interaction zone is directly affecting the phase of the diffracted order, one can calculate [9] that such a jitter corresponds to a CEP shift of about ± 150 mrad (rms), and the measurements in [57] clearly indicate that residual jitters of about 30 mrad can be obtained in laser systems without active stabilization of f_{CE}. Measurements with additional feedback stabilization lead to further reduction of the noise to about 20 mrad, which constitutes the best phase jitter ever reported in CEP stabilization [9]. Provided sufficient passive stability of the system, the additional servo loop can be quite slow, requiring a control bandwidth of much less than a Hertz. This enables mechanical solutions or even thermal or pressure control to be utilized as the actuating mechanism inside the laser oscillator.

6.6 Carrier-Envelope Phase Noise Characterization

In order to evaluate the quality of a CEP lock, it is important to measure the residual phase noise of the set-up [61, 62]. Typically, an rms value $\delta\varphi_{\mathrm{CE}}(f_1, f_2)$ is given for this quantity, and it is related to the spectral phase noise density $\sigma_{\varphi_{\mathrm{CE}}}(f)$ via

$$\delta\varphi_{\mathrm{CE}}(f_1, f_2) = \sqrt{2\int_{f_1}^{f_2} \sigma^2_{\varphi_{\mathrm{CE}}}(f)\,\mathrm{d}f}, \tag{13}$$

where f_1 and f_2 are the frequency limits of the underlying measurement. Typically, the higher frequency f_2 is dictated by the sampling rate of the measurement and f_1 by the inverse duration of the measurement. It is quite customary to derive estimates for $\delta\varphi_{\mathrm{CE}}$ from in-loop measurements, i.e., via measured voltage noise densities $\sigma_{U_{\mathrm{servo}}}(f)$ of the servo signal. For a known proportionality factor

$$\kappa = \frac{\mathrm{d}f_{\mathrm{CEO}}}{\mathrm{d}U_{\mathrm{servo}}} \tag{14}$$

one can then directly compute

$$\delta\varphi_{\mathrm{CE}}(f_1, f_2) = \sqrt{2\int_{f_1}^{f_2} \frac{\kappa^2}{f^2}\sigma^2_{U_{\mathrm{servo}}}(f)\,\mathrm{d}f}. \tag{15}$$

While such in-loop measurements can readily be implemented without the need for any additional equipment, they generally tend to underestimate the actual residual noise [62]. The servo voltage unavoidably contains a signal contribution from measurement noise, typically being caused by detection shot noise as well as by electronic noise in the servo electronics. These noise contributions are also fed back onto the actuating mechanism in the laser, but rather than canceling CEP noise they create extra noise, in particular in the high frequency range. We typically found that the influence of such spurious noise contributions is strongly correlated to the strength of the f_{CE} beat note. If the beat note exceeds the detection noise level by only 30 dB or less, there is a strong tendency for underestimation of $\delta\varphi_{\mathrm{CE}}$ from in-loop measurements. This tendency is effectively reduced with suitable optimization of signal-to-noise ratios, see [9] for a detailed discussion. The only method to safeguard against noise artifacts is a completely independent verification of the noise spectrum with a second f-$2f$ or 0-f interferometer. If the oscillator is locked to a fixed non-zero radio frequency f_{CE}, the carrier of the reference source can be directly used for a phase comparison with the rf signal from the out-of-loop interferometer. Technically, the simplest way is mixing of the two rf signals in a double-balanced mixer with subsequent noise analysis of the signal at the intermediate frequency port. Despite its simplicity, exact calibration of this phase error signal may be cumbersome, due to fluctuations in the rf signal strength. More sophisticated measurement schemes employ rf lock-ins or carrier noise test equipment.

The situation becomes slightly more complicated if offset-free combs are to be analyzed. Even though CEP measurement schemes have been demonstrated that enable measurements at zero f_{CE} [63], these schemes give up one major advantage

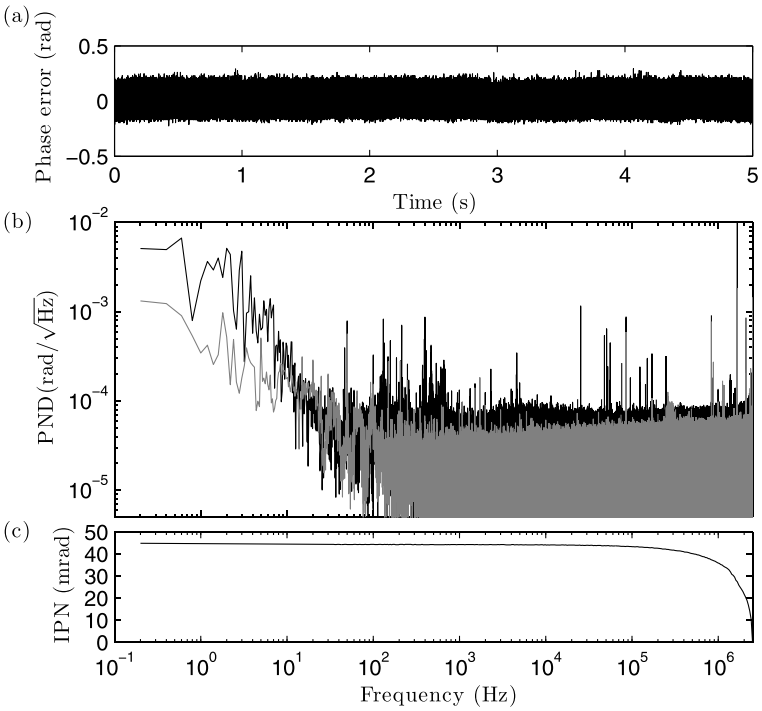

Fig. 6.9 Out-of-loop characterization of residual phase noise measured with the feed-forward scheme presented in [57]. (**a**) 5 s phase error time series sampled at 5 MHz. (**b**) Phase noise density (PND) $\sigma_{\varphi_{\mathrm{CE}}}(f)$ deduced from the time series above (*black trace*) and detection noise (*gray trace*). (**c**) Integrated phase noise (IPN) $\delta\varphi_{\mathrm{CE}}$ as a function of the lower integration limit f_1, see Eq. (13). The upper integration limit f_2 is the Nyquist frequency (2.5 MHz)

of the rf heterodyne schemes, i.e., their immunity to $1/f$ noise. We therefore found it advantageous to synthesize the driver signal for feed-forward schemes and shift f_{CE} from zero to an arbitrary offset for the purpose of noise analysis [57].

In the following, we discuss some examples that were measured with the out-of-loop method. Figure 6.9 shows the residual phase noise analysis from the feed-forward setup in [57]. The 5 s time series sampled at 5 MHz results in a total integrated phase noise of less than 45 mrad. This outstanding stabilization performance is only surpassed by the double stabilization setup presented in [9], where the feed-forward stabilization is combined with a conventional feedback loop in order to address the insufficient passive stability of the oscillator, see Fig. 6.10. These results indicate a residual phase stability of the stabilized laser of 20 mrad, corresponding to a timing jitter between carrier and envelope of only 8 attoseconds.

In both measurements, there are several different types of noise signatures apparent. Generally, one has to distinguish resonant narrowband noise sources and broadband ones. The latter ones show up as a $1/f$-like roll-off of $\sigma_{\varphi_{\mathrm{CE}}}(f)$ towards lower frequencies and a flat pedestal at high frequencies, see Fig. 6.9(b). The pedestal part

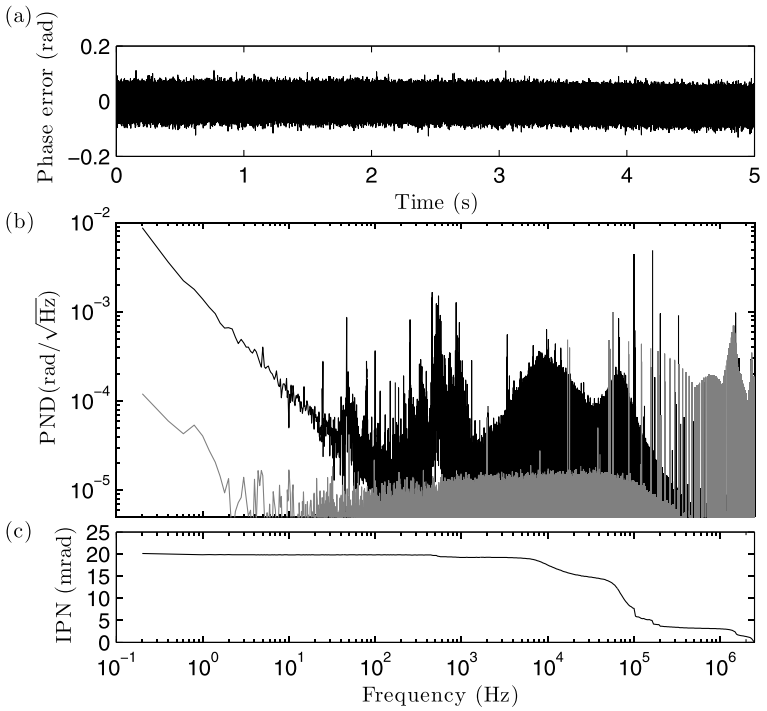

Fig. 6.10 Out-of-loop characterization of residual phase noise measured with the double stabilization scheme presented in [9]. (**a**) 5 s phase error time series sampled at 5 MHz. (**b**) Phase noise density (PND) $\sigma_{\varphi_{\mathrm{CE}}}(f)$ deduced from the time series above (*black trace*) and detection noise (*gray trace*). (**c**) Integrated phase noise (IPN) $\delta\varphi_{\mathrm{CE}}$ as a function of the lower integration limit f_1, see Eq. (13). The upper integration limit f_2 is the Nyquist frequency (2.5 MHz)

stems from detection shot noise and is directly related to the limited signal-to-noise ratio of the beat note as discussed above. Note that the shot noise in Fig. 6.10(b) is roughly one order of magnitude lower, due to the more than 15 dB increased signal-to-noise ratio, therefore revealing much more features in the phase noise density. The $1/f$ flicker noise contribution may stem from a slow interferometer drift or a drift of f_{CE} in the feed-forward scheme. Even though these drift effects are not known as game spoilers of any kind, we are not aware of a single publication that did not observe this effect. The resonant contributions stem from two different effects: acoustic resonances and electronic interference. The latter effect is caused, for example, by line frequency harmonics, causing a number of sharp lines in $\sigma_{\varphi_{\mathrm{CE}}}(f)$ at 50 or 60 Hz and harmonics thereof. Similarly, one often observes lines at 100 and 200 kHz, which clearly go back to switching power supplies. A third type of artifacts are aliasing lines, which are produced by interference of the sampling frequency and high frequency signal contributions. It should be noted that some of these noise contributions are artifacts of the out-of-loop measurement itself, e.g., the equally spaced lines in Fig. 6.10(b) that seem to become more and more dense

to higher frequencies in the logarithmic plot. These lines can be assigned to a disturbance by another electronic device in the lab. However, as all these effects are extremely narrowband, their total influence to rms values, cf. Eq. (13), is quite limited. From a pure visual inspection of phase noise spectra, therefore, the influence of narrowband noise contributions is often overestimated.

Broadband contributions are certainly much more of a limiting factor in CEP stabilization. This class of resonances can be clearly identified by their much lower quality factor as acoustic resonances encompass about one tenth of their center frequency, and they are most abundant in the range between 100 and 1000 Hz. Feedback approaches appear not to be able to fully suppress these resonances. This becomes quite clear when comparing the best results obtained with feedback [54] and those obtained with the feed-forward method [9, 57].

6.7 Outlook and Conclusion

When the phenomenon of CEP noise was first investigated at the turn of the millennium, getting a stable CEP looked like a near-impossible task. Free-running prism-based oscillators may exhibit drifts of f_{CE} of several MHz in a few seconds, and early estimates indicated that a loop bandwidth of several 10 to 100 kHz is required, with no servo mechanism at hand that could even come close to such demanding requirements. It took ten years of development to sort out all these issues, to engineer more rugged laser oscillators with dramatically improved passive stability, to optimize the detection of f_{CE}, and to understand the avoidance of interferometer drift issues in order to finally reach today's capabilities. One recent major step ahead is the transition from conventional feedback servo approaches to the new feed-forward scheme, which has reduced obtainable CEP noise levels by a factor four while at the same time enabling order-of-magnitude higher bandwidths. Current efforts are mostly directed on the improved long-term reliability of CEP stabilized systems. The current goal is to provide CEP-stabilized pulses over days without the need to re-adjust or re-lock the system. Together with the favorable noise properties of the feed-forward approach, this feat clearly enables experiments in attosecond physics and frequency metrology that require extremely long integration times. Further down the road, however, the investigation of attosecond phenomena appears to be limited by the integration time necessary to resolve ever-weaker interactions. In order to keep the pace, few-cycle pulse sources will have to push towards megahertz repetition rates, associated with average powers hard to achieve with present-day systems. Although the power-scalable diode-pump sources exist, their CEP stabilization has only recently come within reach by the advent of feed-forward stabilization. Therefore, these recent developments in CEP stabilization open a new avenue in attosecond science, enabling formerly impossible experiments to provide deeper insight into these blooming fields of optical physics.

Acknowledgements G.S. gratefully acknowledges Florian Helbing, Christian Grebing, and Sebastian Koke for their contributions to CEP stabilization during their PhD thesis work.

References

1. T. Brabec, F. Krausz, Intense few-cycle laser fields: frontiers of nonlinear optics. Rev. Mod. Phys. **72**, 545 (2000)
2. S. Backus, C.G. Durfee, M.M. Murnane, H.C. Kapteyn, High power ultrafast lasers. Rev. Sci. Instrum. **69**, 1207 (1998)
3. G. Steinmeyer, D.H. Sutter, L. Gallmann, N. Matuschek, U. Keller, Frontiers in ultrashort pulse generation: pushing the limits in linear and nonlinear optics. Science **286**, 1507 (1999)
4. G. Steinmeyer, A review of ultrafast optics and optoelectronics. J. Opt. A **5**, R1 (2003)
5. D.H. Sutter, G. Steinmeyer, L. Gallmann, N. Matuschek, F. Morier-Genoud, U. Keller, V. Scheuer, G. Angelow, T. Tschudi, Semiconductor saturable-absorber mirror-assisted Kerr-lens mode-locked Ti:sapphire laser producing pulses in the two-cycle regime. Opt. Lett. **24** (1999)
6. U. Morgner, F.X. Kärtner, S.H. Cho, Y. Chen, H.A. Haus, J.G. Fujimoto, E.P. Ippen, V. Scheuer, G. Angelow, T. Tschudi, Sub-two-cycle pulses from a Kerr-lens mode-locked Ti:sapphire laser. Opt. Lett. **24**, 411 (1999)
7. R. Ell, U. Morgner, F.X. Kärtner, J.G. Fujimoto, E.P. Ippen, V. Scheuer, G. Angelow, T. Tschudi, M.J. Lederer, A. Boiko, B. Luther-Davies, Generation of 5-fs pulses and octave-spanning spectra directly from a Ti:sapphire laser. Opt. Lett. **26**, 373 (2001)
8. L. Xu, C. Spielmann, A. Poppe, T. Brabec, F. Krausz, T.W. Hänsch, Route to phase control of ultrashort light pulses. Opt. Lett. **21**, 2008 (1996)
9. B. Borchers, S. Koke, A. Husakou, J. Herrmann, G. Steinmeyer, Carrier-envelope phase stabilization with sub-10 as residual timing jitter. Opt. Lett. **36**, 4146 (2011)
10. H.R. Telle, G. Steinmeyer, A.E. Dunlop, J. Stenger, D.H. Sutter, U. Keller, Carrier-envelope offset phase control: a novel concept for absolute optical frequency measurement and ultrashort pulse generation. Appl. Phys. B **69**, 327 (1999)
11. T. Udem, R. Holzwarth, T.W. Hänsch, Optical frequency metrology. Nature **416**, 233 (2002)
12. S.T. Cundiff, J. Ye, Colloquium: femtosecond optical frequency combs. Rev. Mod. Phys. **75**, 325 (2003)
13. H. Schnatz, B. Lipphardt, J. Helmcke, F. Riehle, G. Zinner, First phase-coherent frequency measurement of visible radiation. Phys. Rev. Lett. **76**, 18 (1996)
14. K. Osvay, M. Görbe, C. Grebing, G. Steinmeyer, Bandwidth-independent linear method for detection of the carrier-envelope offset phase. Opt. Lett. **32**, 3095 (2007)
15. P. Jójárt, Á. Börzsönyi, B. Borchers, G. Steinmeyer, K. Osvay, Agile linear interferometric method for carrier-envelope phase drift measurement. Opt. Lett. **37**, 836 (2012)
16. A. Baltuška, T. Fuji, T. Kobayashi, Controlling the carrier-envelope phase of ultrashort light pulses with optical parametric amplifiers. Phys. Rev. Lett. **88**, 133901 (2002)
17. T. Fuji, J. Rauschenberger, A. Apolonski, V.S. Yakovlev, G. Tempea, T. Udem, C. Gohle, T.W. Hänsch, W. Lehnert, M. Scherer, F. Krausz, Monolithic carrier-envelope phase-stabilization scheme. Opt. Lett. **30**, 332 (2005)
18. L. Lepetit, G. Cheriaux, M. Joffre, Linear techniques of phase measurement by femtosecond spectral interferometry for applications in spectroscopy. J. Opt. Soc. Am. B **12**, 2467 (1995)
19. M. Mehendale, S.A. Mitchell, J.-P. Likforman, D.M. Villeneuve, P.B. Corkum, Method for single-shot measurement of the carrier envelope phase of a few-cycle laser pulse. Opt. Lett. **25**, 1672 (2000)
20. M. Kakehata, H. Takada, Y. Kobayashi, K. Torizuka, Y. Fujihira, T. Homma, H. Takahashi, Single-shot measurement of carrier-envelope phase changes by spectral interferometry. Opt. Lett. **26**, 1436 (2001)
21. G.G. Paulus, F. Grasbon, H. Walther, P. Villoresi, M. Nisoli, S. Stagira, E. Priori, S. De Silvestri, Absolute-phase phenomena in photoionization with few-cycle laser pulses. Nature **414**, 182 (2001)
22. A.M. Sayler, T. Rathje, W. Müller, K. Rühle, R. Kienberger, G.G. Paulus, Precise, real-time, every-single-shot, carrier-envelope phase measurement of ultrashort laser pulses. Opt. Lett. **36**, 1 (2011)

23. K. Kreß, T. Löfler, M.D. Thomson, R. Dörner, H. Gimpel, K. Zrost, T. Ergler, R. Moshammer, U. Morgner, J. Ullrich, H.G. Roskos, Determination of the carrier-envelope phase of few-cycle laser pulses with terahertz-emission spectroscopy. Nat. Phys. **2**, 327 (2006)
24. A. Apolonski, P. Dombi, G.G. Paulus, M. Kakehata, R. Holzwarth, T. Udem, C. Lemell, K. Torizuka, J. Burgdörfer, T.W. Hänsch, F. Krausz, Observation of light-phase-sensitive photoemission from a metal. Phys. Rev. Lett. **92**, 073902 (2004)
25. M. Krüger, M. Schenk, P. Hommelhoff, Attosecond control of electrons emitted from a nanoscale metal tip. Nature **475**, 78 (2011)
26. J.K. Ranka, R.S. Windeler, A.J. Stentz, Visible continuum generation in air-silica microstructure optical fibers with anomalous dispersion at 800 nm. Opt. Lett. **25**, 25 (2000)
27. D.J. Jones, S.A. Diddams, J.K. Ranka, A. Stentz, R.S. Windeler, J.L. Hall, S.T. Cundiff, Carrier-envelope phase control of femtosecond mode-locked lasers and direct optical frequency synthesis. Science **288**, 635 (2000)
28. T.M. Fortier, A. Bartels, S.A. Diddams, Octave-spanning Ti:sapphire laser with a repetition rate >1 GHz for optical frequency measurements and comparisons. Opt. Lett. **31**, 1011 (2006)
29. C. Grebing, S. Koke, B. Manschwetus, G. Steinmeyer, Performance comparison of interferometer topologies for carrier-envelope phase detection. Appl. Phys. B **95**, 81 (2009)
30. D.J. Jones, T.M. Fortier, S.T. Cundiff, Highly sensitive detection of the carrier-envelope phase evolution and offset of femtosecond mode-locked oscillators. J. Opt. Soc. Am. B **21**, 1098 (2004)
31. R.L. Fork, O.E. Martinez, J.P. Gordon, Negative dispersion using pairs of prisms. Opt. Lett. **9**, 150 (1984)
32. F.W. Helbing, G. Steinmeyer, J. Stenger, H.R. Telle, U. Keller, Carrier-envelope-offset dynamics and stabilization of femtosecond pulses. Appl. Phys. B **74**, S35 (2002)
33. F. Gires, P. Tournois, Interféromètre utilisable pour la compression d'impulsions lumineuses modulées en fréquence. C. R. Acad. Sci. Paris **258**, 6112 (1964)
34. U. Morgner, R. Ell, G. Metzler, T.R. Schibli, F.X. Kärtner, J.G. Fujimoto, H.A. Haus, E.P. Ippen, Nonlinear optics with phase-controlled pulses in the sub-two-cycle regime. Phys. Rev. Lett. **86**, 5462 (2001)
35. F. Lücking, A. Assion, A. Apolonski, F. Krausz, G. Steinmeyer, Long-term carrier-envelope-phase-stable few-cycle pulses by use of the feed-forward method. Opt. Lett. **37**, 2076–2078 (2012)
36. M. Bradler, P. Baum, E. Riedle, Femtosecond continuum generation in bulk laser host materials with sub-μJ pump pulses. Appl. Phys. B **97**, 561 (2009)
37. A. Baltuška, T. Udem, M. Uiberacker, M. Hentschel, E. Goulielmakis, C. Gohle, R. Holzwarth, V.S. Yakoviev, A. Scrinzi, T.W. Hänsch, F. Krausz, Attosecond control of electronic processes by intense light fields. Nature **421**, 611 (2003)
38. M. Frigo, S.G. Johnson, The design and implementation of FFTW3. Proc. IEEE **93**, 216 (2005)
39. A. Silberschatz, B. Gagne, P.B. Galvin, *Operating System Concepts*, 7th edn. (Wiley, New York, 2005)
40. S. Koke, C. Grebing, B. Manschwetus, G. Steinmeyer, Fast f-to-2f interferometer for a direct measurement of the carrier-envelope phase drift of ultrashort amplified laser pulses. Opt. Lett. **33**, 2545 (2008)
41. G. Gademann, F. Plé, P.-M. Paul, M.J.J. Vrakking, Carrier-envelope phase stabilization of a terawatt level chirped pulse amplifier for generation of intense isolated attosecond pulses. Opt. Express **19**, 24922 (2011)
42. A. Baltuška, M. Uiberacker, E. Goulielmakis, R. Kienberger, V.S. Yakovlev, T. Udem, T.W. Hänsch, F. Krausz, Phase-controlled amplification of few-cycle laser pulses. IEEE J. Sel. Top. Quantum Electron. **9**, 972 (2003)
43. M. Kakehata, H. Takada, Y. Kobayashi, K. Torizuka, H. Takamiya, K. Nishijima, T. Homma, H. Takahashi, K. Okubo, S. Nakamura, Y. Koyamada, Carrier-envelope-phase stabilized chirped-pulse amplification system scalable to higher pulse energies. Opt. Express **12**, 2070 (2004)

44. G. Cerullo, A. Baltuška, O.D. Mücke, C. Vozzi, Few-optical-cycle light pulses with passive carrier-envelope phase stabilization. Laser Photonics Rev. **5**, 323 (2011)
45. A. Thai, M. Hemmer, P.K. Bates, O. Chalus, J. Biegert, Sub-250-mrad, passively carrier-envelope-phase-stable mid-infrared OPCPA source at high repetition rate. Opt. Lett. **36**, 3918 (2011)
46. S. Koke, A. Anderson, H. Frei, A. Assion, G. Steinmeyer, Noise performance of a feed-forward scheme for carrier-envelope phase stabilization. Appl. Phys. B **104**, 799 (2011)
47. C. Grebing, M. Görbe, K. Osvay, G. Steinmeyer, Isochronic and isodispersive carrier-envelope phase-shift compensators. Appl. Phys. B **97**, 575 (2009)
48. L. Arissian, J.-C. Diels, Carrier to envelope and dispersion control in a cavity with prism pairs. Phys. Rev. A **75**, 013814 (2007)
49. S. Witte, R. Zinkstok, W. Hogervorst, K. Eikema, Control and precise measurement of carrier-envelope phase dynamics. Appl. Phys. B **78**, 5 (2004)
50. F.W. Helbing, G. Steinmeyer, U. Keller, R.S. Windeler, J. Stenger, H.R. Telle, Carrier-envelope offset dynamics of mode-locked lasers. Opt. Lett. **27**, 194 (2002)
51. M.Y. Sander, E.P. Ippen, F.X. Kärtner, Carrier-envelope phase dynamics of octave-spanning dispersion-managed Ti:sapphire lasers. Opt. Express **18**, 4948 (2010)
52. W.C. Lindsey, C.M. Chie, A survey of digital phase-locked loops. Proc. IEEE **69**, 410 (1981)
53. P. Horowitz, W. Hill, *The Art of Electronics*, 2nd edn. (Cambridge University Press, Cambridge, 1989), pp. 242–249
54. H.M. Crespo, J.R. Birge, E.L. Falcão-Filho, M.Y. Sander, A. Benedick, F.X. Kärtner, Nonintrusive phase stabilization of sub-two-cycle pulses from a prismless octave-spanning Ti:sapphire laser. Opt. Lett. **33**, 833 (2008)
55. E. Goulielmakis, M. Schultze, M. Hofstetter, V.S. Yakovlev, J. Gagnon, M. Uiberacker, A.L. Aquila, E.M. Gullikson, D.T. Attwood, R. Kienberger, F. Krausz, U. Kleineberg, Single-cycle nonlinear optics. Science **320**, 1614 (2008)
56. S. Rausch, T. Binhammer, A. Harth, E. Schulz, M. Siegel, U. Morgner, Few-cycle oscillator pulse train with constant carrier-envelope- phase and 65 as jitter. Opt. Express **17**, 20282 (2009)
57. S. Koke, C. Grebing, H. Frei, A. Anderson, A. Assion, G. Steinmeyer, Direct frequency comb synthesis with arbitrary offset and shot-noise-limited phase noise. Nat. Photonics **4**, 462 (2010)
58. L. Matos, O.D. Mücke, J. Chen, F.X. Kärtner, Carrier-envelope phase dynamics and noise analysis in octave-spanning Ti:sapphire lasers. Opt. Express **14**, 2497 (2006)
59. O. Pronin, J. Brons, C. Grasse, V. Pervak, G. Boehm, M.-C. Amann, V.L. Kalashnikov, A. Apolonski, F. Krausz, High-power 200 fs Kerr-lens mode-locked Yb:YAG thin-disk oscillator. Opt. Lett. **36**, 4746 (2011)
60. C. Schriever, S. Lochbrunner, P. Krok, E. Riedle, Tunable pulses from below 300 to 970 nm with durations down to 14 fs based on a 2 MHz ytterbium-doped fiber system. Opt. Lett. **33**, 192 (2008)
61. F.W. Helbing, G. Steinmeyer, U. Keller, Carrier-envelope offset phase-locking with attosecond timing jitter. IEEE J. Sel. Top. Quantum Electron. **9**, 1030 (2003)
62. T.M. Fortier, D.J. Jones, J. Ye, S.T. Cundiff, Highly phase stable mode-locked lasers. IEEE J. Sel. Top. Quantum Electron. **9**, 1002 (2003)
63. J.-H. Lee, Y.S. Lee, J. Park, T.J. Yu, C.H. Nam, Long-term carrier-envelope-phase stabilization of a femtosecond laser by the direct locking method. Opt. Express **16**, 12624 (2008)

Chapter 7
Probing and Controlling Autoionization Dynamics of Atoms with Attosecond Light Pulses

Wei-Chun Chu and Chii-Dong Lin

Abstract The time evolution of an autoionizing atomic system is studied theoretically in the presence of a moderately intense dressing laser pulse. We first examine how an autoionizing wave packet evolves in time in the absence of an external field, and take the single $2pns(^1P)$ resonances in beryllium as examples. Alternatively, we study the electron dynamics where an attosecond extreme ultraviolet (XUV) pulse excites two autoionizing states in the presence of a strong time-delayed coupling infrared (IR) laser pulse. The IR can be viewed as a probe to extract or a control to modify the autoionization dynamics. The photoelectron and photoabsorption spectra are calculated for various time delays between the XUV and the IR pulses, and the results are compared with the available experiments. Finally, simulation of the coupled $2s2p(^1P)$ and $2s^2(^1S)$ resonances in helium shows substantial spectral modifications by the dressing field parameters. Its analogy to electromagnetically induced transparency in the time domain is discussed.

7.1 Introduction

The recent developments in attosecond light pulses have brought numerous applications in measuring and controlling electron dynamics in the past decade [1–3]. Single attosecond pulses (SAPs), first realized in 2001 [4], have been used in the experiments in atomic [5–7], molecular [8, 9], and condensed systems [10]. These pulses, produced by the high-order harmonic generation (HHG) process of atoms in an intense infrared (IR) light source usually cover up to the extreme ultraviolet (XUV) range and last for as short as a hundred attoseconds. With such energy and time scales, these attosecond pulses are ideal for the study of autoionization dynamics in an atomic or molecular system.

W.-C. Chu · C.-D. Lin (✉)
J. R. Macdonald Laboratory, Department of Physics, Kansas State University, Manhattan, KS 66506, USA
e-mail: cdlin@phys.ksu.edu

W.-C. Chu
e-mail: wcchu@phys.ksu.edu

K. Yamanouchi, K. Midorikawa (eds.), *Progress in Ultrafast Intense Laser Science*, Springer Series in Chemical Physics 104, DOI 10.1007/978-3-642-35052-8_7,

The wave packet of one or several autoionizing states (AISs) initiated by a short XUV pulse evolves in time. This evolution in the absence of an external field after the pump has been formulated and analyzed previously [11–14]. We develop a simple analytical model for the freely propagating wave packet, where the atomic structure is conveniently given by a set of parameters. Taking the $2p4s(^1P)$ resonance in beryllium as an example, the photoelectrons distributed in energy and in space are calculated and analyzed until the end of the autoionization when the energy distribution converges to the well-known Fano lineshape. This process takes about ten times the decay lifetime of the AIS. Our model is further generalized for a series of resonances, demonstrated by the $2pns(^1P)$ series in beryllium. To probe the evolution of the wave packet, a pump-probe spectroscopy with two attosecond XUV pulses is proposed; however, the scheme is currently impractical since the required light sources are still unavailable.

Alternatively, autoionizing systems have been studied in the XUV-plus-IR pump-probe spectroscopy theoretically [15–18] and experimentally [19] with long pulses–typically tens of femtoseconds to picoseconds, which are longer than the resonance lifetimes. In these cases, the total ionization yield versus the photon energy of the probe pulse is measured. Contrary to using long pulses, very recently the decay of the AIS has been measured in the broadband spectra using an XUV SAP and a femtosecond IR [20, 21]. In order to treat the accurate wave packet dynamics in the broadband lights, which has not been done before theoretically, in Sects. 7.3 and 7.4, we calculate the electron and absorption spectra, respectively, with the analyses and comparisons to the available experiments.

In the XUV-plus-IR experiments, a considerably intense IR should be viewed more rigorously as a modification of the dynamics rather than just a probe. In this aspect, in the last part of this chapter, we calculate the $2s2p(^1P)$ and $2s^2(^1S)$ AISs coupled by a dressing laser, and discuss the dynamics manipulated by the tunable dressing pulse. When the dressing field is long, the comprehensive controlling scheme is reduced to the electromagnetically induced transparency (EIT) [22, 23] condition, which is at the heart of many current researches in optical control [24–27]. While the dynamics in our model system would provide a real attosecond electron control, the EIT-like light modification therein would also open a platform for optical control when incorporated with macroscopic effects in the medium.

In this chapter, as a general rule, atomic units (a.u.) are used for the model descriptions in Sects. 7.2, 7.3, and 7.4; electron Volts (eV) and femtoseconds (fs) or attoseconds (as) are used in energy and in time, respectively, for the applications or the simulations, unless otherwise specified. The pulse duration is defined by the full width at half maximum (FWHM) of the intensity.

7.2 Evolution of an Isolated Autoionizing State

Atomic autoionization typically occurs in a few to tens of femtoseconds and is one of the fastest many-electron correlation phenomena. It has been observed in fre-

quency domain for decades via photoionization using synchrotron radiations , where the resonance features can be characterized by Fano's configuration interaction (CI) theory [28]. Tremendous improvements in experiments and theories in the past few decades have matured this research field [29–31]. Recently, with the advances in ultrafast technologies, autoionization dynamics measured in the time domain are beginning to appear with attosecond light pulses [20, 21]. It is thus of interest to formulate theories that would help to understand the evolution of an autoionizing wave packet [32].

7.2.1 Time Evolution of an Autoionizing Wave Packet

Assume that an ultrashort light pulse pumps an atomic system from the ground state to an AIS. After the pulse is over, an isolated autoionizing wave packet is consisting of a bound state $|\alpha\rangle$ and its background continuum $|\beta_E\rangle$. The wave packet can be written either in the configuration basis as

$$\left|\Psi_{\rm ex}(t)\right\rangle = d_\alpha(t)|\alpha\rangle + \int d_E(t)|\beta_E\rangle\, dE, \tag{1}$$

or in the eigenstate basis ($|\psi_E\rangle$) as

$$\left|\Psi_{\rm ex}(t)\right\rangle = \int c_E e^{-iEt}|\psi_E\rangle\, dE. \tag{2}$$

Note that the notations c and d are for eigenstates and for configurations, respectively. Applying Fano's theory of configuration interaction [28], for the atomic Hamiltonian near the resonance given by

$$\begin{aligned} \langle\alpha|H|\alpha\rangle &= E_r, \\ \langle\beta_E|H|\alpha\rangle &= V_E, \\ \langle\beta_{E'}|H|\beta_E\rangle &= E\delta\big(E'-E\big), \end{aligned} \tag{3}$$

the eigenstates in the form of

$$|\psi_E\rangle = a_E|\alpha\rangle + \int b_{EE'}|\beta_{E'}\rangle\, dE', \tag{4}$$

are solved, i.e., a_E and $b_{EE'}$ are obtained. Note that the continuum states $|\beta_E\rangle$ are assume to be real standing waves by convention so that V_E is real. By the further approximation that $|\beta_E\rangle$ differ only slightly across the resonance, the resonance width and the q-parameters, defined by

$$\Gamma \equiv 2\pi V^2, \tag{5}$$

$$q \equiv \left.\frac{\langle\alpha|T|i\rangle}{\pi V\langle\beta_E|T|i\rangle}\right|_{E=E_r}, \tag{6}$$

are taken as constants estimated at E_r.

With Eq. (4), the forms in Eq. (1) and in Eq. (2) are equated to give

$$d_\alpha(t) = \left[d_\alpha^{(0)} e^{-\frac{\Gamma}{2}t} + \int d_E^{(0)} g_E(t)\, dE \right] e^{-iE_r t}, \tag{7}$$

$$d_E(t) = \left[d_\alpha^{(0)} g_E(t) + \int d_{E'}^{(0)} f_{EE'}(t)\, dE' \right] e^{-iE_r t} + d_E^{(0)} e^{-iEt}, \tag{8}$$

where $d_\alpha^{(0)} \equiv \langle \alpha | \Psi_{\rm ex}(0) \rangle = \langle \alpha | T | i \rangle$ and $d_E^{(0)} \equiv \langle \beta_E | \Psi_{\rm ex}(0) \rangle = \langle \beta_E | T | i \rangle$ are the initial values of the bound and continuum coefficients, respectively, for initial (ground) state $|i\rangle$ and pump transition operator T, and $g_E(t)$ and $f_{EE'}(t)$ are defined by

$$g_E(t) \equiv \frac{V}{E - E_r + i\Gamma/2} \left[e^{-i(E-E_r)t} - e^{-\frac{\Gamma}{2}t} \right], \tag{9}$$

$$f_{EE'}(t) \equiv \frac{V}{E - E'} \left[g_E(t) - g_{E'}(t) \right]. \tag{10}$$

The evolution of $\Psi_{\rm ex}(t)$ is uniquely determined once the Fano parameters and the initial values $d_\alpha^{(0)}$ and $d_E^{(0)}$, taken at the end of the pump pulse, are given.

The analytical form of the wave packet has a time scale of $1/\Gamma$ and an energy scale of Γ. In other words, we have arrived in a universal behavior of the autoionizing wave packet by scaling the time and the energy with respect to Γ. This will be shown in more details in the example in Sect. 7.2.2. For an AIS that can be treated independently, this model evaluates its evolution efficiently by importing the Fano parameters without any tedious numerical efforts. However, we have to limit the pump to be weak and short such that it is a one photon process and that the decay starts mainly after the pump. When these conditions are satisfied, our approach is simple and transparent. If the pump beam is strong, *ab initio* calculations are in principle necessary, but the convergence has to be carefully monitored.

For an autoionization process initiated by a broadband pulse, the "electron profile", or simply "profile", of the resonance is defined by the projection of wave packet onto the continuum waves of momentum $\mathbf{k}$ at any given time during the process. The energy-normalized continuum waves are

$$\psi_{\mathbf{k}}(\mathbf{r}) = \sqrt{\frac{2}{\pi k}} \frac{1}{r} \sum_{lm} i^l e^{i\eta_l} u_l(kr) Y_l^m(\hat{r}) Y_l^{m*}(\hat{k}), \tag{11}$$

where $u_l(kr)$ are taken as real standing waves for consistency with $|\beta_E\rangle$. Since the current study concerns only one continuum channel, or one partial wave, we focus on the total energy distribution by integrating the projection over all directions. For the wavefunction in Eq. (1), the profile is a function of energy and time given by

$$P_E(t) = \left| d_E(t) \right|^2. \tag{12}$$

As $t \to \infty$, the bound state decays to zero, and $P_E(t)$ converges to the familiar Fano lineshape. The total probability of the wave packet in Eq. (1) is normalized to 1 since the ground state is not needed after the pump ends. The expression of the model so far is for a single resonance. However, for a broadband SAP that covers multiple resonances, the model is further generalized to deal with a Rydberg series

of resonances embedded in a background continuum by neglecting the higher-order interactions between the AISs.

7.2.2 Applications to the 2p4s Resonance in Beryllium

To fully comprehend the short-time behavior of the wave packet, we look at the photoelectron profile $P_E(t)$ in energy domain and the associated electron density in space. By assuming the pump pulse is perturbative and in a Gaussian envelope shorter than the autoionization time, the initial continuum distribution is given by a Gaussian function whose bandwidth is inversely proportional to the pulse duration. This distribution, consolidated with the q-parameter, determines the initial coefficients $d_\alpha^{(0)}$ and $d_E^{(0)}$. Thus, for given pump parameters and given Fano parameters, the wave packet can be calculated exactly. In the following, we take the isolated $2p4s(^1P)$ resonance and the $2pns(^1P)$ series in the $2s\varepsilon p(^1P)$ background continuum in neutral beryllium as examples. The Fano parameters are taken from the earlier calculation [33] and the experiment [34].

Following the expression in Eq. (1), the isolated $2p4s$ autoionizing wave packet can be projected onto the two-electron coordinate space as

$$\Psi_{\rm ex}(\mathbf{r}_1, \mathbf{r}_2; t) = d_\alpha(t)\phi_\alpha(\mathbf{r}_1, \mathbf{r}_2) + \int d_E(t)\phi_E(\mathbf{r}_1, \mathbf{r}_2)\, dE, \tag{13}$$

where we have assumed only two active electrons. The bound-state configuration $\phi_\alpha(\mathbf{r}_1, \mathbf{r}_2)$ is composed by the $2p$ and $4s$ orbitals, and the continuum-state configuration $\phi_E(\mathbf{r}_1, \mathbf{r}_2)$ is composed by the $2s$ orbital and the εp partial wave, where both configurations are symmetrized between $\mathbf{r}_1$ and $\mathbf{r}_2$. The one-electron radial density for the wave packet is defined by

$$\rho(r, t) = \iiint \left|\Psi_{\rm ex}(\mathbf{r}, \mathbf{r}'; t)\right|^2 r^2 r'^2\, d\Omega\, d\Omega'\, dr'. \tag{14}$$

Figure 7.1 shows the time evolution of the $2p4s$ autoionizing wave packet in beryllium initiated by an 1.5-fs XUV pump. The time scale of the plot is relative to the decay lifetime $T = 3.78$ fs. In Fig. 7.1(a), the 1.2-eV finite bandwidth confines the overall energy distribution throughout the evolution up to $t = 10T$. The profile at $t = T$ is at the halfway between the initial Gaussian function and the final form. After that, the evolution slows down until the profile reaches its final Fano shape at roughly $10T$.

The radial electron density $\rho(r, t)$ at short times and at long times are shown in Fig. 7.1(b) and 7.1(c), respectively. At the start of the process, the $2p4s$ bound-state wavefunction is dominant, as shown by the $t = 0$ curve. Then, the ionized electrons grow and move in a bulk to around 40 a.u. at $0.5T$ and to around 80 a.u. at T, and in the meantime, the bound state component drops. In the $0 < r < 5$ a.u. region, the sharp rising of the density means the increase of the $2s$ electrons in the $2s\varepsilon p$ configuration. As the time passes $10T$, in Fig. 7.1(c), the photoelectrons move

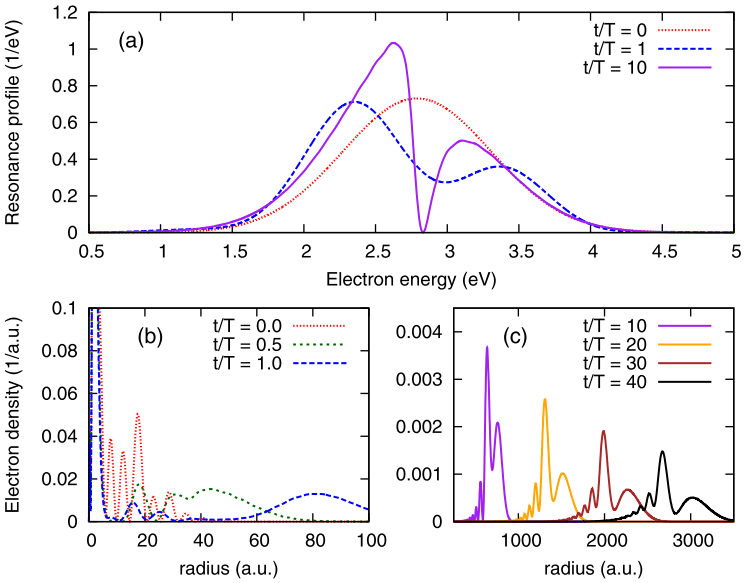

Fig. 7.1 Time evolution of the wave packet describing the autoionization of $2p4s$ in Be, initiated by an 1.5 fs XUV pulse centered at the resonance energy. (**a**) Resonance profiles at $t = 0$, T, and $10T$. The radial density of the autoionized electrons in coordinate space is shown in (**b**) for short times and in (**c**) for long times. The time is scaled by the lifetime of the resonance, $T = 3.78$ fs

outwardly with a constant average speed, but they spread wider in the r-space. This is consistent with the stabilized energy profile for $t \geq 10T$ in Fig. 7.1(a) where the electrons congregate around 2.5 eV and 3.2 eV. These two groups of electrons move farther away from each other in space. Considering $P(E, t)$ and $\rho(r, t)$ together assists us to "visualize" the whole autoionization process.

For the generalized model for multiple resonances, in Fig. 7.2, we show the electron profile of the $2pns$ series at different times, initiated by an 1-fs pulse centered at 2.5 eV. At $t = 0$, the curve represents the directly ionized electrons, whose distribution is proportional to the light spectrum. Then, the bound states start to decay. The decay lifetimes for the $n = 3$, 4, and 5 resonances, at $E_r = 1.6$, 2.8, and 3.3 eV, are 1.3, 3.6, and 7.9 fs, respectively. With these specific lifetimes, as seen in the 2.5- and 5-fs curves, the resonances build up at different speeds. By 100 fs, the profile of the series shows all the resonance shapes quite clearly up to $2p9s$, whose decay lifetime is 55 fs. The experimental photoionization spectrum measured by synchrotron radiation is shown as a reference. The experimental signals are rescaled in our plot range. Other than the background curvature determined by the pulse bandwidth, our model agrees well with the experiment. In particular, the $2p4s$ resonance, which sits at the center of the pulse, is almost unaffected by the pulse profile.

We have developed and tested a simple analytical model for the dynamics of one or a series of autoionizing states that evolve freely after populated by an SAP. In an actual measurement, the retrieval of the time-dependent electron profile that

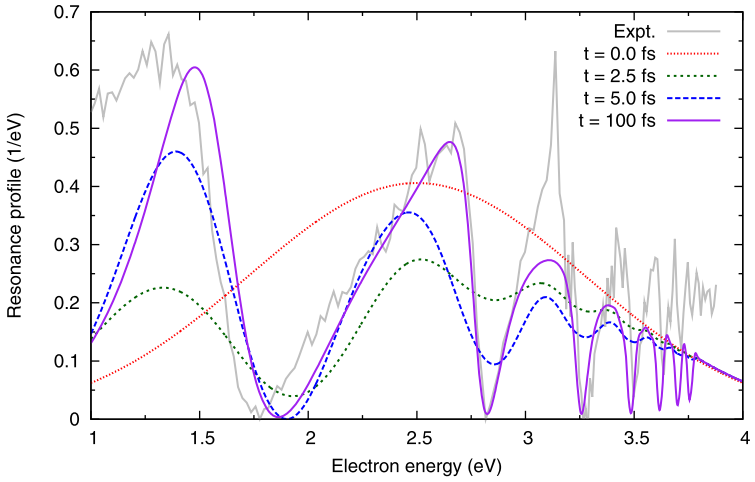

Fig. 7.2 Comparison of $2pns$ resonance series obtained from synchrotron radiation measurement [16] (*light gray solid curve*) with the simulated time-dependent profile of the same series at $t = 0$, 2.5, 5, and 100 fs, populated by an 1-fs pulse (bandwidth is 1.8 eV) centered at 2.5 eV above the threshold. The resonances for $n = 3$–9 are included in the model. The resonance parameters are generated by quantum defect $\mu = 0.6$, $\Gamma\nu^3 = 7.1$ eV where $\nu = n - \mu$, and $q = -0.8$. The experimental data has been scaled to match the calculated $2p4s$ peak at $t = 100$ fs

evolves in only a few femtoseconds is desirable. To this end, we propose a pump-probe scheme [32] where two XUV SAPs are employed. Taking the $2p4s$ resonance analyzed above as an example, the scheme works in the following way. After the pump, a time-delayed 40-eV XUV SAP is applied to the system, which ionizes the $2s$ electron in the Be^+ ion core. These ionized electrons, at 22 eV, are much more energetic than the autoionized electrons at 2.5 eV. In other words, the probe transforms a small fraction of the system to the doubly charged Be^{2+} ions plus the 2.5- and 22-eV electrons. In the meantime, most atoms are not influenced by the probe; they only finish the autoionization process by producing the Be^+ ions and the 2.5-eV autoionized electrons that reach the ideal Fano shape. To single out the profile at the time of the probe, the detector has to record the electron signals in coincidence with the Be^{2+} ions. Theoretically, this scheme enables us to trace the fast-changing photoelectron distribution in the time scale of the pulse durations. However, the required light sources, with moderate intensity for sufficient signal strength, are not available at the present time.

7.3 Electron Dynamics of Laser-Coupled Autoionizing States

The XUV-plus-IR pump-probe scheme has been utilized to study electron dynamics in various systems since the first such experiment a decade ago [5]. Typically, this setup is prepared by the HHG, and the IR is much stronger than the XUV. Thus,

while the IR is sometimes designed to "probe" the dynamics of the system initiated by the XUV, it actually modifies the dynamics. Furthermore, in many occasions, the two pulses are overlapped for better signal strength, where the roles of the pump and the probe are not clearly assigned. Thus, the whole process is more suitably described as the photoionization of a system dressed by a laser pulse.

In such a scheme, photoionization of a system in the structureless region above the ionization threshold is carried out in a number of experiments [4, 35–37], and modeled by the "streaking" theory based on the strong-field approximation (SFA) [38]. If the region contains an AIS, the theory is modified to include the bound-state structure [39], which has been employed in the recent experiment in helium [21]. The simulation therein only considers the ionization of the $2s2p(^1P)$ AIS but not its coupling to the $2p^2(^1S)$ AIS. Such a system with two laser-coupled AISs has been formulated and studied widely for long pulses, where the photoionization spectrum is investigated by the total ionization yield versus the photon energy or detuning of the XUV [15–18]. For the broadband SAP used in Ref. [21], the pulses are much shorter than the decay lifetime, or equivalently, much broader than the resonance widths, such that each XUV shot projects the whole resonance spectrum within its bandwidth. The dynamics of the photoelectron wave packet is our main concern. The model and its simulation for the experiment in Ref. [21] have been previously reported by us [40].

7.3.1 Model for Total Wavefunction

Here we model the time-dependent wavefunction of a three-level system, where the top two levels are AISs coupled by a laser pulse, and an XUV SAP pumps one of them from the ground state. The bound states and the photoelectrons with respect to the AISs are calculated.

The atomic system consists of the ground state $|g\rangle$ and two AISs, $|a\rangle$ and $|b\rangle$, embedded in the background continua $|E_1\rangle$ and $|E_2\rangle$, respectively (see Fig. 7.3). Note that these "states" are not atomic eigenstates, but configurations; we will discuss the wavefunction in eigenstate basis later. Suppose $|a\rangle$ is lower than $|b\rangle$ in energy, i.e., $E_a < E_b$, for the model description. An XUV pulse couples $|g\rangle$ to the $|a\rangle$-$|E_1\rangle$ AIS, and a time-delayed laser pulse couples the two AISs. Here the laser is not necessarily an IR, considering the energy difference between the two AISs; nonetheless, the laser energy is always much lower and well separated from the XUV energy. The total Hamiltonian is $H(t) = H_A + H_X(t) + H_L(t)$, where H_A is the atomic Hamiltonian, and $H_X(t)$ and $H_L(t)$ are the dipole interactions of the atomic system with the XUV and laser, respectively. The Hamiltonian of the field itself is neglected. Both pulses are assumed to be in the form of $E(t) = F(t)e^{i\omega t} + F^*(t)e^{-i\omega t}$, where ω is the carrier frequency, and $F(t)$ is a cosine-square type function. Note that $F(t)$ is in general complex, but now taken as real in the calculation by neglecting the carrier-envelope phase and the chirping. The total wavefunction of this system is

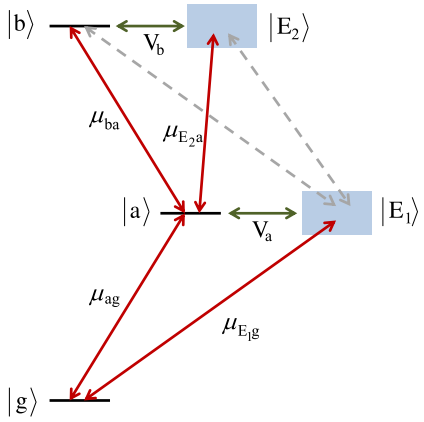

Fig. 7.3 Scheme of the autoionizing three-level system coupled by two ultrashort pulses. The *dashed lines* represent negligible transitions

$$|\Psi(t)\rangle = e^{-iE_g t}c_g(t)|g\rangle + e^{-iE_X t}\left[d_a(t)|a\rangle + \int d_{E_1}(t)|E_1\rangle\, dE_1\right] + e^{-iE_L t}\left[d_b(t)|b\rangle + \int d_{E_2}(t)|E_2\rangle\, dE_2\right], \tag{15}$$

where E_g is the ground state energy, and $E_X \equiv E_g + \omega_X$ and $E_L \equiv E_g + \omega_X + \omega_L$ represent the central energies pumped by the pulses. Since the fast-oscillating terms are factored out, the $c(t)$ and $d(t)$ coefficients are smooth functions of time.

When solving the Schrödinger equation for the wavefunction, the following approximations are taken. Rotating wave approximation is applied since both pulses are nearly resonant. For the atomic systems and the field conditions in our concern, the second-order electron transition between $|E_2\rangle$ and $|b\rangle$ and the free-free electron transition between $|E_1\rangle$ and $|E_2\rangle$ are disregarded. The off-diagonal terms of the Hamiltonian are thus V_a and V_b for the autoionization processes for the two AISs, $-\mu_{ag}E_X(t)$ and $-\mu_{E_1 g}E_X(t)$ for the dipole interactions for the XUV, and $-\mu_{ba}E_L(t)$ and $-\mu_{E_2 a}E_L(t)$ for the dipole interactions for the laser, where μ are dipole matrix elements. All the V and μ are taken as constants because the continuum waves vary slightly across the resonances. The Schrödinger equation then gives the coupled equations for all the coefficients, including the continuum ones by

$$i\dot{d}_{E_1}(t) = (E_1 - E_X)d_{E_1}(t) - \mu_{E_1 g}F_X^*(t)c_g(t) + V_a d_a(t), \tag{16}$$

$$i\dot{d}_{E_2}(t) = (E_2 - E_L)d_{E_2}(t) - \mu_{E_2 a}F_L^*(t)d_a(t) + V_b d_b(t). \tag{17}$$

By adiabatic elimination of the continuum, i.e., assuming $\dot{d}_{E_1}(t) = \dot{d}_{E_2}(t) = 0$, Eqs. (16)–(17) are integrated into other coupled equations to give

$$i\dot{c}_g(t) = -i\frac{\gamma_g(t)}{2}c_g(t) - \lambda_a F_X(t)d_a(t), \tag{18}$$

$$i\dot{d}_a(t) = -\lambda_a F_X^*(t)c_g(t) - \left[\delta_X + i\frac{\Gamma_a + \gamma_a(t)}{2}\right]d_a(t) - \lambda_b F_L(t)d_b(t), \tag{19}$$

$$i\dot{d}_b(t) = -\lambda_b F_L^*(t)d_a(t) - \left[\delta_X + \delta_L + i\frac{\Gamma_b}{2}\right]d_b(t), \tag{20}$$

for the bound-state coefficients, where $\lambda_a \equiv \mu_{ag} - i\pi V_a \mu_{E_1 g}$ and $\lambda_b \equiv \mu_{ba} - i\pi V_b \mu_{E_2 a}$ are the complex dipole matrix elements combining the direct bound-bound transitions and the indirect transitions going through the continua; $\delta_X \equiv \omega_X - (E_a - E_g)$ and $\delta_L \equiv \omega_L - (E_b - E_a)$ are the detunings of the fields; and $\gamma_g(t) \equiv 2\pi |D_{E_1 g} F_X(t)|^2$ and $\gamma_a(t) \equiv 2\pi |D_{2a} F_L(t)|^2$ are the laser-induced broadenings. Note that the q-parameters are uniquely determined by the μ and V values, as shown by Eq. (6). The energy independence of the continua across the resonances removes the ac Stark shifts between $|g\rangle$ and $|E_1\rangle$ and between $|a\rangle$ and $|E_2\rangle$.

By solving Eqs. (18)–(20), the bound-state part of the wavefunction in Eq. (15) is obtained. With the bound coefficients $c_g(t)$, $d_a(t)$, and $d_b(t)$, we return to Eqs. (16)–(17) for the "second iteration" of the continuum coefficients. These newly obtained continuum coefficients, opposing the divergent ones generated by the adiabatic elimination, are the final numerical functions that we apply to the total wavefunction $|\Psi(t)\rangle$ in Eq. (15). For weak fields, the system is completely described by this wavefunction. However, for strong fields, the multiphoton process or tunneling may prompt the electrons to other states or continua that are not included in the current form of $|\Psi(t)\rangle$. In the case of moderately intense laser, which is in our main concern, we have to adjust the resonance widths by adding the ionization rates estimated by the model by Ammosov, Delone, and Krainov (ADK theory) [41] or the model by Perelomov, Popov, and Terent'ev (PPT theory) [42]. In these models, the tunneling of the electrons from a bound state by an electric field is calculated at each instance. In our case, the rates are estimated with respect to the instantaneous electric field strength during the 9-fs laser. Note that while the tunneling rates correct the resonance profiles, the total probability calculated by $|\Psi(t)\rangle$ is no longer conserved.

Equivalent to Eq. (15), the wavefunction can be written in terms of atomic eigenstates as

$$\begin{aligned} \big|\Psi(t)\big\rangle = e^{-iE_g t} c_g(t)|g\rangle + e^{-iE_X t} \int c_E^a(t) \big|\psi_E^a\big\rangle dE \\ + e^{-iE_L t} \int c_E^b(t) \big|\psi_E^a\big\rangle dE, \end{aligned} \tag{21}$$

where the superscripts a and b indicate the eigenstates associated with $|a\rangle$ and $|E_1\rangle$ and with $|b\rangle$ and $|E_2\rangle$, respectively. By incorporating Fano's CI theory, the eigenstate coefficients $c_E(t)$ are given in terms of the bound and continuum coefficients by

$$c_E^a(t) = \frac{\sin \Theta_E^a}{\pi V_a} d_a(t) - \big(\cos \Theta_E^a - i \sin \Theta_E^a\big) d_{E_1}(t)|_{E_1 = E}, \tag{22}$$

where

$$\Theta_E^a \equiv -\tan^{-1} \frac{\Gamma_a/2}{E - E_a} \tag{23}$$

for a, and by the same form for b where all the terms are associated with $|b\rangle$ and $|E_2\rangle$. On one hand, in the configuration basis, the coefficients evolve until both the fields and the decays are over. On the other hand, in the atomic eigenstate basis,

the Hamiltonian is already diagonalized for the autoionization, i.e., the off-diagonal terms are only the dipole transition terms, and the coefficients stop changing at the end of the field. Thus, in the eigenstate basis, the calculation is necessary only up to the end of the external field, and the analytical form in Eq. (22) requires almost no additional efforts. Taking these advantages, the computational steps in the present model are first the bound-state coefficients, then the continuum-state coefficients, finally the eigenstate coefficients, where all the calculations are up to t_f at the end of the external field. The electron profiles for the two resonances are $P^a(E) = |c_E^a(t_f)|^2$ and $P^b(E) = |c_E^b(t_f)|^2$, respectively. The Fano parameters and the dipole matrix elements therein are taken from literatures or generated by preliminary calculations. Their values, involving only the atomic structures, are irrelevant to the formation of the present model.

In the analyses later in this chapter, Rabi oscillation is at the heart of the dynamics. The generalized Rabi frequency, defined by

$$\Omega(t) \equiv \sqrt{\left|\mu E(t)\right|^2 + |\delta|^2}, \tag{24}$$

is often evaluated for the coupling strength between the states. For an ultrashort pulse, $\Omega(t)$ is only instantaneous, so the coupling over the whole pulse is illustrated by the pulse area given by

$$A \equiv \int_{-\infty}^{\infty} \Omega(t)\, dt. \tag{25}$$

Note that the pulse area is calculable only in a good resonance condition where $\Omega(t)$ is finite in time by neglecting δ. For a π-pulse, i.e., $A = \pi$, the population in a two-state system is transferred from one state to the other thoroughly.

7.3.2 Experiment in Helium

The experiment by Gilbertson *et. al.* [21] measures the photoelectrons near the $2s2p(^1P)$ resonance in helium ionized by an XUV pulse with a time-delayed IR pulse. We simulate the spectra and compare the result with the measurement. For the XUV pulse, the central photon energy is $\omega_X = 60$ eV, the duration is $\tau_X = 100$ as, and the intensity is weak (perturbative). For the time-delayed IR, the wavelength is $\lambda_L = 780$ nm ($\omega_L = 1.6$ eV), the duration is $\tau_L = 9$ fs, and the peak intensity is $I_L = 7 \times 10^{11}$ W/cm^2. The time delay t_0 is defined as the separation between the pulse peaks, and $t_0 > 0$ means that the XUV is earlier. With a bandwidth of about 20 eV, the XUV pumps helium from the ground state to the $2snp$ resonance series. Due to the resolution of the spectrometer, only the strongest $2s2p$ state was observed. The natural lifetime of this state is 17 fs. By measuring electron spectra vs. the time delay, the autoionization dynamics of $2s2p$ in the IR field can be followed.

In Ref. [21], a simulation using the SFA model developed by Zhao and Lin [39] was used, with additional account of the ionization by the IR, where the ionization rate was estimated by the PPT theory. The simulation concluded that the intense

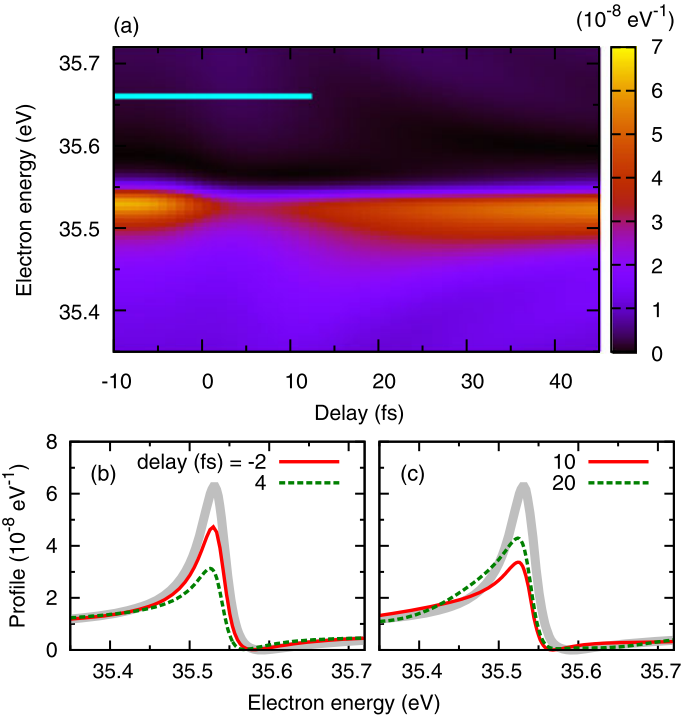

Fig. 7.4 Electron profile of the $2s2p$ resonance in helium. (**a**) Spectrogram for $t_0 = -10$ to 45 fs. The *horizontal cyan bar* indicates the delay range where the two pulses overlap. Particularly, the spectra are shown in (**b**) for $t_0 = -2$ and 4 fs, and in (**c**) for 10 and 20 fs. Original Fano lineshape is shown by the *gray curve*

IR depletes $2s2p$. From the time-delay spectra, the decay rate or lifetime of the state was extracted. Limited by the spectral resolution, however, modifications of the Fano resonance profiles were not reported.

Our simulation, unlike that in Ref. [21], takes the IR coupling between $2s2p$ and the $2p^2(^1S)$ resonance into account. The background continua in the measurement, for the two AISs, are $1s\varepsilon p(^1P)$ and $1s\varepsilon s(^1S)$, respectively. With the given Fano parameters for $2s2p$ [43] and for $2p^2$ [44] and the dipole matrix elements μ_{ag} [18] and μ_{ba} [45], we carry out the model calculation and fit the tunneling parameters in the PPT theory for the experiment. The calculated time-delayed electron spectra are shown in Fig. 7.4. For a negative delay such as $t_0 = -10$ fs, the IR appears before the XUV without affecting the autoionization, and thus the usual Fano profile appears. This Fano lineshape is shown in the figure as a reference. As t_0 increases, the IR strikes the system at the beginning of the decay of $2s2p$, and significantly depletes the $2s2p$ bound state and its autoionized electrons, resulting in a minimum of the profile at $t_0 = 4$ fs, shown as the lowest curve in Fig. 7.4(b). When t_0 increases further, passing the range specified by the horizontal bar in Fig. 7.4(a), the two pulses separate in time. For larger t_0, more decay of the $2s2p$ state has occurred

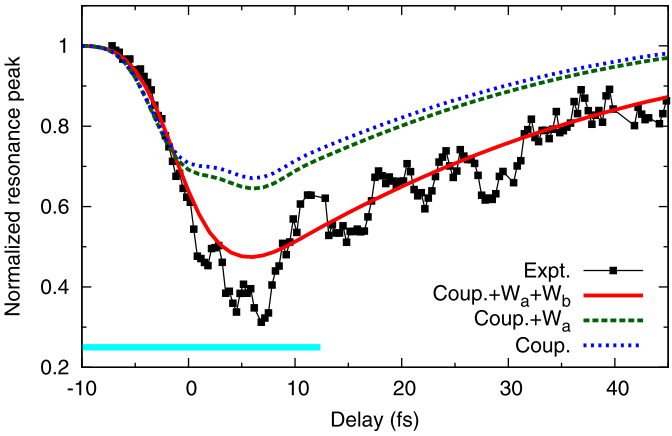

Fig. 7.5 Experimental and theoretical peak values of the $2s2p$ resonance profile. The *cyan bar* indicates the time-delay range where the two pulses overlap. Three sets of theoretical data are shown, where the labels *Coup.*, W_a, and W_b represent the coupling and the ionizations from $2s2p$ and $2p^2$, respectively. For each data set, the signal at $t_0 = -10$ fs is normalized to 1. The experimental data is shifted by 4.5 fs to the positive delay

before the IR acts on the system, and the state is less influenced by the IR, whether by the tunnel ionization or by the coupling to $2p^2$. As shown in Fig. 7.4(c), the profile gradually revives until it reaches the original Fano profile as $t_0 \to \infty$.

Other than the overall depletion and revival, the $2s2p$ profile basically keeps the same shape. Moreover, with the 0.7 eV energy resolution of the spectrometer used in the experiment, no distinguished spectral features can be seen other than the overall depletion, with which the decay lifetime of $2s2p$ can be extracted. In Fig. 7.5, the signal value at the resonance peak is plotted with t_0. As explained earlier, this value drops to the minimum at about $t_0 = 5$ fs, where the IR appears when the autoionization has just started. By adjusting the parameters in the ionization rates, the model agrees with the experiment very well, except an undefined fluctuation in the experimental data, which has not been understood so far. For the analysis, we add two additional calculations to clarify the influence from the tunnel ionization. Without the ionization rate for $2p^2$ (W_b), the depletion is reduced to only half of that with full consideration of all the effects. This is because the binding energy of $2p^2$ (3.3 eV) is much lower than that of $2s2p$ (5.3 eV) so that $2p^2$ is ionized by the IR more easily. We now recognize that both the coupling between the two states and the ionization of $2p^2$ by the IR are responsible for the depletion of the $2s2p$ profile.

Summing up the observation on the simulation and the measurement, the model produces the time-delayed photoelectron spectra of the $2s2p$ resonance that agree well with the experiment by taking the IR coupling and the tunnel ionization into account. Such a three-level photoionization by a single XUV shot has never been modeled before. The Rabi oscillation between the top two levels could potentially change the resonance shape dramatically. However, contradictory to our interest, the

coupling effect is largely smeared and concealed by the tunnel ionization, where the indication of the oscillation does not stand out.

7.4 Photoabsorption of Laser-Coupled Autoionizing States

In spectroscopy, higher spectral resolution is achieved in photoabsorption measurements than in photoelectrons. As demonstrated in Sect. 7.3, detailed study of a resonance profile typically requires electron energy resolution of tens to hundreds meV. In this section, we formulate photoabsorption with the total wavefunction introduced in Sect. 7.3. A simulation is carried out and compared with the experiment by Wang *et al.* [20]. The theory and the simulation were reported in details by us [47].

7.4.1 Model for Photoabsorption

The formulation of photoabsorption in terms of frequency-dependent response function $\tilde{S}(\omega)$ by Gaarde *et al.* [48] is incorporated into our model wavefunction to obtain the absorption spectra.

The total energy absorbed by an atomic system through dipole interaction with a finite light pulse is

$$\Delta U = \int_0^\infty \omega \tilde{S}(\omega)\, d\omega, \tag{26}$$

$$= \int_{-\infty}^\infty \frac{d\mu(t)}{dt} E(t)\, dt, \tag{27}$$

in the energy and time domains, respectively, where ω is the absorbed photon energy, $\mu(t)$ is the dipole moment, and $E(t)$ is the external field. The response function $\tilde{S}(\omega)$ is the probability density of the absorption in the frequency domain, and thus is dubbed "absorption profile". It is related to the absorption cross section by

$$\tilde{\sigma}(\omega) = \frac{4\pi\alpha\omega\tilde{S}(\omega)}{|\tilde{E}(\omega)|^2}, \tag{28}$$

where α is the fine-structure constant. By the Fourier transforms of the real functions $\mu(t)$ and $E(t)$, Eqs. (26)–(27) are combined to give

$$\tilde{S}(\omega) = -2\,\mathrm{Im}\big[\tilde{\mu}(\omega)\tilde{E}^*(\omega)\big], \tag{29}$$

which is positive for absorption and negative for emission.

For the time-dependent wavefunction given by Eq. (21), $\tilde{\mu}(\omega)$ is

$$\tilde{\mu}(\omega) = \frac{1}{\sqrt{2\pi}} \int_{-\infty}^\infty \big[e^{i(\omega_X-\omega)t} u_X(t) + e^{i(\omega_L-\omega)t} u_L(t)\big]\, dt, \tag{30}$$

under the rotating wave approximation, where $u_X(t)$ and $u_L(t)$ are defined by

$$u_X(t) \equiv c_g(t) \int M_E^{ag} c_E^{a*}(t)\, dE, \tag{31}$$

$$u_L(t) \equiv \int c_E^a(t) \int M_{E'E}^{ba} c_{E'}^{b*}(t)\, dE'\, dE, \tag{32}$$

respectively, where M_E^{ag} and $M_{E'E}^{ba}$ are the dipole matrix elements between the eigenstates, i.e.,

$$M_E^{ag} \equiv \langle \psi_E^a | \mu | g \rangle = \frac{\sin \Theta_E^a}{\pi V_a} \mu_{ag} - \cos \Theta_E^a \mu_{E_1 g}, \tag{33}$$

$$M_{E'E}^{ba} \equiv \langle \psi_{E'}^b | \mu | \psi_E^a \rangle = \left(\frac{\sin \Theta_{E'}^b}{\pi V_b} \mu_{ba} - \cos \Theta_{E'}^b \right) \frac{\sin \Theta_E^a}{\pi V_a}. \tag{34}$$

The absorption of the whole target gas is assumed to be linearly proportional to the single-atom response if the gas density is considerably low. Thus, in our simulation, the absorption and transmission profiles are simply taken as $\tilde{S}(\omega)$ and $1 - \tilde{S}(\omega)$, respectively. Since the XUV and laser energies are in general widely separate, the profiles for each of the two pulse is calculated independently by taking only the necessary terms in Eqs. (30) to (34).

7.4.2 Experiments in Argon

Recently, an experiment reported by Wang *et al.* [20] measured the time-delayed XUV transmission spectra in argon to study its autoionization. In the report, the result was analyzed by the simulation based on an earlier model [15, 18]. It concluded that the IR significantly modified the XUV photoabsorption profile and provided a tool for detecting and controlling autoionization. We simulate the experiment and present the comparisons with both the measurement and the calculation therein.

The 140-as SAP covers an energy range from 20 to 40 eV and populates the $[\mathrm{Ne}]3s3p^6np(^1P)$ resonance series in argon. A time-delayed IR pulse with $\lambda_L = 750$ nm and $\tau_L = 7$ fs is applied to the system. Its intensities are 0.5 and 1 TW/cm^2 in two independent arrangements. The energy resolution of the measurement is 50 meV. Figure 7.6(a)–(b) shows the measured transmitted XUV profiles of the $3s3p^64p$ resonance. When the two pulses overlap, the signal is depleted, and the resonance peak roughly shifts upward in energy. As the IR lags behind the XUV, the profile gradually revives toward its Fano lineshape (note that by the convention in Ref. [20], the positive delay is on the left hand side of the plots). The result is similar to the experiment in Sect. 7.3. With two IR intensities, the higher one magnifies the depletion of the transmission, and a break is seen at the overlap of the two pulses.

The simulation in Ref. [20] has been revised after its publication by Zhang [49] recently. The model [15, 18] calculates the total wavefunction of the system that is equivalent to the bound state part of Eq. (15) plus the preliminary continua that are used in the adiabatic elimination. This version of the wavefunction, although unable to derive the photoelectron spectra, preserves the dipole moment quite well since

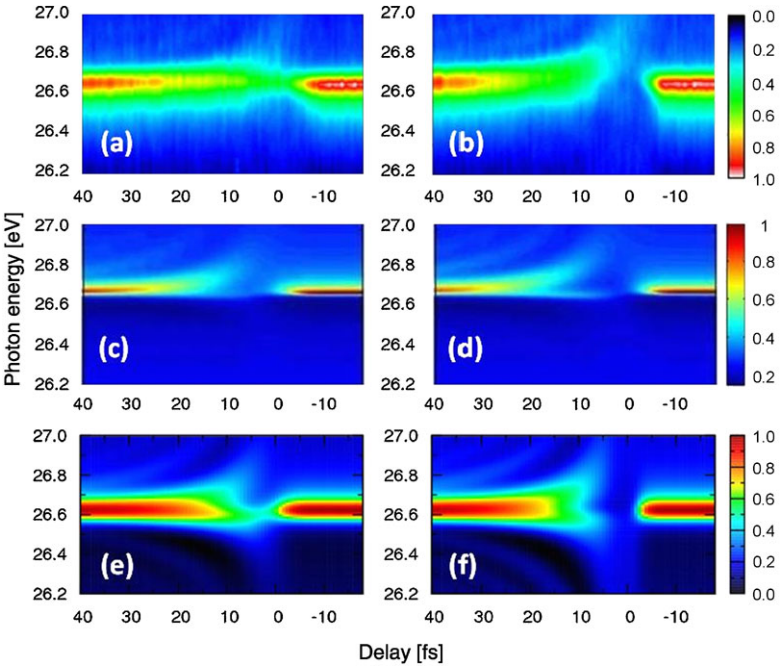

Fig. 7.6 Phototransmission spectrograms of the $3s3p^6 4d$ resonance. The *left* and the *right panels* are for 0.5 and 1 TW/cm^2 IR intensities, respectively. The *top*, *middle*, and *bottom rows* are the measurement and the simulation in Ref. [20], and the present simulation, respectively

the dipole moment is predominantly determined by the bound states. Zhang's simulation, plotted in Fig. 7.6(c)–(d), reproduces the main feature of the measurement, where the resonance profile drops abruptly from the negative delay and ascends slowly at the decay rate of the AIS to the positive delay. However, the difference between the two IR intensities is not as obvious as what the measurement shows; it seems that the simulated IR is not fully responsible for the break representing the strong AIS depletion in the measurement. Comparing our simulation in Fig. 7.6(e)–(f) to Zhang's simulation, the main addition of our model is the IR ionization estimated by the ADK theory, with which the spectral features near the overlap of the pulses are closer to the experiment than the previous ones, including the opening and the stronger upward curved shape of the ridge.

7.5 Resonant Coupling in Autoionizing Helium

By now, we have demonstrated that the dressing laser pulse modifies the electron and absorption profiles by both the coupling between the AISs and their tunnel ionization; however, the effect of the coupling, which serves as the theme of the study, cannot be easily singled out due to the presence of tunneling. Here, we propose a

new XUV-plus-IR scheme in helium where $2s2p$ is coupled to the $2s^2(^1S)$ AIS resonantly with a 540-nm laser pulse. The binding energies for both AISs are high, and the tunnel ionization is totally disregarded; the main dynamics is thus the Rabi oscillation between the AISs. By adjusting the coupling pulse, the resonance profiles can be manipulated more flexibly and forcefully, which would thus provide a tool for the coherent control of electrons and photons. This case study has been proposed and discussed by us for the electron dynamics [40] and photoabsorption [47].

7.5.1 Time-Delayed Electron and Photoelectron Spectra

In the following, we keep the field parameters used in Sect. 7.3 in the helium system but change the laser wavelength to $\lambda_L = 540$ nm. The binding energies of $2s2p$ and $2s^2$ are 5.3- and 7.6-eV, respectively. The dynamics is interpreted only in terms of the coupling between the AISs.

The photoelectron profiles in the $1s\varepsilon p$ and $1s\varepsilon s$ continua, associated with $2s2p$ and $2s^2$, respectively, are calculated against the time delay, as shown in Fig. 7.7(a)–(b). The photoabsorption profiles of the XUV and laser pulses are shown in Fig. 7.7(c)–(d). The four plots are in the same energy and time-delay scales, so their effects in energy and in time can be compared visually. Practically, the absorption signal is adequate only when it is comparable to the incident light signal, i.e., the total light intensity must not overwhelm the absorbed intensity along its propagation through the medium. This has not been considered in our single-atom model. Note that most previous studies concerned only the XUV spectra that are near the resonance energy, while we include the laser spectra which contains abundant controlling features and supports the understanding of the dynamics.

As shown in Fig. 7.7(a)–(b), The dramatic modifications on both electron profiles, including the enhancement, splitting, and inversion of the profile shapes, are sensitively controlled by the time delay. As the delay shifts from $t_0 = -5$ to 5 fs, the $2s2p$ profile evolves from the Fano lineshape to almost its mirror image in energy, i.e., the spectra flips upside down in Fig. 7.7(a) across $t_0 = 0$, in addition to the overall reduction in signal strength; the $2s^2$ profile is maximized for $0 < t_0 < 5$ fs. The pulse area of the 0.7 TW/cm^2 laser is $A = 1.6\pi$, which means that the Rabi oscillation runs 0.8 cycle between the AISs. While the laser appears right after the XUV, most electrons in $2s2p$ are driven to $2s^2$ before they could autoionize. Then, about half of the electrons stay in $2s^2$, while the others swing back to $2s2p$, before both states autoionize. The electrons going back to $2s2p$ change their phase by π due to the Rabi flopping, where the Fano q-parameter changes sign, resulting in the inverse image at $t_0 = 5$ fs. This mechanism is also evident in the very strong peak in Fig. 7.7(b). As t_0 increases, since the laser appears later in the decay of $2s2p$, more electrons are autoionized to from the $2s2p$ profile before the rest are brought to $2s^2$ by the Rabi oscillation. Fewer electrons make a round trip to $2s^2$ and back to $2s2p$, and more electrons never leave $2s2p$. The population without experiencing Rabi flopping grows, which is shown in Fig. 7.7(a) by the lower ridge that merges

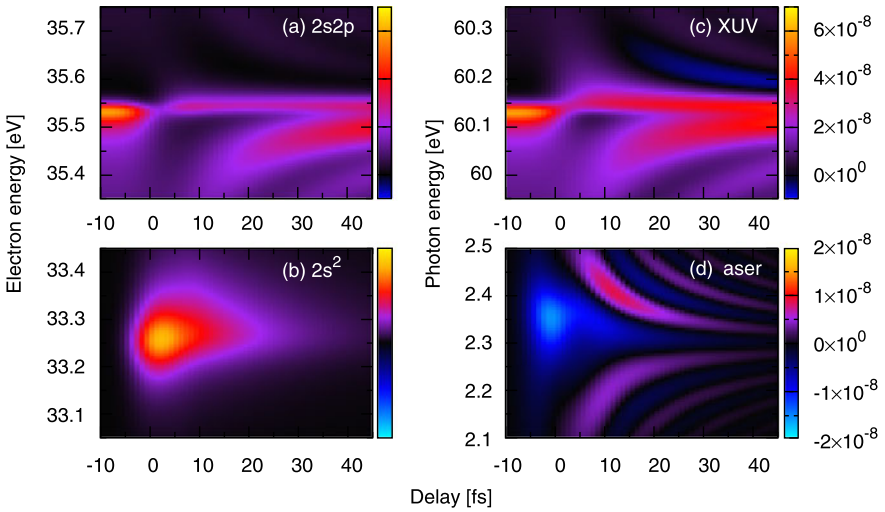

Fig. 7.7 Photoelectron spectrograms for the (**a**) $2s2p$ and (**b**) $2s^2$ resonances, and photoabsorption spectrograms of the (**c**) XUV and (**d**) laser pulses. The *blue* and *cyan colors* appearing in (**c**) and (**d**) represent the negative absorption, or in effect, the photoemission. The *upper* (*lower*) *panels* share the same color codes

upward to meet the inverse profile shape. When the time delay long passes the 17-fs decay lifetime of $2s2p$, all the electrons in $2s2p$ autoionize without ever influenced by the laser, and no electrons show up in $2s^2$. Consequently, the $2s2p$ profile resumes the original Fano lineshape, and the $2s^2$ profile attenuates to zero.

The XUV absorption spectra are similar to the $2s2p$ electron spectra in the general appearance but with higher signals for $t_0 > 0$. This is understood where the XUV absorption is the only path for the electrons to be excited from the ground state, while the excited electrons are distributed between the two resonances at the end. In other words, the XUV primarily supplies the $2s2p$ electrons, but with the existence of the laser, it also supplies the "additional" $2s^2$ electrons via the laser coupling. As for the laser absorption, as shown in Fig. 7.7(d), the spectra appear to be complicated. The large negative peak at 2.35 eV near $t_0 = 0$ represents the light emission corresponding to the population transfer from $2s2p$ to $2s^2$. As t_0 increases, the laser emission and absorption generate the interference pattern.

7.5.2 Wavelength and Intensity Dependence

For a given XUV light, the electron and absorption spectra change significantly with the dressing laser pulse. Here we examine how the laser wavelength and intensity manipulate the spectra, where the duration $\tau_L = 9$ fs and the time delay $t_0 = 15$ fs are unchanged.

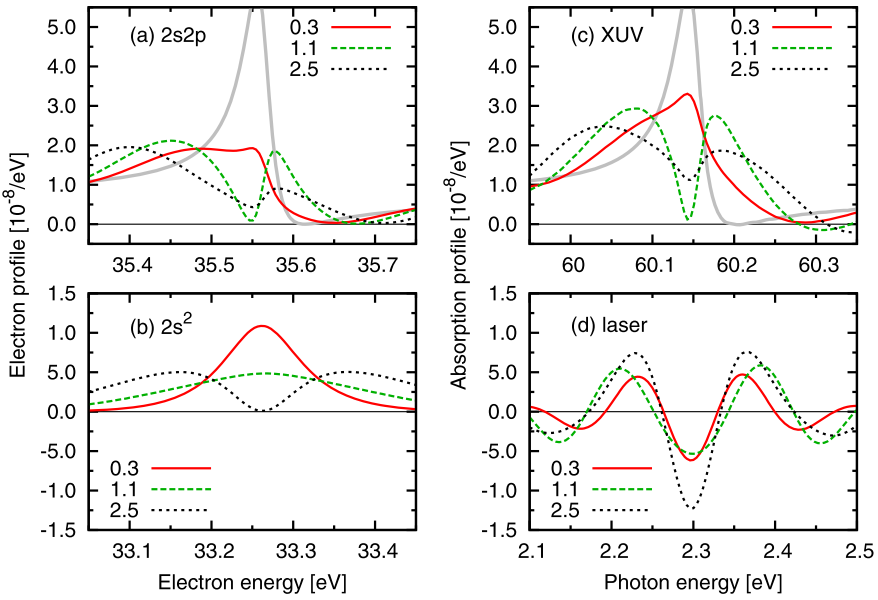

Fig. 7.8 Photoelectron spectra of the (**a**) $2s2p$ and (**b**) $2s^2$ resonances, and photoabsorption spectra of the (**c**) XUV and (**d**) laser pulses, for a fixed 540-nm wavelength and the intensities of 0.3, 1.1, and 2.5 TW/cm^2 of the laser. The negative signals of the absorption represent photoemission. The Fano lineshape is shown in the *gray curve* as a reference. The *black horizontal line* labels zero

In Fig. 7.8, the profiles are shown for peak intensities $I_L = 0.3$, 1.1, and 2.5 TW/cm^2, where the pulse areas are $A = \pi$, 2π, and 3π, respectively, with fixed $\lambda_L = 540$ nm. For $I_L = 0.3$ TW/cm^2, the π-pulse mainly brings the electrons from $2s2p$ to $2s^2$ in a one-way route; the $2s2p$ profile is strongly suppressed and the $2s^2$ profile is highly populated. As I_L proceeds to 1.1 TW/cm^2, the Rabi oscillation forms a round trip in the pulse duration. The $2s^2$ bound electrons return to $2s2p$, and the $2s^2$ profile flattens. As explained previously, the returning electrons carry a phase change of π, and the inverse q is materialized in the mirror peak image at $E \approx 35.6$ eV in Fig. 7.8(a). The $2s2p$ electrons that autoionize before the laser ($t_0 = 15$ fs) form the broad peak at $E = 35.45$ eV. If the intensity increases to $I_L = 2.5$ TW/cm^2, the $2s2p$ electrons move to $2s^2$ again, and the $2s2p$ profile depresses. The electrons relocating to $2s^2$ in the second Rabi cycle unite the electrons already there, and the two groups interfere to form the double-peak profile in Fig. 7.8(b). The same dynamics interprets the XUV profiles in Fig. 7.8(c), which are synonymous with the $2s2p$ electron profiles but having higher signal intensities. As for the laser spectra in Fig. 7.8(d), we observe that by increasing I_L, both the emission and the absorption signals heighten equally, while the profile shapes basically keep the same.

We have kept the laser in the perfect resonance condition so far, i.e., the detuning between the AISs is 0. However, since the laser duration is comparable to the decay

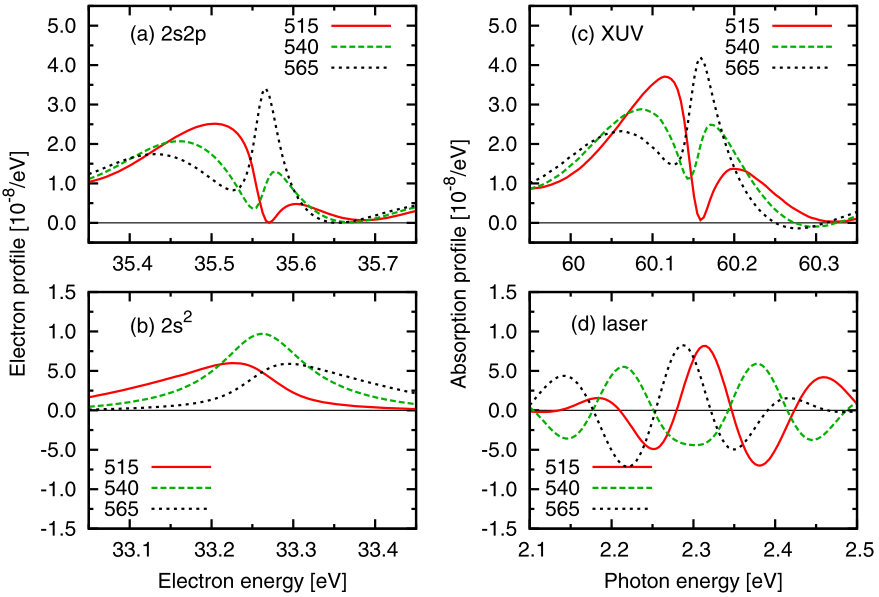

Fig. 7.9 As of Fig. 7.8 but for a fixed 0.7 TW/cm^2 laser intensity and the wavelength of 515, 540, and 565 nm

lifetime, the bandwidth is not wide enough to always cover the resonance region well. Thus, the dependence of the dynamics on the detuning should be taken into account. In Fig. 7.9, the spectra are shown for $I_L = 0.7$ TW/cm^2 and three wavelengths $\lambda_L = 515$, 540, and 565 nm, or the photon energies of $\omega_L = 2.41$, 2.30, and 2.19 eV, respectively. Relative to the perfect resonance condition, the laser profile in Fig. 7.9(d) shifts upward (downward), and the $2s^2$ profile in Fig. 7.9(b) shifts downward (upward), for higher (lower) laser frequency (note that $2s^2$ is the lower-energy AIS). Similar shifts are also seen in the $2s2p$ resonances in Fig. 7.9(a) and the XUV spectra in Fig. 7.9(c); nonetheless, the strong indications for the resonance position, at 35.55 eV electron energy or 60.15 eV photon energy, are unaffected by the laser detuning.

The analysis above show that additional to the time delay between the pulses, the laser intensity and wavelength also manipulate the outcome of the electron and photon spectra in various and sensational ways. These possibilities are provided where Rabi oscillation is the dominant mechanism, and tunnel ionization is too weak to smear the sharp contrasts produced in the spectra. The subtle changes in the spectra, such as the splitting and the flipping of the resonance shape, are measurable only when the spectrometer resolution is well beyond the energy scale of a single resonance. Considering both resolution and efficiency, the measurement of light rather than electrons is more suitable to study the laser manipulation of autoionization.

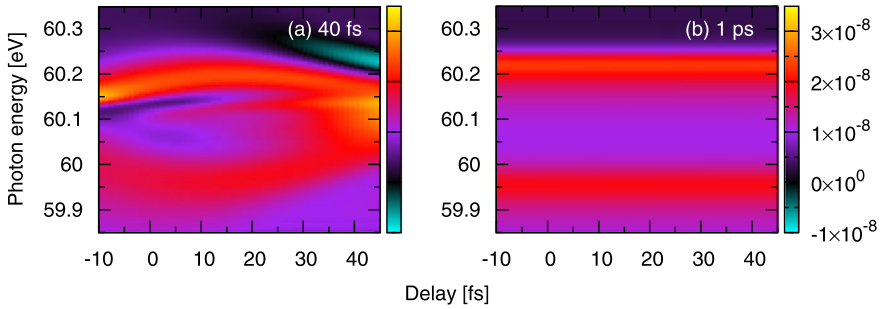

Fig. 7.10 Photoabsorption spectrograms for $\lambda_L = 540$ nm, $I_L = 0.7$ TW/cm^2, and the laser durations τ_L of (**a**) 40 fs and (**b**) 1 ps

7.5.3 Dependence on Pulse Duration

In a pump-probe experiment, the light pulses are ideally shorter than the time scale of the dynamics being studied. This is satisfied in the current case study with an 100-as XUV and a 9-fs laser. However, in the traditional study of a dressed system, the dressing field is long, and it is to change the property of the material rather than the dynamic process. In the following, we will study the transition between short and long dressing fields using the present model.

For the two primary electron dynamics of the $2s2p$ resonance, the autoionization has a decay lifetime of 17 fs, and the Rabi oscillation between $2s2p$ and $2s^2$ has a period of 15.6 fs, evaluated at the 0.7 TW/cm^2 pulse peak, of 15.6 fs. In other words, both dynamic processes have roughly the same speed, and the 9-fs laser pulse, which is shorter than these dynamics, provides a qualified temporal resolution. In Fig. 7.10, we show the XUV absorption spectrograms for two longer dressing pulses, $\tau_L =$ 40 fs and 1 ps, compared with the short dressing case in Fig. 7.7(c). For $\tau_L = 40$ fs, many spectral features seen for $\tau_L = 9$ fs, such as the inverse q and the exponential revival of the Fano peak along t_0, disappear. The major effect is the splitting of the resonance peak between $t_0 = -10$ and 30 fs. The temporal dependence is confined by the 40-fs pulse duration, and thus the autoionization and the Rabi flopping cannot be resolved anymore. Nonetheless, by changing the delay, the magnitude of the splitting can still be controlled. For $t_L = 1$ ps, as shown in Fig. 7.10(b), the time delay becomes meaningless while any temporal dependence is totally washed out in the spectrogram. The system is reduced to a simple ac dressed system. The EIT condition is recovered, where an Autler–Townes doublet [50] is seen with the energy splitting of 0.26 eV.

Autler–Townes doublet is interpreted as the splitting of an energy level due to the diagonalization of the Hamiltonian when the external field contributes the coupling terms. Essentially, the $\tau_L = 40$ fs case just produces a tunable doublet that exists before the AISs decay, i.e., have the two states been actually bound states, the tunability would vanish. This type of temporal control of EIT has been studied experimentally by Loh *et al.* [45] and theoretically by Tarana and Greene [46] with

the $2s2p$ and $2p^2$ AISs in helium. In brief, we have demonstrated the spectral features in an autoionizing system controlled by a coupling laser pulse whose duration is compared with the autoionization and the Rabi oscillation in the system.

7.6 Summary

This chapter aims to utilize the SAP to study and to control the electron and photon dynamics in an autoionizing system. The evolving wave packet for an isolated Fano resonance is calculated in energy and in space analytically by incorporating Fano's theory. For the recently available SAP-plus-IR experiments, we expand a previous three-level model to contemplate the photoelectrons promoted by the broadband XUV pulse. By including tunnel ionization, the simulated electron emission and photoabsorption of the laser-coupled AISs achieve good agreements with the measurements. To maximize the degree of manipulation in the autoionization dynamics, we propose a scheme where the Rabi oscillation between the two AISs surpasses the tunneling effect, and the electron and light spectra sensitively depend on the dressing parameters. The results show a promising ability of coherent quantum control in the attosecond timescale.

Acknowledgements This work was supported in part by Chemical Sciences, Geosciences and Biosciences Division, Office of Basic Energy Sciences, Office of Science, U.S. Department of Energy. W.-C.C. greatly appreciates the discussions with Steve Gilbertson, Chang-Hua Zhang, and He Wang.

References

1. P.B. Corkum, F. Krausz, Attosecond science. Nat. Phys. **3**, 381–387 (2007)
2. F. Krausz, M. Ivanov, Attosecond physics. Rev. Mod. Phys. **81**, 163–234 (2009)
3. G. Sansone, L. Poletto, M. Nisoli, High-energy attosecond light sources. Nat. Photonics **5**, 655–663 (2011)
4. M. Hentschel, R. Kienberger, Ch. Spielmann, G.A. Reider, N. Milosevic, T. Brabec, P. Corkum, U. Heinzmann, M. Drescher, F. Krausz, Attosecond metrology. Nature **414**, 509–513 (2001)
5. M. Drescher, M. Hentschel, R. Kienberger, M. Uiberacker, V. Yakovlev, A. Scrinzi, Th. Westerwalbesloh, U. Kleineberg, U. Heinzmann, F. Krausz, Time-resolved atomic inner-shell spectroscopy. Nature **419**, 803–807 (2002)
6. M. Uiberacker et al., Attosecond real-time observation of electron tunnelling in atoms. Nature **446**, 627–632 (2007)
7. M. Schultze et al., Delay in photoemission. Science **328**, 1658–1662 (2010)
8. F. Kelkensberg et al., Molecular dissociative ionization and wave-packet dynamics studied using two-color XUV and IR pump-probe spectroscopy. Phys. Rev. Lett. **103**, 123005 (2009)
9. G. Sansone et al., Electron localization following attosecond molecular photoionization. Nature **465**, 763–766 (2010)
10. A.L. Cavalieri, Attosecond spectroscopy in condensed matter. Nature **449**, 1029–1032 (2007)
11. S. Cavalieri, R. Eramo, Time-delay spectroscopy of autoionizing resonances. Phys. Rev. A **58**, R4263–R4266 (1998)

12. M. Wickenhauser, J. Burgdörfer, F. Krausz, M. Drescher, Time resolved Fano resonances. Phys. Rev. Lett. **94**, 023002 (2005)
13. Th. Mercouris, Y. Komninos, C.A. Nicolaides, Time-dependent formation of the profile of the He $2s2p\ ^1P^o$ state excited by a short laser pulse. Phys. Rev. A **75**, 013407 (2007)
14. E. Skantzakis, P. Tzallas, J.E. Kruse, C. Kalpouzos, O. Faucher, G.D. Tsakiris, D. Charalambidis, Tracking autoionizing-wave-packet dynamics at the 1-fs temporal scale. Phys. Rev. Lett. **105**, 043902 (2010)
15. P. Lambropoulos, P. Zoller, Autoionizing states in strong laser fields. Phys. Rev. A **24**, 379–397 (1981)
16. H. Bachau, P. Lambropoulos, R. Shakeshaft, Theory of laser-induced transitions between autoionizing states of He. Phys. Rev. A **34**, 4785–4792 (1986)
17. L.B. Madsen, P. Schlagheck, P. Lambropoulos, Laser-induced transitions between triply excited hollow states. Phys. Rev. Lett. **85**, 42–45 (2000)
18. S.I. Themelis, P. Lambropoulos, M. Meyer, Ionization dynamics in double resonance involving autoionizing states in helium: the effect of pulse shapes. J. Phys. B, At. Mol. Opt. Phys. **37**, 4281–4293 (2004)
19. N.E. Karapanagioti, O. Faucher, Y.L. Shao, D. Charalambidis, H. Bachau, E. Cormier, Observation of autoionization suppression through coherent population trapping. Phys. Rev. Lett. **74**, 2431–2434 (1995)
20. H. Wang, M. Chini, S. Chen, C.-H. Zhang, F. He, Y. Cheng, Y. Wu, U. Thumm, Z. Chang, Attosecond time-resolved autoionization of argon. Phys. Rev. Lett. **105**, 143002 (2010)
21. S. Gilbertson, M. Chini, X. Feng, S. Khan, Y. Wu, Z. Chang, Monitoring and controlling the electron dynamics in helium with isolated attosecond pulses. Phys. Rev. Lett. **105**, 263003 (2010)
22. S.E. Harris, J.E. Field, A. Imamoglu, Nonlinear optical processes using electromagnetically induced transparency. Phys. Rev. Lett. **64**, 1107–1110 (1990)
23. M. Fleischhauer, A. Imamoglu, J.P. Marangos, Electromagnetically induced transparency: optics in coherent media. Rev. Mod. Phys. **77**, 633–673 (2005)
24. M.D. Lukin, Trapping and manipulating photon states in atomic ensembles. Rev. Mod. Phys. **75**, 457–472 (2003)
25. T.E. Glover, M.P. Hertlein, S.H. Southworth, T.K. Allison, J. van Tilborg, E.P. Kanter, B. Krässig, H.R. Varma, B. Rude, R. Santra, A. Belkacem, L. Young, Controlling X-rays with light. Nat. Phys. **6**, 69–74 (2010)
26. E. Ignesti, R. Buffa, L. Fini, E. Sali, M.V. Tognetti, S. Cavalieri, Frequency shift by optical coherent control. Phys. Rev. A **81**, 023405 (2010)
27. E. Ignesti, R. Buffa, L. Fini, E. Sali, M.V. Tognetti, S. Cavalieri, Controlling the spectrum of light pulses by dynamical electromagnetically induced transparency. Phys. Rev. A **83**, 053411 (2011)
28. U. Fano, Effects of configuration interaction on intensities and phase shift. Phys. Rev. **124**, 1866–1878 (1961)
29. H. Kjeldsen, Photoionization cross sections of atomic ions from merged-beam experiments. J. Phys. B, At. Mol. Opt. Phys. **39**, R325–R377 (2006)
30. D.H. Bilderback, P. Elleaume, E. Weckert, Review of third and next generation synchrotron light sources. J. Phys. B, At. Mol. Opt. Phys. **38**, S773–S797 (2005)
31. J.B. West, Photoionization of atomic ions. J. Phys. B, At. Mol. Opt. Phys. **34**, R45–R91 (2001)
32. W.-C. Chu, C.D. Lin, Theory of ultrafast autoionization dynamics of Fano resonances. Phys. Rev. A **82**, 053415 (2010)
33. W.-C. Chu, H.-L. Zhou, A. Hibbert, S.T. Manson, Photoionization of the Be isoelectronic sequence: total cross sections. J. Phys. B, At. Mol. Opt. Phys. **42**, 205003 (2009)
34. R. Wehlitz, D. Lukić, J.B. Bluett, Resonance parameters of autoionizing Be $2pnl$ states. Phys. Rev. A **68**, 052708 (2003)
35. T. Remetter et al., Attosecond electron wave packet interferometry. Nat. Phys. **2**, 323–326 (2006)

36. E. Goulielmakis, V.S. Yakovlev, A.L. Cavalieri, M. Uiberacker, V. Pervak, A. Apolonski, R. Kienberger, U. Kleineberg, F. Krausz, Attosecond control and measurement: lightwave electronics. Science **317**, 769–775 (2007)
37. J. Mauritsson, P. Johnsson, E. Mansten, M. Swoboda, T. Ruchon, A. L'Huillier, K.J. Schafer, Coherent electron scattering captured by an attosecond quantum stroboscope. Phys. Rev. Lett. **100**, 073003 (2008)
38. M. Kitzler, N. Milosevic, A. Scrinzi, F. Krausz, T. Brabec, Quantum theory of attosecond XUV pulse measurement by laser dressed photoionization. Phys. Rev. Lett. **88**, 173904 (2002)
39. Z.X. Zhao, C.D. Lin, Theory of laser-assisted autoionization by attosecond light pulses. Phys. Rev. A **71**, 060702R (2005)
40. W.-C. Chu, S.-F. Zhao, C.D. Lin, Laser-assisted-autoionization dynamics of helium resonances with single attosecond pulses. Phys. Rev. A **84**, 033426 (2011)
41. M.V. Ammosov, N.B. Delone, V.P. Krainov, Tunnel ionization of complex atoms and of atomic ions in an alternating electromagnetic field. Sov. Phys. JETP **64**, 1191–1194 (1986)
42. A.M. Perelomov, V.S. Popov, M.V. Terent'ev, Ionization of atoms in an alternating electric field. Sov. Phys. JETP **23**, 924 (1966)
43. M. Domke, K. Schulz, G. Remmers, G. Kaindl, D. Wintgen, High-resolution study of $^1P^o$ double-excitation states in helium. Phys. Rev. A **53**, 1424–1438 (1996)
44. A. Burgers, D. Wintgen, J.-M. Rost, Highly doubly excited S states of the helium atom. J. Phys. B **28**, 3163–3183 (1995)
45. Z.-H. Loh, C.H. Greene, S.R. Leone, Femtosecond induced transparency and absorption in the extreme ultraviolet by coherent coupling of the He $2s2p$ ($^1P^o$) and $2p^2$ ($^1S^e$) double excitation states with 800 nm light. Chem. Phys. **350**, 7–13 (2008)
46. M. Tarana, C.H. Greene, Femtosecond transparency in the extreme-ultraviolet region. Phys. Rev. A **85**, 013411 (2012)
47. W.-C. Chu, C.D. Lin, Photoabsorption of attosecond XUV light pulses by two strongly laser-coupled autoionizing states. Phys. Rev. A **85**, 013409 (2012)
48. M.B. Gaarde, C. Buth, J.L. Tate, K.J. Schafer, Transient absorption and reshaping of ultrafast XUV light by laser-dressed helium. Phys. Rev. A **83**, 013419 (2011)
49. C.-H. Zhang, Private communication
50. S.H. Autler, C.H. Townes, Stark effect in rapidly varying fields. Phys. Rev. **100**, 703–722 (1955)

Chapter 8
Attosecond Absorption Spectroscopy

Michael Chini, He Wang, Baozhen Zhao, Yan Cheng, Shouyuan Chen, Yi Wu, and Zenghu Chang

Abstract Photoabsorption spectroscopy with isolated attosecond pulses provides a means for all-optical time-domain measurement of ultrafast dynamics in bound and quasi-bound states of atoms and molecules, as well as near absorption edges in condensed matter systems. Due to the strong oscillator strength in atoms and molecules in the extreme ultraviolet and soft X-ray spectral regions as well as the high detection efficiency of the transmitted photon signal, attosecond transient absorption spectroscopy is an attractive alternative to traditional photoelectron spectroscopy techniques. We present measurements of the laser-perturbed photoabsorption of helium 1s*n*p singly excited states and quasi-bound autoionizing states of argon with a few-femtosecond autoionization lifetime. In both systems, we observe laser-induced changes in the photoabsorption spectrum which evolve on the single-femtosecond timescale, faster than the laser light oscillation period.

8.1 Introduction

Isolated attosecond optical pulses have in the last decade allowed first access to time-domain measurements of the fastest dynamics of a chemical reaction—the dynamics of the electron [4, 25]. However, due to the low photon flux of isolated attosecond pulses, attosecond science has been unable to take advantage of the wealth of spectroscopic techniques developed for chemical and biological applications with femtosecond lasers, most of which require interaction of the sample with one (or more) photons from both a "pump" pulse and a delayed "probe" pulse of the laser. Instead, pump-probe studies using isolated attosecond pulses have so far only been performed using an intense, few-cycle femtosecond pulse as either the pump or the probe.

M. Chini · Y. Cheng · Y. Wu · Z. Chang (✉)
CREOL and Department of Physics, University of Central Florida, 4000 Central Florida Blvd, Orlando, FL 32816, USA
e-mail: Zenghu.Chang@ucf.edu

H. Wang · B. Zhao · S. Chen
J. R. Macdonald Laboratory, Department of Physics, Kansas State University, Manhattan, KS 66506, USA

K. Yamanouchi, K. Midorikawa (eds.), *Progress in Ultrafast Intense Laser Science*, Springer Series in Chemical Physics 104, DOI 10.1007/978-3-642-35052-8_8,

Nearly all attosecond measurements have so far relied on attosecond "streaking" spectroscopy, which is based in pump-probe photoelectron spectroscopy [20, 23]. In attosecond streaking, the attosecond pulse produces free electrons by single-photon ionization of the target (gas or solid) with ionization potential I_p smaller than the photon energies included in the attosecond pulse spectrum. The kinetic momentum of the continuum electron wavepacket is then modified by interaction with a moderately intense ($I_0 \sim 10^{12}$ W/cm^2) streaking laser pulse (typically in the NIR), with the energy shift approximately following the vector potential of the streaking laser. The kinetic energy distribution of the laser-modified photoelectron spectrum is then detected as a function of the delay between the attosecond pulse and the NIR laser pulse. Because the streaking laser electric field varies rapidly within one optical cycle, the attosecond streaking technique is capable of measuring sub-laser-cycle events with attosecond time resolution and has been used extensively to measure the attosecond pulse duration [7, 9, 16, 34]. More recently, attosecond streaking and similar techniques have been used to perform time-domain measurements of the autoionization lifetime in doubly-excited states of helium [13], time-domain interferences between electron wavepackets from different ionization pathways [32], as well as intrinsic time delays in photoionization of electrons from core and conduction bands in condensed matter [2] and from core and valence orbitals in atoms [36].

However, attosecond streaking and other photoelectron spectroscopy techniques have two distinct disadvantages. The first is a fundamental limitation: photoelectron spectroscopy relies on the measurement of free electrons which are the product of ionization by the attosecond pulse. This requirement limits the scope of experiments to allow only measurement of dynamic processes which result in ionization (for example, experiments which probe the photoionization process itself or electron emission through autoionization or Auger processes). On the other hand, dynamic chemical processes of interest are often initiated by photo*excitation* rather than photo*ionization*, and interpretation of the ultrafast electron dynamics from the emitted photoelectron spectrum is difficult. The second is a practical limitation: attosecond streaking experiments suffer from extremely low count rates (typically $\sim$1 photoelectron per laser shot) due to the low photon flux of currently available attosecond light sources, the limited transmission of metal filters used to isolate the attosecond pulse from the driving laser, and the low probability of photoionization of the target, resulting in a tradeoff between integration time and signal-to-noise ratio [43]. Although significant effort is currently being invested in generating high-flux attosecond sources [5, 10, 15, 22, 31, 35, 37, 39], measurements of multi-electron dynamics will require coincident detection of multiple electrons as well as the positive ions, further complicating the experiments and limiting the available count rate.

Attosecond transient absorption spectroscopy offers an attractive alternative to attosecond streaking and other photoelectron spectroscopy techniques which resolves the disadvantages of photoelectron spectroscopy and yields complimentary information on the target. Because transient photoabsorption spectroscopy measures changes in the photoabsorption (dipole) spectrum induced by the NIR laser and not

only the electron or ion yields, it allows for dynamic study of all processes initiated by photoabsorption, including photoexcitation to bound [17, 19] and quasi-bound states [28, 44] as well as photoionization [27]. When performed with isolated attosecond pulses, the broad continuous spectrum of the attosecond pulse allows study of several of these bound or quasi-bound states, such as in excited state manifolds, simultaneously and unambiguously. Furthermore, because transient absorption spectroscopy relies only on the measurement of the light spectrum transmitted through the target medium, it benefits from the large number of available photons as well as the relatively high detection efficiency for photons in the XUV and soft X-ray wavelength regions, thereby reducing the necessary integration time. In this chapter, we will present an experimental apparatus for transient absorption spectroscopy and describe two experiments in which time-resolved laser-induced changes in the absorption structures corresponding to singly-excited bound states ($1snp$) of helium and core-excited quasi-bound states ($3s3p^6np$) in argon were measured using isolated attosecond pulses. Our results clearly show changes in the photoabsorption which occur within one femtosecond, faster than the oscillation period of the dressing laser.

8.2 Experimental Setup for Attosecond Transient Absorption Spectroscopy

Figure 8.1 shows the experimental setup for attosecond transient absorption spectroscopy [44]. The setup consists of Mach–Zehnder type interferometer with a variable delay introduced between the two interferometer arms. The 1.2 mJ, 6 fs NIR laser pulses with 1 kHz repetition rate, which were produced by compressing 30 fs pulses from a commercially available regenerative amplifier (Coherent Legend Elite Duo™) using a neon-filled hollow-core fiber and chirped mirror pulse compressor, were split into the two arms of the interferometer by a broadband dielectric beamsplitter. The spectrum and temporal profile of the laser, as measured by FROG, are shown in Fig. 8.2.

In one arm of the interferometer, half of the laser energy was used to drive the generation of the isolated attosecond pulses, which then passed through a 300 nm aluminum foil filter to block the residual NIR and compensate the intrinsic chirp of the attosecond pulses and were focused by a toroidal mirror ($f = 250$ mm, 9.6 degree grazing incidence angle) through the hole in a hole-drilled mirror. In the other arm, the other half of the pulse was sent through an equal optical path length before being recombined with the attosecond pulse with a variable time delay controlled by a piezoelectric transducer (PZT) stage (PhysikInstrumente P-752.1 CD), focused by a lens ($f = 420$ mm) and recombined collinearly with the attosecond pulse upon reflection by the hole-drilled mirror.

The two pulses were focused together to the target gas cell, in which the absorption occurred. The XUV light then passed through a second aluminum foil filter in

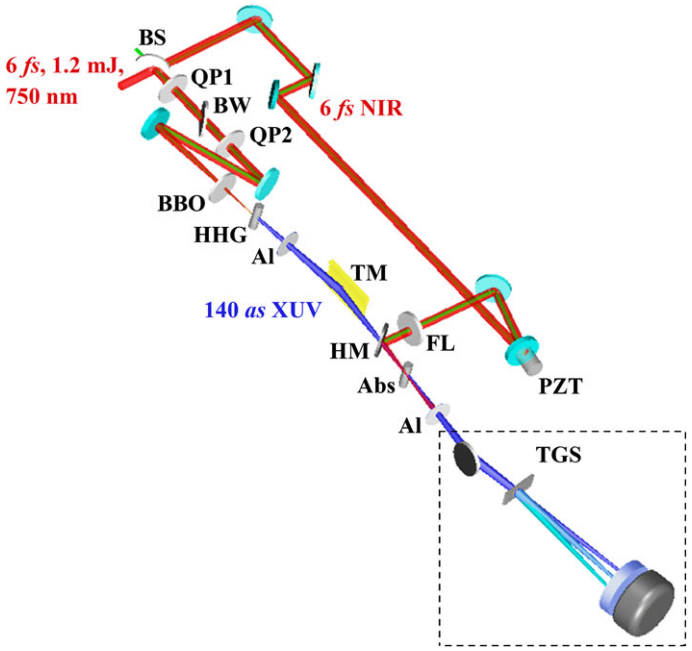

Fig. 8.1 Experimental setup for attosecond transient absorption. The input laser is 6 fs in duration, with 1.2 mJ pulse energy with 750 nm central wavelength. The components are *BS*: broadband beamsplitter; *QP1* and *QP2*, *BW*, and *BBO*: quartz plates, Brewster window, and second harmonic generation crystal for generalized double optical gating; *Al*: aluminum filters; *TM*: toroidal focusing mirror; *HM*: hole-drilled flat mirror; *PZT*: piezoelectric transducer stage; *FL*: focusing lens; *Abs*: absorption cell; *TGS*: transmission grating spectrometer

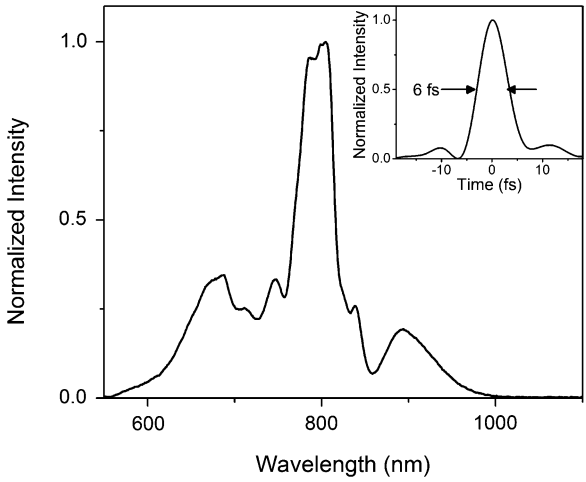

Fig. 8.2 Spectrum of the laser pulse after the hollow-core fiber and chirped mirror pulse compressor. The *inset* shows the 6 fs pulse retrieved from FROG

order to block the NIR light and was then dispersed using a transmission grating spectrometer [33] onto an MCP/phosphor detector which was imaged using a CCD camera. The transmitted XUV spectrum was recorded as a function of the time delay between the attosecond pulse and the NIR pulse.

8.2.1 Isolated Attosecond Pulses from Generalized Double Optical Gating

Most atoms and molecules have the bulk of their oscillator strength in the XUV wavelength region, corresponding to transitions from the atomic ground state to near threshold excited bound and quasi-bound states. For example, both the helium $1snp$ bound states and the argon $3s3p^6np$ autoionizing states in which we are interested lie between 20 and 30 eV above their respective atomic ground states. Therefore, in order to probe these states, it is necessary to have an attosecond source with spectrum spanning this spectral region.

In order to generate such attosecond pulses, we utilized the generalized double optical gating technique (GDOG) [9]. Double optical gating [30], which is a combination of polarization gating and two-color gating, exploits the dependence of high harmonic generation on the ellipticity of the driving laser field. Whereas for linearly polarized light, the recombination process which results in attosecond pulse generation has a relatively high probability, elliptically polarized light will drive the electron away from its parent ion and strongly reduces the probability of recombination. However, this ellipticity dependence depends upon the harmonic order, as electrons with larger excursions will be more strongly affected by the elliptically polarized laser. Therefore, the lower order plateau harmonics, such as those between 20 and 30 eV, are less susceptible to the elliptical field and are more difficult to "gate" than the cutoff orders. For this reason, we use the generalized double optical gating, which results in a narrow gate width for even the lowest orders. Generalized double optical gating also has the advantage that it can be used with lasers which do not have carrier-envelope phase stabilization [14], as the gate width can be made to be much less than one optical cycle, allowing generation of only a single attosecond pulse.

To generate the two-color field with time-dependent ellipticity for the generalized optical gating, the 6 fs laser pulse was sent through the GDOG optics [9, 12], consisting of two quartz plates, a pair of Brewster angle windows to reject a portion of the driving field, and a BBO crystal. The laser was then focused by a spherical mirror ($f = 350$ mm) to a gas cell (ID = 1 mm) filled with 20 Torr of argon gas in which the isolated attosecond pulses were generated. The attosecond pulses were characterized separately in an attosecond streak camera and the pulse duration retrieved by the PROOF technique [7] was $\sim$140 as.

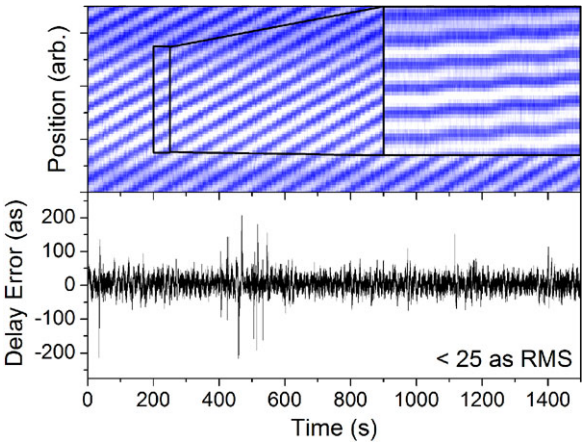

Fig. 8.3 Interferometer delay scan with locking. (*Top*) Spatial interference fringes from the green laser beam as a function of time. The delay was scanned in steps of 280 as in this case, remaining at each delay for 10 seconds before moving to the next step over 3 seconds. This step-like structure can be seen in the *inset*. (*Bottom*) Error between measured and desired delay. The RMS delay error is less than 25 as

8.2.2 Delay Control

The time delay between the XUV and NIR laser was introduced by a PZT stage. In order to control the delay on the attosecond timescale and to minimize the effects of vibration as well as thermally- and acoustically-induced changes to the optical path length during the experiment, a continuous wave green laser ($\lambda = 532$ nm) was co-propagated in both arms of the interferometer [6]. The green laser beam path utilized the same optics as the XUV and NIR laser beams. The aluminum foil filter following the attosecond pulse generation was mounted to a fused silica substrate, which allowed the outer parts of the green laser beam to pass and reflect from the toroidal mirror. A portion of the green laser was then reflected from the backside of the hole-drilled mirror. Similarly, in the other arm of the interferometer, the green laser co-propagated with the NIR laser, and a portion was transmitted through the hole in the hole-drilled mirror. Spatial interference fringes between the two paths were detected outside the vacuum chamber using a CCD camera. Spatial shifts of the interference fringes corresponded to changes in the optical path length, which could be corrected by feeding back to the PZT. Furthermore, attosecond time delays between the XUV and NIR pulse could be introduced by measurement of the phase shift in the green laser beams and control of the PZT. Figure 8.3 shows a typical measurement of the spatial fringe pattern as the delay is scanned during the experiment. The delay control has accuracy better than 25 as.

8.2.3 Absorption Gas Cell

When the XUV pulse passes through the target gas cell, it is partially absorbed. The transmission function can be expressed as:

$$T(\omega) = \exp\left[-\rho\sigma(\omega)L\right],$$

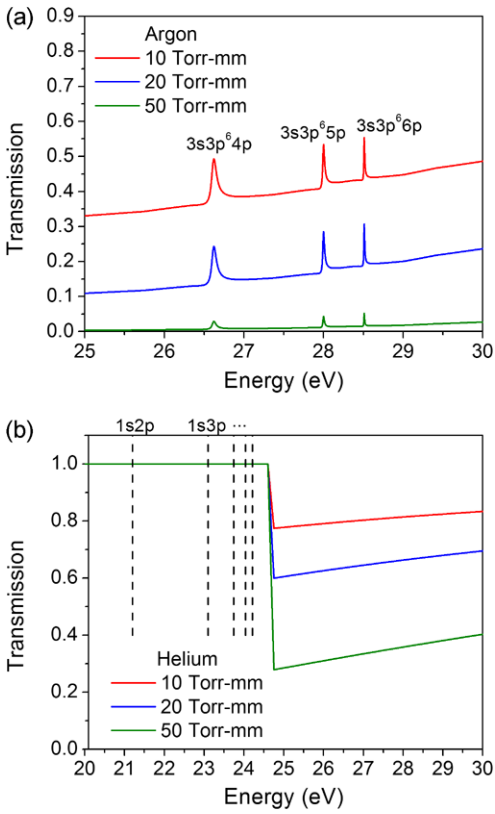

Fig. 8.4 Calculated transmission of (**a**) argon and (**b**) helium for various pressure-length products. The argon transmission was calculated using known absorption cross-section and Fano lineshape parameters using the Fano theory. Higher-lying 3s3p6np autoionizing states are not considered. Helium transmission above its ionization potential was taken from known cross-section data. Positions of absorption lines due to $1s^2 \rightarrow 1snp$ transitions are indicated. Absorption cross-sections near 1snp lines is $\sim 1000\times$ stronger than above the ionization potential, and transmission near these lines should ideally be nearly zero

where ρ is the target gas density which is proportional to the gas backing pressure P and L is the length of the target gas cell [3]. Therefore, the transmission is determined by the pressure-length product of the absorption cell. Here, we have assumed that the gas pressure is nearly constant across the length of the gas cell, and that the pressure outside the cell is nearly zero. These assumptions were confirmed by simulations using the ANSYS Fluent software package, which confirmed that the pressure-length product of our target gas cell is nearly equal to the backing pressure of the gas cell multiplied by the inner diameter of the cell. The energy-dependent cross-section $\sigma(\omega)$ depends upon the specific gas target (in our case, helium or argon) which was used.

For each gas, it is necessary to choose the pressure-length product such that the absorption structures of interest are well-separated from the unabsorbed background signal. The transmission functions of argon (near the 3s3p^6np autoionizing state manifold) and helium (near the 1snp excited state manifold and first ionization potential) are plotted in Fig. 8.4 for different pressure-length products. The argon transmission was calculated using known absorption cross-section [18] and measured lineshape parameters [29] using the Fano theory [8]. Helium transmission above its ionization potential was taken from known cross-section data [18].

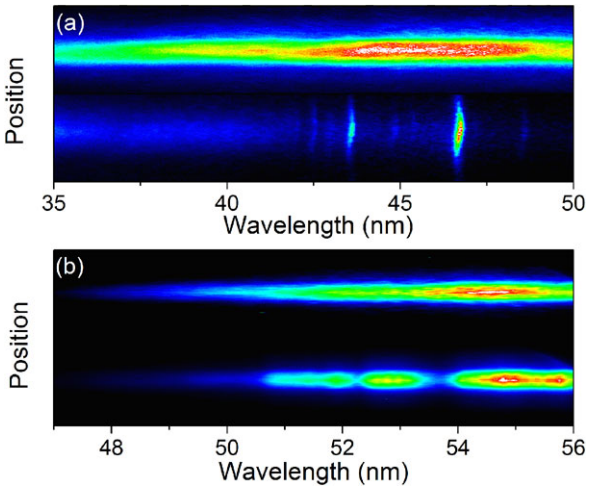

Fig. 8.5 CCD images of the dispersed spectra for (**a**) argon and (**b**) helium. For each, the *top image* is the unabsorbed spectrum and the *bottom image* is taken after absorption. In argon, sharp peaks can be seen in the *bottom image*, corresponding to increased transparency near the autoionization lines. In helium, holes in the transmitted spectrum corresponding to increased absorption near 1s*n*p transitions are observed, as well as the absorption edge near 51 nm, corresponding to the ionization potential of helium

Due to the required background pressure of $<10^{-6}$ Torr near the MCP/phosphor detector and the limited pumping speed of the turbo pumps on the chamber, the backing pressure in the gas cell was limited to ∼50 Torr. For helium, we therefore used a gas cell with inner diameter of 2 mm in order to achieve relatively large pressure-length products, whereas in argon, a pressure of 20 Torr with a length of 1 mm was more than sufficient to achieve high signal levels above the background. Experimentally obtained CCD images of the dispersed spectra after absorption in the target gas are shown in Fig. 8.5.

8.2.4 Transmission Grating Spectrometer

The signal-to-background ratio, however, is not only determined by the pressure-length product of the absorption cell. Because the absorption structures in which we are interested are relatively narrow (on the order of ∼1–100 meV) compared to the background structure of the unabsorbed attosecond pulse continuum spectrum, insufficient spectrometer resolution tends to broaden and weaken the narrow absorption lines corresponding to the bound and quasi-bound states. This effect is demonstrated in Fig. 8.6 for both the argon states of interest, in which the theoretical transmissions have been convoluted with Gaussian resolution functions with varying width. Theoretical widths of the helium 1s*n*p states in the presence of the laser field are not available.

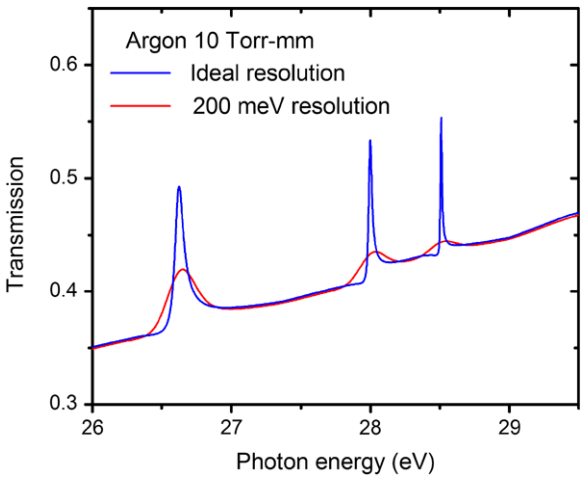

Fig. 8.6 Transmission of argon assuming a spectrometer with energy resolution of 200 meV as compared with the ideal case

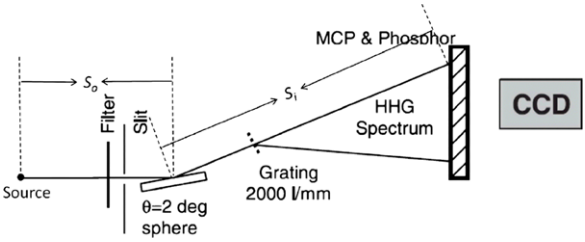

Fig. 8.7 Layout of the XUV spectrometer. S_o is the object distance, and S_i is the image distance. The XUV source was imaged by a spherical mirror at 2° grazing incidence, and a 2000 line/mm grating was used to disperse the spectrum

The layout of the transmission grating spectrometer [33] is shown in Fig. 8.7. The XUV source is imaged by a spherical mirror (radius of curvature $R = 29.1$ m, grazing incidence angle $\theta = 2°$). Immediately following the mirror was a transmission grating with a groove density of 2000 lines/mm. The object and image distances were $S_o = 94$ cm and $S_i = 106$ cm, respectively, yielding a spatial dispersion of the XUV spectrum on the MCP detector of $\frac{dE}{dl} \approx 250$ meV/mm near 25 eV photon energies. Since the dimension of the XUV source is roughly 30 μm, its image on the MCP should also be around this size as the magnification is close to 1. However, the spatial resolution of the MCP/phosphor and CCD detector is limited to ∼100 μm. Based on this, we anticipate that the resolution can be no better than 25 meV.

In Fig. 8.8, the experimentally-obtained transmitted spectrum of argon is shown, with the peak widths of each autoionizating state labeled. By comparing the experimental results to the convoluted theoretical results, we find that the spectrometer resolution is ∼50 meV.

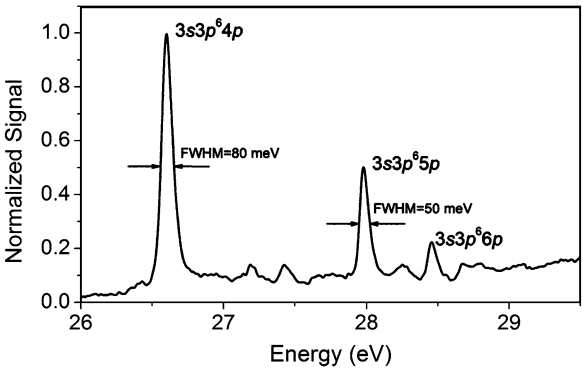

Fig. 8.8 Measured transmitted signal near the argon $3s3p^6np$ autoionizing states. The resolution, determined from the measured $3s3p^65p$ state width, is 50 meV

8.3 Sub-cycle Transient Absorption in Helium 1s*n*p Excited States

As discussed above, one of the strengths of attosecond transient absorption spectroscopy is in observing the dynamics of bound systems, where ionization plays little if any role. Since transient absorption spectroscopy does not rely on the production of photoions, small laser-induced changes in the absorption lines corresponding to bound-bound transitions can be directly observed. In this section, we observed modification of the helium 1s*n*p absorption line manifold caused by a moderately intense laser field. We observe that the strengths and shapes of the absorption lines are modified on the sub-femtosecond timescale.

Much attention has been paid recently to the theoretical calculation of the laser-dressed absorption in helium. Calculations of the XUV absorption cross-section in the presence of the NIR laser field have been calculated using a Floquet model and infinitely long dressing laser pulses [41] as well as by direct solution of the TDSE in the single active electron approximation [11]. Both calculations show anomalous shifting and splitting of the 1s2p absorption line, which is attributed to complicated multi-photon dynamics due to strong coupling of the 1s2p and 1s2s states by the NIR laser, as well as a quasi-linear energy shift of the 1s3p and higher-lying states with increasing laser intensity. This energy shift is attributed to the cycle-averaged AC Stark shift. However, due to the long pulse durations used in both calculations, no sub-cycle dynamics could be observed.

In the experiment, the absorption lines corresponding to the 1s3p and higher-lying states were measured for different time delays between the attosecond and NIR pulses. The time delay was scanned finely with a delay step size of 115 as. Negative delays indicate that the XUV pulse arrived on the target before the NIR pulse, whereas positive delays indicate that the NIR pulse arrived first. The NIR laser pulse intensity was approximately 3×10^{12} W/cm^2. The delay-dependent transmitted spectra are plotted in Fig. 8.9. Here, the red color indicates regions of high transparency, whereas the blue color indicates regions of strong absorption near the laser-dressed excited states.

Clearly, the absorption structures are observed to change on two timescales, as indicated in the figure. The first timescale is that of the laser pulse envelope, and the

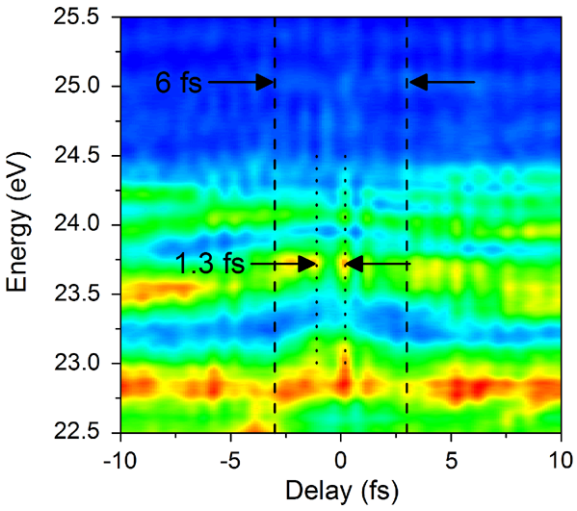

Fig. 8.9 Transmitted spectrum as a function of the XUV-NIR delay. Note the changes to the absorption structure on the timescales of both the laser pulse envelope (6 fs) and the laser half-cycle period (1.3 fs)

energy level shift observed is in good agreement with the calculated cycle-averaged AC Stark shifts calculated by Tong and Toshima [41], Gaarde et al. [11], and observed experimentally by Swoboda et al. [38]. More interestingly, however, the absorption structures are also observed to change on the sub-optical-cycle timescale with a modulation frequency of twice per laser cycle. We find that the absorption line is redistributed periodically by the oscillating laser field, with the amplitude, energy, and width of the absorption line exhibiting sub-cycle changes. This indicates that the excited states are in some way able to follow the oscillating laser field and not only the cycle-averaged intensity.

8.4 Attosecond Time-Resolved Autoionization in Argon

Attosecond transient absorption also offers a complementary technique to attosecond streaking in systems for which photoabsorption to a quasi-bound state leads to production of photoions. For such a system, resonant structures can be observed in both the transmitted photon spectrum and the photoelectron kinetic energy spectrum. This situation occurs for autoionizing states, quasi-bound states which lie above the ionization potential of the atom or molecule, where the delayed ionization process results in the Fano resonance profile in both the transmitted photon and ejected photoelectron spectra [8]. Study of the formation and decay of the Fano resonance using attosecond streaking spectroscopy was first proposed by Wickenhauser et al. [45] and recently realized experimentally by Gilbertson et al. [13] in doubly-excited states of helium. While the results of the experiments could be accurately reproduced using a modified strong-field approximation based on the model of Tong and Lin [40], the presence of the streaked photoelectron background signal caused by direct photoionization of the atom by the broad, continuous attosecond pulse spectrum complicates interpretation of the experimental results.

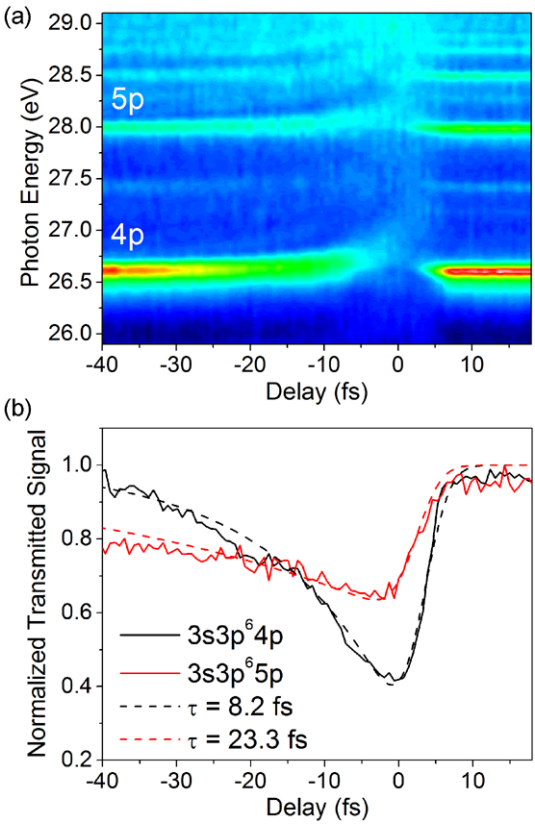

Fig. 8.10
(**a**) Delay-dependent transmitted spectra of argon near the $3s3p^6np$ autoionization manifold. Note the asymmetric shifting of the transmission peaks near zero delay. (**b**) Signal near the unperturbed transmission peaks as a function of the XUV-NIR time delay. By fitting the decay of the resonance structure, the autoionization lifetime can be observed in the time domain

In the case of attosecond transient absorption; however, the background transmission signal far from any absorption structure does not vary with the time delay and can therefore be easily removed. Furthermore in the case of the $3s3p^6np$ autoionizing state manifold in argon, the Fano resonance results in high transparency near the autoionizing state, as shown in Fig. 8.5. The background signal, on the other hand, is strongly absorbed and does not contribute much to the transmitted signal.

Figure 8.10(a) shows the delay-dependent transmitted spectrum as a function of the time delay between the two pulses [44]. Negative delays again correspond to the case in which the XUV pulse arrives on the target before the NIR pulse. The laser intensity was approximately 1×10^{12} W/cm^2. At long delays, three resonance peaks can be identified as the $3s3p^64p$, $3s3p^65p$, and $3s3p^66p$, as indicated in the figure. As the time delay approaches zero, the resonance peaks are shifted to higher energies and, in the case of the $3s3p^64p$ state, split into an asymmetric two-peak structure. For negative delays, absorption structures change slowly, eventually returning to the unperturbed Fano lineshapes at long negative delays. By tracing the transmission at the energies of the unperturbed states as a function of the delay, these slow changes to the absorption follow an exponential decay, with a timescale that exactly matches

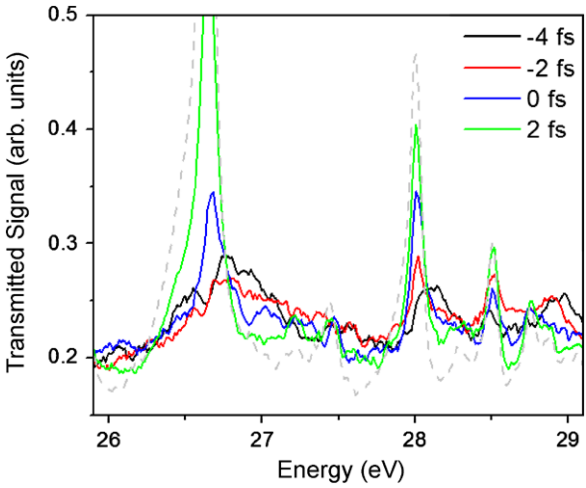

Fig. 8.11 Transmitted spectra of argon near the $3s3p^6np$ autoionization manifold near zero delay. Note that the recovery of the Fano lineshape primarily occurs for delays between 0 and 2 fs

the autoionizing state lifetime (8.2 fs for $3s3p^64p$ and 23.3 fs for $3s3p^65p$) as shown in Fig. 8.10(b).

The formation of the Fano profile at positive delays, on the other hand, proceeds very quickly. In Fig. 8.11, we plot lineouts of the transmitted spectrum for different time delays near zero delay. The gray dashed line indicates the unperturbed Fano profile measured without the NIR laser present. Over the delay range from -4 to $+2$ fs, equal to the pulse duration of the NIR pulse, the transmitted signal is changed from being nearly featureless to exhibiting the Fano autoionization peaks. In fact, this recovery of the Fano lineshape occurs primarily between 0 and 2 fs delay, indicating dramatic changes to the absorption spectrum on a timescale smaller than the laser optical cycle.

8.5 Summary and Outlook

In this chapter, we have described the novel technique of attosecond transient absorption spectroscopy and demonstrated the capability to observe laser-induced changes in the atomic absorption spectrum which occur on the single-femtosecond timescale, faster than the oscillation period of the laser. Attosecond transient absorption spectroscopy can be applied to the study of bound state dynamics, as in the case of the helium $1snp$ excited states, and of short-lived doubly-excited or core-excited states, as in the case of the argon autoionizing states.

Current progress in attosecond source development is following two paths: high repetition rate ($\sim$MHz) attosecond sources for high average powers [21, 24, 42] and high energy ($\sim\mu$J) attosecond pulses for high intensities [5, 10, 15, 22, 31, 35, 37, 39]. Attosecond transient absorption spectroscopy stands to benefit from both of these technologies. Attosecond sources with high average power allow experimentalists to achieve higher signal-to-noise ratios than is currently available with

reasonable integration times. This will allow study of weaker and more complex absorption structures in more complicated systems than atoms, such as molecules, nanostructures, and thin films. High energy attosecond pulses will allow the study of nonlinear dynamics in XUV photoabsorption. By using a single, intense attosecond pulse, one can observe non-perturbative formation of autoionizing states [26] by measuring the changes to the resonance profile as a function of the attosecond pulse intensity. The dynamics of the formation can then be measured using the transient absorption of a second, delayed attosecond pulse as the probe. Furthermore, transient absorption attosecond pump-attosecond probe experiments have been proposed to observe the valence- and inner-shell dynamics of electrons in krypton [1]. By applying high-energy isolated attosecond pulses in a transient absorption pump-probe setup, true observation of attosecond dynamics in the absence of a strong laser field can be observed in the near future.

Acknowledgements The authors acknowledge helpful discussions and theoretical support from Suxing Hu with regard to the helium experiments and from Chang-hua Zhang, Feng He, and Uwe Thumm with regard to the argon experiments. He Wang is currently at Lawrence Berkeley National Laboratory, Berkeley CA. Baozhen Zhao and Shouyuan Chen are currently at University of Nebraska, Lincoln NE.

References

1. J.C. Baggesen, E. Lindroth, L.B. Madsen, Theory of attosecond absorption spectroscopy in krypton. Phys. Rev. A **85**, 013415 (2012)
2. A.L. Cavalieri, N. Muller, Th. Uphues, V.S. Yakovlev, A. Baltuska, B. Horvath, B. Schmidt, L. Blumel, R. Holzwarth, S. Hendel, M. Drescher, U. Kleineberg, P.M. Echenique, R. Kienberger, F. Krausz, U. Heinzmann, Attosecond spectroscopy in condensed matter. Nature (London) **449**, 1029 (2007)
3. Z. Chang, *Fundamentals of Attosecond Optics* (CRC Press, Boca Raton, 2011)
4. Z. Chang, P.B. Corkum, Attosecond photon sources: the first decade and beyond. J. Opt. Soc. Am. B **27**, B9 (2010) [Invited]
5. D. Charalambidis, P. Tzallas, E.P. Benis, E. Skantzakis, G. Maravelias, L.A.A. Nikolopoulos, A. Peralta Conde, G.D. Tsakiris, Exploring intense attosecond pulses. New J. Phys. **10**, 025018 (2008)
6. M. Chini, H. Mashiko, H. Wang, S. Chen, C. Yun, S. Scott, S. Gilbertson, Z. Chang, Delay control in attosecond pump-probe experiments. Opt. Express **17**, 21459 (2009)
7. M. Chini, S. Gilbertson, S.D. Khan, Z. Chang, Characterizing ultrabroadband attosecond lasers. Opt. Express **18**, 13006 (2010)
8. U. Fano, Effects of configuration interaction on intensities and phase shifts. Phys. Rev. **124**, 1866 (1961)
9. X. Feng, S. Gilbertson, H. Mashiko, H. Wang, S.D. Khan, M. Chini, Y. Wu, K. Zhao, Z. Chang, Generation of isolated attosecond pulses with 20 to 28 femtosecond lasers. Phys. Rev. Lett. **103**, 183901 (2009)
10. F. Ferrari, F. Calegari, M. Lucchini, C. Vozzi, S. Stagira, G. Sansone, M. Nisoli, High-energy isolated attosecond pulses generated by above-saturation few-cycle fields. Nat. Photonics **4**, 875–879 (2010)
11. M.B. Gaarde, C. Buth, J.L. Tate, K.J. Schafer, Transient absorption and reshaping of ultrafast XUV light by laser-dressed helium. Phys. Rev. A **83**, 013419 (2011)

12. S. Gilbertson, H. Mashiko, C. Li, S.D. Khan, M.M. Shakya, E. Moon, Z. Chang, A low-loss, robust setup for double optical gating of high harmonic generation. Appl. Phys. Lett. **92**, 071109 (2008)
13. S. Gilbertson, M. Chini, X. Feng, S. Khan, Y. Wu, Z. Chang, Monitoring and controlling the electron dynamics in helium with isolated attosecond pulses. Phys. Rev. Lett. **105**, 263003 (2010)
14. S. Gilbertson, S.D. Khan, Y. Wu, M. Chini, Z. Chang, Isolated attosecond pulse generation without the need to stabilize the carrier-envelope phase of driving lasers. Phys. Rev. Lett. **105**, 093902 (2010)
15. S. Gilbertson, Y. Wu, S.D. Khan, M. Chini, K. Zhao, X. Feng, Z. Chang, Isolated attosecond pulse generation using multicycle pulses directly from a laser amplifier. Phys. Rev. A **81**, 043810 (2010)
16. E. Goulielmakis, M. Schultze, M. Hofstetter, V.S. Yakovlev, J. Gagnon, M. Uiberacker, A.L. Aquila, E.M. Gullikson, D.T. Attwood, R. Kienberger, F. Krausz, U. Kleineberg, Single-cycle nonlinear optics. Science **320**, 1614 (2008)
17. E. Goulielmakis, Z.-H. Loh, A. Wirth, R. Santra, N. Rohringer, V.S. Yakovlev, S. Zherebtsov, T. Pfeiffer, A.M. Azzeer, M.F. Kling, S.R. Leone, F. Krausz, Real-time observation of valence electron motion. Nature (London) **466**, 739 (2010)
18. E. Gullikson, http://henke.lbl.gov/optical_constants/
19. M. Holler, F. Schapper, L. Gallmann, U. Keller, Attosecond electron wave-packet interference observed by transient absorption. Phys. Rev. Lett. **106**, 123601 (2011)
20. J. Itatani, F. Quere, G.L. Yudin, M.Yu. Ivanov, F. Krausz, P.B. Corkum, Attosecond streak camera. Phys. Rev. Lett. **88**, 173903 (2002)
21. R.J. Jones, K.D. Moll, M.J. Thorpe, J. Ye, Phase-coherent frequency combs in the vacuum ultraviolet via high-harmonic generation inside a femtosecond enhancement cavity. Phys. Rev. Lett. **94**, 193201 (2005)
22. S.D. Khan, Y. Cheng, M. Moller, K. Zhao, B. Zhao, M. Chini, G.G. Paulus, Z. Chang, Ellipticity dependence of 400 nm-driven high harmonic generation. Appl. Phys. Lett. **99**, 161106 (2011)
23. R. Kienberger, E. Goulielmakis, M. Uiberacker, A. Baltuska, V. Yakovlev, F. Bammer, A. Scrinzi, Th. Westerwalbesloh, U. Kleineberg, U. Heinzmann, M. Drescher, F. Krausz, Atomic transient recorder. Nature (London) **427**, 817 (2004)
24. S. Kim, J. Jin, Y.-J. Kim, I.-Y. Park, Y. Kim, S.-W. Kim, High-harmonic generation by resonant plasmon field enhancement. Nature (London) **453**, 757 (2008)
25. F. Krausz, M. Ivanov, Attosecond physics. Rev. Mod. Phys. **81**, 163 (2009)
26. P. Lambropoulos, P. Zoller, Autoionizing states in strong laser fields. Phys. Rev. A **24**, 379 (1981)
27. Z.-H. Loh, M. Khalil, R.E. Correa, R. Santra, C. Buth, S.R. Leone, Quantum state-resolved probing of strong-field-ionized xenon atoms using femtosecond high-order harmonic transient absorption spectroscopy. Phys. Rev. Lett. **98**, 143601 (2007)
28. Z.-H. Loh, C.H. Greene, S.R. Leone, Femtosecond induced transparency and absorption in the extreme ultraviolet by coherent coupling of the He 2s2p (^1P_o) and $2p^2$ (^1S_e) double excitation states with 800 nm light. Chem. Phys. **350**, 7 (2008)
29. R.P. Madden, D.L. Ederer, K. Codling, Resonances in the photo-ionization continuum of Ar I (200-150 eV). Phys. Rev. **177**, 136 (1969)
30. H. Mashiko, S. Gilbertson, C. Li, S.D. Khan, M.M. Shakya, E. Moon, Z. Chang, Double optical gating of high-order harmonic generation with carrier-envelope phase stabilized lasers. Phys. Rev. Lett. **100**, 103906 (2008)
31. H. Mashiko, S. Gilbertson, C. Li, E. Moon, Z. Chang, Optimizing the photon flux of double optical gated high-order harmonic spectra. Phys. Rev. A **77**, 063423 (2008)
32. J. Mauritsson, T. Remetter, M. Swoboda, K. Klunder, A. L'Huillier, K.J. Schafer, O. Ghafur, F. Kelkensberg, W. Siu, P. Johnsson, M.J.J. Vrakking, I. Znakovskaya, T. Uphues, S. Zherebtsov, M.F. Kling, F. Lepine, E. Benedetti, F. Ferrari, G. Sansone, M. Nisoli, Attosecond

electron spectroscopy using a novel interferometric pump-probe technique. Phys. Rev. Lett. **105**, 053001 (2010)
33. D.A. Mossessian, P.A. Heimann, E. Gullikson, R.K. Kaza, J. Chin, J. Akre, Transmission grating spectrometer for characterization of undulator radiation. Nucl. Instrum. Methods Phys. Res. A **347**, 244 (1994)
34. G. Sansone, E. Benedetti, F. Calegari, C. Vozzi, L. Avaldi, R. Flammini, L. Poletto, P. Villoresi, C. Altucci, R. Velotta, S. Stagira, S. De Silvestri, M. Nisoli, Isolated single-cycle attosecond pulses. Science **314**, 443 (2006)
35. G. Sansone, L. Poletto, M. Nisoli, High-energy attosecond light sources. Nat. Photonics **5**, 655 (2011)
36. M. Schultze, M. Fieß, N. Karpowicz, J. Gagnon, M. Korbman, M. Hoftstetter, S. Neppl, A.L. Cavalieri, Y. Komninos, Th. Mercouris, C.A. Nicolaides, R. Pazourek, S. Nagele, J. Feist, J. Burgdorfer, A.M. Azzeer, R. Ernstorfer, R. Kienberger, U. Kleineberg, E. Goulielmakis, F. Krausz, V.S. Yakovlev, Delay in photoemission. Science **328**, 1658 (2010)
37. J. Seres, V.S. Yakovlev, E. Seres, Ch. Streli, P. Wobrauschek, Ch. Spielmann, F. Krausz, Coherent superposition of laser-driven soft-X-ray harmonics from successive sources. Nat. Phys. **3**, 878 (2007)
38. M. Swoboda, T. Fordell, K. Klunder, J.M. Dahlstrom, M. Miranda, C. Buth, K.J. Schafer, J. Mauritsson, A. L'Huillier, M. Gisselbrecht, Phase measurement of resonant two-photon ionization in helium. Phys. Rev. Lett. **104**, 103003 (2010)
39. E. Takahashi, Y. Nabekawa, K. Midorikawa, Generation of 10-μJ coherent extreme-ultraviolet light by use of high-order harmonics. Opt. Lett. **27**, 1920 (2002)
40. X.M. Tong, C.D. Lin, Double photoexcitation of He atoms by attosecond XUV pulses in the presence of intense few-cycle infrared lasers. Phys. Rev. A **71**, 033406 (2005)
41. X.M. Tong, N. Toshima, Controlling atomic structures and photoabsorption processes by an infrared laser. Phys. Rev. A **81**, 063403 (2010)
42. A. Vernaleken, J. Weitenberg, T. Sartorius, P. Russbueldt, W. Schneider, S.L. Stebbings, M.F. Kling, P. Hommelhoff, H.-D. Hoffman, R. Poprawe, F. Krausz, T.W. Hansch, T. Udem, Single-pass high-harmonic generation at 20.8 MHz repetition rate. Opt. Lett. **36**, 3428 (2011)
43. H. Wang, M. Chini, S.D. Khan, S. Chen, S. Gilbertson, X. Feng, H. Mashiko, Z. Chang, Practical issues of retrieving isolated attosecond pulses. J. Phys. B, At. Mol. Opt. Phys. **42**, 134007 (2009)
44. H. Wang, M. Chini, S. Chen, C.H. Zhang, F. He, Y. Cheng, Y. Wu, U. Thumm, Z. Chang, Attosecond time-resolved autoionization of argon. Phys. Rev. Lett. **105**, 143002 (2010)
45. M. Wickenhauser, J. Burgdorfer, F. Krausz, M. Drescher, Time resolved Fano resonances. Phys. Rev. Lett. **94**, 023002 (2005)

Chapter 9
Shot-by-Shot Photoelectron Spectroscopy of Rare Gas Atoms in Ultrashort Intense EUV Free-Electron Laser Fields

Mizuho Fushitani, Yasumasa Hikosaka, Akitaka Matsuda, Eiji Shigemasa, and Akiyoshi Hishikawa

Abstract Nonlinear processes of rare gas atoms in intense extreme ultraviolet (EUV) free-electron laser (FEL) fields have been investigated by photoelectron spectroscopy. Simultaneous recording of fluctuating laser spectra from self-amplified spontaneous emission (SASE) FEL and nonlinear responses of target atoms provided a deeper understanding on the multiphoton processes in (i) double ionization of Ar and (ii) double excitation of He, in intense EUV laser fields. Results on two-color time-resolved experiment are also presented.

9.1 Introduction

Recent progress in free electron laser (FEL) technology has realized generation of ultrashort intense laser pulses in the extreme ultraviolet (EUV), soft- and hard-X ray regions [1–3]. Nonlinear responses of target materials exposed to such high-frequency intense laser pulses are expected to be different from those in the visible and near infrared [4, 5], in two respects. First, the ponderomotive potential U_p is much smaller than the corresponding values in the visible and infrared regions, because U_p scales quadratically with the wavelength. For example, at the field intensity of 10^{14} W/cm^2, we have $U_p = 59$ eV for an 800 nm laser field, while it is only 0.59 eV at 80 nm, and much smaller in X-ray. Therefore, for a given target with an ionization potential I_p, the Keldysh parameter [6] $\gamma = \sqrt{I_p/2U_p}$ is often much larger than unity ($\gamma \gg 1$), indicating that the ionization in EUV and X-ray intense laser fields tends to proceed by multiphoton absorption rather than field ionization.

M. Fushitani · A. Matsuda · A. Hishikawa (✉)
Department of Chemistry, Graduate School of Science, Nagoya University, Nagoya, Aichi 464-8602, Japan
e-mail: hishi@chem.nagoya-u.ac.jp

Y. Hikosaka
Department of Environmental Science, Niigata University, Niigata, Niigata 950-2181, Japan

E. Shigemasa
Institute for Molecular Science, National Institutes of Natural Sciences, Okazaki, Aichi 444-8585, Japan

K. Yamanouchi, K. Midorikawa (eds.), *Progress in Ultrafast Intense Laser Science*, Springer Series in Chemical Physics 104, DOI 10.1007/978-3-642-35052-8_9,

Second, both valence and inner-shell electrons can participate in photo-absorption in EUV and X-ray laser fields because of the high photon energy. In contrast, it is mostly the valence electrons that are driven by the intense laser fields in optical region.

Isolated atoms serve as a benchmark to understand the behavior of more complex systems in intense EUV and X-ray laser fields. Previous studies carried out at SCSS [7–17], FLASH [18–31] and LCLS [32–34], show that a typical non-linear response of atoms and molecules to intense EUV and X-ray laser fields is multiple ionization. For example, intense FEL pulses at 93 eV ($\lambda = 13.3$ nm, $I = 7.8 \times 10^{15}$ W/cm^2) ionize Xe atoms into highly charged states (Xe^{Z+}) up to $Z = 21$ [22]. The energy required for the ion production is estimated to be more than 5 keV, which corresponds to absorption of more than 57 photons. It is pointed out that the perturbative treatment is insufficient to explain a creation of such a large number of charges by multiphoton absorption, indicating contributions from a new ionization mechanism beyond the single-active electron picture [29].

The responses of atoms and molecules have been investigated so far mainly by ion detection. The charge number distribution of the ions and the dependence of the ion yield upon FEL intensity allow us to discuss the ionization mechanism in terms of the number of photons required for each ionization step. Ion momentum imaging provides more detailed information to identify whether the electron emission proceeds in a sequential or non-sequential manner [20, 23, 35]. Compared with these studies, photoelectron spectroscopy has a clear advantage in identifying the ionization pathways, because kinetic energies of photoelectrons reflect intermediate or final electronic states populated in multiphoton ionization processes [11, 14, 21, 26]. This unique feature allows us to distinguish different ionization pathways leading to the same charge states and to understand which electrons in different shells are driven by the laser fields.

Another important feature of photoelectron spectroscopy is its capability of characterizing the spectral properties of laser pulses [11, 36]. Since the signal intensity and the kinetic energy of photoelectrons ejected by single-photon absorption are determined by the intensity and wavelength distributions of the laser pulse, the spectrum can be characterized by the photoelectron spectroscopy. This unique feature is important in a detailed investigation of the multiple ionization processes. This is because EUV and X-ray pulses from FELs running in the self-amplified spontaneous emission (SASE) scheme fluctuate both in wavelength and intensity due to their statistical origin [18]. The wavelength fluctuation may blur the details of the ionization processes, particularly the resonance effect which should be sensitive to the FEL spectrum.

Here we review our recent work on shot-by-shot photoelectron spectroscopy of rare gas atoms in intense EUV FEL fields. In Sect. 9.2, we describe the EUV FEL source and the experimental setup for shot-by-shot photoelectron spectroscopy. Three-photon double ionization process of Ar atoms is discussed in Sect. 9.3, placing an emphasis on importance of resonance effects. In Sect. 9.4, multiphoton double excitation of He is described. Time-resolved measurements using optical laser pulses synchronized with the EUV FEL are presented in Sect. 9.5.

9.2 Experimental

9.2.1 SPring-8 SASE Compact Source (SCSS)

The experiments were carried out at SPring-8 SASE Compact Source (SCSS) facility of RIKEN HARIMA Institute [2, 37, 38], which delivers horizontally polarized intense FEL pulses in the wavelength range between 50 and 61 nm at a repetition rate of 30 Hz. The variable gap undulators allow us a fine-tuning of the wavelength without changing electron beam parameters. Typical pulse energy and duration were 10 μJ and ∼100 fs, respectively. The intensity of each FEL pulse was measured by a gas-ionization monitor. The FEL pulses contain small contributions from the second and third harmonics, which are about 0.1 and 1 % of the fundamental in intensity, respectively. A pair of elliptical and cylindrical mirrors ($f = 1000$ mm) with a total throughput of 35 % was used to focus the FEL pulses to gaseous samples. The diameter of the focal spot was about 25 μm. The FEL field intensity at the focus was estimated to be ∼5 TW/cm^2. The fundamental FEL pulse intensity can be attenuated by an Ar gas filter placed upstream in the beam line.

For two-color measurements, a femtosecond Ti:Sapphire regenerative amplifier laser system (800 nm, 3 mJ, 50 fs, 1 kHz) with an optical parametric amplifier was used. The laser was electronically synchronized to the FEL via the RF signal from the accelerator. The laser beam was focused by an optical lens ($f = 1000$ mm) and introduced to the interaction region with a small angle (∼1°) relative to the FEL beam.

9.2.2 Magnetic Bottle Type Photoelectron Spectrometer

We have employed a magnetic bottle-type time-of-flight (TOF) photoelectron spectrometer for the shot-by-shot photoelectron spectroscopy [11, 14]. A conical permanent magnet creates an inhomogeneous magnetic field (0.7 T) across the focus of the FEL beam, which guides photoelectrons ejected in 4π steradians toward the entrance of a TOF tube by the magnetic mirror effect. A weak magnetic field (1 mT) generated by a solenoid coil wound around the TOF tube leads the photoelectrons to a micro channel plate (MCP) detector placed in the other end of the tube (see Fig. 9.1). Photoelectron signals from the MCP detector were acquired with a digital oscilloscope and the stored data were transferred to a personal computer for every FEL shot. The electron kinetic energy was calibrated by the photoelectron spectra of autoionizing O* [39] (produced from O_2 by the fundamental FEL) and of Xe 4d Auger process [40] (by the second and third harmonics).

The total detection efficiency is estimated to be about 50 % for photoelectrons with an energy $E < 40$ eV, which is mainly determined by a detection efficiency of the MCP detector. The high electron collection efficiency of the spectrometer allows us to reduce the sample density to minimize the space charge effect and, in addition, to obtain a high energy resolution by using a long flight tube. The spectrometer

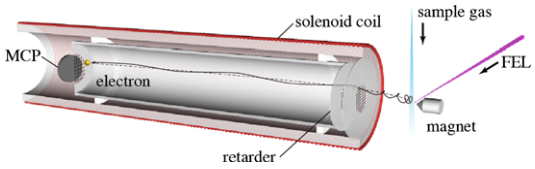

Fig. 9.1 Schematic of the magnetic bottle type photoelectron spectrometer used in the present study. FEL is focused to sample gas in front of a conical permanent magnet. Magnetic fields generated by the magnet and solenoid coil guide emitted electrons toward a MCP detector through a time-of-flight tube with a retarder

is equipped with a 1.5 m-long TOF tube, which provides an energy resolution of $E/\Delta E \sim 20$ for $E < 40$ eV under the present experimental conditions. The energy resolution is high enough to retrieve spectral properties of FEL pulses from photoelectron spectra.

In order to record the photoelectron spectra on the shot-by-shot basis, it is important to suppress unwanted electrons. Since the peak power of EUV FEL pulses is remarkably high and the photon energy is larger than the work function of most materials, a large amount of electrons are readily produced, thereby preventing precise measurements of photoelectron spectra. Such background signals are minimal in the magnetic bottle type spectrometer, since the spectrometer detects the electrons produced in front of the tip of the permanent magnet only.

9.2.3 Shot-by-Shot Photoelectron Spectroscopy

Figures 9.2(a) and (b) show photoelectron spectra of Ar by single-photon ionization with FEL pulses (21.4 eV) averaged for 2000 laser shots and the corresponding single-shot photoelectron spectra for the FEL shot number from #805 to #809, respectively. The single-shot photoelectron spectra clearly demonstrate that the energy and intensity of the Ar^+ photoelectron peak vary by each laser shot, reflecting the fluctuation of the spectral properties of the FEL pulse. The mean photon energy ($h\nu$) of FEL is obtained by a simple relation,

$$h\nu = E + \mathrm{IP},$$

where IP is the ionization potential of Ar. The relative intensity of each FEL pulse can be obtained by the Ar^+ peak intensity. It should be noted, however, that single photon ionization is often saturated at high FEL field intensities achieved at the focus of the FEL beam. In the present studies, therefore, we use the single-shot photoelectron spectra for the mean photon energy only, while the monitor equipped in the upper stream of the beam line is used to obtain the absolute intensity of each FEL pulse. The correlation between the mean photon energy and intensity thus obtained is plotted in Fig. 9.2(c). From the correlation map, the full width at half maximum (FWHM) of the mean photon energy distribution is found to be 0.13 eV and the standard deviation (σ) for the intensity is 17 %. These values are in good agreement

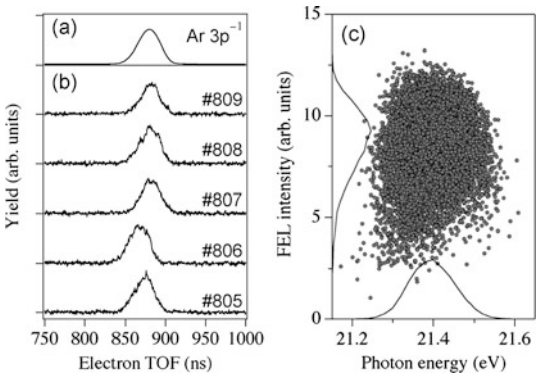

Fig. 9.2 (**a**) Electron time-of-flight spectra of Ar by using FEL at 58.0 nm for 2000 laser shots. (**b**) Single-shot spectra for the FEL shot number #805∼809 during the accumulation of trace (**a**). (**c**) A correlation map between the intensity and photon energy of SCSS FEL at 58.0 nm

with the previous results, FWHM = 0.13 eV and σ = 10–12 %, obtained by using an optical spectrometer [37], demonstrating the feasibility of the single-shot spectral monitoring of FEL by photoelectron spectroscopy.

9.3 Three-Photon Double Ionization of Ar

Figure 9.3(a) shows a photoelectron spectrum of Ar in intense FEL fields (∼5 TW/cm^2) at a wavelength of 58.0 nm ($h\nu = 21.4$ eV) for 15000 shots [11]. A strong photoelectron peak observed at an electron kinetic energy of 5.6 eV is assigned to the single-photon ionization to the Ar^+3p^{-1} state described above. Besides the Ar^+ peak, three additional peaks are identified in the electron kinetic energy range of 10–16 eV. Based on conservation of energy, these peaks are assigned to the two-photon ionization to the ^{1}S, ^{1}D, ^{3}P levels of $Ar^{2+}3p^{-2}$ state from the ground state of Ar^+ ion (see Fig. 9.4(a)). The total yield of these Ar^{2+} peaks exhibits a non-linear dependence on the FEL intensity as shown in Fig. 9.4(b), confirming that the double ionization involves absorption of more than two photons. Besides the three-photon sequential pathway via the formation of Ar^+ identified here, double ionization to Ar^{2+} can take place directly from the Ar ground state, because the three photon energy (64.2 eV) exceeds the double ionization potential (43.4 eV). However, the observed spectra show no broad photoelectron distribution associated with energy sharing of the excess energy (20.8 eV) by the two electrons. Thus, the three-photon double photoionization of Ar proceeds dominantly in a sequential manner [11].

A detailed picture of the three-photon double ionization can be obtained by the shot-by-shot analysis of the photoelectron spectra (Fig. 9.3(b)). The single-shot spectra are sorted by the mean photon energy estimated from the Ar^+ peak, and then averaged within narrow photon energy ranges that divide the whole photon energy range into 13 segments. To cover a wide photon energy range (0.4 eV), which is larger than the fluctuation width of 0.13 eV (see Fig. 9.2(c)), single-shot photoelectron spectra measured with FEL set at 21.0, 21.2 and 21.4 eV are used together

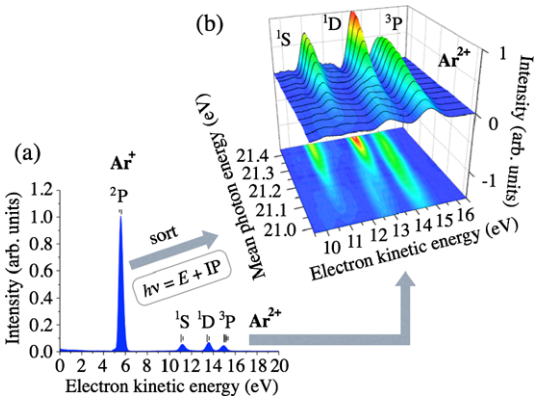

Fig. 9.3 (**a**) Photoelectron spectra of Ar averaged for 15000 FEL shots at 58.0 nm. (**b**) Three-dimensional (3D) plot of the Ar^{2+} peaks in a mean photon energy range of 21.0–21.4 eV. In order to cover a wide photon energy range, the data were recorded at nominal FEL energies of 21.0, 21.2 and 21.4 eV. The 3D diagram is obtained by sorting single-shot photoelectron spectra according to the mean photon energy determined for each FEL shot from the electron kinetic energy of the Ar^{+} peak

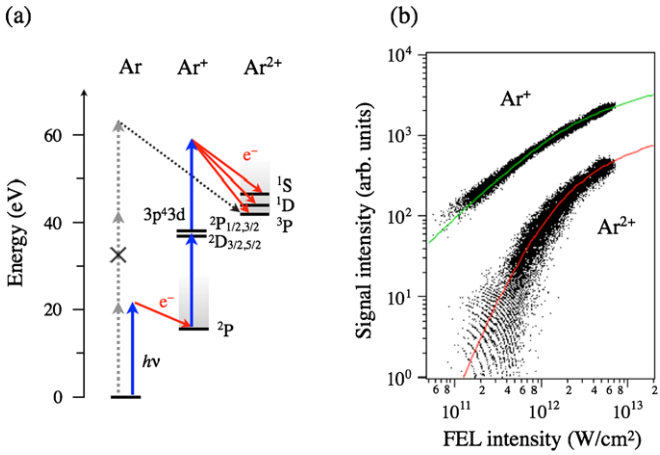

Fig. 9.4 (**a**) Energy levels of Ar, Ar^{+} and Ar^{2+} relevant in the three-photon double photoionization. (**b**) FEL intensity dependence of the yield of Ar^{+} peak and the total yield of Ar^{2+} peaks in the kinetic energy range of 10–16 eV. Results of numerical simulation based on a set of rate equations formulated for the sequential three-photon double ionization [11] are also shown (*solid lines*)

in the sorting. The resultant spectra in Fig. 9.3(b) show that both the peak intensity and position of the three Ar^{2+} peaks exhibit drastic dependences on the FEL photon energy, clearly indicating contributions from resonant ionization in the two-photon process.

Figure 9.5 illustrates the yields of the ^3P, ^1D and ^1S components as a function of the mean photon energy. The intensity of the ^3P component becomes the maximum

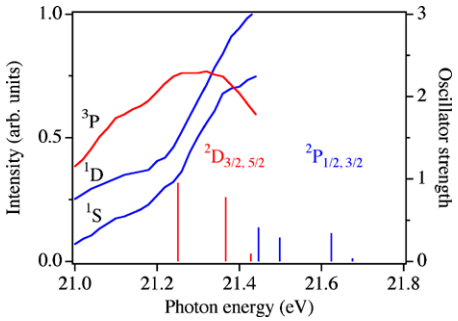

Fig. 9.5 Intensities of the ^{1}D, ^{1}S and ^{3}P components of the Ar^{2+} peaks plotted against the FEL mean photon energy. Oscillator strengths f from the $3p^{-1}$ ground state to the $^2D_{1/2,3/2}$ and $^2P_{3/2,5/2}$ excited states in the $[3p^{-2}(^1D)]3d$ configuration of Ar^+ [41] are plotted against the transition energies [56] as *red* and *blue sticks*, respectively

around 21.3 eV while those of the ^{1}D and ^{1}S components monotonically increase up to 21.4 eV. The contrasting behavior of these components indicates some resonances with different intermediate states in the second ionization process. For Ar^+, electronically excited states with $[3p^{-2}(^1D)]3d$ configuration are located around 21 eV above the ground $3p^{-1}(^2P)$ state (see Fig. 9.4(a)). The oscillator strengths [41] from the $3p^{-1}$ ground state to these electronically excited states are also shown in Fig. 9.5. Comparison of the oscillator strengths with the experimental curves suggests that the two-photon ionization to the ^{3}P states of Ar^{2+} is enhanced by the $^2D_{3/2,5/2}$ resonance states of the $[3p^{-2}(^1D)]3d$ configuration, while the $^2P_{1/2,3/2}$ states of the same configuration are responsible for the ^{1}D and ^{1}S channels.

A 2D contour map of Fig. 9.3(b) is shown in Fig. 9.6. The maximum positions of the Ar^{2+} peaks shift as the photon energy increases. When one assumes that two-photon ionization proceeds non-resonantly, the energies of the Ar^{2+} peaks should be expressed as

$$E = 2h\nu - \left[E\left(Ar^{2+}\right) - E\left(Ar^{+}\right)\right],$$

where $E(Ar^{2+})$ and $E(Ar^+)$ represent the energies of an electronic state of Ar^{2+} and the ground state of Ar^+, respectively. The calculated energies in Fig. 9.6 deviate considerably from the slope of the observed Ar^{2+} peaks, especially for the ^{1}S and ^{1}D components. In the case of resonant ionization, the electron kinetic energy of the Ar^{2+} peaks is given by

$$E = h\nu - \left[E\left(Ar^{2+}\right) - E\left(Ar^{+*}\right)\right],$$

where $E(Ar^{+*})$ represents the energy of a resonance state of Ar^+. The expected energy positions for each Ar^{2+} peak are shown in Fig. 9.6, using the $^2D_{3/2,5/2}$ states for the ^{3}P component and the $^2P_{1/2,3/2}$ states for the ^{1}D and ^{1}S as the resonance states. The calculated energy shift of each Ar^{2+} peak is in good agreement with the experimental results. Therefore, the photon energy dependence of the peak shift also supports resonance effects in the two-photon ionization of Ar^+ and the above assignments of the intermediate states for the resonances [11].

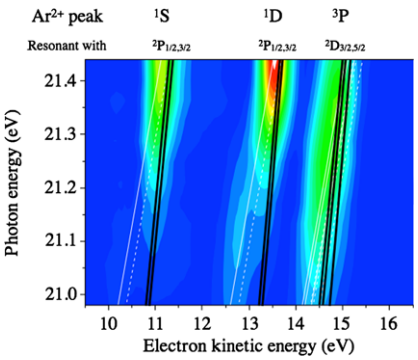

Fig. 9.6 Two-dimensional contour plot of the Ar^{2+} peaks as a function of photon energy. The *diagonal lines* with the slope of 2 describe the kinetic energies expected for two-photon absorption from the $Ar^{+}3p^{-1}$ spin-orbit levels, where the starts from the $^2P_{3/2}$ and $^2P_{1/2}$ levels are shown in *solid* and *dashed white lines*, respectively. The *black lines* with the slope of 1 denote the energies of photoelectrons emitted on one-photon ionization from Ar^{+*} ($^2P_{1/2,3/2}$ and $^2D_{3/2,5/2}$)

The configuration of the intermediate states, $[3p^{-2}(^1D)]3d$, shows that the dominant character of the Ar^{2+} core is ^1D state, so that the ionization to the Ar^{2+} ^1S state from these intermediate states is expected to be less efficient than that to the ^1D state [15, 42]. Recent theoretical studies show that the anomaly strong ^1S peak in Fig. 9.3(b) is due to additional resonances to autoionizing states above the Ar^{2+} threshold [42].

9.4 Nonlinear Double Excitation of He

Photoelectron spectra of He recorded with FEL at 51.0 nm ($I_0 = 5$ TW/cm^2) are shown in Fig. 9.7(a) [14]. Doublet peaks observed at 10.8 and 12.2 eV are attributed to 5p photoelectrons from Xe, mixed in the sample gas for the shot-by-shot analysis. The most prominent peak (A) seen at 6.9 eV is assigned to photoelectrons formed by three-photon ionization to electronically excited ($N = 2$) state of He^+ (see Fig. 9.8(a)). The photoelectron yield shows a nonlinear dependence upon the variation the FEL intensity (I_0, $0.6I_0$, $0.3I_0$), supporting that this peak originates from multiphoton absorption process. The energies of two other photoelectron peaks (B) and (C), 24 and 48 eV, correspond to two-photon and three-photon ionization to the He^+ ground ($N = 1$) state, respectively. These two peaks, however, depend only weakly on the FEL intensity. This is because the second and third harmonics of FEL, whose intensities are not affected by the gas attenuator, contribute significantly to these peaks. The contributions from the second and third harmonics appear as a constant baseline in the FEL intensity dependences, while those from the two- and three-photon process are observed only at the highest field intensities ($\sim$5 TW/cm^2). The net signal intensities from the non-linear process, obtained by subtracting the baseline due to the harmonics are 23:1:0.4 for peak (A), (B) and (C). This shows

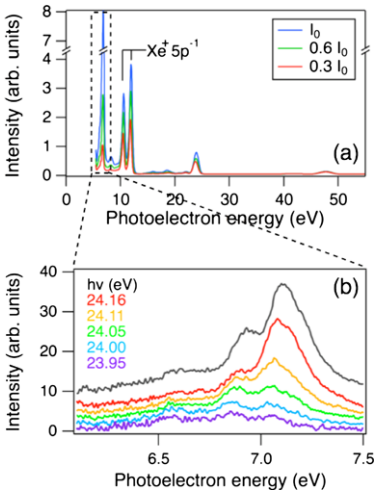

Fig. 9.7 (**a**) Photoelectron spectra of He for three different intensities of EUV FEL at 51.0 nm. A small amount of Xe is premixed in the sample for the shot-by-shot analysis. (**b**) Expanded view of photoelectron peak (A) as a function of the mean photon energy determined from the Xe $5p^{-1}$ peaks for each FEL shot. Photoelectron spectra are sorted according to the mean photon energy, and then averaged within narrow photon energy ranges that divide the whole photon energy range (23.95–24.17 eV) into 5 segments

that the three-photon process (A) + (C) is more than 20 times efficient than the two-photon process at the FEL intensity of $I_0 = 5$ TW/cm^2.

The key to understand the enhancement of the three-photon process over the two-photon process can be found in a closer look at the photoelectron peak (A) shown in Fig. 9.7(b). The expanded view reveals that peak (A) has substructures. The single-shot analysis, sorting each photoelectron spectrum by the FEL photon energy (determined by the Xe photoelectron peaks), shows that these subpeaks do not shift by the changes in the mean photon energy. This indicates that electron

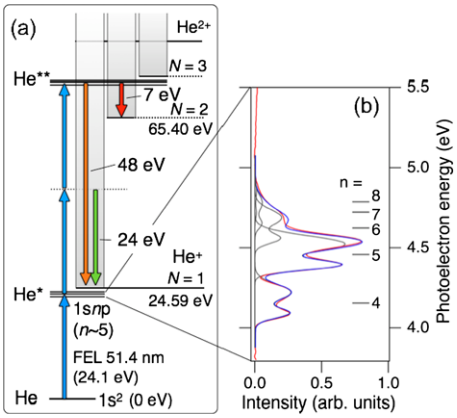

Fig. 9.8 (**a**) Energy levels of He relevant to the multiphoton ionization. (**b**) Photoelectron spectra of He obtained by two-color two-photon ionization with FEL at 51.0 nm and UV laser at 250 nm

emissions take place resonantly from electronic states around three-photon energy level (∼72 eV).

Previous studies on single photon ionization of He show that doubly excited states converging to He^+ $N = 3$ state are located in the 70 eV energy region [43, 44] (see Fig. 9.8(a)). The EUV multiphoton excitation to these doubly excited states is confirmed by the theoretical calculation solving the time-dependent Schrödinger equation for two-electrons of He [14]. The simulated photoelectron spectra well reproduce the experimental data, and show that the substructure is formed by doubly excited states in which one electron of the two electrons is excited to $N = 3$ and the other to $n \sim 5$.

In order to understand the three-photon double excitation process more in detail, a UV laser (250 nm) pulse was introduced 50 ps after the EUV FEL pulse. The resultant photoelectron spectra exhibits several peaks at ∼4.5 eV, showing that Rydberg states converging to $N = 1$ threshold of He^+ with the principal quantum numbers of $n = 4$–8 are excited by the single photoabsorption of the FEL pulse. Since the principal quantum numbers of the outer electrons in the doubly excited states are almost unchanged, the double excitation proceeds in a stepwise manner. First the one of the two 1s electrons is excited to $n \sim 5$ by the single photon absorption, and then, two other photons are absorbed to excite the remaining 1s electron to the $N = 3$ state.

Resonances with these Rydberg states contribute to the enhancement of the three-photon process against the two-photon process. First, the propensity to the excitation $\Delta A = 0$ identified in the single photon absorption [43, 44] is removed, since the correlation of the two electrons are not significant in the $n \sim 5$ Rydberg states. Therefore all the possible states with $A = +1, 0, -1$ can be excited by the three-photon absorption via the $n \sim 5$ Rydberg states. The increase in the number of the resonance states enhances the three-photon absorption. Second, the two-photon ionization becomes unfavorable by the excitation of the first electron to the Rydberg states, due to the small overlap between the diffuse Rydberg wavefunctions and the highly oscillatory wavefunction of the high-energy ionization continuum (∼20 eV above the first ionization threshold). Therefore, the two-photon absorption of the remaining 1s electron to couple with the tightly bound $3l$ states becomes more efficient than the one photon absorption of the Rydberg electron, resulting in the enhancement of the three-photon process than the two-photon process.

9.5 Two-Color Above Threshold Ionization of Ar

Synchronization between FEL and external laser pulses is important in time-resolved studies. The timing jitter of the system, rather than the pulse duration, often limits a temporal resolution of the ultrafast pump-probe spectroscopy [32, 45, 46]. Here, we present cross-correlation measurements at SCSS using two-color above threshold ionization of Ar to evaluate the temporal resolution.

Figure 9.9(a) shows photoelectron spectra of Ar gas obtained by using FEL at 52.2 nm (∼7 TW/cm^2) and NIR laser pulse at 800 nm (6 TW/cm^2). When the NIR pulse precedes the FEL pulse by $\Delta t = -1.1$ ps, a strong peak is observed at 8.1 eV,

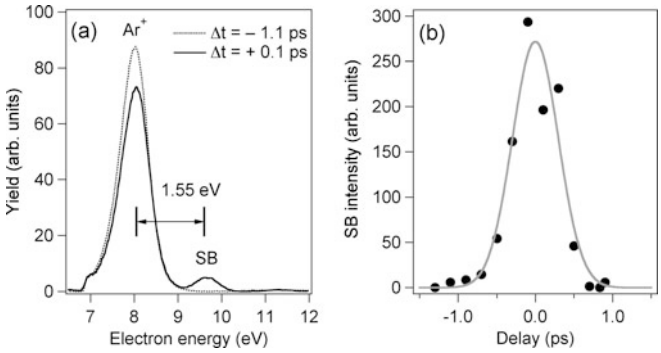

Fig. 9.9 (**a**) Two-photon above threshold photoelectron spectra of Ar with FEL (52.2 nm) and NIR laser (800 nm) pulses at −1.1 (*dotted*) and +0.1 (*solid*) ps. The Ar^+ peak due to one-photon ionization by the FEL appears at 8.1 eV. A sideband (SB) at 9.7 eV in the trace at +0.1 ps is attributed to photoelectrons above threshold ionization by the FEL and NIR laser pulses. A retardation voltage of −7 V was applied. (**b**) The cross-correlation trace obtained by the sideband (SB) intensity in (**a**). The FWHM is 0.7(1) ps from the least squares fitting with a Gaussian function

which is assigned to photoelectrons produced by single photon absorption of FEL, $Ar + h\nu \rightarrow Ar^+ + e^-$. On the other hand, when these pulses are introduced almost at the same time ($\Delta t = +0.1$ ps), the photoelectron spectrum shows an additional peak on the higher energy side (9.7 eV), while the main peak is reduced in intensity [45, 46]. The peak energy difference between the main and the sideband corresponds to the amount of one NIR photon (1.55 eV), showing that the sideband is formed by above threshold ionization by the FEL and NIR pulses. The evolution of the sideband intensity as a function of the time delay between the FEL and NIR pulses is shown in Fig. 9.9(b). From the least squares fitting of the data to a Gaussian function, the FWHM of the cross-correlation trace is determined to be 0.7(1) ps. Since durations of the FEL and NIR laser pulses are expected to be ∼100 and 50 fs, respectively, the observed cross-correlation width of 0.7 ps is mainly attributed to the timing jitter between the two pulses.

9.6 Summary

We demonstrated that the photoelectron spectroscopy is powerful in unveiling nonlinear processes in intense EUV free electron laser (FEL) fields. In particular, the shot-by-shot analysis enables us to study the effect of small changes in the mean photon energy (∼0.02 eV), which clarifies the pathways of multiphoton absorption involving one or two electrons via resonance states. Isolated atoms serve as an ideal benchmark to understand the responses of a more complex system such as protein molecules and bulk materials exposed to intense EUV and X-ray laser fields. Their understanding will establish the basics for the future applications of ultrashort intense pulses from FELs, such as static and dynamical X-ray diffraction imaging [47–51], ultrafast optical switching [52, 53], and creation of warm dense matters [54, 55].

Acknowledgements We acknowledge the staff in the SCSS Test Accelerator Group at RIKEN and Dr. C.-M. Tseng at Institute for Molecular Science for their support in the experiments. We thank Prof. T. Morishita at University of Electro-Communications and Prof. C.-N. Liu at Fu-Jen Catholic University for theoretical calculations of double excitation of He and valuable discussions.

References

1. W. Ackermann et al., Nat. Photonics **1**, 336–342 (2007)
2. T. Shintake et al., Nat. Photonics **2**, 555–559 (2008)
3. P. Emma et al., Nat. Photonics **4**, 641–647 (2010)
4. B. Sheehy, L.F. DiMauro, Annu. Rev. Phys. Chem. **47**, 463–469 (1996)
5. J.H. Posthumus, Rep. Prog. Phys. **67**, 623–665 (2004)
6. L.V. Keldysh, Sov. Phys. JETP **20**, 1307–1314 (1965)
7. T. Sato et al., Appl. Phys. Lett. **92**, 154103 (2008)
8. H. Fukuzawa et al., Phys. Rev. A **79**, 031201(R) (2009)
9. H. Iwayama et al., J. Phys. B **42**, 134019 (2009)
10. K. Motomura et al., J. Phys. B **42**, 221003 (2009)
11. Y. Hikosaka et al., Phys. Rev. Lett. **105**, 133001 (2010)
12. S.Y. Liu et al., Phys. Rev. A **81**, 031403(R) (2010)
13. H. Fukuzawa et al., J. Phys. B **43**, 111001 (2010)
14. A. Hishikawa et al., Phys. Rev. Lett. **107**, 243003 (2011)
15. N. Miyauchi et al., J. Phys. B **44**, 071001 (2011)
16. M. Nagasono et al., Phys. Rev. Lett. **107**, 193603 (2011)
17. T. Sato et al., J. Phys. B **44**, 161001 (2011)
18. H. Wabnitz et al., Phys. Rev. Lett. **94**, 023001 (2005)
19. M. Meyer et al., Phys. Rev. A **74**, 011401(R) (2006)
20. R. Moshammer et al., Phys. Rev. Lett. **98**, 203001 (2007)
21. M. Nagasono et al., Phys. Rev. A **75**, 051406 (2007)
22. A.A. Sorokin et al., Phys. Rev. Lett. **99**, 213002 (2007)
23. A. Rudenko et al., Phys. Rev. Lett. **101**, 073003 (2008)
24. C. Bostedt et al., Phys. Rev. Lett. **100** (2008)
25. P. Johnsson et al., J. Phys. B **42**, 134017 (2009)
26. M. Kurka et al., J. Phys. B **42**, 141002 (2009)
27. M.G. Makris, P. Lambropoulos, A. Mihelič, Phys. Rev. Lett. **102**, 033002 (2009)
28. M. Martins et al., Phys. Rev. A **80**, 023411 (2009)
29. M. Richter et al., Phys. Rev. Lett. **102**, 163002 (2009)
30. M. Meyer et al., Phys. Rev. Lett. **104**, 213001 (2010)
31. M. Richter et al., J. Phys. B **43**, 194005 (2010)
32. J.M. Glownia et al., Opt. Express **18**, 17620–17630 (2010)
33. L. Young et al., Nature **466**, 56–61 (2010)
34. M. Meyer et al., Phys. Rev. Lett. **108**, 063007 (2012)
35. G. Zhu et al., Phys. Rev. Lett. **103**, 103008 (2009)
36. M. Wellhöfer et al., J. Instrum. **3**, P02003 (2008)
37. T. Shintake et al., Phys. Rev. Spec. Top., Accel. Beams **12**, 070701 (2009)
38. T. Togashi et al., Opt. Express **19**, 317–324 (2010)
39. A.A. Wills, A.A. Cafolla, J. Comer, J. Phys. B **24**, 3989 (1991)
40. T.X. Carroll et al., J. Electron Spectrosc. Relat. Phenom. **125**, 127–132 (2002)
41. A. Hibbert, J.E. Hansen, J. Phys. B **27**, 3325–3347 (1994)
42. E.V. Gryzlova et al., Phys. Rev. A **84**, 063405 (2011)
43. D.W. Lindle et al., Phys. Rev. A **31**, 714–726 (1985)
44. M. Domke et al., Phys. Rev. A **53**, 1424 (1996)

45. P. Radcliffe et al., Appl. Phys. Lett. **90**, 131108 (2007)
46. M. Meyer et al., J. Phys. B **43**, 194006 (2010)
47. R. Neutze et al., Nature **406**, 752–757 (2000)
48. Y. Nishino et al., Appl. Phys. Express **3**, 102701 (2010)
49. A.P. Mancuso et al., New J. Phys. **12**, 035003 (2010)
50. H.N. Chapman et al., Nature **470**, 73–77 (2011)
51. Y. Huismans et al., Science **331**, 61–64 (2011)
52. H. Yoneda et al., Opt. Express **17**, 23443–23448 (2009)
53. T.E. Glover et al., Nat. Phys. **6**, 69–74 (2010)
54. B. Nagler et al., Nat. Phys. **5**, 693–696 (2009)
55. N.A. Inogamov et al., Contrib. Plasma Phys. **51**, 419–426 (2011)
56. E.B. Saloman, J. Phys. Chem. Ref. Data **39**, 033101 (2010)

Chapter 10
Rescattering Photoelectron Spectroscopy of Atoms and Molecules in Intense Laser Fields

Misaki Okunishi and Kiyoshi Ueda

Abstract Angle resolved photoelectron spectra of rescattered electrons by the target ion contain rich information on the electron–(target) ion interaction potential, and therefore target structure. We have measured momentum distributions of rescattered electrons for rare gas atoms, O_2, CO_2 and C_2H_4 molecules induced by intense ultrashort laser pulses. Using recently developed quantitative rescattering theory, we have extracted differential cross sections (DCSs) for elastic scattering of free-electrons from the parent ions. We compare these DCSs with theoretically calculated DCSs and get reasonable agreement between the experimentally extracted DCSs and the theoretical calculations. It confirms that the structural information of the target is involved in the rescattering electron spectra.

10.1 Introduction

Recently the interaction of an atom or molecule with an intense laser field continues to attract much interest because of the discoveries of many new exciting phenomena. (See, for example, [1] and references therein.) Photoelectron spectroscopy is an effective tool to investigate the photoionization of atoms and molecules in intense laser fields. Figure 10.1 illustrates a schematic photoelectron spectrum of an atom or molecule irradiated by a linearly polarized intense laser pulse, whose field intensity matches the intra-molecular (or intra-atomic) Coulombic field. Here ponderomotive energy U_p, cycle averaged kinetic energy of electron's quiver motion in the laser electric field, is used as a unit of electron energy.

From simple classical and semiclassical considerations, it is known that the spectrum consists of two regions [2]. In the low energy region up to $2U_p$, electron yield rapidly decreases as a function of the electron energy. These low energy electrons

M. Okunishi · K. Ueda (✉)
Institute of Multidisciplinary Research for Advanced Materials, Tohoku University,
2-1-1 Katahira, Aobaku, Sendai 980-8577, Japan
e-mail: ueda@tagen.tohoku.ac.jp

M. Okunishi
e-mail: okunishi@tagen.tohoku.ac.jp

K. Yamanouchi, K. Midorikawa (eds.), *Progress in Ultrafast Intense Laser Science*,
Springer Series in Chemical Physics 104, DOI 10.1007/978-3-642-35052-8_10,

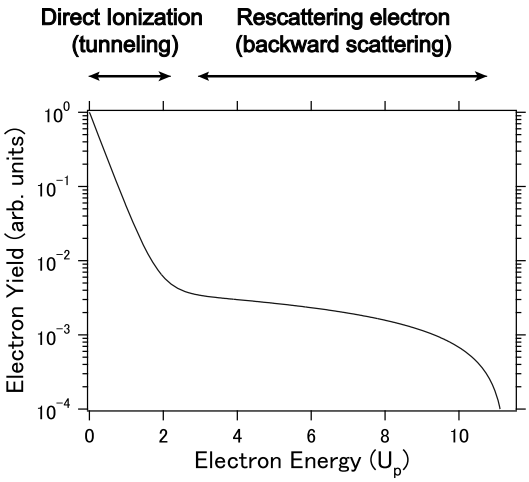

Fig. 10.1 Schematic photoelectron spectrum of an atom or molecule induced by an intense laser pulse. The U_p is used as a unit of photoelectron energy

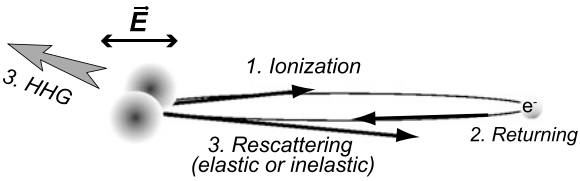

Fig. 10.2 Schematic view of the three step model for electron rescattering

are induced by direct tunneling ionization of the target. In the second high-energy region, the electron kinetic energy distribution exhibits a plateau. These high-energy electrons are caused by the large-angle backward rescattering of the returning electron. These rescattering photoelectrons have a sharp cutoff around $10U_p$ as indicated in Fig. 10.1.

The rescattering process can be explained qualitatively by a well-known three-step model [3, 4]. (See Fig. 10.2.) First, an atom or a molecule in an intense laser field is tunnel ionized near the peak of the oscillating electric field [5, 6]. Since the released electron is placed in the oscillating field, it may return (2nd step) and recollide (3rd step) with the parent ion with an maximum kinetic energy of $3.17U_p$. As a result, the electron rescatters elastically (or inelastically), or recombines with the target ion to produce an extreme ultraviolet (EUV) photon by high-order harmonic generation (HHG). The backward rescattering electron obtains additional drift momentum from the electric field and then released as a high-energy rescattering photoelectron with an energy up to $10U_p$. The drift momentum is given by the vector potential (A_0) of the laser field at the time of recollision.

The HHG process is an inverse process of photoionization and considered as a half-collision of the electron with the target ion. In contrast, the elastic or inelastic rescattering can be seen as a full-collision process. Through the electron-ion collisions, the HHG spectra and rescattering photoelectron spectra must have structural information of the target, or more accurately, of the interaction potential between the electron and the target ion within a single active-electron approximation. Since

the rescattering process takes place within one optical cycle of the laser field, it may become a useful tool for determining the structure of the molecule with a temporal resolution of femto- or subfemtoseconds.

The HHG spectroscopy is most widely used to study the rescattering process and to obtain structural information of the target [7–12]. For example, Itatani *et al.* [8] reported that the highest occupied molecular orbital (HOMO) of the N_2 molecule can be reconstructed from the HHG spectra using a tomographic procedure. This result has generated a wave of excitement. However, their reconstructed orbital wave function relies on a number of unchecked assumptions [13–16]. In particular, they used a plane wave as a continuum wavefunction of the returning electron. The collision energy of the returning electron is less than several tenth eV. In such low energy collisions, the plane wave approximation usually fails to explain the collision process properly. So to make their idea as a practical tool for retrieving structural information it still needs a careful investigation of the underlying assumptions.

Rescattering photoelectron spectroscopy (RPS) is another method to study the electron rescattering. High-energy electrons that form the plateau region were observed in 1990s [17, 18] and interpreted as the backward rescattering photoelectrons [19]. However, due to the lack of theory bridging between the RPS spectra and quantitative structural information of the target, the accurate retrieval of the target structure was impossible until very recently. Meckel *et al.* [20] was the first who measured RPS spectra of laser aligned N_2 and O_2 molecules and tried to extract the structural information. However, they used a plane wave approximation, which may not be valid as in the case of HHG spectroscopy.

Recently, C.D. Lin and coworkers developed so called quantitative rescattering (QRS) theory to deal with the rescattering process quantitatively. (See their recent review [21] and references therein.) The QRS theory can connect the RPS spectra and elastic scattering differential cross sections (DCSs) of a free electron from a target ion using a simple factorization formula. Once the DCSs are extracted from the RPS spectra, we can use a standard scattering theory of electron collisions to estimate the interaction potential between the electron and the target ion.

We have recently observed angle-resolved RPS spectra of rare gas atoms (Ne, Ar, Kr, and Xe) [22, 23] and several small molecules [24–27]. Based on the QRS theory, we have extracted the elastic electron-ion DCSs for these rare gas species [22, 23] and O_2, CO_2, and C_2H_4 molecules [26, 27]. The extracted DCSs are compared with theoretical calculations of the DCSs of electron-ion field free scattering using ab-initio electron-ion interaction potentials to confirm the validity of the extraction procedure. The purpose of this article is to introduce our recent works and to discuss what kind of information we can extract from the RPS spectra.

10.2 Experimental Apparatus and the QRS Theory

10.2.1 Experimental Apparatus

The purpose of the experimental apparatus described in Fig. 10.3 is to measure the electron spectra of gas phase atoms and molecules and the corresponding angular

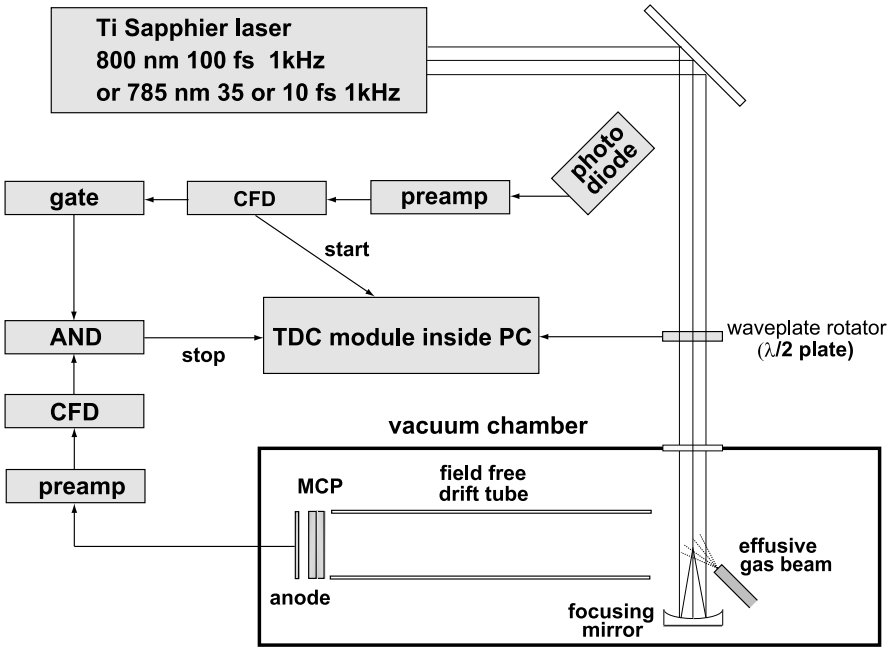

Fig. 10.3 Schematic experimental setup

distributions with respect to the direction of linear polarization of the laser light as a function of the kinetic energy of the electron and the incident laser intensity.

The experimental apparatus consists of a 1 kHz amplified Ti:sapphire laser system and a time-of-flight electron spectrometer installed in an ultra-high vacuum chamber. To cover a wide range of laser intensities, we used three different pulse widths from the two different laser systems for O_2 and CO_2 experiments. At the lowest laser intensities, we used 100 fs laser pulse at a wavelength of 800 nm (Quantronix, Integra). For higher laser intensities, we used shorter pulse duration, 35 fs and 10 fs, at 785 nm (KMlabs, Dragon), in order to reduce the effect of depletion of the sample molecules within the focus of the laser beam. To generate the laser pulses of 10 fs duration, the pulses of 35 fs duration were compressed in an argon-filled hollow-core fiber. For rare gas and C_2H_4 experiments, we use only the 100 fs laser system. The polarization direction can easily be rotated in any direction perpendicular to the beam by using a $\lambda/2$ plate. The laser beam is introduced through a quartz window into the vacuum chamber, where it is focused by a small $f = 60$ mm lens for 100 fs laser pulses or $f = 100$ mm mirror for 35 fs and 10 fs pulses. The base pressure of the vacuum chamber is better than 2×10^{-10} torr. This is achieved by using a 1000 l/s turbo molecular pump (TMP) that is backed by a second small 70 l/s TMP. Sample gas is introduced as an effusive beam through a grounded copper needle positioned 10 mm above the laser focus. During the measurement with gas load the background pressure of the vacuum chamber was varied from 1×10^{-9} to 2×10^{-6} torr. The magnetic field inside the vacuum chamber was

compensated by three pairs of Helmholtz coils mounted outside the vacuum. The residual field was smaller than 4 μT.

The electron spectrometer is a 264 mm long time-of-flight spectrometer with a limited acceptance angle of $0.0014 \times 4\,\pi sr$. The electrons are detected by a double stack of 40 mm diameter micro channel plates followed by an anode. The noise level was below 20 Hz. So the chance to detect a noise count inside the time interval of 1 μs after one laser shot where the photoelectrons arrive at the detector is less than 2×10^{-5}. Such low noise levels are essential for the high dynamic range of the apparatus, which is necessary for the measurements of the RPS spectra. The time difference between the laser pulse (provided by a photo-diode receiving scattered light) and the arrival time of the electron was recorded by a 500 ps time-to-digital converter (TDC). The signals from the photo-diode and the anode are amplified, discriminated and converted to logic signals by two standard constant fraction discriminators. The TDC can record up to 16 hits per laser shot and input channel. Most of the signal intensity were in a time interval of typically 200 ns. The sample gas pressure was set to a level where typically 1 electron was detected per laser shot with this time window. For measurements dedicated to the weak high energy part of the spectra, an electronic gate was used to mask slow electrons. Again the gas pressure was adjusted to a level where typically 1 electron per laser shot fell into the selected time window.

The electron yield produced by strong field ionization sharply depends on variations of the laser intensity. Thus, we need to reduce the effect of the laser power fluctuation to obtain reliable angular distributions of the RPS spectra. In our experiment, the $\lambda/2$ plate was mounted on a rotator with a constant rotation period of 60000 laser shots. One of the additional channels of the TDC module was used to record the absolute position of the rotator. In this way, the data for the spectra all angles can be recorded at virtually the same time. Averaging over several hours of rotation the angular distributions were almost free of the effects due to laser power variations.

10.2.2 Theoretical Background

Based on the QRS theory, we can extract the large-angle DCSs for elastic backscattering of a free electron from the parent ion. Details of the QRS theory is described in recent series of papers by C. D. Lin and his colleagues [21, 28–32]. Thus, only a brief account for the extraction of the DCSs used in the present study will be presented here. The key point of the theory is the factorization of the rescattering electron yields into a product of the electron scattering DCSs with a "wave packet" representing the momentum distribution of the returning electron [28]. In this section, the formulation for linear molecules such as O_2 and CO_2 molecules will be presented [26].

For fixed-in-space linear molecules where the molecular axis is represented by angles $\hat{\mathbf{R}}' = \{\Theta', \Phi'\}$ with respect to the laser's polarization along the z-axis, rescat-

tering photoelectron momentum distributions $S(\mathbf{p}, \hat{\mathbf{R}}')$ having the electron momentum of $\mathbf{p}$ can be expressed as

$$S\left(\mathbf{p}, \hat{\mathbf{R}}'\right) = W\left(p_r, \hat{\mathbf{R}}'\right)\sigma\left(\mathbf{p}_r, \hat{\mathbf{R}}'\right), \tag{1}$$

where $\sigma(\mathbf{p}_r, \hat{\mathbf{R}}')$ is the fixed-in-space elastic DCS for the scattering of free electrons by the target ion with final momentum $\mathbf{p}_r = \{p_r, \theta_r, \phi_r\}$. Here $W(p_r, \hat{\mathbf{R}}')$ is the momentum distribution of the returning electron at the time of recollision. We need the relation between the final momentum $\mathbf{p}_r$ and rescattering photoelectron momentum $\mathbf{p}$ to use the Eq. (1). In the QRS theory, the ratio of the recollision momentum to the drift momentum A_0 is assumed to be 1.26 ($= p_r/A_0$). Then we have

$$\mathbf{p} = \pm A_0\hat{\mathbf{z}} + \mathbf{p}_r = \pm\left(p_r/1.26\right)\hat{\mathbf{z}} + \mathbf{p}_r \tag{2}$$

where the "+" and "−" signs refer to electrons that, before scattering, are moving toward the ion from the $z > 0$ and the $z < 0$ directions, respectively. The ratio ($p_r/A_0 = 1.26$) is estimated from the cutoff electrons with maximum collision energy ($3.17U_p$). So Eq. (2) can in principle be used only for the cutoff electrons. In practice, however, recent theoretical and experimental studies [23, 29, 30, 33] revealed that the Eq. (2) can be used to extract the DCSs for rare gas targets with kinetic energies lower than the cutoff $10U_p$.

The wave packet of Eq. (1) is approximated by $N(\Theta')\bar{W}(p_r)$, where $N(\Theta')$ is proportional to the angle-dependent ionization rate. The photoelectron momentum distribution for randomly oriented molecules is then obtained as

$$S(\mathbf{p}) = \bar{W}(p_r)\bar{\sigma}(p_r, \theta_r), \tag{3}$$

where $\bar{\sigma}(p_r, \theta_r)$ is the DCS convoluted over the alignment angles as,

$$\bar{\sigma}(p_r, \theta_r) = \int N\left(\Theta'\right)\sigma\left(\mathbf{p}_r, \hat{\mathbf{R}}'\right) d\hat{\mathbf{R}}'. \tag{4}$$

The electron spectra as well as the convoluted DCSs exhibit cylindrical symmetry along the z-axis and thus we can omit the azimuthal angle ϕ_r after the convolution.

The angle dependent ionization rate depends very weakly on laser intensity. The relation between $\mathbf{p}_r$ and $\mathbf{p}$ is independent of laser intensity. Thus, we can integrate the Eq. (3) over the focus volume of laser beam. Then we obtain the final formula

$$S_{I_0}(\mathbf{p}) = \bar{W}_{I_0}(p_r)\bar{\sigma}(p_r, \theta_r), \tag{5}$$

where $S_{I_0}(\mathbf{p})$ is the volume-integrated photoelectron momentum distributions with a peak laser intensity of I_0 at the laser focus, and represents the angle-resolved electron momentum distribution measured experimentally. $\bar{W}_{I_0}(p_r)$ is the volume-integrated wave packet. It can be a complex function of the laser pulse properties like intensity, pulse shape, wavelength, etc., but does not depend on the rescattering angle θ_r.

Equation (5) can be applied not only for linear molecules, but also for rare gas atoms and non-linear polyatomic molecules (like C_2H_4) with minor modifications of the formulation. For rare gas atoms, there is no molecular alignment effect and we can simplify the formulation by neglecting the contributions coming from the

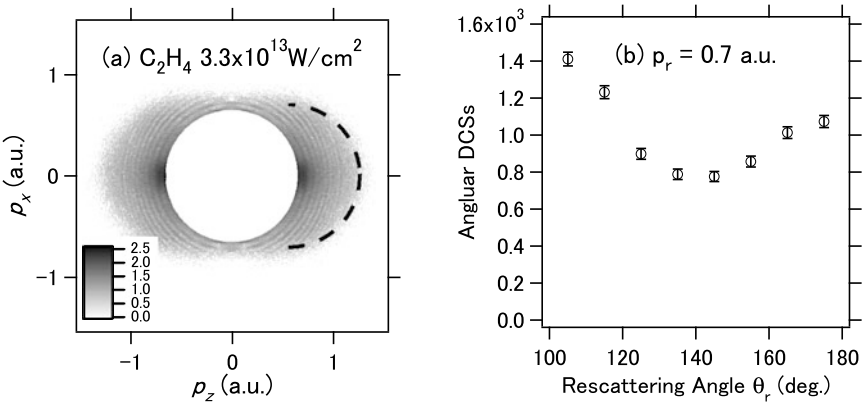

Fig. 10.4 (*Left*) Laser-induced 2D RPS spectrum for C_2H_4 at a laser intensity of 3.3×10^{13} W/cm^2. The electron intensity is plotted in logarithmic scale. The laser polarization direction is along the z axis. The elastic scattering of a returning electron with momentum p_r is represented by a *dashed arc* with a shifted center from the origin by A_0. (*Right*) Electron Yield along the arc for the elastic scattering with the returning electron momentum $p_r = 0.7$ (a.u.) as a function of the rescattering angle θ_r. This is proportional to the elastic DCSs of the returning electrons scattered by the target ion

dependence on the angles $\hat{\mathbf{R}}' = \{\Theta', \Phi'\}$. For non-linear polyatomic molecules, we need one more angle to identify the molecular frame. So the angles $\hat{\mathbf{R}}' = \{\Theta', \Phi'\}$ must be replaced by Euler angles $\hat{\mathbf{R}}' = \{\Theta', \Psi', \Phi'\}$ and the angle dependent ionization rate also depends on the two angles, $\{\Theta', \Psi'\}$.

The procedure for the extraction of the DCSs from the experimental data is presented here. As an example, we pick up the two dimensional (2D) momentum distribution of plateau electrons for C_2H_4 measured at the laser intensity of 3.3×10^{13} W/cm^2 shown in Fig. 10.4(a). We have chosen the horizontal axis to be along the direction of the light polarization and the vertical axis along any direction perpendicular to it (due to cylindrical symmetry of the linearly polarized light). From the Eq. (2), we can draw the arc corresponding to the elastic rescattering of electrons with the rescattering momentum p_r as shown in the dashed line in Fig. 10.4(a). By measuring the electron yields along this arc, we can extract the θ_r dependence of the $S_{I_0}(\mathbf{p})$ in Eq. (5) for each value of the p_r. Because $\bar{W}_{I_0}(p_r)$ does not depend on θ_r in Eq. (5), this angular dependence is identical to the angular dependence of the DCSs as shown in Fig. 10.4(b).

Momentum (p_r) distributions of the DCSs are difficult to extract from the experimental data only, because the experimental electron yields $S_{I_0}(\mathbf{p})$ is the product of rescattering electron wavepacket, $\bar{W}_{I_0}(p_r)$, and the DCSs, $\bar{\sigma}(p_r, \theta_r)$, in Eq. (5). So the momentum dependence of the electron yields is included in both the wavepacket and DCSs. Then we use the calculated DCSs of free electrons in collisions with target ion at one fixed angle as a reference and estimate the wavepacket $\bar{W}_{I_0}(p_r)$ from the experimental momentum distributions ($S_{I_0}(\mathbf{p})$). It means that the experimentally extracted DCSs are always normalized by the calculated ones at one fixed angle in

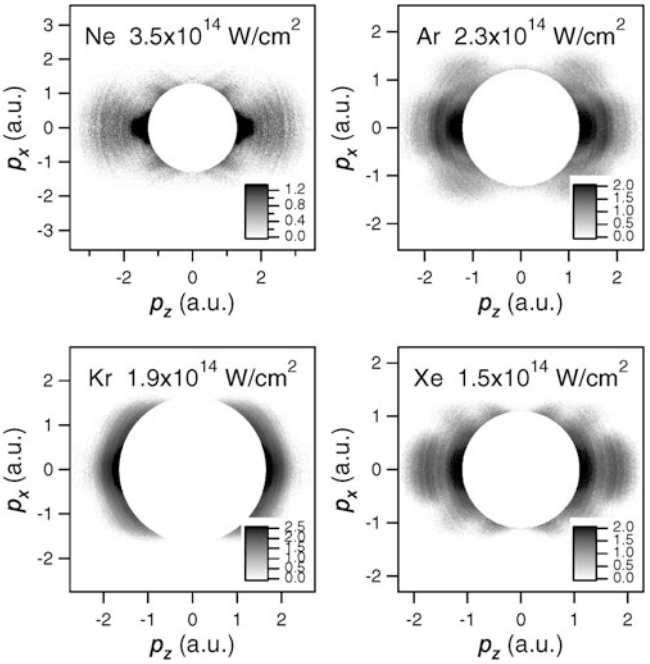

Fig. 10.5 2D electron momentum distributions of rare gas atoms using 100 fs laser pulses at laser intensities indicated in the figures

the present studies. If we can obtain relatively reliable calculation of the DCSs, we can extract the $\bar{W}_{I_0}(p_r)$, and then, the convoluted DCSs, $\bar{\sigma}(p_r, \theta_r)$, as a function of rescattering momentum (p_r) and rescattering angle (θ_r).

10.3 Results and Discussions

10.3.1 Rare Gas Atoms—Simplest Targets

As a first experimental verification of the QRS theory, extractions of large-angle DCSs were carried out for rare gas atoms by two groups [22, 23, 33, 34]. The 2D momentum distributions of high-energy electrons for four rare gas atoms (Ne, Ar, Kr, and Xe) in our experiments [22, 23] are shown in Fig. 10.5. In Fig. 10.5, the photoelectron distributions for Ne, Ar, Kr, and Xe show quite different interference pattern. From these 2D momentum spectra, we extracted the elastic DCSs for elastic scatterings by free electrons as shown in Fig. 10.6. To smooth out the ATI peaks, the extracted DCSs are obtained by integrating over a bin of $\Delta p = 0.05$ a.u. and $\Delta\theta = 10°$.

In Fig. 10.6, we compare the experimentally extracted DCSs with theoretical calculations of the DCSs for electron-ion field free scatterings. The calculations of

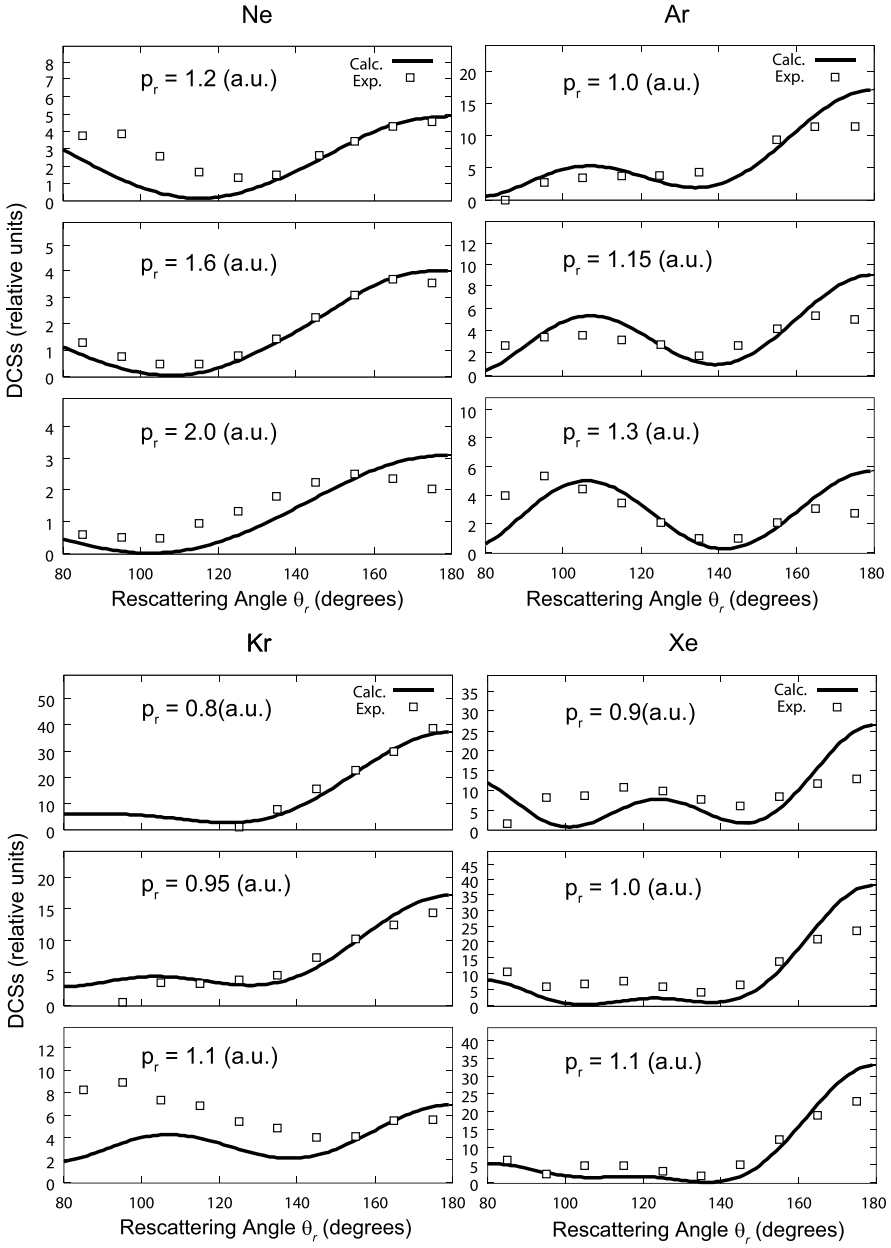

Fig. 10.6 Comparison of theoretically calculated and experimentally extracted elastic DCSs for rare gas atoms at selected values of electron momentum. Experimental error bars represent statistical uncertainties estimated by the square root of the electron counts

the DCSs are carried out in a single active electron model, in which we use a model potential to approximate the interaction between the active electron and the ion core. The effective potential used in these calculations are shown elsewhere [22, 35]. We can see a large degree of agreement between each pair in a broad range of angles and momenta, indicating that the QRS model in the form of Eq. (5) works very well for the experimental results.

The interference structures of the DCSs shown in Figs. 10.5 and 10.6 can be interpreted as due to the interference between the scattering amplitudes corresponding to Coulombic potential and the remaining short range potential. Here the short range potential is used as a part of the screened Coulombic potential, which describes the interaction potential between the active electron and the ion core.

10.3.2 O_2 and CO_2 Molecules—Linear Molecules

For molecular targets, the most attractive point is the possibility of extracting molecular structure through diffraction of the electron waves scattered by different atoms within the molecule, because it may open a new way for time dependent imaging of a transient molecule. As a first demonstration for molecular targets, we selected O_2 and CO_2 molecules [26]. The HOMOs of O_2 and CO_2 are π_g symmetry and thus have the lobs at $\sim$45° relative to the molecular axis. As a result, the angle-dependent ionization rate has a sharp maximum for the molecules aligned at $\sim$45° relative to the laser polarization direction. Thus, without a special alignment technique, we can measure the RPS spectra and extract the DCSs for the (partially) aligned molecule.

The 2D momentum distributions of rescattered electrons for the O_2 molecule measured at four different laser intensities are shown in Fig. 10.7. We covered a very wide range of laser intensities from 7×10^{13} W/cm^2 to 9×10^{14} W/cm^2 using three different pulse widths and extracted DCSs in a wide range (0.7–3.3 a.u.) of electron momentum (p_r) as shown in the lower panel of Fig. 10.8. This 2D map of the DCSs is a patchwork of the 2D maps extracted from the 2D momentum distributions measured at several laser intensities, which correspond to different momentum ranges. We used two 2D spectra with 100 fs laser ($I_0 = 0.7$ and 1.3×10^{14} W/cm^2), which cover $p_r = 0.6$–1.25 a.u., two spectra with 35 fs laser ($I_0 = 1.4$ and 1.8×10^{14} W/cm^2), which cover $p_r = 1.25$–1.7 a.u., and four spectra with 10 fs laser ($I_0 = 0.35$, 0.5, 0.7, and 0.9×10^{15} W/cm^2), which cover $p_r = 1.7$–3.3 a.u. The extracted DCSs are obtained by integrating over a bin of $\Delta p = 0.1$ a.u. and $\Delta\theta = 10°$. There are some overlaps between the momentum ranges for different laser intensity pulses. In these cases, we used the lowest laser intensity to extract the DCSs, because the present procedure of the DCS extraction is the best for the largest momentum range near the cutoff region. Electron counts are very low near the cutoff and thus values of the DCSs extracted in this region are more scattered than those extracted from the lower momentum region for each laser intensity. Therefore, for quantitative comparison of the DCSs, we need to use one-dimensional angular DCSs

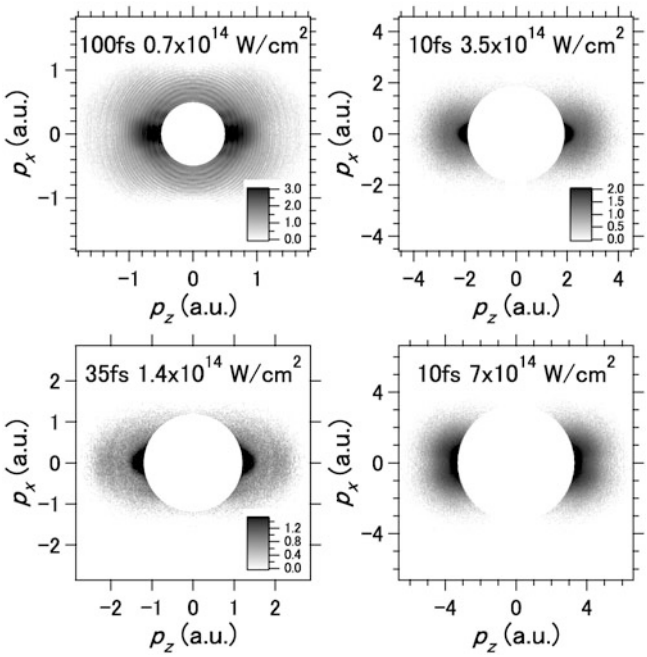

Fig. 10.7 2D electron momentum distributions of O_2 molecule at selected laser intensities

with error bars as shown in Fig. 10.6 for rare gas targets. Here, we focus on qualitative comparison between the extracted and theoretical DCSs. Therefore, we exhibit only the 2D map of the DCSs in Fig. 10.8.

A 2D map of theoretically calculated DCSs is also shown in upper panel of Fig. 10.8. At first, we perform *ab initio* calculations of DCSs for elastic scattering of free electrons from the space-fixed O_2^+ molecular ion [36]. Then the calculated DCSs, $\bar{\sigma}(p_r, \theta_r)$, are obtained from Eq. (4) using $N(\Theta')$ calculated from the MO-ADK theory [37]. Finally, they are convoluted over the experimental angular resolution and bin sizes used for the extraction of the experimental DCSs. In the calculations, the interatomic distance is fixed to its experimental equilibrium value. The dynamical alignment effects within the laser pulse before the ionization is not incorporated, because this effect is less significant than the effect of the alignment dependent ionization rate incorporated in the present calculation.

The experimental DCSs are normalized to the calculated DCSs at $\theta_r = 160°$ to compare with the calculated DCSs in the 2D maps in Fig. 10.8. The origin of the modulations of the DCSs can be found in the *ab initio* DCSs for the space-fixed O_2^+ at the most probable alignment angle of 45°, as shown in lower panel of Fig. 10.9. The modulation is significant especially at ∼180° where the electrons are backscattered. This modulation is mainly due to the double slit type interference as illustrated in upper panel of Fig. 10.9. The returning electron wave packet is rescattered by the two O atoms, aligned at around 45° relative to the polarization direction, and

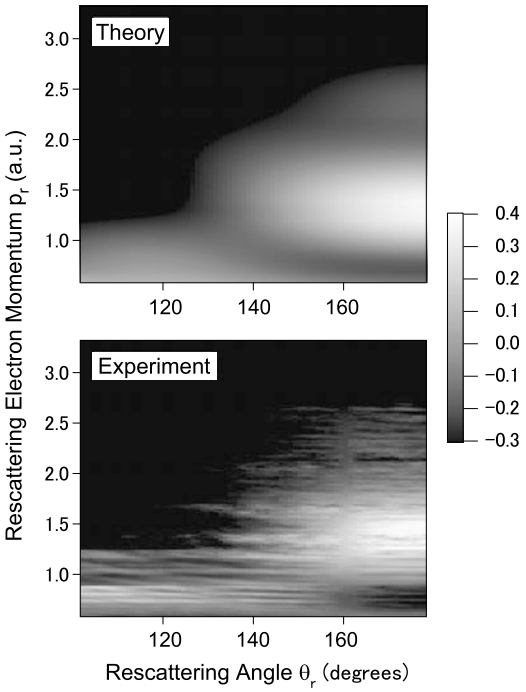

Fig. 10.8 Comparison of theoretically calculated and experimentally extracted elastic 2D DCSs for O_2 molecules as a function of electron momentum (p_r) and rescattering angle (θ_r). The DCSs are plotted in logarithmic scale. Experimental DCSs are normalized by the calculated DCSs at $\theta_r = 160°$

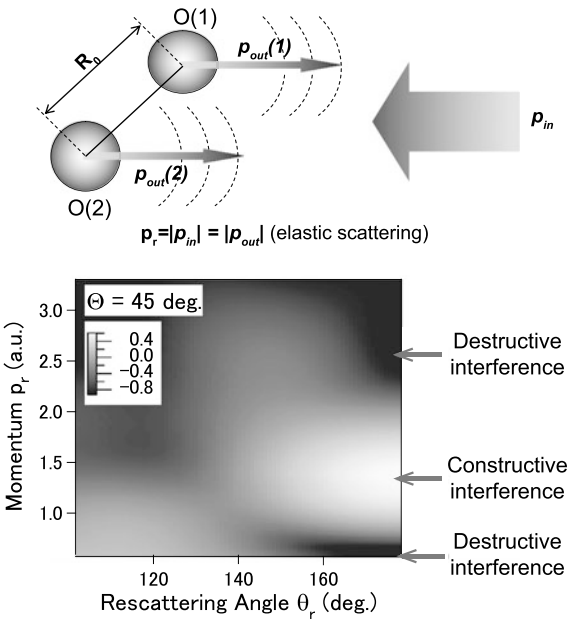

Fig. 10.9 (*Lower*): Calculated DCSs for elastic scattering of free electrons with space-fixed O_2^+ as a function of p_r and θ_r. Molecular axis is fixed at 45° with respect to the laser polarization, but the DCSs are averaged over azimuthal angle, Φ'. (*Upper*): Schematic view of double slit type interference originated from the diffraction of two rescattering electron waves coming from the different O atoms

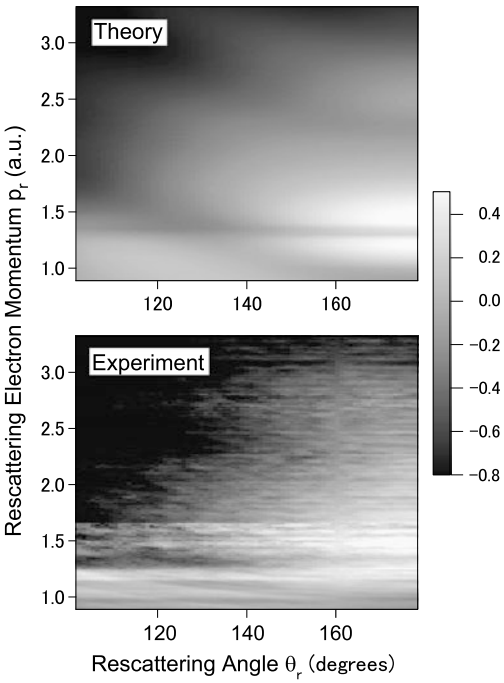

Fig. 10.10 Comparison of theoretically calculated and experimentally extracted elastic 2D DCSs for CO_2 molecules as a function of p_r and θ_r. The DCSs are plotted in logarithmic scale. Experimental DCSs are normalized by the calculated DCSs at $\theta_r = 160°$

thus the back-scattered waves exhibit double slit type interference. The minimums at ∼0.7 and ∼2.7 a.u. correspond to the destructive interference and the maximum at ∼1.5 a.u. corresponds to the constructive interference. After averaging over all possible alignment angles, the calculated DCSs have less clear contrast, as shown in Fig. 10.8, but still observable footprint for this double slit type interference.

There are some discrete-looking features in the momentum dependence of the experimental DCSs in Fig. 10.8. These features do not appear in the theoretical calculations. Some of these come from the boundary of the momentum regions measured with different laser intensities. Rough connections at some boundary regions partially explain these discrete-like features. It should be noted once again that the DCS was extracted at each rescattering electron momentum and that the rescattering momentum distribution was normalized with the theoretical one at 160 degrees. The artificial stripe structure seen in Fig. 10.8 would therefore not affect the retrieval of the molecular structure from the extracted DCSs.

The experimentally extracted and theoretically calculated DCSs for CO_2 molecule are shown in Fig. 10.10. They are obtained using the same procedures used for O_2. To construct this 2D map, we combined one 2D spectrum measured with 100 fs laser ($I_0 = 1.3 \times 10^{14}$ W/cm^2), which covers $p_r = 0.9$–1.25 a.u., four spectra with 35 fs laser ($I_0 = 1.4$, 1.8, 2.5, and 4.0×10^{14} W/cm^2), which cover $p_r = 1.25$–2.3 a.u., and two spectra with 10 fs laser ($I_0 = 0.6$ and 0.8×10^{15} W/cm^2), which cover $p_r = 2.3$–3.3 a.u.

Overall shape of the experimental DCSs is well reproduced by the calculations and this indicates the validity of the extraction method based on the QRS theory for this triatomic molecule. Furthermore a clear dip for large angle scatterings at around $p_r = 1.3$ (a.u.) is observed in the DCSs. This pronounced feature of the dip is not seen for O_2. In theoretical calculation, this dip is attributed to the interference between two shape resonances (σ_u and π_g resonances) [38, 39]. The detailed investigation about these shape resonances is now in progress. Because the shape resonances are sensitive to the interaction potential between the electron and the molecular ion, it may be helpful to determine this interaction potential.

10.3.3 C_2H_4 Molecule—A Non Linear Polyatomic Molecule

As a first target for non-linear polyatomic molecules, we select a C_2H_4 molecule [27]. This molecule has a planer configuration in the ground electronic state. The HOMO is π type orbital, which is perpendicular to the molecular plane. Field ionization by the intense laser pulse will predominantly occur for the molecules whose lobes of the HOMO are aligned in the direction of the laser polarization direction. The wave function of the HOMO has a broad distribution perpendicular to the C–C bond and the angle-dependent ionization rate has a broad peak when the laser polarization is perpendicular to the molecular plane. This means that we can measure the RPS spectra and extract the DCSs for partially aligned C_2H_4, without specific alignment or orientation techniques.

Experimentally extracted DCSs and theoretically calculated DCSs are shown in Fig. 10.11. We used five laser intensities in the range from 3.3×10^{13} W/cm^2 to 8.0×10^{13} W/cm^2 of 100 fs laser pulses to measure the electron momentum distributions, from which the experimental DCSs are extracted as shown in the upper panel of Fig. 10.11. In the calculation of the DCSs in lower panel, angle dependent ionization rates calculated using the weak-field asymptotic theory developed in [40] are used to convolute the space-fixed DCSs.

Angular dependence of the calculated DCSs shows pronounced modulations for $p_r \leq 0.8$ a.u. The modulations disappear in higher momentum region. Experimental DCSs well reproduces this dependence. The good agreement between the experimental and theoretical DCSs indicates that the present extraction procedure can be applied to the nonlinear polyatomic molecules. In the calculation, the revival of the modulations appears for $p_r \geq 1.5$ a.u. In our experiment, however, we could not extend the momentum region due to the depletion of molecules at higher laser intensities with 100 fs pulse width.

10.4 Summary and Outlook

We have measured the angle resolved momentum distributions of the rescattering electron for rare gas atoms, O_2, CO_2 and C_2H_4 molecules induced by intense ultrashort laser pulses. Based on the QRS theory, we have extract the elastic scattering

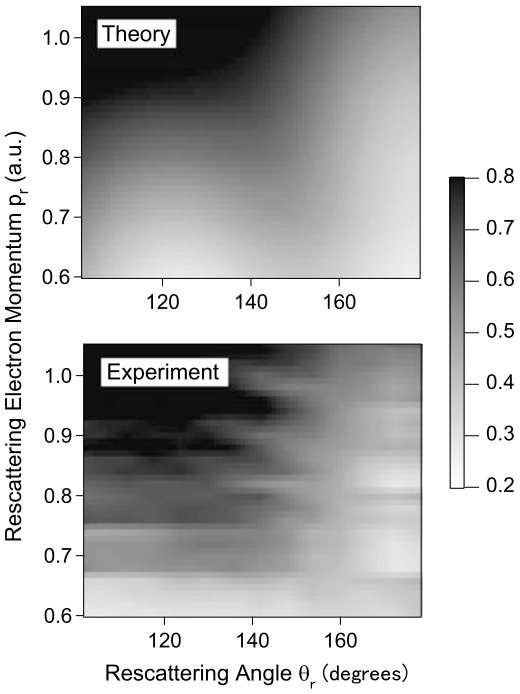

Fig. 10.11 Comparison of theoretically calculated and experimentally extracted elastic 2D DCSs for C_2H_4 molecules as a function of p_r and θ_r. The DCSs are plotted in logarithmic scale. Experimental DCSs are normalized by the calculated DCSs at $\theta_r = 160°$

DCSs of free electrons by target ions. The extracted DCSs were compared with the theoretically calculated DCSs. For rare gas atoms, the short range potentials due to the electron–electron correlations gives rise to the interference patten of the DCSs. For O_2, the interference between the electron waves scattered by two different O atoms can explain the modulation of the DCSs as a function of rescattering angles and electron momentum. For CO_2, we show the existence of shape resonance in the extracted DCSs. Shape resonance is a molecular dependent phenomenon determined by the interaction potential between a free electron and a molecular ion core and may be used as an important guide to know this interaction potential. Even for non-linear polyatomic molecule, C_2H_4, we can extract the DCSs accurately from the experiment and the characteristic modulation pattern of the DCSs are well reproduce by the theoretical calculations.

Potential applications of the present technique are dynamic imaging of transient molecules. Nowadays laser pulses of a few femtoseconds duration are available. Using the present RPS as a probe, structural changes of the transient molecules may be revealed as a function of delay time between the pump and probe laser pulses. Thus, the RPS with ultrashort laser pulses may become a powerful tool for dynamic imaging of transient molecules with temporal resolution of a few femtoseconds. Spatial resolution depends on the collision energy of the rescattering electron and thus the intensity and the wavelength of the laser. A recent experiment using mid-infrared laser pulses reported that the spacial resolution of less than 0.1 Å is achieved [41]. In the present RPS we rely on the fact that the target molecule is partially aligned

due to strong anisotropy of the ionization rate. For retrieval of molecular structure, this approach limits us to extract 1D structure. To extract 2D and 3D structures of non-linear molecules, one has to prepare 2D and 3D spatial alignments of the molecules in advance.

Acknowledgements We would like to thank all collaborators in the present studies including Toru Morishita, Robert Lucchese, Hiromichi Niikura, Shin-ich Watanabe, Zhangjin Chen, Chii-Dong Lin, O.I. Tolstikhin, L.B. Madsen, Georg Prümper, Kozo Shimada, Ryousuke Itaya and Chuncheng Wang. This work was supported in part by Grants-in-Aid for Scientific Research from JSPS, the Budget for "Promotion of X-ray Free Electron Laser Research" from MEXT, by the Cooperative Research Program of "Network Joint Research Center for Materials and Devices", IMRAM research program, and Matsuo Foundation.

References

1. K. Yamanouchi, S.L. Chin, P. Agostini, G. Ferrante (eds.), *Progress in Ultrafast Intense Laser Science* (Springer, Berlin, 2006)
2. W. Becker, F. Grasbon, R. Kopold, D.B. Milošević, G.G. Paulus, H. Walther, Adv. At. Mol. Opt. Phys. **48**, 35 (2002)
3. P.B. Corkum, P.B. Corkum, Phys. Rev. Lett. **71**, 1994 (1993)
4. K. Schafer, B. Yang, L.F. DiMauro, K.C. Kulander, Phys. Rev. Lett. **70**, 1599 (1993)
5. L.V. Keldysh, Sov. Phys. JETP **20**, 1307 (1964)
6. M.V. Ammosov, N.B. Delone, V.P. Krainov, Sov. Phys. JETP **64**, 1191 (1986)
7. M. Lein, N. Hay, R. Velotta, J.P. Marangos, P.L. Knight, Phys. Rev. Lett. **88**, 183903 (2002)
8. J. Itatani, J. Levesque, D. Zeidler, H. Niikura, H. Pépin, J.C. Kieffer, P.B. Corkum, D.M. Villeneuve, Nature **432**, 867 (2004)
9. T. Kanai, S. Minemoto, H. Sakai, Nature (London) **435**, 470 (2005)
10. C. Vozzi, F. Calegari, E. Benedetti, J.-P. Caumes, G. Sansone, S. Stagira, M. Nisoli, R. Torres, E. Heesel, N. Kajumba, J.P. Marangos, C. Altucci, R. Velotta, Phys. Rev. Lett. **95**, 153902 (2005)
11. W. Boutu, S. Haessler, H. Merdji, P. Breger, G. Waters, M. Stankiewicz, L.J. Frasinski, R. Taieb, J. Caillat, A. Maquet, P. Monchicourt, B. Carre, P. Salieres, Nat. Phys. **4**, 545 (2008)
12. H.J. Wörner, J.B. Bertrand, P. Hockett, P.B. Corkum, D.M. Villeneuve, Phys. Rev. Lett. **104**, 233904 (2010)
13. S. Patchkovskii, Z. Zhao, T. Brabec, D.M. Villeneuve, Phys. Rev. Lett. **97**, 123003 (2006)
14. V.-H. Le, A.-T. Le, R.-H. Xie, C.D. Lin, Phys. Rev. A **76**, 013414 (2007)
15. J. Levesque, D. Zeidler, J.P. Marangos, P.B. Corkum, D.M. Villeneuve, Phys. Rev. Lett. **98**, 183903 (2007)
16. Z.B. Walter, S. Tonzani, C.H. Greene, J. Phys. Chem. **112**, 9439 (2008)
17. B. Yang, K.J. Schafer, B. Walker, K.C. Kulander, P. Agostini, L.F. DiMauro, Phys. Rev. Lett. **71**, 3770 (1993)
18. G.G. Paulus, W. Nicklich, H. Xu, P. Lambropoulos, H. Walther, Phys. Rev. Lett. **72**, 2851 (1994)
19. G.G. Paulus, W. Becker, W. Nicklich, H. Walther, J. Phys. B, At. Mol. Opt. Phys. **27**, L703 (1994)
20. M. Meckel, D. Comtois, D. Zeidler, A. Staudte, D. Pavicic, H.C. Bandulet, H. Pépin, J.C. Kieffer, R. Dörner, D.M. Villeneuve, P.B. Corkum, Science **320**, 1478–1482 (2008)
21. C.D. Lin, A.-T. Le, Z. Chen, T. Morishita, R. Lucchese, J. Phys. B, At. Mol. Opt. Phys. **43**, 122001 (2010)
22. M. Okunishi, T. Morishita, G. Prümper, K. Shimada, C.D. Lin, S. Watanabe, K. Ueda, Phys. Rev. Lett. **100**, 143001 (2008)

23. T. Morishita, M. Okunishi, K. Shimada, G. Prümper, Z. Chen, S. Watanabe, K. Ueda, C.D. Lin, J. Phys. B, At. Mol. Opt. Phys. **42**, 105205 (2009)
24. M. Okunishi, R. Itaya, K. Shimada, G. Prümper, K. Ueda, M. Busuladžić, A. Gazibegović-Busuladžić, D.B. Milošević, W. Becker, J. Phys. B, At. Mol. Opt. Phys. **41**, 201004 (2008)
25. M. Okunishi, R. Itaya, K. Shimada, G. Prümper, K. Ueda, M. Busuladžić, A. Gazibegović-Busuladžić, D.B. Milošević, W. Becker, Phys. Rev. Lett. **103**, 043001 (2009)
26. M. Okunishi, H. Niikura, R.R. Lucchese, T. Morishita, K. Ueda, Phys. Rev. Lett. **106**, 063001 (2011)
27. C. Wang, M. Okunishi, R.R. Lucchese, T. Morishita, O.I. Tolstikhin, L.B. Madsen, K. Shimada, D. Ding, K. Ueda, J. Phys. B, At. Mol. Opt. Phys. **45**, 131001 (2012)
28. T. Morishita, A.-T. Le, Z. Chen, C.D. Lin, Phys. Rev. Lett. **100**, 013903 (2008)
29. Z. Chen, A.-T. Le, T. Morishita, C.D. Lin, J. Phys. B, At. Mol. Opt. Phys. **42**, 061001 (2009)
30. Z. Chen, A.-T. Le, T. Morishita, C.D. Lin, Phys. Rev. A **79**, 033409 (2009)
31. T. Morishita, A.-T. Le, Z. Chen, C.D. Lin, New J. Phys. **10**, 025011 (2008)
32. J. Xu, Z. Chen, A.-T. Le, C. Lin, Phys. Rev. A **82**, 033403 (2010)
33. D. Ray, Z. Chen, S. De, W. Cao, I. Litvinyuk, A.T. Le, C. Lin, M. Kling, C. Cocke, Phys. Rev. A **83**, 013410 (2011)
34. D. Ray, B. Ulrich, I. Bocharova, C. Maharjan, P. Ranitovic, B. Gramkow, M. Magrakvelidze, S. De, I. Litvinyuk, A.T. Le, T. Morishita, C. Lin, G. Paulus, C. Cocke, Phys. Rev. Lett. **100**, 143002 (2008)
35. X.M. Tong, C.D. Lin, J. Phys. B, At. Mol. Opt. Phys. **38**, 2593 (2005)
36. R.E. Stratmann, R.W. Zurales, R.R. Lucchese, J. Chem. Phys. **104**, 8989 (1996)
37. S.-F. Zhao, C. Jin, A.-T. Le, T.F. Jiang, C.D. Lin, Phys. Rev. A **81**, 033423 (2010)
38. R.R. Lucchese, V. McKoy, Phys. Rev. A **26**, 1406 (1982)
39. R.R. Lucchese, J. Chem. Phys. **92**, 4203 (1990)
40. O.I. Tolstikhin, T. Morishita, L.B. Madsen, Phys. Rev. A **84**, 053423 (2011)
41. C.I. Blaga, J. Xu, A.D. DiChiara, E. Sistrunk, K. Zhang, P. Agostini, T.A. Miller, L.F. DiMauro, C.D. Lin, Nature **483**, 194 (2012)

Chapter 11
Few-Femtosecond and Attosecond Electron Dynamics at Surfaces

Elisabeth Bothschafter, Stefan Neppl, and Reinhard Kienberger

Abstract Attosecond science recently celebrated its first decade which brought fascinating new insights into the dynamics of electrons in atoms and simple molecules. Most of these achievements are enabled by implementing attosecond extreme-ultraviolet (XUV) light bursts together with few-cycle near-infrared (NIR) and ultraviolet (UV) laser pulses in different pump-probe configurations. However, the application of these novel experimental tools for time-resolving attosecond and few-femtosecond electron dynamics in the solid state is still very limited. The study of electron dynamics in bulk materials, their surfaces and interfaces is crucial for both advancing our fundamental understanding of these processes and their application in future technological devices. In this chapter, electron dynamics in condensed matter will be reviewed in the light of open questions that can be addressed with state-of-the-art time-resolved spectroscopy. Experimental prerequisites particular to the study of condensed matter systems are discussed. The potential of using ultrashort light pulses to investigate electron dynamics at surfaces on ultrashort timescales is illustrated by few-femtosecond transient UV-reflectivity and attosecond time-resolved XUV-photoemission experiments on metal surfaces, semiconductors, and more complex adsorbate-substrate systems.

List of abbreviations

ATP	Above-threshold photoemission
CB	Conduction band
CEP	Carrier-envelope phase

E. Bothschafter · R. Kienberger (✉)
Physikdepartment E11, TU München, James-Franck-Str., 85748 Garching, Germany
e-mail: reinhard.kienberger@tum.de

E. Bothschafter
e-mail: elisabeth.bothschafter@tum.de

E. Bothschafter · R. Kienberger
Max Planck Institute of Quantum Optics, Hans-Kopfermannstr. 1, 85748 Garching, Germany

S. Neppl
Physikdepartment E20, TU München, James-Franck-Str., 85748 Garching, Germany
e-mail: s.neppl@mytum.de

K. Yamanouchi, K. Midorikawa (eds.), *Progress in Ultrafast Intense Laser Science*, Springer Series in Chemical Physics 104, DOI 10.1007/978-3-642-35052-8_11,

CHC	Core-hole-clock spectroscopy
FROG	Frequency resolved optical gating
FWHM	Full width at half-maximum
HEA	Hemispherical energy analyzer
HH(G)	High harmonic (generation)
LAPE	Laser-assisted photoemission
LEED	Low-energy electron diffraction
NIR	Near-infrared
PWP	Photoelectron wave packet
SPIDER	Spectral phase interferometry for direct electric-field reconstruction
S/N	Signal to noise ratio
TDSE	Time-dependent Schrödinger equation
TOF	Time-of-flight spectrometer
TR-2PPE	Time resolved two-photon photoemission
UHV	Ultrahigh vacuum
UV	Ultraviolet
VIS	Visible
XUV	Extreme ultraviolet

11.1 Introduction

Our understanding of condensed matter is formed by the active interplay between the theoretical, quantum mechanical description of the coupled properties of atoms and electrons in ordered structures and the experimental investigation of these systems by elaborate spectroscopic methods with constantly improving temporal and spatial resolution. In the same way as electrons are responsible for the formation of chemical bonds and thus determine the macroscopic configuration and orientation of molecules, the interaction of electrons with the lattice potential of a solid governs its crystal structure and its macroscopic optical and electronic properties. From a theoretical point of view, a full description of such true many-body systems is extremely difficult and various approximations have to be made in order to keep computational efforts at a reasonable level. Due to the reduced possibility to exploit symmetry properties of the system, the theoretical modeling of irregular lattices, interfaces and surfaces is even more challenging, in particular when the dynamic behavior of the electrons such as scattering, charge transfer and carrier relaxation, or collective effects like screening and plasmon formation have to be considered. On a fundamental level, all these processes are driven by the motion and mutual interaction of individual electrons. Studying the time-dependence of these elementary electronic phenomena in condensed matter is therefore important for testing and refining established theoretical models, and in the long run, to harness these processes in technological applications such as photovoltaics, sensors, heterogeneous catalysis and future nano-scale electronic and plasmonic devices.

The natural timescale of electronic motion in an atom is often illustrated in the simplistic but intuitive picture of an electron orbiting at the Bohr-radius around the

hydrogen atom, where one orbit takes only ∼150 attoseconds (1 as = 10^{-18} s). Some aspects of electron dynamics in solids can be studied with pico- and few-hundred femtosecond (1 fs = 10^{-15} s) time resolution, especially when they are coupled to the slower phonon-dynamics of the lattice [68] or are of collective nature [36]. However, the fundamental dynamics driving these processes often evolve on much faster timescales and therefore take place in the low-fs to sub-fs time domain. Under certain conditions, such ultrafast electronic dynamics can be accessed indirectly in the energy domain, e.g., the analysis of line-shapes observed in high-resolution photoemission can provide information on the ultrafast decay of the transiently created inner-shell vacancy. However, if more than one decay channel or processes of different duration are involved, energy domain measurements can not provide sufficient information, especially when the time dependence of the decay is non-exponential. In a more advanced application, resonant photoemission allows the observation to few-fs and even sub-fs charge transfer from atomic or molecular adsorbates to the unoccupied conduction band states of a substrate [10, 71]. Here, the branching into resonant and non-resonant decay channels of an initially neutral core-excited state can be translated into an effective charge transfer or delocalization time of the resonantly excited electron using the core-hole lifetime as an internal time reference [10]. Despite its success, the resolution of this so-called "core-hole-clock" (CHC) spectroscopy is intrinsically limited by the decay time of the core hole, which is of the order of ∼10 fs for the K-shell vacancies of carbon, nitrogen and oxygen atoms that are the major constituents of almost all technologically and biologically relevant molecules. Furthermore, CHC spectroscopy only yields accurate quantitative results when the electron dynamics under scrutiny proceed on a similar timescale as the fixed lifetime of the core-hole, which severely limits its range of applications. Even more importantly, CHC studies only provide access to the time constants of electronic processes but do not allow tracking their complete evolution over time.

These restrictions might be overcome in direct time-domain measurements using short light pulses for both triggering and probing the dynamics of the electronic system. Over the last decade, advances in ultrashort laser pulse technology enabled the generation of coherent radiation in the ultraviolet (UV) and extreme-ultraviolet (XUV) part of the electromagnetic spectrum by frequency up-conversion of intense optical laser pulses in rare gases. Further improvements and developments eventually culminated in the generation of today's shortest light pulses with durations of less than 4 fs in the NIR [12], less than 3 fs [60] in the UV and only ∼80 as in the XUV spectral range [30]. In addition, due to recent progress at large-scale free electron lasers, these facilities are now able to deliver few-fs (and possibly sub-fs [79]) pulses of soft and hard X-rays with extremely high pulse energies [1]. The emerging field of attosecond science founded on these new light sources holds great promise to improve our understanding of elementary processes in condensed matter in a similar way as the availability of femtosecond laser pulses brought new possibilities to investigate chemical reactions between atoms and molecules, which led to the nowadays well-established field of femtochemistry [75].

The aim of this chapter is to give an overview on recent progress and developments in the field of attosecond and few-fs dynamics in solids and at surfaces employing time-resolved spectroscopy with ultrashort light pulses. Electron dynamics relevant at these extremely short timescales are reviewed in the following section. Experimental prerequisites and the basic principles of the spectroscopic techniques that are capable to address these phenomena in the time domain will be outlined in Sect. 11.3 and Sect. 11.4. Finally, a selection of recent experiments, such as few-femtosecond transient reflectivity of noble metal surfaces and time-resolved photoemission from metals, semiconductors and adsorbate-substrate systems using attosecond XUV pulses in combination with few-cycle NIR pulses are presented in Sect. 11.5. They provide insight into the latest advances and future prospects for using ultrashort light pulses to probe sub-fs electron dynamics at surfaces.

11.2 Surface Electron Dynamics at Ultrashort Timescales

The interaction of electrons in solids with the surrounding matrix upon excitation are ubiquitous and possible time-scales cover at least nine orders of magnitude ranging from nanoseconds for slow electron-phonon thermalization to sub-fs electron-electron scattering times. Here we mainly focus on fundamental electronic processes in solids and their surfaces that unfold on the few-fs or even attosecond timescale, and which are likely to become accessible in the time domain by contemporary high-harmonic driven ultrashort light sources. By discussing some benchmark time-resolved experimental results, we give a taste of the exciting insights into surface dynamics and spectroscopy that can be expected when probing the response of solid-state systems to the excitation with few-fs or attosecond light pulses. For a more detailed and comprehensive discussion, we refer to recent reviews, e.g., by Haarlammert [33] or Bauer *et al.* [4].

11.2.1 Excitation and Relaxation of Non-equilibrium Populations

Electrons in solids can be excited from occupied states below the Fermi level to unoccupied states below the vacuum level by absorption of photons with sufficient energy. The resulting initial non-equilibrium distribution of electrons mirrors the excitation spectrum convolved with the joint density of states of the system. The subsequent thermalization process encompasses a variety of different mechanisms. On very short timescales, electron-electron scattering prevails above other processes and leads to a ('hot') electron energy distribution which can be described by a Fermi-Dirac distribution with a uniform temperature of the electronic subsystem. On a longer timescale, this excess energy will be dissipated from the electronic subsystem by electron-phonon/defect scattering and carrier diffusion into the entire crystal via excitation of lattice vibrations. Changes in the electronic structure after excitation

can be probed indirectly by transient absorption or reflectance (see, e.g., [9, 24]), or in a more direct way by time-resolved two-photon photoemission (TR-2PPE), see [43]. For example, by using TR-2PPE electron thermalization times in metals have been shown to depend on the excitation density [23, 64]. At high excitation levels, which can be easily reached with ultrashort, intense laser pulses in the UV spectral range [31, 61], extremely fast carrier-carrier scattering processes at the order of femtoseconds are expected [59]. Whereas the relaxation mechanisms of hot electrons in solids have been studied extensively in the past with TR-2PPE and optical techniques employing pulses of longer durations [42, 59], new insights into the early dynamics of these excited electrons as well as the onset of their relaxation can be expected when using few-fs to sub-fs UV and XUV pulses for triggering and/or probing [18, 52].

11.2.2 Electronic Response Effects in Solid-State Photoemission

It is well known that the process of photoemission cannot be described accurately in a single-active electron picture. Upon ejection of a photoelectron from an atom, the electron distribution in the remaining ion will respond dynamically to the formation of the vacancy and will rearrange to minimize the total energy of the system. Due to this intra-atomic relaxation, the photoelectron's binding energy is usually smaller than predicted by Koopman's theorem [37, 46]. However, if the relaxation is incomplete at the time the electron has reached the continuum, part of the excitation energy will remain within the ion. This gives rise to additional features in the photoelectron spectrum, such as shake-off or shake-up satellites, that appear at higher binding energies than the primary, fully relaxed photoemission line [37]. Since the interaction time between the photoelectron and its parent ion is governed by the duration of the excitation, one could expect different intensities of the photoemission satellites depending on the pulse length of the ionizing radiation. The largest contrast can be expected for spectra recorded with synchrotron radiation (pulse durations of several ps) and spectra acquired with attosecond light pulses. Following the satellite content as a function of the pulse duration might therefore provide insight into the relaxation dynamics of the excited electronic system.

In contrast to isolated atoms, where only local excitations are present, the more complicated excitation spectrum of solids entails additional collective modes such as plasmons, which play a crucial role in the screening dynamics of the transient photo-generated hole. The dynamical rearrangement within the electronic system in response to the sudden creation of a hole, as well as the strength of the interaction are inextricably linked to the polarizability of the surrounding matrix and the density of free charge carriers. Theoretical investigations predict that the timescale on which the electronic response evolves from a ballistic regime, where electrons react more or less individually to the charge perturbation, to the formation of collective modes involving the entire electronic system is of the order of half the plasma period of the material [7, 55]. In semiconductors, this transition takes place on a femtosecond

timescale and could therefore be followed in real time with conventional fs-laser-based pump-probe schemes [36]. In metals, on the other hand, due to the much higher conduction band electron density, the build-up of these collective excitations proceeds in the attosecond domain and could so far not be observed experimentally.

11.2.3 Lifetimes of Surface States

Due to the broken translational symmetry, the density of states at the surface of a solid can be quite different from the bulk. A general consequence is the existence of new electronic states located in the energy gap of the surface-projected bulk bands. Additionally, such surface states can be induced and affected by relaxation or reconstruction of the crystal lattice in the surface-near region. Since these states represent a two-dimensional electron system, they can be discriminated in photoemission from bulk transitions as they exhibit strictly free-electron-like dispersion normal to the crystal surface and react sensitively to the adsorption of impurity atoms.

The lifetime of electrons and holes in surface states does not depend on the surface-state energy (in contrast to bulk states) but on the wave function's overlap with bulk states [19, 59]. When the surface-state energy lies within the fundamental bandgap of the bulk, its lifetime is increased. Surface resonances occur when bulk bands overlap in a certain energy range with the surface state, which allows the surface-state wavefunction to penetrate deeper into the bulk, where enhanced scattering can reduce their lifetime to only a few fs or even less [59]. The delocalization dynamics of electrons from these states into the bulk is important for many photochemical surface reactions and influences the electron transport efficiency across interfaces, which has important implications for example in photovoltaics where carrier trapping in surface states and interface states is a major concern.

11.2.4 Charge Transfer and Transport Dynamics

When atoms or molecules bound to a solid support absorb light, a greater variety of decay channels is available compared to the isolated case since the adsorbate can exchange charge and energy with the substrate. This interaction has gained considerable attention over the last decade especially in the view of enhancing the efficiency of dye-sensitized solar cells and also for the design of new catalytic surfaces [35]. The timescale for such charge transfer reactions can range from a few hundred attoseconds for strongly chemisorbed systems [26] to a few hundred femtoseconds for weakly interacting physisorbates [10].

As mentioned in the introduction, investigations of excitation lifetimes and electron transfer by energy-domain techniques, like line-shape analysis or CHC spectroscopy, are inherently limited in their range of applicability and accuracy for systems where inhomogeneous broadening due to unresolved multiple decay channels

occurs. Hence, for the investigation of more complex systems, direct observation in the time-domain is preferred. A conceivable approach would be to monitor the dynamic core-level shift that occurs for atoms in a light-absorbing molecule upon spatial rearrangement of the molecule's electronic charge in the excited state. In this way, ultrafast intra-molecular charge transfer could be detected. Moreover, if the molecule is attached to the substrate via an anchor group containing an atom with a unique photoemission line, the dynamical chemical shift of this transition could be used to follow heterogeneous electron transfer from the adsorbate to the conduction band of the solid support in real time and to discriminate it from purely intra-molecular charge transfer pathways.

As first step towards such kind of experiments, Miaja-Avila *et al.* demonstrated in 2008 the first direct measurement of core-level relaxation dynamics in a simple surface-adsorbate system [54]. By comparing the time evolution of the laser-assisted photoemission from the conduction band of a Pt(111) surface with the delayed Auger electron emission stemming from the de-excitation of the xenon adsorbate, the lifetime of the Xe4d^{-1} core vacancy was measured to be 7.1 ± 1.1 fs, which is consistent with the value deduced from the line-width in gas-phase measurements. In another experiment, ultrafast changes in the bonding of O_2 molecules to a Pt surface could be followed by two-color photoemission spectroscopy with few-fs IR-pump and XUV-probe pulses [5]. The mechanism behind this reaction was further investigated by simultaneously monitoring the IR-induced hot electron distribution and changes in the oxygen valence states [47]. These experiments suggest that the surface reaction is triggered by the excited electrons near the Fermi level and their ultrafast transfer into the lowest unoccupied orbital of the adsorbate.

11.2.5 Dynamics of the Photo-Electric Effect

Today, most of our knowledge on the electronic properties of solids is based on the analysis and interpretation of photoemission experiments. In this elementary process of light-matter interaction an electron is ejected from the solid upon absorption of a photon. Measuring the energy, momentum and spin of the emitted electrons allows mapping the energy bands, the elemental composition, and the atomic and magnetic structure of a solid. Almost all experimental investigations of the above-mentioned time-dependent phenomena draw on variants of this technique. Understanding the dynamics of the fundamental process of photo-excitation and electron emission from solids becomes increasingly important as the time resolution approaches the timescale of the photoemission events themselves.

While photoelectrons in gas-phase experiments are ejected into simple continuum states, photoemission from solids is more intricate involving the excitation of electrons into energy band states which arise from the interaction of all the remaining electrons in the solid with the periodic potential of the crystal lattice [63]. For a more intuitive discussion of solid-state photoemission, the whole process is often artificially decomposed into three separate steps, consisting of the optical excitation

of an allowed interband transition within the solid, the propagation of the excited electrons towards the surface of the crystal and finally their escape through the surface into vacuum where they can be analyzed in terms of energy and momentum. On their way to the surface, the photoelectrons suffer energy losses due to inelastic electron-phonon and electron-electron scattering or the excitation of collective modes of the electronic system e.g., plasmons (comp. Sect. 11.2.2) which limits their escape depth to only a few nanometers or even less. The momentum of the photoelectrons can also be altered by elastic collisions. Only electrons that do not lose energy will contribute to the primary electron spectrum with a characteristic photoemission peak, whose position is uniquely defined by the corresponding initial state. Although this three-step model is often sufficient to reproduce the main features of a photoemission experiment, it is nevertheless an approximation since it neglects different pathways for the release of a photoelectron that arise from the interference between electron excitation, transport and transmission. In a rigorous quantum-mechanical approach, the whole photoemission event has therefore to be treated as a single coherent process [37, 46]. Within certain approximations such calculations are nowadays possible and reproduce stationary photoemission spectra, e.g., recorded with synchrotron radiation, with very high accuracy. On the other hand, an explicit time-dependence of the many-body interactions accompanying the photoemission process is often ignored in these descriptions. Thus, time-resolved investigations of photoemission could put currently available models to the test and might unveil new effects and properties that have not yet been included in the calculations.

An intriguing example of such a new effect is the time delay in photoemission from a tungsten surface observed by Cavalieri *et al.* in 2007 [13] by using the attosecond streaking technique [40]. The experiment revealed a difference of 110 ± 70 attoseconds between the release of photoelectrons from the conduction band (CB) and $4f$ core-level states of the crystal, with the CB electrons leaving the surface earlier than the $4f$ electrons. A schematic depiction of the experiment and the detection principle is shown in Fig. 11.1. For a more detailed description of the technique, we refer to Sect. 11.4. This time delay was originally explained by final-state effects in the static band-structure of tungsten, which resulted in a larger group velocity for the escaping CB electrons and consequently in a shorter average propagation time towards the surface compared to the core-level electrons. This explanation in terms of band-structure-dominated electron transport was challenged in a subsequent theoretical study by Kazansky *et al.*, where the time-dependent Schrödinger equation (TDSE) was solved for a one-dimensional (1D) model crystal mimicking the energy levels of tungsten [39]. The interaction of the photoelectrons with the 1D crystal lattice was modeled using a pseudo-potential with parameters originally optimized for the (111) surface of copper, whereas the interaction with the remaining photo-hole in the solid was explicitly taken into account only for electrons released from localized states. Moreover, the IR field strength was assumed to vanish completely in the interior of the crystal and the escape depth for the electron was fixed to a realistic value of $\lambda \approx 5$ Å. With these assumptions, the authors calculate a time delay of $\Delta\tau = 85$ asec for the photoelectrons emitted from the localized

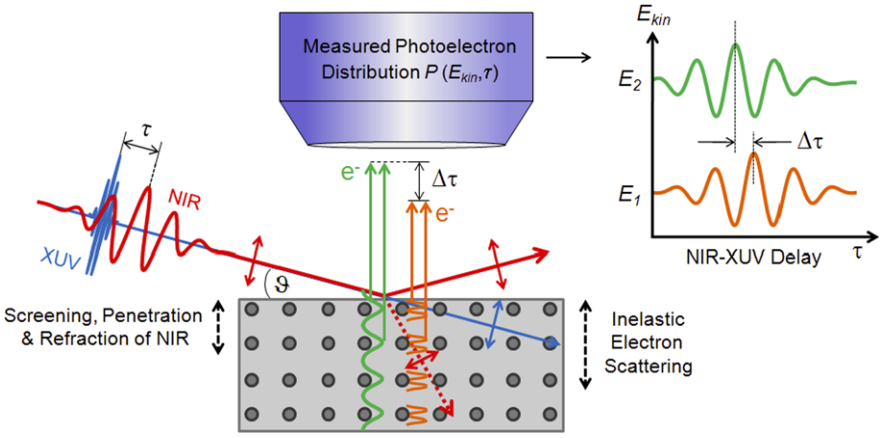

Fig. 11.1 Scenario for attosecond streaking at a solid surface. The attosecond XUV pulses photo-excite electrons from different initial states of the solid within a region exceeding the escape depth of the electrons. Pictorial wave functions for localized core electrons (*orange*) and delocalized conduction band electrons (*green*) are indicated. The generated electrons propagate towards the surface in a (possibly) spatially inhomogeneous IR streaking field. Any time delay $\Delta\tau$ occurring between photoelectrons released from different energy levels manifests itself in a corresponding offset $\Delta\tau$ between their streaked electron distributions $P(E_{\mathrm{kin}}, \tau)$ which are measured as a function of the relative IR-XUV pump-probe delay τ. In general, $\Delta\tau$ may be attributed to the interplay of IR field penetration and refraction at the surface, the strength of inelastic electron scattering, differences in the electron velocity and the initial state character of the involved electronic levels

energy level compared to those released from the delocalized band states, which is in good agreement with the experimental result. However, within this model the time delay arises primarily from the different spatial confinement of the involved initial states (localized core state vs. delocalized conduction band state). The influence of final-state effects was found to be only of the order of $\sim$10 asec. The absence of band structure effects was attributed to the short-term interaction of the outgoing photoelectrons with the crystal lattice, caused by the small electron escape depth and the short duration of the formed electron wave packets, which prevents a modification of the photoelectron velocity by the periodic potential. In sharp contrast, recent calculations by Krasovskii *et al.* indicate that, even for almost vanishing escape depths of the electrons, band structure effects may give rise to relative time shifts in attosecond photoemission of up to $\sim$150 asec [45].

A rather different explanation for the observed time delay was inferred from quantum-mechanical calculations by Zhang *et al.* [76, 77]. By adapting the one-step approach of stationary photoemission to laser-dressed emission, transition matrix elements were calculated using damped Volkov wave functions as final states. For the description of the initial states of the metal conduction band, the jellium model was applied which entails completely delocalized wave functions. In accord with [39], the W4f states were modeled with localized atomic-like wave functions. As opposed to [13] and [39], the IR field was assumed to be constant inside the solid, i.e.

any attenuation due to screening and refraction was ignored. Again, the escape depth λ was included as an adjustable parameter, and the time shift of $\Delta\tau = 110$ asec could be reproduced for $\lambda = 2.5$ Å [77]. Furthermore, these calculations suggest that only the temporal evolution of the electron wave packet released from the localized core states is affected by the finite escape depth. The time delay with respect to the CB emission was found to be the result of interference between core-level photoelectrons originating from different layers of the solid. In a refined model including also the interaction of the emitted electron with the dielectric response of the solid, the authors emphasize the role of this self-interaction for the temporal evolution of the CB photoemission [78].

Finally, Lemell *et al.* performed classical transport simulations on the electron release from W(110) for the experimental conditions in the streaking measurement reported by Cavalieri *et al.* [48]. The electrons are treated as point-like particles with Gaussian-like initial source distributions spatially confined to the lattice sites of the tungsten crystal. Only the contribution of the 6*s* states to the W(110) conduction band was modeled by a jellium-like distribution. In analogy to [13], the change of the streaking field upon crossing the vacuum-tungsten interface was taken into account by solving the Fresnel equations. Elastic and inelastic scattering cross-sections were derived from calculations based on a muffin-tin potential approximation and the dielectric function of tungsten, respectively. Using the same distribution of group velocities as in [13] for the propagation of the electrons, a time delay of $\Delta\tau = 33$ as was retrieved from the simulated streaking spectrogram. Similar to [13], the origin of this time delay could be traced back to the difference in velocities and in mean escape depth of the involved electrons. In addition, the authors find an increase of the time shift to $\Delta\tau = 42$ as when the IR field strength inside the crystal is set to zero in the simulations. This was attributed to an effective reduction of the electron escape depth due to enhanced scattering of the electrons moving inside the solid in the presence of the deflecting streaking field.

The validity of these rather different theoretical models can only be tested in further experimental studies. However, the wealth of new theoretical considerations and approaches triggered by the first attosecond time-resolved measurement in a solid indicates that established concepts like band structure, electronic response and screening, which are successful in describing static photoemission, might have to be questioned on an attosecond timescale.

11.3 Ultrashort Light Pulses for Time-Resolved Spectroscopy

For achieving temporal resolution in the few femtosecond to attosecond regime, coherent light pulses with a corresponding duration have to be reliably generated in a repeatable manner. Laser pulse durations very close to the single cycle limit have been achieved at the 100 μJ-level in the near-infrared (NIR)/visible (VIS) spectral range [12, 72]. Due to time-bandwidth restrictions, pulse durations in the lower attosecond range can only be realized in the XUV part of the electromagnetic spec-

trum. Schemes for frequency up-conversion of the aforementioned short laser pulses are therefore an essential tool in attosecond science. In the following, the generation of attosecond pulses and their metrology and a method for combining the generation of ultrashort UV and XUV pulses in a inherently synchronized manner will be discussed.

11.3.1 Generation and Characterization of Isolated Attosecond XUV Pulses

The most common method for generation of sub-fs pulses relies on frequency up-conversion of intense femtosecond NIR laser pulses using rare gases as a nonlinear medium. In contrast to low-order harmonic conversion, which depends solely on the nonlinear polarizability of the medium, the up-conversion from the NIR to the XUV spectral region by high harmonic generation (HHG) involves electrical-field-driven ionization and recombination dynamics of the electrons in the rare gas atoms. It can be described in a semi-classical model as a three-step process [16]: close to the crests of the driving NIR laser field, electrons can be freed from the atomic potential by tunneling ionization. Subsequently, the electrons are accelerated by the oscillating electric field of the linearly polarized NIR pulse. As the laser field reverses direction, the electrons are driven back to their parent ions and recombine with a small but nonzero probability with the core. In this case, the energy gained by the electrons during acceleration in the laser field (plus the ionization potential of the atom) is emitted in form of high-energy photons. Since both the ionization and recombination of the electrons happen within a fraction of a half-cycle of the driving NIR field, the released radiation has a sub-fs temporal structure. Generally, by using many-cycle driving pulses, which exhibit several field maxima of comparable strength, a pulse train of attosecond bursts can be generated. For the generation of isolated attosecond pulses, which are more versatile and simpler to implement in pump-probe spectroscopy, the emission process has to be confined to a single half-cycle.

This can by achieved by manipulating the waveform of the laser field driving the HHG process with different gating techniques. Tailoring the electric field in such a way that the polarization is linear only during one half cycle of the NIR pulse provides a route for generating isolated attosecond pulses as the recombination step in HHG is only possible for linear polarization. This so-called polarization gating, which can be realized by two delayed counter-rotating laser fields [17], is capable of producing isolated attosecond pulses [62, 67] from few-cycle NIR driving pulses and can be even extended to NIR pulse durations as long as ∼28 fs [25] by adding a weak second harmonic field to the two circularly-polarized NIR fields (so-called double optical gating). In a more direct approach, sub-2-cycle NIR pulses [12] with a controlled wave form exhibiting only one pronounced electric field maximum (cosine-pulse) are used for driving the HHG process. In this amplitude gating scheme, a single isolated attosecond pulse can be obtained by spectral filtering the

high-energy part, the so-called cut-off, of the generated harmonic radiation, which is exclusively generated within a single half cycle following the most pronounced maximum of the instantaneous field strength under the pulse envelope [41].

An obvious difficulty lies in the characterization of such short isolated XUV pulses. Common nonlinear optical concepts like autocorrelation, frequency-resolved optical gating (FROG) and spectral phase interferometry for direct electric-field reconstruction (SPIDER) require appropriate nonlinear media which are rare for low intensity high harmonics. Two-photon ionization of atoms enables autocorrelation of low-frequency attosecond pulses, but for photon energies exceeding ~30 eV the 2-photon-ionization cross-section is extremely small. So, the so-called attosecond streaking technique allows access to both the envelope and the spectral phase of sub-fs XUV pulses [34, 40]. The essence of this method, which was theoretically described by Itatani *et al.* [38], is to cross-correlate a photoelectron replica of the XUV pulse with the same, intrinsically synchronized, NIR driving field used for their generation via HHG. To illustrate the basic principle, let's assume a linearly polarized laser field $E_L(t) = E_0 \cos(\omega_L t + \phi)$ with its polarization parallel to the direction of electron detection. If the duration of the isolated XUV pulse is shorter than half the period of the NIR laser field, the photoelectron wave packets (PWPs) generated by this pulse from an atomic or solid target in the presence of the laser field will experience an additional shift of their final momentum $\Delta p = eA_L(t_r)$ that is proportional to the laser vector-potential $A_L(t_r) = \int_{t_r}^{\infty} E_L(t)\,dt$ at the moment of their release t_r into the NIR field. In this way, the temporal profile of the PWP, which in the absence of photoemission resonances is simply a replica of the XUV pulse [73], is uniquely mapped onto a 'streaked' kinetic energy distribution of photoelectrons. By scanning the relative delay τ between the ionizing XUV pulse and the NIR laser pulse a full streaking spectrogram $P(\tau, E_{\text{kin}})$ is obtained from which not only the PWP's duration and spectral phase can be retrieved, but also the waveform of the NIR streaking pulse. Due to the similarity to the FROG technique, a similar retrieval algorithm [28] can be applied to extract the characteristics of the XUV pulse (or more generally the characteristics of the PWPs) from a measured spectrogram [30, 40].

11.3.2 Collinear Generation of Attosecond XUV and Few-fs UV Pulses

With the availability of isolated attosecond XUV pulses, their combination with intense few-fs UV pulses would allow to extend the conventional TR-2PPE towards sub-fs temporal resolution. The UV pulse can serve as a pump pulse, exciting electrons in previously unoccupied states below vacuum level, which are then probed by a subsequent attosecond XUV pulse at well-defined time-delays.

Since no suitable broadband laser material is available in the ultraviolet domain, the generation of ultrashort UV laser pulses relies on nonlinear frequency mixing and frequency up-conversion of femtosecond laser pulses in solids [6] and gases

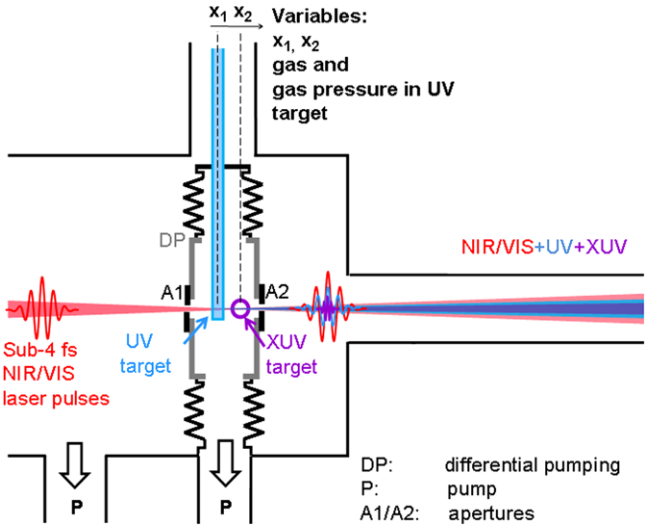

Fig. 11.2 Collinear generation of UV and XUV pulses in two subsequent gas targets. The targets, formed by 2 to 3 mm thick nickel tubes, can be positioned independently (x_1, x_2). They are situated inside a vacuum setup in a small, differentially pumped vacuum chamber with two apertures (diameter: 0.7 mm) for transmission of the few-cycle 720 nm NIR pulses (sub-4 fs, 400 μJ) and the generated harmonic radiation. The NIR beam is focused into the XUV gas target (*purple*) which is supplied with 0.2–0.3 bar Ne. The UV target (*blue*) is placed in front of the XUV target and supplied with Ar or Ne at variable pressure of 2–6 bar

[2, 21, 27, 31, 44]. Third-harmonic generation from Fourier-limited few-cycle NIR laser pulses in noble gases directly provides intense sub-4 fs pulses in the deep ultraviolet spectral range [31]. While this process relies on the induced polarization due to the third-order electric susceptibility $\chi^{(3)}$ of the gas, and is therefore favored in high-density media (e.g. solids or high-pressure gas-cells), the efficient generation of XUV pulses requires low-density gases [49, 50]. It has been shown, that employing two independent static gas-cells situated in close vicinity along the propagation direction in the focus of a sub-4 fs NIR laser (see Fig. 11.2) with a peak intensity of $\sim 7 \cdot 10^{14}$ W/cm^2, UV pulses with a pulse energy up to ~ 1 μJ and XUV pulses with up to $3.5 \cdot 10^6$ photons per pulse and a cut-off photon energy of more than 100 eV can be generated simultaneously [8].

In order to minimize the effect of dispersion and reabsorption on the generated pulses, the background pressure due to the high gas load emerging especially from the high-pressure UV target has to be minimized by a differential pumping scheme (depicted in Fig. 11.2). Thanks to this scheme, the collinearly generated UV and XUV pulses are expected to exhibit a similar temporal structure compared to the situations where these pulses are produced independently [30, 31]. The UV pulse energy can be tuned by varying the gas pressure in the first gas cell with only little change in the UV spectrum, which extends over a more than 1 eV bandwidth centered at 5 eV and therefore supports a bandwidth-limited pulse duration <3 fs. Equally important for pump-probe measurements, this collinear generation scheme

offers the same intrinsic synchronization between the UV and the XUV pulses as for the NIR and XUV pulses in the streaking technique described in the previous section.

11.4 Principle and Setup for Time-Resolved Experiments on Surfaces with Few-fs to Sub-fs Resolution

In principle, the ultrashort NIR, UV and XUV light pulses can be combined in various pump-probe configurations to study electron dynamics in solids and at surfaces. Here we concentrate on ultrafast UV-UV transient reflectivity and NIR-dressed attosecond XUV-photoemission spectroscopy. Both methods can yield complementary information owing to their very different surface sensitivity. Two time-resolved experimental techniques utilizing such ultrashort UV and XUV light pulses, namely transient reflectivity and attosecond streaking spectroscopy, will be introduced. Special experimental conditions, necessary when applying these spectroscopic methods to the study of surface electron dynamics, will also be addressed.

11.4.1 Transient Reflectivity

Electronic excitation with intense light pulses can lead to excitation of coherent phonons e.g., via Raman scattering, but also to the excitation of bulk and surface plasmons which is expected to happen at the typical timescale of electron-electron scattering, i.e., a few hundreds of attoseconds. Coupled electron-lattice dynamics are accompanied by transient changes in the solid's dielectric function which can be monitored by its transmittance and reflectance. Since the absorption length in the VIS/UV range of most materials is at the order of nanometers, the influence of the surface condition plays usually a minor role in these experiments. Non-equilibrium dynamics in noble metals for example have been investigated by pump-probe measurements investigating the transient reflectivity of the sample [9, 24, 65]. As typical changes in these optical properties are at the best on the order of 1 % but usually much smaller and buried in the noise for integrating acquisition, the detection of the time-dependent signal is challenging. There are two standard ways to detect such a delay dependent signal at levels down to 10^{-6}, either a time-differential technique, where the delay is modulated at a certain frequency with small amplitude and the signal is filtered and amplified using a lock-in amplifier, or a fast scanning of the delay and averaging of the signal over many traces for the whole delay range to overcome the slow noise. In the all-reflective setup used in our one-color transient reflectivity measurements on solids, the UV-pump and the delayed UV-probe beam are derived from the same 3rd-harmonic source (comp. Sect. 11.3.2) by means of a piezo-actuated split-mirror, as schematically shown in Fig. 11.3.

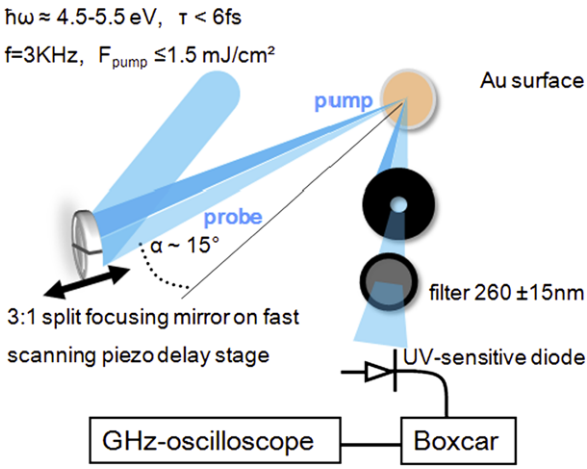

Fig. 11.3 Experimental setup for UV-UV transient reflectivity of Au with the fast-scanning technique: The pump and probe beam are separated from a single UV beam by means of a split-mirror, one of which is movable with a fast-scanning piezo delay stage. After reflection from the target, the probe is separated from the pump and detected with a UV-sensitive diode and recorded by fast averaging the integrated signal

11.4.2 Laser-Assisted Photoemission: Streaking vs. Sideband Regime

More direct access to the dynamics of electrons in the surface-near region is granted by photoemission, since the typical escape depth λ of photoelectrons excited by XUV photons is in the range of 5–10 Å, which corresponds to only 2–3 lattice constants [74]. The conceptually simplest way to resolve attosecond dynamics by photoemission would be to perform pump-probe measurements using attosecond XUV pulses for both triggering and probing. However, this approach is so far frustrated by the low intensity available with contemporary high-harmonic light sources. A high time-resolution can be nevertheless achieved by so-called laser-assisted photoemission (LAPE), where the one-photon photo-ionization is initiated by an XUV pulse in the presence of a strong NIR laser field. Depending on the duration of the excitation pulse τ_{xuv}, two regimes can be distinguished: if the duration of the emitted electron wave-packet is longer than half the oscillation period of the laser field, the XUV-photoelectron can exchange several laser photons with the dressing field. Such free-free transitions can be observed in the energy spectrum as sidebands of the NIR field-free XUV-photoemission line separated by multiples of the NIR photon energy $h\nu_{NIR}$ [15, 70]. This side band formation has been applied successfully to atoms [29, 69] and recently also to solid-state systems and atomic adsorbates on surfaces [53, 54]. A quite different behavior can be observed when the duration of the XUV-induced photoelectron wave-packet (PWP) becomes shorter than half the period of the dressing field (~1.3 fs for NIR pulses). In this case, the PWP's energy is modified according to the vector potential of the dressing field at the instant of emission. This is the streaking regime, which was introduced in Sect. 11.3.1 as a tool for characterizing sub-fs light pulses.

Both the magnitude of the sidebands, as well as the NIR-induced energy shift in streaked electron spectra, depend sensitively on the instant of time the electrons enter the laser-dressed continuum. Therefore, relative time delays $\Delta\tau$ between the

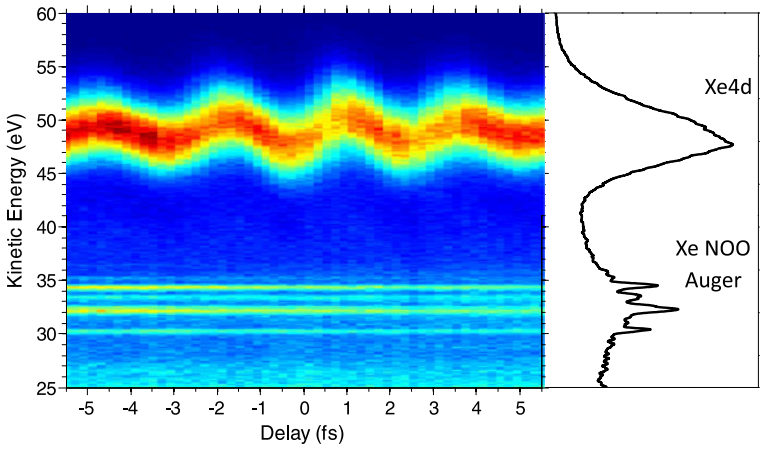

Fig. 11.4 Laser-assisted photoemission from xenon in the gas phase initiated with isolated ∼450 as XUV pulse with a central photon energy of ∼120 eV [56]. The direct Xe4*d* photoelectrons are streaked by the dressing field and therefore reveals the time-evolution of the vector-potential of NIR pulse. In contrast, the NOO Auger electron emission is governed by the ∼8 fs lifetime of the Xe4d^{-1} vacancy, which results in the formation of sidebands

release of photoelectrons from different electronic states can be resolved by varying the relative delay τ between the NIR and the XUV pulse, since any time delay in emission will be mapped onto a relative shift between the resulting cross-correlation traces along the NIR-XUV delay axis (see also Fig. 11.1). Obviously, the resolving power in such experiments is much higher for the streaking regime due to the sub-cycle modulation of the cross-correlation traces [13, 66]. It has to be emphasized that the PWP's duration is not only set by the duration τ_{xuv} of the ionizing XUV pulse, but also by the lifetime of the excited electronic state. This is illustrated in Fig. 11.4, which shows a LAPE measurement performed with $\tau_{xuv} \approx 450$ as XUV pulses on xenon atoms in the gas phase [56]: the streaking effect is only visible for the direct photoemission line originating from the Xe4*d* levels, whereas sidebands are observed for the electrons resulting from the NOO Auger decay of the Xe4d^{-1} core-hole, whose lifetime of ∼8 fs is imprinted on the duration of the Auger electron wave-packets and therefore exceeds the period of the NIR streaking field.

The typical experimental setup necessary for attosecond streaking measurements on solids is summarized in Fig. 11.5: high-harmonic (HH) radiation is generated by exposing neon atoms to intense, waveform-controlled few-cycle NIR laser pulses (violet beam). A thin metal filter spatially separates the low-divergent XUV radiation (blue beam) from the residual NIR light. The two collinear beams are reflected by a two-component mirror. The outer part of this mirror is fixed and focuses the NIR pulses onto the sample while the inner part serves as a bandpass reflector and filters isolated sub-fs XUV pulse from the HH cut-off continuum. It is attached to a piezo-electric translation stage allowing to introduce a delay between the XUV and NIR pulses. Both pulses are spatially and temporally overlapped on the sample surface positioned in the focus of the double mirror assembly [20]. In the actual mea-

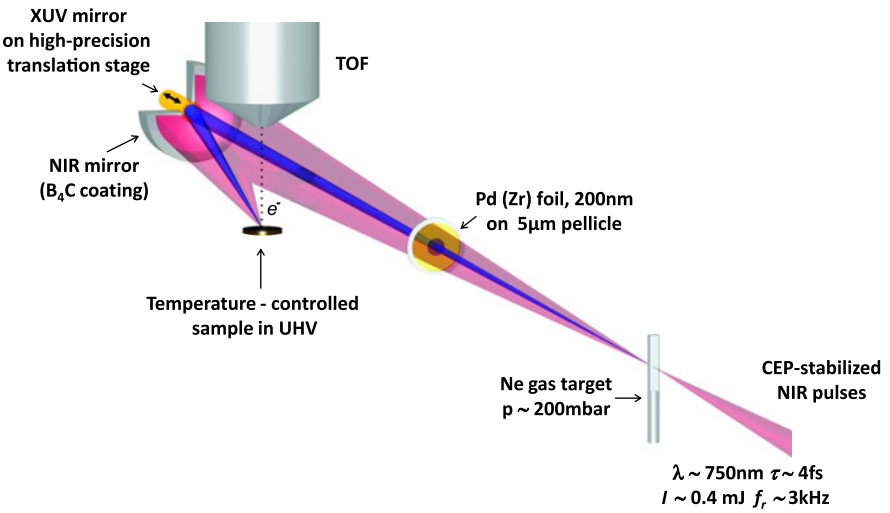

Fig. 11.5 Simplified overview of the setup used for attosecond time-resolved photoemission experiments of surfaces (adapted from [13])

surement, the kinetic energies of the XUV-induced photoelectrons emitted along the surface normal are analyzed by a time-of-flight spectrometer (TOF) as a function of the relative delay between the NIR and XUV pulses.

Owing to the high surface sensitivity of the XUV photoemission, the experiments have to be performed under excellent ultra-high vacuum (UHV) conditions (base pressure $<10^{-10}$ mbar) to avoid the disturbing influence by the adsorption of impurity atoms on the surface [56]. Similar to the principle depicted in Fig. 11.2, the transition from the high background pressure in the HHG chamber to UHV conditions in the experimental area is achieved by several differential pumping stages employing turbo-molecular and titanium-sublimation pumps [51]. The experimental end-station is divided into two segments. The first chamber accommodates several surface-science tools like a sputter gun, evaporators, a gas-dosing system and a low-energy electron diffraction (LEED) system, which are necessary for preparing and characterizing atomically clean single-crystal surfaces and well-defined adsorbate layers [74]. Sample transfer from the ambient into the UHV system is enabled by a load-lock system. The sample is mounted on a motorized 360°-rotatable xyz-manipulator. Full temperature control of the sample in the range of 10–2500 K is provided by an integrated flow-cryostat (operated with liquid helium) and the combination of heating filaments with a variable sample potential up to 1 kV. The second chamber is connected to the NIR-XUV beamline and is dedicated to LAPE experiments. It houses different electron analyzers (TOF or hemispherical energy analyzer (HEA)), the double-mirror assembly and a static-gas cell to allow pulse characterization via gas-phase streaking experiments. A cross-sectional view of the UHV system is schematically depicted in Fig. 11.6.

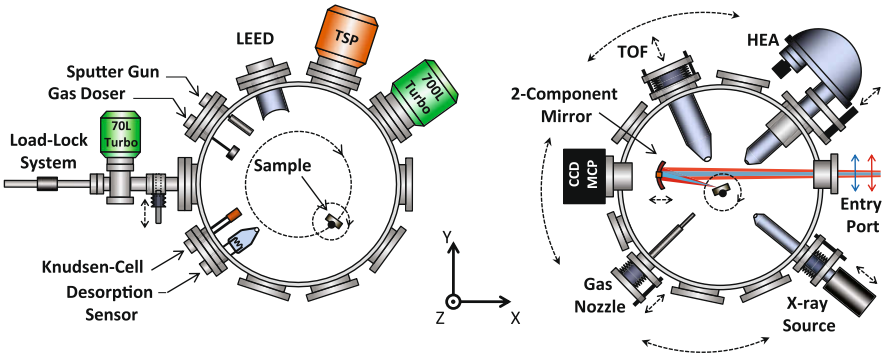

Fig. 11.6 Apparatus for attosecond photoemission experiments in UHV. The sample is transferred from ambient into the preparation chamber (*left*), where an atomically clean surface can be prepared under UHV conditions. The LAPE experiments are preformed in a second UHV chamber (*right*), which is connected to the NIR-XUV beamline and incorporates different electron energy analyzer. The various degrees of freedom for positioning of the individual components are indicated by *dashed arrows*

11.5 Recent Experimental Advances in Probing Ultrafast Dynamics at Surfaces

The experimental methods described in the previous section promise to enable new insights in few-fs to attosecond electron dynamics. In the following, we present our latest advances in the application of these methods to metals, semiconductor and even dielectrics to probe sub-fs electron dynamics at surfaces.

11.5.1 Transient UV-Reflectivity of Noble Metal Surfaces

As mentioned in Sect. 11.4.1, time-resolved measurements of the optical properties like reflectance or transmittance yield information about electron and lattice dynamics in the bulk as the interaction happens well within the material. Despite their abundance of conduction electrons, noble metals exhibit interesting electron dynamics upon off-resonant and resonant excitation [24, 32], including electron-phonon relaxation processes happening at a picosecond timescale [68] and electron-electron dominated relaxation well in the few-hundred femtosecond regime [24]. Especially for excitation from d-bands in vicinity of the interband transition threshold of Au at 2.5 eV [14, 22, 68], fast relaxation dynamics of an initially athermal electron distribution created by a strong fs pump pulse have been observed. Brida et al. [9] investigated the electron distribution dynamics in thin gold films triggered by sub-15-fs NIR pump pulses probed by 5-fs pulses in the visible. They observe in real-time the build-up and decay of the thermal electron distribution by transient transmission measurements with high spectral resolution.

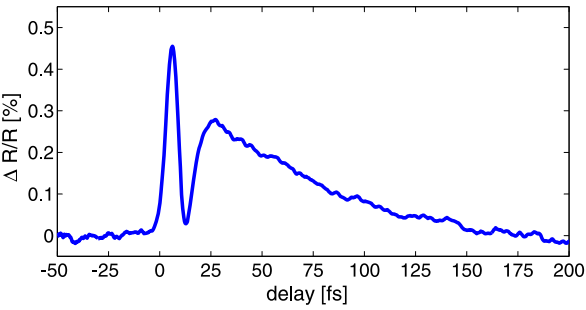

Fig. 11.7 $\Delta R/R$ of a plain Au surface recorded with UV pump-UV probe spectroscopy

In our experiment, we explore the dynamics of a non-equilibrium electron distribution high above the Fermi-level created by sub-6-fs pulses in the ultraviolet and observe the unfolding changes in UV-reflectivity of a plain gold surface in the same wavelength range. The pump and probe pulses are derived from the 3rd harmonic of sub-4 fs, 400 μJ NIR pulses. The 3rd harmonic is generated by focusing a few-cycle NIR beam with a central wavelength of 780 nm from a 3 kHz Ti:Sapphire laser system [12] in a static gas cell supplied with neon at a pressure of 4 bar, similar to the setup described in Sect. 11.3.2 using only the UV target. The pump and probe spectrum is centered at 4.5 eV and has a spectral width (FWHM) of 40 nm [8] which supports sub-3-fs pulses in the Fourier limit. Both beams are focused onto a plain gold surface and the relative change in reflectivity $\Delta R/R_0$ of the sample was recorded by fast scanning of the delay at ≈10 Hz over the whole delay range and averaging the recorded signal over several ten thousand scans, as described in Sect. 11.4.1.

With the pump and probe spectrum in the UV, interband transitions become accessible and the observed signal is expected to be sensitive to changes in the electronic structure high above the Fermi-level at elevated electronic temperatures exhibiting fast relaxation dynamics as shown in the transient reflectivity changes of Au, shown in Fig. 11.7. The time-resolved positive change in reflected UV-intensity shows two distinct features, a short lived peak within the first 10 fs and one with a longer lifetime of about 80 fs which seems to occur only after the first peak has disappeared. Such a fast transient change has not been observed so far by probing the optical response below the interband transition threshold in the near-infrared or visible spectral region.

11.5.2 Attosecond Streaking Experiments on Surfaces

The application of the attosecond streaking concept to surfaces hast first been demonstrated by Cavalieri *et al.* in 2007 [13]. The $\Delta\tau = 110 \pm 70$ as time delay between the photoemission from conduction band (CB) and $4f$ core-level states in tungsten constitutes the first time-domain measurements of attosecond electron dynamics in condensed matter. However, as highlighted in Sect. 11.2.5, the origin of

$\Delta\tau$ is currently highly debated in the literature. In this section we show that attosecond streaking spectroscopy can be applied to various different condensed matter systems. The high quality of the obtained streaking spectrograms holds promise to further elucidate the mechanisms behind time delays in solid-state photoemission and to test existing theoretical models.

11.5.2.1 Rhenium-Verification of the CB-4f Time Delay

The time delay measured in the first proof-of-principle experiment with ∼300 as XUV pulses centered at near 90 eV came with a comparably large uncertainty [12]. The accuracy with which such time shift can be extracted from a streaking spectrogram depends mainly on the depth of the NIR-induced modulation in the photoelectron spectra, the energetic separation between the photoemission lines whose emission-timing should be analyzed and the signal-to-noise (S/N) ratio of the photoelectron spectra. Experimentally, the modulation depth can be controlled by the NIR field intensity which, however, has to be restricted to much lower values compared to gas-phase experiments in order to avoid an excessive background due to above-threshold photoemission (ATP) electrons. The ATP stems from the CB electrons of the solid and are generated by the absorption of multiple NIR photons from the streaking field. To enable an unambiguous analysis of the streaked electron distributions, this background should not overlap with the XUV-induced photoemission lines. In this respect, the use of higher XUV photon energies is beneficial.

In a first attempt to corroborate the existence of time delays in attosecond photoemission from solids, we performed streaking experiments on the (0001) surface of rhenium, which exhibits a similar electronic structure as tungsten. Figure 11.8(a) shows the photoemission spectrum obtained from this surface with ∼350 as XUV pulses with a central photon energy of 125 eV. Prior to the measurements, the rhenium crystal was freed from surface contamination by repeated cycles of Ar^+ sputtering, oxidation and annealing cycles in a pure O_2 atmosphere followed by short temperature flashes to 2300 K. Two emission lines corresponding to the 4f and the CB states are well-resolved, but are superimposed by a background originating from inelastically scattered XUV photoelectrons. This background (blue dashed line) has to be subtracted from the spectra prior to the analysis, which represents a further complication compared to gas-phase streaking experiments. A background-corrected spectrogram obtained with a $4 \cdot 10^{11}$ W/cm^2 strong NIR dressing field is depicted in panel (b) with the CB intensity scaled by factor ×7 [11]. The time delay between the NIR and XUV pulse was scanned in steps of 100 as. The entire measurements was completed within only 35 minutes and obviously exhibits an excellent S/N ratio. To determine the relative timing between the release of the CB and 4f electrons from the surface, we compare the first moments of their kinetic energy distributions in function of the relative NIR-XUV delay. The results are shown as crosses in panel (c), along with a global fit of both traces to the same parameterized NIR-waveform (shown as solid lines). A relative shift of the 4f trace to positive

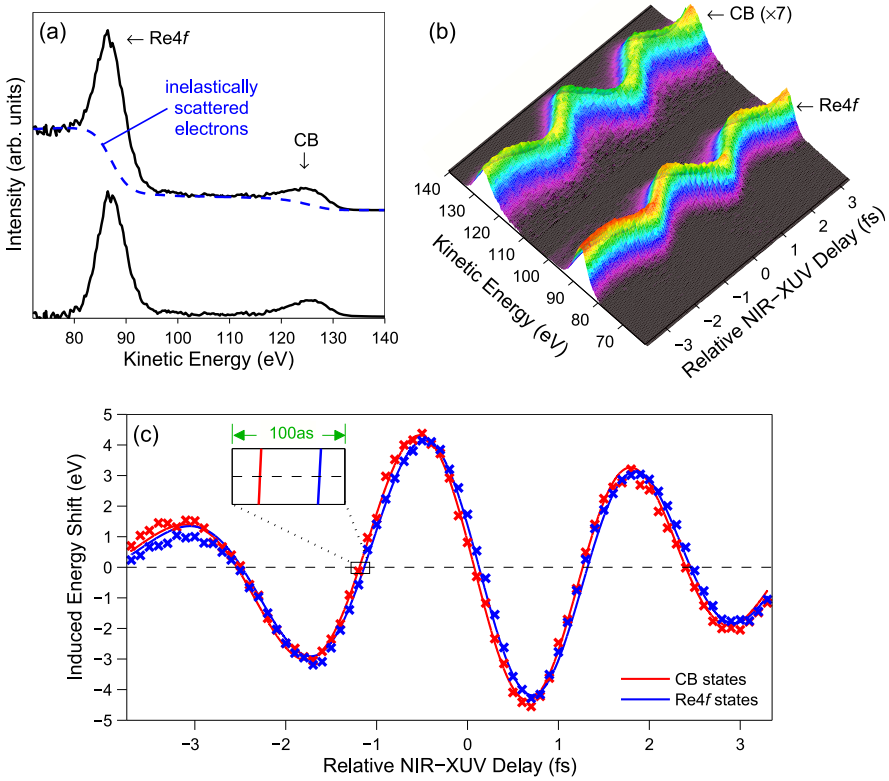

Fig. 11.8 Attosecond time-resolved photoemission from the (0001) surface of rhenium [57]. (**a**) Static photoelectron emission from rhenium (in the absence of the NIR streaking field) obtained with HH radiation filtered by a 6 eV (FWHM) bandwidth mirror centered near 125 eV. The background of inelastically scattered electrons (*blue dashed line*) is removed before the analysis. The full streaking spectrogram is shown in panel (**b**). The comparison of the first moments of the streaked electron distributions as a function of the NIR-XUV delay, shown in panel (**c**), reveals a delayed emission of the $4f$ photoelectrons from the metal surface compared to the photoelectrons released from the conduction-band states

NIR-XUV delays is clearly discernible, which indicates a delayed emission of the $4f$ electrons with respect to the CB electrons [57]. Similar experiments with different XUV photon energies will help to clarify the importance of the final-state band structure effects for time delays in attosecond photoemission from solids.

11.5.2.2 GaAs-Timing the Photoemission from Two Different Core-States

In order to experimentally address the question, raised by the different theoretical models, to which extent the localization of the initial states and resulting interfer-

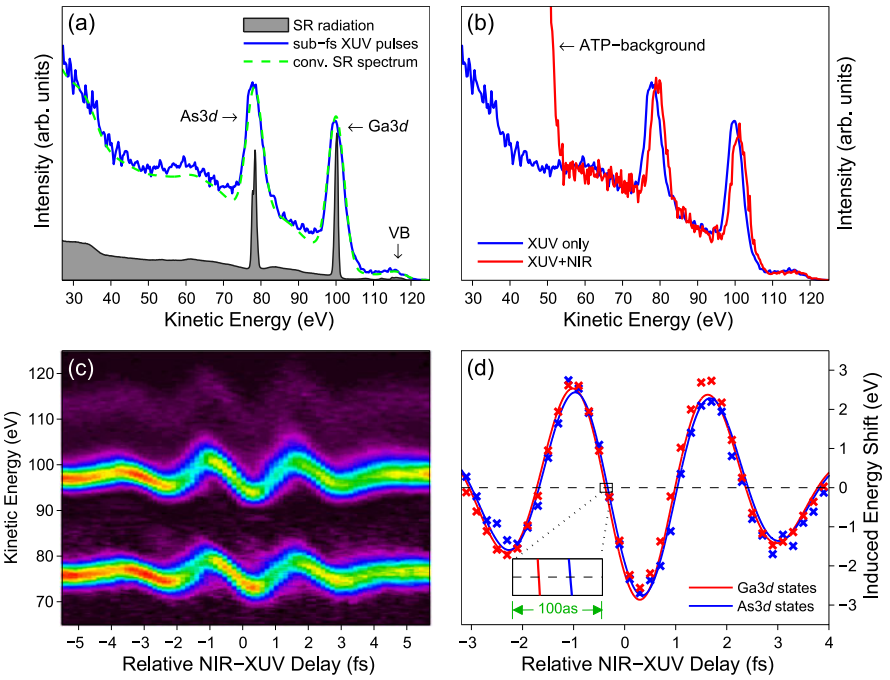

Fig. 11.9 (**a**) Stationary photoemission from Ga-rich GaAs(110) surface using a synchrotron source (*SR*, *gray-shaded area*) and a HHG source filtered with a 4.2 eV bandwidth mirror centered at ∼120 eV (*blue solid line*). The XUV photoemission spectrum using HH radiation corresponds well to the synchrotron spectrum convolved with the XUV mirror reflectivity response curve (*green dashed line*). Panel (**b**) shows the photoemission of the two core-states with XUV radiation only (*blue*) and with the ATP background caused by the NIR streaking field (*red*). Panel (**c**) shows a complete spectrogram containing both emission lines and (**d**) the timing analysis of the photoelectrons based on a comparison of the first moments of the corresponding electron energy distributions [58]

ence effects may contribute to the observed time delay, the relative timing of the photoelectron release from two localized core states may be of special interest. Excluding possible effects introduced by the angular momentum of the involved PWPs, we investigate the streaked photoemission of the Ga3*d* and As3*d* core states from the compound semiconductor GaAs(110), which possess the same orbital symmetry. Additionally, the chosen ⟨110⟩ direction of the zincblende structure of GaAs, with its alternating layers of Ga and As, offers the possibility to study photoemission either from a Ga-rich or an As-rich surface depending on the surface preparation. Thus, the average emission depth for the Ga3*d* and As3*d* electrons can be changed precisely by one atomic layer, which enables the study of transport effects in the attosecond photoemission process in a controlled fashion. Preliminary results obtained from a Ga-rich surface, prepared from a commercial GaAs wafer by soft Ne^+-sputtering and annealing cycles, are summarized in Fig. 11.9 [58].

Panel (a) compares the static photoemission from GaAs using a narrow bandwidth synchrotron source and XUV light generated via HHG from a few-cycle NIR pulse, filtered with a multilayer XUV mirror with 4.5 eV bandwidth. Apparently, the photoemission from both 3*d* levels occurs with a sufficiently high cross-section, which allows for high-quality streaking measurements. However, the NIR streaking field intensity has to be limited to intensities where the high-energetic ATP background is still far below the kinetic energy of the As3*d* emission (see panel (b)). A representative streaking spectrogram featuring the Ga3*d* and As3*d* emission is shown in panel (c). The analysis based on the first moments of the corresponding electron distributions reveals a relative temporal shift between the two streaking traces, with the emission of the Ga3*d* occurring a few attoseconds earlier than the As3*d* emission. Future comparison with results from As-terminated surfaces will enable to estimate transport contributions to photoemission time delays. Furthermore, this first demonstration of streaking spectroscopy on semiconductors might pave the way for studying electron transport in well-tailored semiconductor heterostructures.

11.5.2.3 Xe on Rhenium-Extension to Adsorbate Systems

So far, streaking spectroscopy only revealed relative time delays occurring in the photoemission from different energy levels, however without providing information on the average propagation time needed by any of the involved photoelectrons to reach the surface of the solid. Such a measurement can be performed by referencing the substrate photoemission to a reference state located above the surface of the solid [3]. We demonstrate the experimental feasibility of this approach by performing attosecond streaking measurements on a single atomic layer of xenon atoms adsorbed on the rhenium surface at a sample temperature of 50 K.

The corresponding spectrogram is shown in Fig. 11.10(a). It features three well-resolved emission lines corresponding the CB and $4f$ states of the metal substrate, and the Xe4*d* core-level state of the xenon adsorbate [57]. The latter may be used to estimate the absolute travel times of the substrate photoelectrons towards the surface. We note that such kind of measurements are also possible for higher xenon coverages [56]. For example, a streaking spectrogram recorded from a multilayer of xenon, which represents a model system for dielectric solids, is depicted in Fig. 11.10(b). These experiments demonstrate that the investigation of weakly-bound adsorbate systems are in principle not compromised by NIR-induced desorption, and that streaking spectroscopy can even be extended to dielectric materials.

11.5.3 Future Directions and Perspectives

The high time-resolution offered by sub-fs light pulses entails a reduced spectral resolution and consequently the observed states have to be well separated in energy to be discernible. Still, the application of few-fs to attosecond spectroscopy

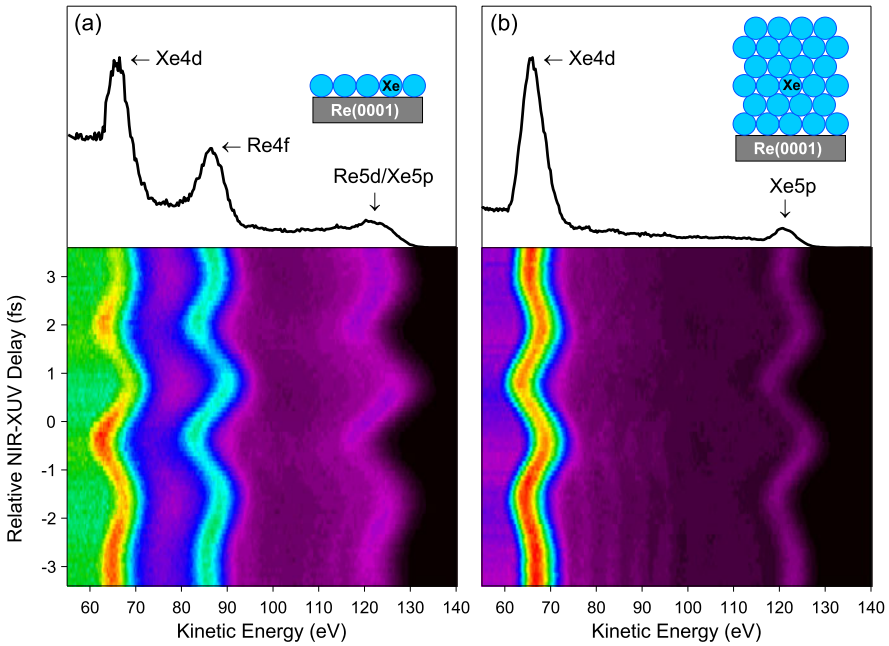

Fig. 11.10 Streaked attosecond photoemission originating from a monolayer (**a**) and a multilayer (**b**) of xenon atoms adsorbed on the (0001) surface of rhenium [57]

to solids offers intriguing new possibilities for example in the investigation of excited electron dynamics capable of resolving the formation and early relaxation of photo-excited electrons in valence states. The test of theoretical models for the fundamental process of photoemission in the time-domain by attosecond streaking will eventually lead to a better understanding of transport, scattering and screening processes in condensed matter. As the velocity of charge-transfer dynamics in adsorbate-substrate systems is a key factor determining the efficiency of the process, monitoring the core-level-shifts resulting from changes in the oxidation state of tracer atoms, with attosecond time-resolution might reveal the relative importance of competing processes. Due to high technical and methodological requirements attosecond surface experiments are still challenging but hold promise of exciting new discoveries in the near future.

Acknowledgements Important contributions to the experimental setup, the experiments as well as to the data analysis and discussion by A. Cavalieri, R. Ernstorfer, P. Feulner, F. Krausz, E. Magerl, N. Karpowicz, J. Barth, A. Paarmann and M. Stanislawski are gratefully acknowledged. Financial support by the Deutsche Forschungsgemeinschaft through the Excellence Cluster Munich Centre for Advanced Photonics, is gratefully acknowledged. R.K. acknowledges support by an ERC Starting Grant.

References

1. W. Ackermann et al., Operation of a free-electron laser from the extreme ultraviolet to the water window. Nat. Photonics **1**(6), 336–342 (2007). http://www.nature.com/doifinder/10.1038/nphoton.2007.76. doi:10.1038/nphoton.2007.76
2. N. Aközbek, A. Iwasaki, A. Becker, M. Scalora, S. Chin, C. Bowden, Third-harmonic generation and self-channeling in air using high-power femtosecond laser pulses. Phys. Rev. Lett. **89**(14), 14–17 (2002). http://link.aps.org/doi/10.1103/PhysRevLett.89.143901. doi:10.1103/PhysRevLett.89.143901
3. J.C. Baggesen, L.B. Madsen, Theory for time-resolved measurements of laser-induced electron emission from metal surfaces. Phys. Rev. A **78**, 032903 (2008). http://link.aps.org/abstract/PRA/v78/e032903
4. M. Bauer, Femtosecond ultraviolet photoelectron spectroscopy of ultra-fast surface processes. J. Phys. D, Appl. Phys. **38**(16), R253–R267 (2005). http://stacks.iop.org/0022-3727/38/i=16/a=R01?key=crossref.5c0a1a32458dc1f51c40275b46a68cc7. doi:10.1088/0022-3727/38/16/R01
5. M. Bauer, C. Lei, K. Read, R. Tobey, J. Gland, M. Murnane, H. Kapteyn, Direct observation of surface chemistry using ultrafast soft-X-ray pulses. Phys. Rev. Lett. **87**(2), 1–4 (2001). http://link.aps.org/doi/10.1103/PhysRevLett.87.025501. doi:10.1103/PhysRevLett.87.025501
6. P. Baum, S. Lochbrunner, E. Riedle, Tunable sub-10-fs ultraviolet pulses generated by achromatic frequency doubling. Opt. Lett. **29**(14), 1686–1688 (2004). http://www.ncbi.nlm.nih.gov/pubmed/15309860
7. A. Borisov, D. Sánchez-Portal, R. Díez Muiño, P.M. Echenique, Building up the screening below the femtosecond scale. Chem. Phys. Lett. **387**, 95 (2004). http://www.sciencedirect.com/science/article/B6TFN-4BSW32W-4/2/1a16530aec0c85ff59fec75691073d21
8. E.M. Bothschafter, A. Schiffrin, V.S. Yakovlev, A.M. Azzeer, F. Krausz, R. Ernstorfer, R. Kienberger, Collinear generation of ultrashort UV and XUV pulses. Opt. Express **18**(9), 9173–9180 (2010). http://www.ncbi.nlm.nih.gov/pubmed/20588764
9. D. Brida, G. Cerullo, Electron thermalization in gold on the 10-fs timescale, in *2010 Conference on Lasers and Electro-Optics (CLEO)* (2010), pp. 2–3
10. P.A. Brühwiler, O. Karis, N. Mårtensson, Charge-transfer dynamics studied using resonant core spectroscopies. Rev. Mod. Phys. **74**, 703 (2002). http://link.aps.org/abstract/RMP/v74/p703
11. A. Cavalieri, R. Ernstorfer, S. Neppl, et al., unpublished results
12. A.L. Cavalieri, E. Goulielmakis, B. Horvath, W. Helml, M. Schultze, M. Fieß, V. Pervak, L. Veisz, V.S. Yakovlev, M. Uiberacker, A. Apolonski, F. Krausz, R. Kienberger, Intense 1.5-cycle near infrared laser waveforms and their use for the generation of ultra-broadband soft-X-ray harmonic continua. New J. Phys. **9**(7), 242 (2007). http://stacks.iop.org/1367-2630/9/i=7/a=242?key=crossref.c8853a078987c15542c906c0692977b1. doi:10.1088/1367-2630/9/7/242
13. A.L. Cavalieri, N. Müller, T. Uphues, V.S. Yakovlev, A. Baltuska, B. Horvath, B. Schmidt, L. Blümel, R. Holzwarth, S. Hendel, M. Drescher, U. Kleineberg, P.M. Echenique, R. Kienberger, F. Krausz, U. Heinzmann, Attosecond spectroscopy in condensed matter. Nature **449**(7165), 1029–1032 (2007). http://www.ncbi.nlm.nih.gov/pubmed/17960239. doi:10.1038/nature06229
14. N. Christensen, B. Seraphin, Relativistic band calculation and the optical properties of gold. Phys. Rev. B **4**(10), 3321 (1971). http://prb.aps.org/abstract/PRB/v4/i10/p3321_1
15. A. Cionga, A. Maquet, R. Taieb, Laser-assisted X-ray. Phys. Rev. **47**(3) (1993)
16. P. Corkum, Plasma perspective on strong field multiphoton ionization. Phys. Rev. Lett. **71**(13), 1994–1997 (1993). http://link.aps.org/doi/10.1103/PhysRevLett.71.1994
17. P.B. Corkum, N.H. Burnett, M.Y. Ivanov, Subfemtosecond pulses. Opt. Lett. **19**(22), 1870–1872 (1994). doi:10.1364/OL.19.001870

18. H. Dachraoui, M. Michelswirth, P. Siffalovic, P. Bartz, C. Schäfer, B. Schnatwinkel, J. Mattay, W. Pfeiffer, M. Drescher, U. Heinzmann, Photoinduced reconfiguration cycle in a molecular adsorbate layer studied by femtosecond inner-shell photoelectron spectroscopy. Phys. Rev. Lett. **106**(10), 46–49 (2011). http://link.aps.org/doi/10.1103/PhysRevLett.106.107401. doi:10.1103/PhysRevLett.106.107401
19. P. De Andres, P. Echenique, F. Flores, Lifetime in a two-dimensional image-potential-induced electron band. Phys. Rev. B, Condens. Matter **35**(9), 4529 (1987). http://ukpmc.ac.uk/abstract/MED/9942015
20. M. Drescher, M. Hentschel, R. Kienberger, G. Tempea, C. Spielmann, G.A. Reider, P.B. Corkum, F. Krausz, X-ray pulses approaching the attosecond frontier. Science **291**, 1923 (2001). http://www.sciencemag.org/cgi/content/abstract/291/5510/1923. doi:10.1126/science.1058561
21. C. Durfee III, A. Rundquist, S. Backus, C. Herne, M. Murnane, H. Kapteyn, Phase matching of high-order harmonics in hollow waveguides. Phys. Rev. Lett. **83**(11), 2187–2190 (1999). http://link.aps.org/doi/10.1103/PhysRevLett.83.2187
22. P.G. Etchegoin, E.C. Le Ru, M. Meyer, An analytic model for the optical properties of gold. J. Chem. Phys. **125**(16), 164705 (2006). http://www.ncbi.nlm.nih.gov/pubmed/17092118. doi:10.1063/1.2360270
23. W.S. Fann, R. Storz, H.W.K. Tom, J. Bokor, Direct measurement of nonequilibrium electron-energy distributions in subpicosecond laser-heated gold films. Phys. Rev. Lett. **68**(18), 2834–2837 (1992). http://link.aps.org/doi/10.1103/PhysRevLett.68.2834. doi:10.1103/PhysRevLett.68.2834
24. N.D. Fatti, C. Voisin, M. Achermann, S. Tzortzakis, D. Christofilos, F. Valle, Nonequilibrium electron dynamics in noble metals. Phys. Rev. B **61**(24), 956–966 (2000)
25. X. Feng, S. Gilbertson, H. Mashiko, H. Wang, S.D. Khan, M. Chini, Y. Wu, K. Zhao, Z. Chang, Generation of isolated attosecond pulses with 20 to 28 femtosecond lasers. Phys. Rev. Lett. **103**(18), 28–31 (2009). http://link.aps.org/doi/10.1103/PhysRevLett.103.183901. doi:10.1103/PhysRevLett.103.183901
26. A. Föhlisch, P. Feulner, F. Hennies, A. Fink, D. Menzel, D. Sánchez-Portal, P.M. Echenique, W. Wurth, Direct observation of electron dynamics in the attosecond domain. Nature **436**, 373 (2005). doi:10.1038/nature03833
27. T. Fuji, T. Horio, T. Suzuki, Generation of 12 fs deep-ultraviolet pulses by four-wave mixing through filamentation in neon gas. Opt. Lett. **32**(17), 2481–2483 (2007). http://www.ncbi.nlm.nih.gov/pubmed/17767278
28. J. Gagnon, E. Goulielmakis, V. Yakovlev, The accurate frog characterization of attosecond pulses from streaking measurements. Appl. Phys. B **92**, 25 (2008). doi:10.1007/s00340-008-3063-x
29. T. Glover, R. Schoenlein, A. Chin, C. Shank, Observation of laser assisted photoelectric effect and femtosecond high order harmonic radiation. Phys. Rev. Lett. **76**(14), 2468–2471 (1996). http://www.ncbi.nlm.nih.gov/pubmed/10060707
30. E. Goulielmakis, M. Schultze, M. Hofstetter, V.S. Yakovlev, J. Gagnon, M. Uiberacker, A.L. Aquila, E.M. Gullikson, D.T. Attwood, R. Kienberger, F. Krausz, U. Kleineberg, Single-cycle nonlinear optics. Science (New York) **320**(5883), 1614–1617 (2008). http://www.ncbi.nlm.nih.gov/pubmed/18566281. doi:10.1126/science.1157846
31. U. Graf, M. Fiess, M. Schultze, R. Kienberger, F. Krausz, E. Goulielmakis, Intense few-cycle light pulses in the deep ultraviolet. Opt. Express **16**(23), 18956–18963 (2008). http://www.ncbi.nlm.nih.gov/pubmed/19581987
32. R. Groeneveld, R. Sprik, Femtosecond spectroscopy of electron-electron and electron-phonon energy relaxation in Ag and Au. Phys. Rev. B **51**(17) (1995). http://prb.aps.org/abstract/PRB/v51/i17/p11433_1
33. T. Haarlammert, H. Zacharias, Application of high harmonic radiation in surface science. Curr. Opin. Solid State Mater. Sci. **13**(1–2), 13–27 (2009). http://linkinghub.elsevier.com/retrieve/pii/S1359028608000545. doi:10.1016/j.cossms.2008.12.003

34. M. Hentschel, R. Kienberger, C. Spielmann, G.A. Reider, N. Milosevic, T. Brabec, P. Corkum, U. Heinzmann, M. Drescher, F. Krausz, Attosecond metrology. Nature **414**(6863), 509–513 (2001). http://www.ncbi.nlm.nih.gov/pubmed/11734845. doi:10.1038/35107000
35. C. Hess, S. Funk, M. Bonn, D. Denzler, M. Wolf, G. Ertl, Femtosecond dynamics of chemical reactions at surfaces. Appl. Phys. A, Mater. Sci. Process. **71**(5), 477–483 (2000). http://www.springerlink.com/index/gjg4v2g8l5gjn5hb.pdf
36. R. Huber, F. Tauser, A. Brodschelm, M. Bichler, G. Abstreiter, A. Leitenstorfer, How many-particle interactions develop after ultrafast excitation of an electron-hole plasma. Nature **414**, 286 (2001). doi:10.1038/35104522
37. S. Hüfner, *Photoelectron Spectroscopy—Principles and Applications* (Springer, Berlin, 2003)
38. J. Itatani, F. Quéré, G. Yudin, M. Ivanov, F. Krausz, P. Corkum, Attosecond streak camera. Phys. Rev. Lett. **88**(17), 1–4 (2002). http://link.aps.org/doi/10.1103/PhysRevLett.88.173903. doi:10.1103/PhysRevLett.88.173903
39. A. Kazansky, P. Echenique, One-electron model for the electronic response of metal surfaces to subfemtosecond photoexcitation. Phys. Rev. Lett. **102**(17), 1–4 (2009). http://link.aps.org/doi/10.1103/PhysRevLett.102.177401. doi:10.1103/PhysRevLett.102.177401
40. R. Kienberger, E. Goulielmakis, M. Uiberacker, A. Baltuška, V. Yakovlev, F. Bammer, A. Scrinzi, T. Westerwalbesloh, U. Kleineberg, U. Heinzmann, M. Drescher, F. Krausz, Atomic transient recorder. Nature **427**, 817 (2004). doi:10.1038/nature02277
41. R. Kienberger, M. Hentschel, M. Uiberacker, C. Spielmann, M. Kitzler, A. Scrinzi, M. Wieland, T. Westerwalbesloh, U. Kleineberg, U. Heinzmann, M. Drescher, F. Krausz, Steering attosecond electron wave packets with light. Science **297**, 1144 (2002). http://www.sciencemag.org/cgi/content/abstract/297/5584/1144. doi:10.1126/science.1073866
42. E. Knoesel, A. Hotzel, M. Wolf, Temperature dependence of surface state lifetimes, dephasing rates and binding energies on Cu(111) studied with time-resolved photoemission. J. Electron Spectrosc. Relat. Phenom. **91**, 577–584 (1998). http://www.sciencedirect.com/science/article/pii/S0368204897001783. doi:10.1016/S0368-2048(97)00178-3
43. R. Knorren, K.H. Bennemann, R. Burgermeister, M. Aeschlimann, Dynamics of excited electrons in copper and ferromagnetic transition metals: theory and experiment. Phys. Rev. B **61**(14), 9427–9440 (2000). http://prb.aps.org/pdf/PRB/v61/i14/p9427_1. doi:10.1103/PhysRevB.61.9427
44. K. Kosma, S.A. Trushin, W.E. Schmid, W. Fuss, Vacuum ultraviolet pulses of 11 fs from fifth-harmonic generation of a Ti:sapphire laser. Opt. Lett. **33**(7), 723–725 (2008). http://www.ncbi.nlm.nih.gov/pubmed/18382530
45. E.E. Krasovskii, Attosecond spectroscopy of solids: streaking phase shift due to lattice scattering. Phys. Rev. B **84**, 195106 (2011). http://link.aps.org/doi/10.1103/PhysRevB.84.195106. doi:10.1103/PhysRevB.84.195106
46. E.E. Krasowskii, W. Schattke, P. Jiricek, M. Vondracek, O.V. Krasovska, V.N. Antonov, A.P. Shpak, I. Bartos, Photoemission from Al(100) and (111): experiment and ab initio theory. Phys. Rev. B **78**(16), 165406 (2008). http://link.aps.org/doi/10.1103/PhysRevB.78.165406
47. C. Lei, M. Bauer, K. Read, R. Tobey, Y. Liu, T. Popmintchev, M. Murnane, H. Kapteyn, Hot-electron-driven charge transfer processes on O_2/Pt(111) surface probed by ultrafast extreme-ultraviolet pulses. Phys. Rev. B **66**(24), 1–10 (2002). http://link.aps.org/doi/10.1103/PhysRevB.66.245420. doi:10.1103/PhysRevB.66.245420
48. C. Lemell, B. Solleder, K. Tőkési, J. Burgdörfer, Simulation of attosecond streaking of electrons emitted from a tungsten surface. Phys. Rev. A **79**(6), 1–8 (2009). http://link.aps.org/doi/10.1103/PhysRevA.79.062901. doi:10.1103/PhysRevA.79.062901
49. A. L'Huillier, P. Balcou, High-order harmonic generation in rare gases with a 1-ps 1053-nm laser. Phys. Rev. Lett. **70**(6), 774–777 (1993). http://link.aps.org/doi/10.1103/PhysRevLett.70.774
50. J. Macklin, J. Kmetec, C. Gordon III, High-order harmonic generation using intense femtosecond pulses. Phys. Rev. Lett. **70**(6), 766–769 (1993). http://link.aps.org/doi/10.1103/PhysRevLett.70.766

51. E. Magerl, S. Neppl, A.L. Cavalieri, E.M. Bothschafter, M. Stanislawski, T. Uphues, M. Hofstetter, U. Kleineberg, J.V. Barth, D. Menzel, F. Krausz, R. Ernstorfer, R. Kienberger, P. Feulner, A flexible apparatus for attosecond photoelectron spectroscopy of solids and surfaces. Rev. Sci. Instrum. **82**, 063104 (2011). doi:10.1063/1.3596564
52. S. Mathias, L. Miaja-Avila, M.M. Murnane, H. Kapteyn, M. Aeschlimann, M. Bauer, Angle-resolved photoemission spectroscopy with a femtosecond high harmonic light source using a two-dimensional imaging electron analyzer. Rev. Sci. Instrum. **78**(8), 083105 (2007). http://www.ncbi.nlm.nih.gov/pubmed/17764311. doi:10.1063/1.2773783
53. L. Miaja-Avila, C. Lei, M. Aeschlimann, J. Gland, M. Murnane, H. Kapteyn, G. Saathoff, Laser-assisted photoelectric effect from surfaces. Phys. Rev. Lett. **97**(11), 1–4 (2006). http://link.aps.org/doi/10.1103/PhysRevLett.97.113604. doi:10.1103/PhysRevLett.97.113604
54. L. Miaja-Avila, G. Saathoff, S. Mathias, J. Yin, C. La-o vorakiat, M. Bauer, M. Aeschlimann, M. Murnane, H. Kapteyn, Direct measurement of core-level relaxation dynamics on a surface-adsorbate system. Phys. Rev. Lett. **101**(4), 1–4 (2008). http://link.aps.org/doi/10.1103/PhysRevLett.101.046101. doi:10.1103/PhysRevLett.101.046101
55. R.D. Muiño, D. Sánchez-Portal, V.M. Silkin, E.V. Chulkov, P.M. Echenique, Time-dependent electron phenomena at surfaces. Proc. Natl. Acad. Sci. **108**(3), 971–976 (2011). http://www.pnas.org/content/108/3/971.abstract. doi:10.1073/pnas.1008517107
56. S. Neppl, Attosecond time-resolved photoemission from surfaces and interfaces. PhD Thesis, Technische Universität München, 2012
57. S. Neppl, A. Cavalieri, R. Ernstorfer, et al., unpublished results
58. S. Neppl, R. Ernstorfer, E. Bothschafter, et al., unpublished results
59. H. Petek, S. Ogawa, Femtosecond time-resolved two-photon photoemission studies of electron dynamics in metals. Prog. Surf. Sci. **56**(4), 239–310 (1997). http://www.sciencedirect.com/science/article/pii/S0079681698000021
60. F. Reiter, U. Graf, M. Schultze, W. Schweinberger, H. Schröder, N. Karpowicz, A.M. Azzeer, R. Kienberger, F. Krausz, E. Goulielmakis, Generation of sub-3 fs pulses in the deep ultraviolet. Opt. Lett. **35**(13), 2248–2250 (2010). http://ol.osa.org/abstract.cfm?URI=ol-35-13-2248. doi:10.1364/OL.35.002248
61. F. Reiter, U. Graf, M. Schultze, W. Schweinberger, H. Schröder, N. Karpowicz, A.M. Azzeer, R. Kienberger, F. Krausz, E. Goulielmakis, Generation of sub-3 fs pulses in the deep ultraviolet. Opt. Lett. **35**(13), 2248–2250 (2010). http://www.ncbi.nlm.nih.gov/pubmed/20596209
62. G. Sansone, E. Benedetti, F. Calegari, C. Vozzi, L. Avaldi, R. Flammini, L. Poletto, P. Villoresi, C. Altucci, R. Velotta, S. Stagira, S. De Silvestri, M. Nisoli, Isolated single-cycle attosecond pulses. Science (New York) **314**(5798), 443–446 (2006). http://www.ncbi.nlm.nih.gov/pubmed/17053142. doi:10.1126/science.1132838
63. W. Schattke, M.A.V. Hove, *Solid-State Photoemission and Related Methods: Theory and Experiment* (Wiley-VCH, Weinheim, 2003)
64. C. Schmuttenmaer, C. Cameron Miller, J. Herman, J. Cao, D. Mantell, Y. Gao, R. Miller, Femtosecond time-resolved photoemission study of hot electron relaxation at the GaAs(100) surface. Chem. Phys. **205**(1–2), 91–108 (1996). http://linkinghub.elsevier.com/retrieve/pii/0301010495003282. doi:10.1016/0301-0104(95)00328-2
65. R. Schoenlein, W. Lin, J. Fujimoto, G. Eesley, Femtosecond studies of nonequilibrium electronic processes in metals. Phys. Rev. Lett. **58**(16), 1680–1683 (1987). http://link.aps.org/doi/10.1103/PhysRevLett.58.1680
66. M. Schultze, M. Fiess, N. Karpowicz, J. Gagnon, M. Korbman, M. Hofstetter, S. Neppl, A.L. Cavalieri, Y. Komninos, T. Mercouris, C.A. Nicolaides, R. Pazourek, S. Nagele, J. Feist, J. Burgdörfer, A.M. Azzeer, R. Ernstorfer, R. Kienberger, U. Kleineberg, E. Goulielmakis, F. Krausz, V.S. Yakovlev, Delay in photoemission. Science **328**, 1658 (2010). http://www.sciencemag.org/cgi/content/abstract/328/5986/1658
67. I.J. Sola, E. Mével, L. Elouga, E. Constant, V. Strelkov, L. Poletto, P. Villoresi, E. Benedetti, J.P. Caumes, S. Stagira, C. Vozzi, G. Sansone, M. Nisoli, Controlling attosecond electron dynamics by phase-stabilized polarization gating. Nat. Phys. **2**(5), 319–322 (2006). http://www.nature.com/doifinder/10.1038/nphys281. doi:10.1038/nphys281

68. C. Sun, F. Vallee, L. Acioli, E. Ippen, Femtosecond investigation of electron thermalization in gold. Phys. Rev. B **48**(16) (1993). http://prb.aps.org/abstract/PRB/v48/i16/p12365_1
69. E. Toma, H. Muller, P. Paul, P. Breger, M. Cheret, Ponderomotive streaking of the ionization potential as a method for measuring pulse durations in the XUV domain with fs resolution. Phys. Rev. A **62**, 1–4 (2000). http://pra.aps.org/abstract/PRA/v62/i6/e061801
70. V. Veniard, Two-color multiphoton ionization of atoms using high-order harmonic radiation. Phys. Rev. Lett. **74**(21), 4161–4164 (1995). http://link.aps.org/doi/10.1103/PhysRevLett.74.4161
71. L. Wang, W. Chen, A.T.S. Wee, Charge transfer across the molecule/metal interface using the core hole clock technique. Surf. Sci. Rep. **63**(11), 465–486 (2008). http://linkinghub.elsevier.com/retrieve/pii/S0167572908000502. doi:10.1016/j.surfrep.2008.06.001
72. A. Wirth, M.T. Hassan, I. Grguras, J. Gagnon, A. Moulet, T.T. Luu, S. Pabst, R. Santra, Z.A. Alahmed, A.M. Azzeer, V.S. Yakovlev, V. Pervak, F. Krausz, E. Goulielmakis, Synthesized light transients. Science (New York) **195**(2011) (2011). http://www.ncbi.nlm.nih.gov/pubmed/21903778. doi:10.1126/science.1210268
73. V.S. Yakovlev, J. Gagnon, N. Karpowicz, F. Krausz, Attosecond streaking enables the measurement of quantum phase. Phys. Rev. Lett. **105**, 073001 (2010). http://link.aps.org/doi/10.1103/PhysRevLett.105.073001. doi:10.1103/PhysRevLett.105.073001
74. A. Zangwill, *Physics at Surfaces* (Cambridge University Press, Cambridge, 1988)
75. A.H. Zewail, Femtochemistry: atomic-scale dynamics of the chemical bond. J. Phys. Chem. A **104**, 5660 (2000). doi:10.1021/jp001460h
76. C.H. Zhang, U. Thumm, Attosecond photoelectron spectroscopy of metal surfaces. Phys. Rev. Lett. **102**(12), 1–4 (2009). http://link.aps.org/doi/10.1103/PhysRevLett.102.123601. doi:10.1103/PhysRevLett.102.123601
77. C.H. Zhang, U. Thumm, Erratum: Attosecond photoelectron spectroscopy of metal surfaces [Phys. Rev. Lett. **102**, 123601 (2009)]. Phys. Rev. Lett. **103**, 239902 (2009). http://link.aps.org/doi/10.1103/PhysRevLett.103.239902. doi:10.1103/PhysRevLett.103.239902
78. C.H. Zhang, U. Thumm, Probing dielectric-response effects with attosecond time-resolved streaked photoelectron spectroscopy of metal surfaces. Phys. Rev. A **84**(6), 1–7 (2011). http://link.aps.org/doi/10.1103/PhysRevA.84.063403. doi:10.1103/PhysRevA.84.063403
79. A.A. Zholents, W.M. Fawley, Proposal for intense attosecond radiation from an X-ray free-electron laser. Phys. Rev. Lett. **92**, 224801 (2004). http://link.aps.org/doi/10.1103/PhysRevLett.92.224801. doi:10.1103/PhysRevLett.92.224801

Chapter 12
From Above-Threshold Photoemission to Attosecond Physics at Nanometric Tungsten Tips

M. Krüger, M. Schenk, J. Breuer, M. Förster, J. Hammer, J. Hoffrogge, S. Thomas, and P. Hommelhoff

Abstract The interaction of few-cycle laser pulses with a nanometric metal tip is described. We find many effects that the strong-field physics community has discovered with atoms in the last 30 years, and describe them here in experiments with solid nanotips. Starting with a clear identification of several photon orders in above-threshold photoemission, via strong-field effects such as peak shifting and peak suppression, to the observation of a pronounced plateau in electron spectra, we show that we have reached the level of control necessary for attosecond physics experiments. In particular, we observe electronic wavepacket dynamics on the attosecond time scale. Namely, by variation of the carrier-envelope phase of the driving laser pulses, we observe a qualitative change in the electron spectra: For cosine pulses we obtain an almost flat plateau part, whereas for minus-cosine pulses the plateau part clearly shows photon orders. We interpret this change by the occurrence of a single or a double slit configuration in time causing electronic matter wave interference in the time-energy domain.

12.1 Introduction

Control of electric and magnetic fields in both space and time lies at the heart of a plethora of scientific experiments and devices, mostly to steer charged particles or particle matter waves. Probably one of the most well-known instruments is the electron microscope, which exploits the small de Broglie wavelength of electrons to image structures on length scales down to atomic dimensions (see, e.g., [1]). It is the control of DC electric and magnetic fields to the highest degrees that allows these instruments to reach this tremendous resolution (see, e.g., [2]).

Further, high-level control of AC electric fields in the radio frequency and microwave domain is utilized to guide and accelerate charged particles. In the low-energy regime, Paul traps have recently been used to guide electrons in a

M. Krüger · M. Schenk · J. Breuer · M. Förster · J. Hammer · J. Hoffrogge · S. Thomas · P. Hommelhoff (✉)
Ultrafast Quantum Optics Group, Max-Planck-Institut für Quantenoptik, Hans-Kopfermann-Str. 1, 85748 Garching, Germany
e-mail: peter.hommelhoff@mpq.mpg.de

K. Yamanouchi, K. Midorikawa (eds.), *Progress in Ultrafast Intense Laser Science*, Springer Series in Chemical Physics 104, DOI 10.1007/978-3-642-35052-8_12,

two-dimensional confining potential [3]. On the other end of the energy scale, microwave-driven particle accelerators operate. Currently the most prominent example is the Large Hadron Collider (LHC) at CERN in Geneva, Switzerland. Here, as in most other accelerators, charged particles traverse microwave cavities to pick up momentum. It is the phase-synchronicity between the particle arrival time and the microwave phase that allows acceleration in the electric microwave field. Phase synchronicity is achieved by matching the size and position of the cavities as well as the phase of the microwave to the position of the particles while they travel in the ring.

These days, attempts are being made to accelerate electrons with *optical* electromagnetic fields in order to achieve larger acceleration gradients [4]. The basic idea bears great similarity to microwave accelerators, namely to achieve phase-synchronicity between the driving laser field and the propagating electron pulses. Not only acceleration, but also steering of electrons in all directions seems possible, in great analogy to microwave accelerators [5]. Because optical wavelengths are around five orders of magnitude smaller than microwaves, the structures need to be smaller by roughly the same amount. Hence, the typical structure size is reduced from the decimeter to the (sub-)micron scale.

Surprisingly, attosecond physics is closely related, in the sense that the steering of electrons by the laser electric laser field lies at the core of it (see, e.g., [6]). Phase-synchronicity, however, does not need to be maintained by the experimenter but is guaranteed by the very nature of the processes involved. Yet, the typical size of the electron's excursion in the laser field follows the above-mentioned scaling. Typical energies of electrons laser-emitted from a solid tip are on the order of 1 eV, corresponding to a speed of around 1 nm/fs. Hence, the typical time scales of the driving laser field in the femtosecond range (at 800 nm the optical period equals 2.7 fs) result in propagation distances of several nanometers.

It is this simple argument that shows why attosecond physics needs to be matched by nanoscale materials. If the great achievements of attosecond physics, for example the imaging of a gas phase molecule with the light-field-steered electron (taken from the molecule) [7, 8], shall be extended to solid-state systems, a nanoscale system is needed.

One of the simplest and best controlled nanoscale systems is a sharp metal tip. These tips, which can be routinely made from tungsten, gold and other materials, can be etched down to radii of curvature of a few nanometers. They are being used in many high-resolution electron microscopes in DC operation, emitting electrons via field emission. They are rugged, stable, and can be inspected by various means. The most powerful ones are field emission microscopy and field ion microscopy, which can be performed in situ and rely on the stereoscopic projection imaging of the tip's surface onto a charged particle detector centimeters away from the tip [9, 10]. Because of the different lengths scales involved, a magnification of one million is routinely achieved, which allowed the first direct imaging of single atoms with the field ion microscope technique [11].

Furthermore, the tips can be cleaned and made perfectly smooth on the atomic scale, see Fig. 12.1. In field ion microscope operation, the electric field at the tip

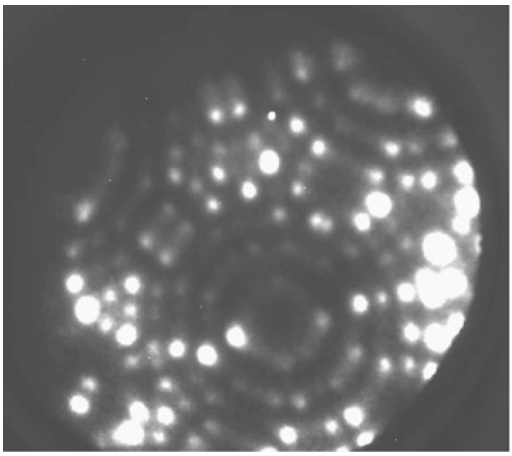

Fig. 12.1 A field ion microscope image of a sharp tungsten tip after field evaporation cleaning. Crystal planes can be seen, as well as crystal structure steps and individual atoms

apex can reach such high values that protruding structures and atoms on the surface can be "field-evaporated," leading to the formation of an atomically smooth hemisphere. This way, the surface shape and morphology is well known, which is of great interest if experimental and theoretical data shall be compared. Furthermore, this way a single well-defined "hot-spot" of electron emission is achieved.

The resulting small source size of field emission tips leads to an extremely high brightness and transverse coherence. This makes them ideal sources for accelerator, coherent X-ray and time resolved electron diffraction setups [12].

Here we will focus our attention on strong-field and attosecond physics at and with sharp tips. In the following, we will describe the experimental setup, show results on above-threshold spectra and the gradual increase of strong-field physics phenomena with intensity, until we discuss the domain where liberated electrons are steered by the laser electric field, thus entering the attosecond science arena.

Before we start describing the setup, we mention one effect that relaxes requirements on the laser system a lot. If the typical dimension of a structure interacting with light is smaller than the light's wavelength, the electric field is locally enhanced right at the structure. This effect is called field enhancement, see Fig. 12.2. For typical parameters, such as a tungsten tip with a radius on the order of 10 nm and a driving wavelength of 800 nm, the field enhancement factor is around 5. This means that the intensity at the tip's apex is 25 times higher than the intensity in a bare laser focus [13] and allows tip-based experiments to operate with laser oscillators only, rendering complex and expensive laser amplifier systems dispensable. In the same way, field enhancement at bow tie nanostructures allowed for high harmonic generation from a gas at oscillator repetition rates [14].

Other groups have employed femtosecond laser driven electron emission from metal tips to study surface imaging with short electron pulses [15], to study other strong-field and polarization dependent emission effects [16, 17], and to examine the suitability as free-electron-laser electron sources [18, 19].

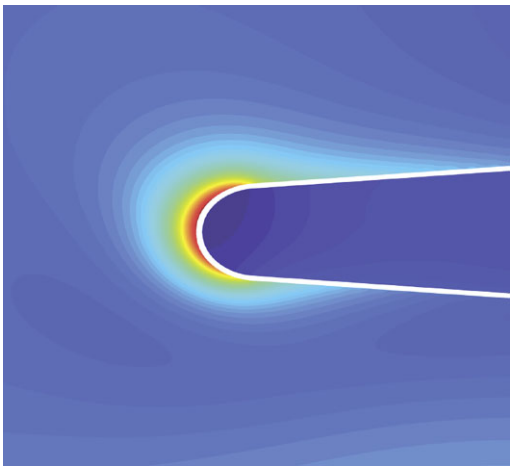

Fig. 12.2 Field enhancement at a tip with radius of curvature of 30 nm, opening angle of 5° and 800 nm laser wavelength. Incoming radiation from the bottom is enhanced at the tip because of the small apex dimensions. The color scale indicates the maximum of the electric field, with *blue* indicating the non-enhanced field, and *red* showing the enhancement. Field enhancement at the tip relaxes the requirements on the laser pulse energy by at least one order of magnitude

12.2 Experimental Setup

The experimental setup, depicted in Fig. 12.3, is compact and simple as compared to attosecond experiments operating with gas jets. An electro-chemically etched tip is mounted in an ultrahigh vacuum chamber. We pump the chamber with a turbo-molecular, an ion, and a titanium-sublimation pump and reach a pressure of $\sim 2 \times 10^{-10}$ mbar. We observe that this pressure is necessary such that the tip stays atomically clean for at least 10 minutes. The laser beam is focused on the tip with the help of an off-axis parabolic mirror with a focal length of 15 mm. Because of the small focal length, the focusing mirror is mounted inside the vacuum chamber. In order to overlap the focal spot with the tip, the tip can be moved in all three spatial dimensions with the help of nanopositioning stages.

We employ a commercial few-cycle double-chirped-mirror dispersion controlled Kerr-lens mode-locked Titanium: sapphire laser oscillator, which we pump with close to 6 W at 532 nm. The oscillator can be carrier-envelope phase stabilized with a home-built f-2f interferometer. More details on the whole setup can be found in [20–23].

The off-axis parabolic mirror allows focussing of the beam down to $\sim$2.4 μm ($1/e^2$ intensity radius), so that a pulse duration of 6.5 fs and a pulse energy of 1 nJ result in peak intensities of 1.7×10^{12} W/cm^2 in the bare focus.

Emitted electrons can either be detected with a chevron-type microchannel plate detector (MCP), which amplifies each incoming charged particle to produce a light signal on a phosphor screen mounted right behind the MCP. Figure 12.1 was recorded this way. Alternatively, we can, without opening the vacuum chamber, position a retarding field spectrometer in front of the tip, which allows us to measure the electrons' energy. While the spatial image is important for inspection and preparation purposes, the spectrometer allows us to identify laser-driven processes, as will be shown in the following.

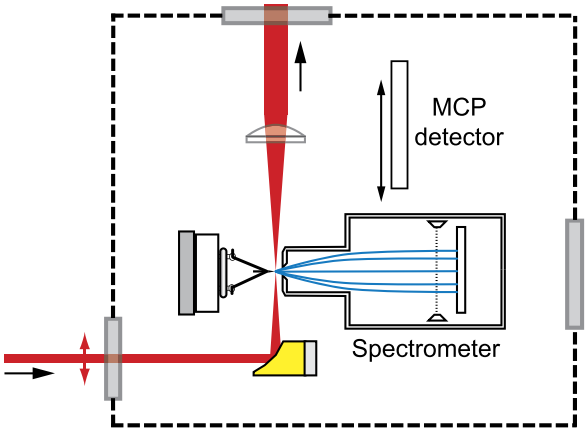

Fig. 12.3 Overview of the experimental setup. The laser beam is focused with the help of an off-axis parabolic mirror onto the sharp tip, which is mounted on a standard electron microscope filament holder. Emitted electrons travel away from the tip into the spectrometer, where they are detected with a multiplying detector. In front of the detector a set of copper meshes is situated, which allows applying a counter voltage, such that only electrons with a given forward kinetic energy can pass. Hence, by measuring the current as function of counter voltage, spectra can be obtained after differentiation. Imaging of the tip's apex can be achieved by moving the spectrometer away from the tip (here out of plane), and instead moving a microchannel plate electron detector in front of the tip. Electron emission can be visualized with the help of a phosphor screen that is mounted behind the microchannel plate, and that is monitored with a camera outside of the vacuum chamber (*dashed line*)

12.3 Above-Threshold Photoemission

The work function of tungsten, i.e., the energy difference between vacuum and Fermi level, is ∼4.5 eV, while the mean photon energy corresponding to the output spectrum of the oscillator is ∼1.5 eV. Obviously, direct photoemission is prohibited. By applying an electric field F, the Schottky effect [9, 24] considerably reduces the effective barrier height by

$$\Delta\Phi = -\sqrt{\frac{e^3 F}{4\pi\varepsilon_0}}, \tag{1}$$

with e being the electron charge and ε_0 the permittivity of free space. However, it is technically not feasible to obtain an effective barrier height of less than the photon energy as this would require applied voltages way above the onset of DC field emission leading to the destruction of the tip. Hence, the direct photoeffect is not able to liberate electrons from the tip even if a DC electric field is present at the tip.

For a strongly bent barrier, photo-assisted tunneling has been observed, where the electron is promoted in energy by the absorption of one photon and subsequently tunnels through the barrier [25]. However, with few-cycle laser pulses this process only takes place at a considerable rate if, as mentioned, the tunnel barrier is sufficiently small. This also means that a non-negligible DC tunnel current is emitted.

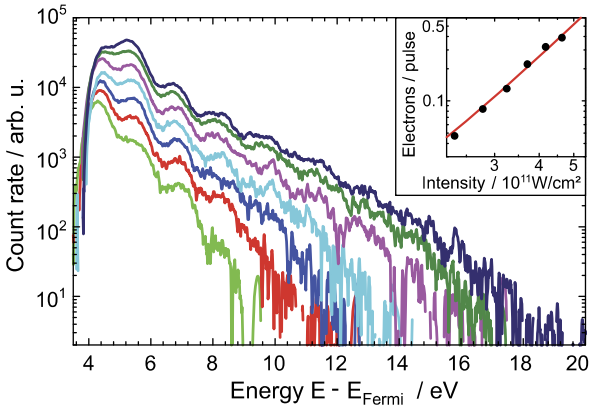

Fig. 12.4 Electron spectra for different laser intensities. The curves correspond to laser intensities of $\{1.9, 2.3, 2.8, 3.2, 3.7, 4.2, 4.6\} \times 10^{11}$ W/cm^2, starting from the bottom. For details, see text. The *inset* shows the total electron current as function of laser intensity. The slope is given by the photon order, but not much more can be extracted from this curve, highlighting the importance of spectral measurements

For the remainder of the paper, we restrict the discussion to DC fields that are so small that DC field emission as well as photo-assisted tunnel emission can be neglected for the parameters given.

With high laser intensities, non-linear photoemission processes become observable. It has been known for many decades already that multiphoton photoemission can liberate electrons from matter [26]. Multiphoton photoemission describes the emission of an electron from a metal by the absorption of more than one photon resulting in a kinetic energy of

$$E_{\mathrm{kin}} = n\hbar\omega - \Phi. \tag{2}$$

Here, n is the smallest integer that makes the expression non-negative, $\hbar$ the reduced Planck constant, ω the driving laser's circular frequency and Φ the workfunction of the metal.

E_{kin} is the smallest possible kinetic energy an emitted electron can obtain. If the electron's energy is larger by one, two, three, or several times the photon energy

$$E_{\mathrm{ATP}} = E_{\mathrm{kin}} + m\hbar\omega = (n+m)\hbar\omega - \Phi \tag{3}$$

one speaks of above-threshold photoemission (m integer). $(n + m)$ is called the photon order, while m is the above-threshold order.

While much work has been done and beautiful results have been achieved with atoms in the gas phase, starting with the first observation of above-threshold orders by Agostini et al. [27], only a limited amount of papers has been published on high-intensity photoemission experiments from solids. In terms of above-threshold orders, Ref. [28] represents the record high number of $m = 7$ that has been uniquely identified from a solid. Also Aeschlimann et al. report on higher kinetic energy photons, yet no clear photon orders could be identified [29].

The combination of a well-controlled sharp metal tip with nanometric dimensions, hence a single hot-spot emitting electrons from a tiny emission area with typical dimensions of 10 nm, with femtosecond laser pulses allowed us to observe unambiguously several above-threshold photon orders. Figure 12.4 shows typical

spectra. The laser intensity is given in the caption, the DC voltage applied to the tip is 150 V, resulting in a DC field at the tip apex[1] of around 1.2 GV/m.

Clearly, apart from the dominant peak at ∼4.3 eV, several more peaks are visible, with photon orders $(n+m) = 3 \ldots 9$ or $m = 0 \ldots 6$. Hence, above-threshold photoemission can now be clearly observed from a solid—owing to the field-enhancement effect, the single small emission area and the shortness of the laser pulse.

12.4 Strong-Field Effects: Peak Shifting and Peak Suppression

When we increase the laser intensity, not only do more photon orders show up, but also do spectral features start to shift to smaller energies. Furthermore, the lowest order peak is being overtaken in yield by the next higher one, see Fig. 12.4.

These effects are also very well known from atomic physics experiments [30]. They clearly indicate the onset of strong-field effects, where the laser field becomes so strong that it noticeably shifts the energy levels involved. Here, it is the AC Stark shift of the continuum states that is responsible for the observed features [20]. An intuitive way of looking at this effect considers the ponderomotive energy U_p of an electron in an oscillating laser field of amplitude E. This energy, given by

$$U_\mathrm{p} = \frac{e^2 E^2}{4m\omega^2}, \tag{4}$$

has to be imparted on the electron when it is emitted into the laser field (assuming that the initial state is unaffected by the laser field). Because the laser pulse is gone before the electron can leave the area of the enhanced field (so-called short pulse limit [31]), the electron loses the ponderomotive energy again. This leads to a decreased energy of the detected electron, so that Eq. (3) needs to be augmented by one more term, the ponderomotive energy:

$$E_\mathrm{kin} = n\hbar\omega - \Phi - U_\mathrm{p}. \tag{5}$$

In Eq. (5), we neglect a possible shift of the initial electronic state. Below the Fermi level the local density of states is dominated by the tungsten s and d bands [32]. While the delocalized s band is also subject to the AC Stark shift, the more localized d band is hardly affected [33]. Furthermore, the laser field is strongly screened inside the metal tip's apex in the vicinity of the surface, so that the shift experienced by any electronic state should be much smaller than U_p. We hence neglect the AC Stark shift of the initial state here, but expect that future, more elaborate and precise studies might reveal its influence.

Figure 12.5 shows how typical features of the spectrum scale when we vary the laser intensity. The slope of this shift directly gives U_p, hence the shift of the photon

[1] Note that the intensity values given here are the correct ones, where the ones in [20] are by a factor of 2 wrong. A careful reanalysis of the local dc electric fields at the tip apex has yielded a value of (1.2 ± 0.25) GV/m, whereas in [20] we mention 0.8 GV/m.

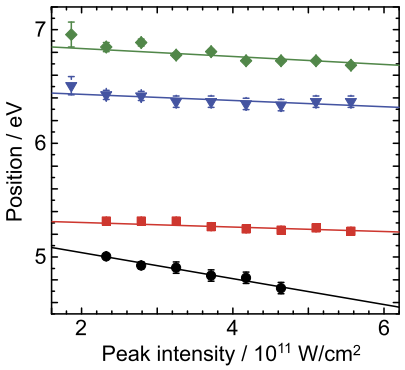

Fig. 12.5 Spectral position of the second and third maximum (*squares* and *diamonds*) and of the first and second minimum (*balls* and *triangles*) of Fig. 12.4. One can see that all features shift to smaller energies with increasing laser intensities. For more details, see text

orders allows us to measure the enhanced laser intensity right at the tip apex—which includes the field enhancement effect.

Measuring a field enhancement factor is notoriously hard, but because we can observe and follow the photon orders when we change the intensity I, it is rather straight-forward here. We obtain $U_p/I = (-5 \pm 3)$ eV/(10^{13} W/cm^2), while we calculate from our experimental parameters (not taking into account field enhancement, i.e., the presence of the tip in the laser focus) $U_p/I = -0.55$ eV/(10^{13} W/cm^2). The square-rooted ratio is 3.0 ± 0.8 and represents the field enhancement factor for these particular parameters.

Note that the field enhancement factor depends sensitively on the radius of the tip and the driving laser wavelength. In fact, we find that it almost only depends on the ratio between the tip radius and the driving wavelength of the laser, provided that the dielectric function does not significantly change over the range of wavelengths studied [13].

12.5 Attosecond Physics: Elastic Recollision

For slightly different parameters, we find that a plateau structure builds up in the spectra. Yet again, this feature is well known from the gas-phase analog with atoms [34]. It has been shown that the plateau is indicative of the liberated electron wave packet recolliding with the parent surface elastically before it travels to the detector ("rescattering").

Figure 12.6(a) shows the plateau structure in photoemission from a sharp tip. Meanwhile, together with our colleagues from Vienna, we could show that it is indeed the rescattering mechanism at the metal tip that is responsible for the appearance of the plateau structure [35]. Interestingly, to the best of our knowledge, even theoretically rescattering at a solid has only been touched upon briefly in a single paper before [36].

We expect the rescattering mechanism at solids to enable new tools for ultrafast surface imaging techniques because the rescattered electron wavepacket spreads out

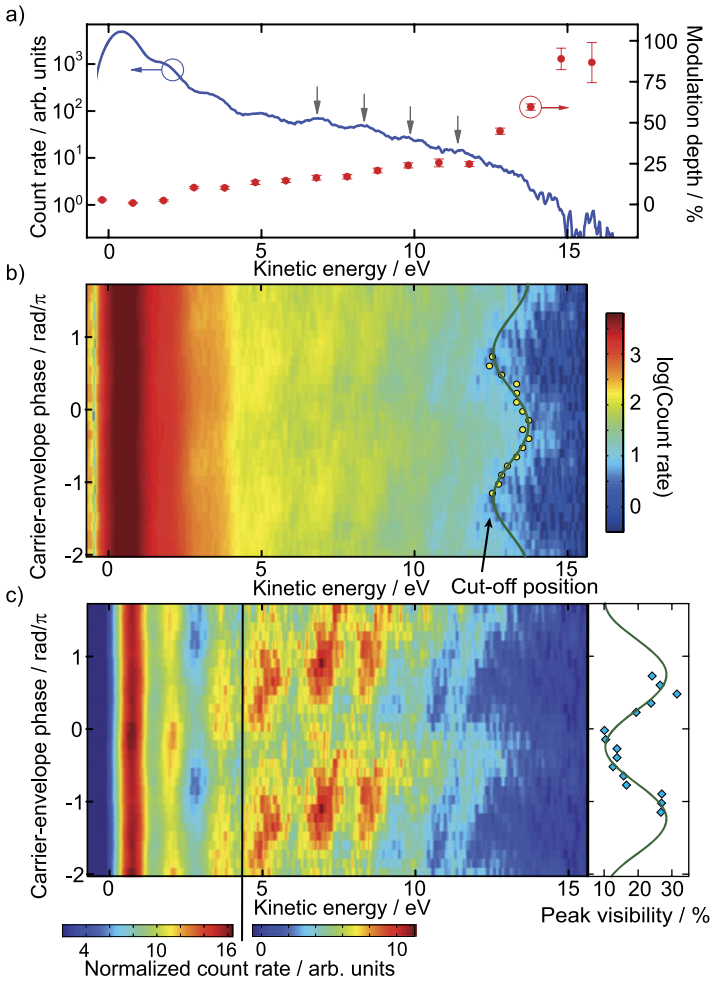

Fig. 12.6 (**a**) Electron spectrum with a clear plateau structure (*solid line*). The points indicate the current modulation depth upon variation of the CEP. The laser intensity (not including field enhancement) is 4×10^{11} W/cm^2. (**b**) CEP dependent spectrum. The *yellow points* and *solid line* indicate the maximum kinetic energy. Clearly, the maximum kinetic energy is modulated by the CEP by more than 10 %. (**c**) In order to better visualize CEP effects, two exponential slopes have been subtracted from the data in (**b**). The two different slopes have been subtracted on the left and on the right of the black vertical line, which indicates the beginning of the plateau part. Now, photon orders can be seen much more clearly for certain CEP settings, whereas for other CEP settings, hardly any photon peaks are visible. The visibility of the photon orders is shown on the right

transversally while it is driven away from and back towards the tip. Hence, upon recollision the electronic matter wave function interacts with roughly 7.5 surface unit cells for a W(310) surface and typical experimental parameters [35]. With a longer

driving laser wavelength, the classical excursion of the electron increases, and so does the lateral spread. Hence, by careful choice of the parameters different surface areas might be imaged with the returning electron. Together with synchronized attosecond pump pulses, this might lead to novel attosecond pump–rescattering electron probe spectroscopy, a new time-resolved surface science tool.

12.6 Matter Wave Interference in the Time-Energy Domain—Carrier-Envelope Phase Effects

With carrier-envelope phase (CEP) controlled laser pulses we record spectra as shown in Fig. 12.6. As a quite remarkable feature, we observe that both the visibility of the photon orders as well as the maximum kinetic energy gained by the electrons depend on the CEP. For CEP settings at which the maximum kinetic energy is highest the peak visibility is lowest. Vice versa, shifting the CEP by π results in the lowest maximum energy and the highest peak contrast [22].

We could explain the observed behavior, namely the appearance and disappearance of photon orders and the concomitant variation of the maximum kinetic electron energy with the help of the simple-man model, also known as three-step model [22, 37]. Photon orders appear within a single laser pulse if two temporally separated instances of electron emission can contribute to a given final energy, leading to interference in the time-energy domain, with a spacing of the maxima given by $\Delta E = h/\Delta t$. Since Δt equals almost exactly the laser period, ΔE equals the photon energy. For other CEP settings, only a single window in time contributes, leading to the absence of matter wave interference, and hence to a flat spectrum.

12.7 Outlook: From Attosecond Physics at Solids to Lightwave Electronics

The presented results show that attosecond techniques can now be applied to solids, most easily because of field enhancement at the nanometric metal tip. Indeed, a nanometrical metal tip represents an ideal model system to study strong-field effects at solids. In combination with a single-atom tip [38–42], intriguing comparative studies between attosecond physics at atoms in the gas phase and a single atom at a solid can potentially be performed. Further, the attosecond techniques, namely the control and steering of the liberated electron with the help of the well-controlled few-cycle light field, might enable coherent electron optical imaging techniques of surfaces on the one hand. On the other hand, a device that allows control of an electronic current with the optical electric field is intriguing in itself, as it may represent a field effect transistor, operating at attosecond time scales: lightwave electronics.

References

1. J. Spence, *High-Resolution Electron Microscopy*. Monographs on the Physics and Chemistry of Materials (Oxford University Press, Oxford, 2009)
2. R. Erni, M.D. Rossell, C. Kisielowski, U. Dahmen, Phys. Rev. Lett. **102**, 096101 (2009)
3. J. Hoffrogge, R. Fröhlich, M.A. Kasevich, P. Hommelhoff, Phys. Rev. Lett. **106**, 193001 (2011)
4. T. Plettner, P.P. Lu, R.L. Byer, Phys. Rev. Spec. Top., Accel. Beams **9**, 111301 (2006)
5. T. Plettner, R.L. Byer, C. McGuinness, P. Hommelhoff, Phys. Rev. Spec. Top., Accel. Beams **12**, 101302 (2009)
6. P.B. Corkum, F. Krausz, Nat. Phys. **3**(6), 381 (2007)
7. H. Niikura, F. Légáre, R. Hasbani, A.D. Bandrauk, M.Y. Ivanov, D.M. Villeneuve, P.B. Corkum, Nature **417**, 917 (2002)
8. S. Baker, J.S. Robinson, C.A. Haworth, H. Teng, R.A. Smith, C.C. Chirila, M. Lein, J.W.G. Tisch, J.P. Marangos, Science **312**(5772), 424 (2006)
9. G. Fursey, *Field Emission in Vacuum Microelectronics* (Kluwer Academic/Plenum, New York, 2005)
10. T.T. Tsong, *Atom-Probe Field Ion Microscopy* (Cambridge University Press, Cambridge, 1990)
11. E.W. Müller, K. Bahadur, Phys. Rev. **102**, 624 (1956)
12. J. Hoffrogge, J.P. Stein et al., to be published
13. S. Thomas, M. Krüger, M. Förster, M. Schenk, P. Hommelhoff. arXiv:1209.5195 (2012, submitted for publication)
14. S. Kim, J. Jin, Y. Kim, I. Park, Y. Kim, S. Kim, Nature **453**(7196), 757 (2008)
15. C. Ropers, D.R. Solli, C.P. Schulz, C. Lienau, T. Elsaesser, Phys. Rev. Lett. **98**, 043907 (2007)
16. R. Bormann, M. Gulde, A. Weismann, S.V. Yalunin, C. Ropers, Phys. Rev. Lett. **105**, 147601 (2010)
17. H. Yanagisawa, C. Hafner, P. Doná, M. Klöckner, D. Leuenberger, T. Greber, M. Hengsberger, J. Osterwalder, Phys. Rev. Lett. **103**, 257603 (2009)
18. R. Ganter, R. Bakker, C. Gough, S.C. Leemann, M. Paraliev, M. Pedrozzi, F. Le Pimpec, V. Schlott, L. Rivkin, A. Wrulich, Phys. Rev. Lett. **100**(6), 064801 (2008)
19. S. Tsujino, F. le Pimpec, J. Raabe, M. Buess, M. Dehler, E. Kirk, J. Gobrecht, A. Wrulich, Appl. Phys. Lett. **94**(9), 093508 (2009)
20. M. Schenk, M. Krüger, P. Hommelhoff, Phys. Rev. Lett. **105**(25), 257601 (2010)
21. M. Schenk, M. Krüger, P. Hommelhoff, in *Joint Conference of the IEEE International Frequency Control and the European Frequency and Time Forum (FCS)*, 2011 (2011), pp. 404–406
22. M. Krüger, M. Schenk, P. Hommelhoff, Nature **475**(7354), 78 (2011)
23. M. Krüger, M. Schenk, M. Förster, P. Hommelhoff, J. Phys. B, At. Mol. Opt. Phys. **45**, 074006 (2012)
24. W. Schottky, Phys. Z **15**, 872 (1914)
25. P. Hommelhoff, Y. Sortais, A. Aghajani-Talesh, M.A. Kasevich, Phys. Rev. Lett. **96**, 077401 (2006)
26. G.S. Voronov, N.B. Delone, JETP Lett. **1**, 66 (1965)
27. P. Agostini, F. Fabre, G. Mainfray, G. Petite, N.K. Rahman, Phys. Rev. Lett. **42**(17), 1127 (1979)
28. G. Farkas, C. Tóth, A. Kőházi-Kis, Opt. Eng. **32**(10), 2476 (1993)
29. M. Aeschlimann, C.A. Schmuttenmaer, H.E. Elsayed-Ali, R.J.D. Miller, J. Cao, Y. Gao, D.A. Mantell, J. Chem. Phys. **102**(21), 8606 (1995)
30. N.B. Delone, V.P. Krainov, *Multiphoton Processes in Atoms* (Springer, Berlin, 1994)
31. P.H. Bucksbaum, R.R. Freeman, M. Bashkansky, T.J. McIlrath, J. Opt. Soc. Am. B **4**(5), 760 (1987)
32. N.E. Christensen, B. Feuerbacher, Phys. Rev. B **10**, 2349 (1974)

33. G. Saathoff, L. Miaja-Avila, M. Aeschlimann, M.M. Murnane, H.C. Kapteyn, Phys. Rev. A **77**(2), 022903 (2008)
34. G.G. Paulus, W. Nicklich, H. Xu, P. Lambropoulos, H. Walther, Phys. Rev. Lett. **72**, 2851 (1994)
35. G. Wachter, C. Lemell, J. Burgdörfer, M. Schenk, M. Krüger, P. Hommelhoff, ArXiv e-prints 1201.0462 (2012)
36. F.H.M. Faisal, J.Z. Kamiński, E. Saczuk, Phys. Rev. A **72**(2), 023412 (2005)
37. P.B. Corkum, Phys. Rev. Lett. **71**, 1994 (1993)
38. H.W. Fink, Phys. Scr. **38**, 260 (1988)
39. T.Y. Fu, L.C. Cheng, C.H. Nien, T.T. Tsong, Phys. Rev. B **64**(11), 113401 (2001)
40. H.S. Kuo, I.S. Hwang, T.Y. Fu, J.Y. Wu, C.C. Chang, T.T. Tsong, Nano Lett. **4**(12), 2379 (2004)
41. C.C. Chang, H.S. Kuo, I.S. Hwang, T.T. Tsong, Nanotechnology **20**, 115401 (2009)
42. P. Hommelhoff, C. Kealhofer, A. Aghajani-Talesh, Y.R. Sortais, S.M. Foreman, M.A. Kasevich, Ultramicroscopy **109**(5), 423 (2009)

Index

K. Yamanouchi, K. Midorikawa (eds.), *Progress in Ultrafast Intense Laser Science*, Springer Series in Chemical Physics 104, DOI 10.1007/978-3-642-35052-8,